DETERMINATION OF POLARIMETRIC CAPABILITIES OF ASTRONOMICAL TELESCOPES

A Thesis

Submitted for the Degree of

Doctor of Philosophy (Technology)

Submitted by

RAMYA M ANCHE

Department of Applied Optics & Photonics

University College of Technology

University of Calcutta

February 2019

To my family, teachers, and friends

for their continuous support throughout my

Ph.D.

List of Publications

1. **Refereed Journal Articles**

   (a) **Analysis of polarization introduced due to the telescope optics of the Thirty Meter Telescope** - *Ramya Manjunath Anche, Asoke Kumar Sen, Gadiyara Chakrapani Anupama, Kasiviswanathan Sankarasubramanian, and Warren Skidmore*, Journal of Astronomical Telescopes, Instruments, and Systems 4.1, 018003, 2018.[1]

   (b) **Preliminary design techniques to mitigate the polarization effects due to telescope optics of the Thirty Meter Telescope (TMT)** - *Ramya M Anche, G. C. Anupama, & K. Sankarasubramanian*, Journal of Optics, 47(2), 166-173, 2018.[2]

   (c) **Optical spectroscopic and polarization properties of 2011 outburst of the recurrent nova T Pyxidis** - *M. Pavana, Ramya M Anche, G. C. Anupama, A. N. Ramaprakash, and G. Selvakumar*, accepted in Astronomy and Astrophysics, 2019. doi: 10.1051/0004-6361/201833728.[3]

2. **Refereed Conference Proceedings**

   (a) **Analytical modelling of Thirty Meter Telescope optics polarization** - *Ramya M. Anche, G. C. Anupama, Krishna Reddy, Asoke Sen, K. Sankarasubramanian, A. N. Ramaprakash, Sujan Sengupta, Warren Skidmore, Jenny Atwood, Sivarani Tirupathi, and Shashi Bhushan Pandey*, International Conference on Optics

---

[1]Presented in Chapter 4
[2]Presented in Chapter 4
[3]Presented in Chapter 2

and Photonics, Proc. SPIE 9654, 965408, 2015.[4]

(b) **Estimation of polarization aberrations and its effect on the point spread function of the Thirty Meter Telescope** - ***Ramya M. Anche***, *G. C. Anupama, S. Sriram, K. Sankarasubramanian, Warren Skidmore*, In Proc. of SPIE, Adaptive Optics Systems VI. Vol. 10703, 2018.[5]

(c) **The estimation of the instrumental polarization and crosstalk at the focus of the mid-infrared imaging system for the Thirty Meter Telescope** - ***Ramya M. Anche***, *Chris Packham, G. C. Anupama, K. Sankarasubramanian, Maheswar Gopinathan, and Manoj Puravankara*, In Proc. of SPIE, vol. 10702, pp. 1070298-1, 2018.[6]

(d) **Polarimetric analysis of the Thirty Meter Telescope (TMT) for modeling instrumental polarization characteristics** - *Jenny Atwood, Warren Skidmore, G. C. Anupama,* ***Ramya M. Anche****, Krishna Reddy, and Asoke Sen* Proc. SPIE 9150, Modeling, Systems Engineering, and Project Management for Astronomy VI, 915013, 2014.[7]

3. **Under Preparation**

(a) **Polarization model for the Multi-Application Solar Telescope (MAST) at the Udaipur Solar Observatory (USO)** ***Ramya M Anche***, *Shibu Mathew, Mohana Krishna, K. Sankarasubramanian, G C Anupama, Raja Bayanna, Ramya Bireddy and*

---

[4]Presented in Chapter 3
[5]Presented in Chapter 5
[6]Presented in Chapter 8
[7]Used in Chapter 4, 5

Rahul Yadav.[8]

(b) **Polarization effects due to the segmented primary of the Thirty Meter Telescope (TMT)** *Ramya M Anche, S. Sriram, G C Anupama, and K. Sankarasubramanian.*[9]

(c) **Polarimetric studies of Novae using a photopolarimeter** *Ramya M Anche, M. Pavana, G. C. Anupama, and S. Muneer.*[10]

---

[8]Presented in Chapter 7
[9]Presented in Chapter 6
[10]Presented in Chapter 2

Presentations

(a) **Estimation of polarization Aberrations for TMT** - - *Ramya M. Anche, G. C. Anupama, S. Sriram, K. Sankarasubramanian, and Warren Skidmore*, SPIE conference on Astronomical Instrumentation held at Texas, USA, June, 2018, **Poster presentation**.

(b) **The estimation of the instrumental polarization and crosstalk at the focus of the mid-infrared imaging system for the Thirty Meter Telescope** - - *Ramya M. Anche, Chris Packham, G. C. Anupama, K. Sankarasubramanian, Maheswar Gopinathan, and Manoj Puravankara*, SPIE conference on Astronomical Instrumentation held at Texas, USA, June, 2018, **Poster presentation**.

(c) **Polarimetric studies of Novae using a photopolarimeter** - - *Ramya M Anche, G. C. Anupama, & S. Muneer*, Asia-Pacific Regional International Astronomical Union meeting held at Taipei, Taiwan, 2017, **Oral presentation**.

(d) **Preliminary design techniques to mitigate the polarization effects from Thirty Meter Telescope (TMT)** - - *Ramya M Anche, G. C. Anupama, & K. Sankarasubramanian*, International conference on light and light based technologies held at Tezpur university, India, **Oral presentation**.

(e) **Mueller Matrices of the mirrors of the Thirty Meter Telescope (TMT)** - - *Ramya M Anche, G. C. Anupama, & K. Sankarasubramanian*, Astronomical society of India meeting at university of Kashmir, Srinagar, **Poster presentation**.

(f) **Analytical modelling of TMT telescope polarization** - - *Ramya M Anche, G. C Anupama. & et al.,* International conference on optics and photonics (ICOP) held at Calcutta university, Calcutta, **Oral presentation**.

(g) **Polarization properties of the 2011 outburst of the recurrent nova T-Pyxidis** - - *Ramya M Anche, G. C. Anupama, A N Ramaprakash, and V Mohan,* Astronomical society of India Meeting held at Pune, India, **Poster presentation**.

Abstract

Polarimetric observations of celestial objects reveal information regarding magnetic field, scattered dust and planetary atmosphere. The degree of polarization, which is of interest to astronomers, ranges from 10^{-5} to a few tens of percent. A potential problem in carrying out polarimetry in astronomy is the polarization introduced by the telescope and instrument optics to the incoming light. Hence, it is necessary to estimate the polarization effects for any telescope prior to the design of a polarimeter.

We have developed a polarization model to estimate the polarization effects from the telescope optics of one of the next generation large telescopes, the Thirty Meter Telescope (TMT). Analysis has been carried out to study the effects of the segments of the primary mirror of TMT and to understand their impact on instrumental polarization and crosstalk. The dependence of polarization effects on the field of view and zenith angle of the telescope at different instrument ports of the TMT has been determined. Polarization aberrations due to telescope optics have been estimated for the adaptive optics system to ascertain their effect on the final PSF of the telescope. This is useful in the design of second generation instruments for TMT with high contrast and high spatial resolution capabilities. We also propose a design technique for the mitigation of the polarization effects due to the telescope optics in future polarimetric instruments.

The polarization ray tracing algorithm which was used to develop the polarization model for TMT was also used to develop a polarization model for the Multi-Application Solar Telescope (MAST). The results of the analytical model were verified experimentally to understand the deviations between the model and the observations. The Stokes parameters were measured for different input polarizations at the wavelength of 6173 Å using an imaging spectro-polarimeter. A fairly good match is seen between the model and the observed Mueller matrix elements.

Finally, for an understanding of the science requirements, we have studied the polarimetric properties of a few nova systems as a case study. The studies were conducted using linear polarization data obtained with imaging and photopolarimeters available on the existing 1-2 m class telescopes.

Contents

List of Figures

List of Tables

Chapter 1

Introduction

1.1 Astronomical polarimetry

The three main observational techniques in astronomy are photometry, spectroscopy, and polarimetry. Photometry measures the brightness/magnitude of the source, spectroscopy measures the frequency/wavelength dependent flux which reveals the chemical composition of the source, and polarimetry determines the direction of the electric field vector in the incident light. Polarization, in general, arises as the consequence of the asymmetry or breakage of the symmetry either during the generation or the propagation of the light. Light from most stars is unpolarized owing to their spherical symmetry. Common asymmetries originate from magnetic fields, interstellar dust, distribution of scattered radiation (Leroy, 2000). Polarimetry helps probe the internal structure of the source. It enables detection of the magnetic fields ranging from 10 μG in interstellar medium to 10^{13} G in the case of pulsars (Tinbergen, 2005). The Zeeman effect (Landstreet, 1992) and Hanle effect (Stenflo, 2013) are used to determine the photospheric fields in magnetically active regions in the case of the Sun and other similar stars (Clarke, 2009). The observed polarization in the above cases could be either linear or circular in nature.

With reference to polarization arising from scattering, it can be (i) Thomp-

son scattering – scattering particles are free electrons present in hot stellar atmospheres; (ii) Rayleigh scattering – scattering by the molecules (e.g. the appearance of the blue sky); (ii) Mie scattering – scattering by dust particles (neither free electrons nor molecules). Measurement of linear polarization helps in identifying the scattering mechanism and provides information about the scattering medium (e.g. size, shape, refractive index of the particles) (Leroy, 2000). Multi-wavelength polarimetry is useful to get an insight into the size and composition of dust grains (ingredients of planets) in the planetary disks (Fukagawa et al., 2006). Detailed spatial structures of planet-forming disks can be imaged using high-angular-resolution and contrast (Keller, 2006). As disk scattered light is polarized while the starlight is unpolarized, the bright starlight can be removed quite effectively in polarimetry as shown in Figure 1.1. In principle, polarimetry can then be used to detect planets around stars.
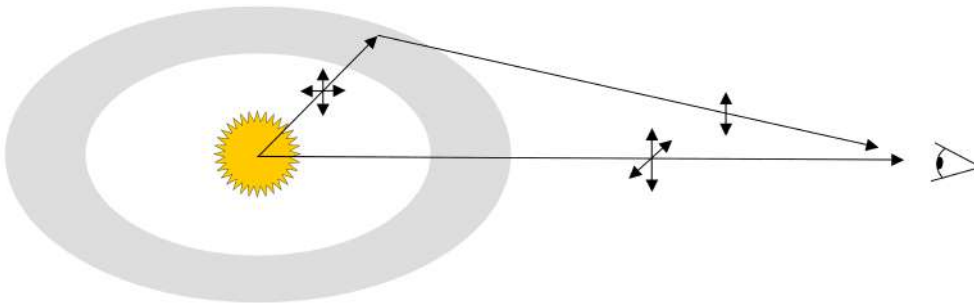
Figure 1.1: The unpolarized light is emitted by the central star; it becomes polarized due to scattering by the circumstellar material. Though the intensity from the central star dominates, measurements of the polarization provides details regarding the circumstellar material and disk (Keller, 2006)

.

In addition to these, polarimetry is useful in understanding the dichroic absorption of radiation by the interstellar dust and radiation processes such as synchrotron (the Crab Nebula and supernova remnants) or cyclotron emissions (Tinbergen, 2005).

1.2   Basic physics of polarimetry

Elliptical polarization is the most general form of polarization with linear and circular polarizations being its particular cases. The tip of the electric field vector traces out a straight line with time for linear polarization, and a circle for circular polarization (See Figure 1.2). The orientation of the electric field vector is random for unpolarized light. Partially polarized light is the incoherent sum of polarized and unpolarized components. In Figure 1.2, the
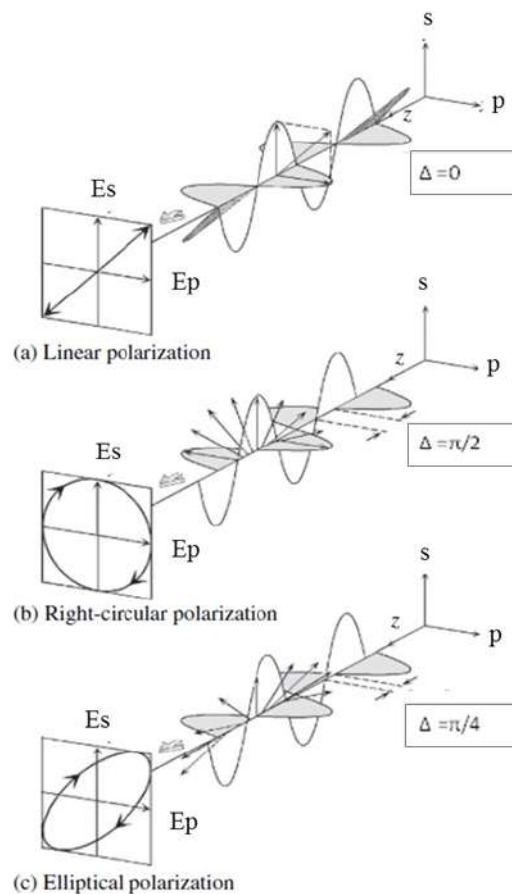
Figure 1.2: Schematic showing different types of polarizations (Fujiwara, 2007).

$s - p$ correspond to the reference coordinate system similar to Cartesian coordinates, E_p and E_s are the electric field vectors projected in and perpendicular to the plane of the paper, respectively.

1.2.1 Mathematical representation of polarization

The widely used formalisms for the representation of polarized light is Jones vectors and Stokes parameters. The Stokes parameters describe the polarization of light in terms of intensity measurements whereas Jones formalism describes in terms of amplitude and phase of the electric field vector. Jones calculus describe only 100% polarized light while Stokes parameters describe unpolarized and partially polarized light.

1.2.1.1 Jones calculus

The Jones calculus (Jones, 1941) are used when the phase information of the input polarized light is essential. Typically they are used to determine the polarization aberrations in the optical system. The Jones formalism uses Jones vectors to describe the polarization state of the light and Jones matrices to describe the optical elements. The Jones vector is,

$$\overrightarrow{J} = \begin{pmatrix} E_x(t) \\ E_y(t) \end{pmatrix} = \begin{pmatrix} E_x \exp^{i(kz-wt+\phi_x)} \\ E_y \exp^{i(kz-wt+\phi_y)} \end{pmatrix} \tag{1.1}$$

where, E_x and E_y are the x and y components of the electric field of the light wave propagating along the z-axis respectively, and ϕ_x and ϕ_y are the phase components of the electric field. The Jones matrix is of the form,

$$\begin{pmatrix} J_{11} & J_{12} \\ J_{21} & J_{22} \end{pmatrix} \tag{1.2}$$

where J_{ij} elements are complex.

1.2.1.2   Stokes parameters and Mueller matrix

Stokes parameters (Stokes, 1852) can be defined by the time average of the polarization ellipse,

$$
\begin{pmatrix} I \\ Q \\ U \\ V \end{pmatrix} = \begin{pmatrix} <E_x E_x^* + E_y E_y^*> \\ <E_x E_x^* - E_y E_y^*> \\ <E_x E_y^* + E_y E_x^*> \\ <i(E_x E_y^* - E_y E_x^*)> \end{pmatrix} = \begin{pmatrix} E_x^2 + E_y^2 \\ E_x^2 - E_y^2 \\ 2E_x E_y \cos(\delta) \\ 2E_x E_y \sin(\delta) \end{pmatrix} \tag{1.3}
$$

where E_x and E_x^* are the real and complex amplitudes of the electric field vector in the x-direction. δ is the phase difference between E_x and E_y components of the electric field. The degree of polarization and the position angle can be defined using the Stokes parameters as,

$$
\text{Degree Of Polarization (DOP)} = \frac{\sqrt{Q^2 + U^2 + V^2}}{I} \tag{1.4}
$$

$$
\text{Position Angle (PA)} = \frac{1}{2} \tan^{-1}\left(\frac{U}{Q}\right) \tag{1.5}
$$

The 4×4 matrix representation which is used to study the interaction of polarized (or unpolarized) light with elements that modify the polarization is **Mueller matrix** given by Mueller (1948). If S_{in} and S_{out} are the input and output Stokes vectors, then, the linear transformation between the input and output Stokes vectors is represented by the matrix **M**, $S_{out} = MS_{in}$ where,

$$
\begin{pmatrix} I_{out} \\ Q_{out} \\ U_{out} \\ V_{out} \end{pmatrix} = \begin{pmatrix} M11 & M12 & M13 & M14 \\ M21 & M22 & M23 & M24 \\ M31 & M32 & M33 & M34 \\ M41 & M42 & M43 & M44 \end{pmatrix} \begin{pmatrix} I_{in} \\ Q_{in} \\ U_{in} \\ V_{in} \end{pmatrix}. \tag{1.6}
$$

$M11$ represents that transformation of input intensity to output intensity and hence is always positive, and other elements can be positive or negative. Mueller matrices are used to represent polarizers (which changes the amplitude of the orthogonal components of the electric field unequally), retarders

(which introduces a phase shift between the orthogonal electric field components) and a rotator (which rotates the orthogonal components by an angle θ). The Mueller matrix of a linear polarizer with its transmission axis set at an angle θ is,

$$M(\theta) = \begin{pmatrix} 1 & \cos 2\theta & \sin 2\theta & 0 \\ \cos 2\theta & \cos^2 2\theta & \sin 2\theta \cos 2\theta & 0 \\ \sin 2\theta & \sin 2\theta \cos 2\theta & \sin^2 2\theta & 0 \\ 0 & 0 & 0 & 0 \end{pmatrix} \tag{1.7}$$

Similarly, the Mueller matrix for a retarder with ϕ being the orientation of fast axis and δ as retardance is,

$$M(\phi, \delta) = \begin{pmatrix} 1 & 0 & 0 & 0 \\ 0 & \cos^2 2\phi + \sin^2 2\phi \cos \delta & \sin 2\phi \cos 2\phi (1 - \cos \delta) & \sin 2\phi \sin \delta \\ 0 & \sin 2\phi \cos 2\phi (1 - \cos \delta) & \sin^2 2\phi + \cos^2 2\phi \cos \delta & \cos 2\phi \sin \delta \\ 0 & \sin 2\phi \sin \delta & -\cos 2\phi \sin \delta & \cos \delta \end{pmatrix} \tag{1.8}$$

Mueller matrix calculus is used in the measurement of the polarization in astronomy (Beck et al., 2005; Sanchez et al., 1991).

1.3 Measurement of polarization

All polarimeters whether imaging polarimeter or spectropolarimeter, follow the same principle in the measurement of the polarization. A simple polarimeter can be built using a rotating retarder (polarization modulator) and a linear polarizer (polarization analyzer) shown in Figure 1.3. The polarization of light is measured in terms of various intensity measurements corresponding to different Stokes parameters (Goldstein, 2003). The difference in intensity at two predefined states of the modulator divided by the total intensity is a measure of the polarization. When the input is unpolarized light, the detector will see a constant intensity irrespective of the state of the modulator. Various modulators used are crystal waveplates with rotating mount, photoelastic modulators, Pockels cells and liquid crystals (modulated by the application
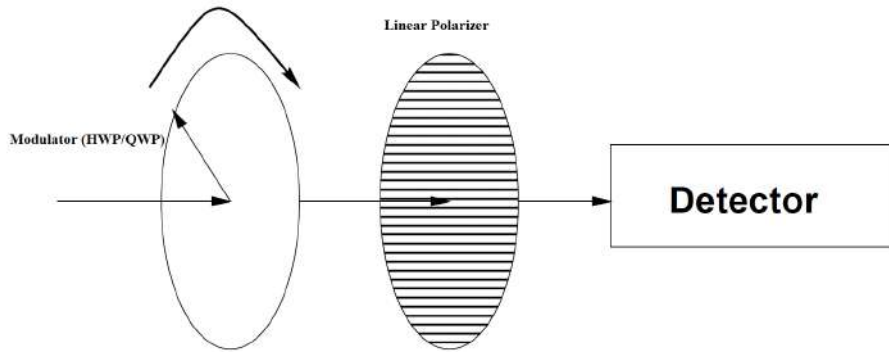
Figure 1.3: A simple polarimeter with a rotating modulator and a fixed linear polarizer (Keller, 2002)

of voltages). The analyzers are usually dual-beam polarizing prisms, such as Wollaston prisms (shown in figure 1.4), Glan-Thompson prism and polarizing beam displacer. The dual beam polarizing prisms produce two beams corresponding to both orthogonal polarization states thereby facilitating the simultaneous imaging of both the components on to the detector. It helps in achieving greater accuracy and most efficient use of the incident light (Hough, 2006). The modulation employed in the polarimeters using dual beam polariz-
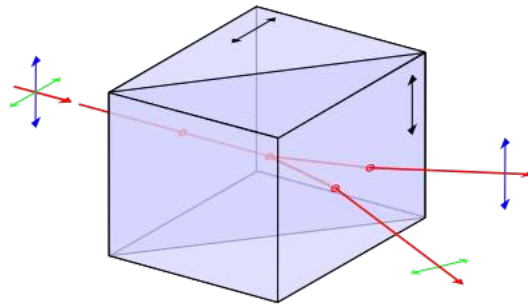
Figure 1.4: Wollaston prism showing the two orthogonal components of electric field. Image credits:Wikipedia

ers is referred to as spatial modulation as it allows simultaneous measurement of two or more Stokes parameters. Consequently, if the Stokes parameters are measured serially as in the case of Figure 1.3, the modulation is referred to as temporal modulation. Depending on the science requirements, modern sensitive polarimeters use a combination of both the modulation schemes to obtain optimal measurements.

1.4 Challenges in astronomical polarimetry

Astronomical polarimetry is limited by systematic errors which can be comparable to statistical errors (photon noise/ read-out noise). Some of the common errors associated with polarimetry can originate from atmospheric seeing, a modification by telescope/instrument or from the variable polarized sky background. The major challenge involves minimizing the polarization modification by the telescope optics as it is the first optical element in astronomical observations. Ideally, the telescope and instrument optics should not alter or introduce any polarization to the incoming light. However, instrumental polarization and polarization aberrations are introduced by the lenses and mirrors in the telescope and instruments (e.g. McGuire & Chipman (1988); Stenflo (1989)). Oblique reflections on the mirror surfaces produce both polarizer and retarder actions which are minimal at the normal incidence. If the polarization measured at the telescope focus is nonzero for unpolarized incoming light, then it is termed as instrumental polarization (IP). Depolarization is the loss of polarization due to the telescope optics when a 100% linearly polarized light is incident and is measured as (100-P)%, where P is the polarization measured at the focus. Additionally, if the telescope system converts the incoming linear polarization to circular or vice-versa, it is called crosstalk (CT) (Sanchez et al., 1992).

If the optical system has an inherent cylindrical (or azimuthal) symmetry and the object is on the optical axis of the telescope, the polarization introduced by the optics will be canceled out mutually, resulting in zero IP and CT (Sanchez et al., 1992). In general, a Cassegrain system as shown in Figure 1.5 (with the object on the axis of the telescope) is preferred for polarization observations, as it is expected to be free of instrumental polarization (Leroy, 2000; Tinbergen, 2005). But, for the off-axis images, the symmetry is broken even in the case of the Cassegrain system as shown by Sen & Kakati (1997). In a real scenario, there are several other factors which alter the polarization of incoming light such as inhomogeneities in the thickness, composition, oxi-

dation, and aging of the coating (Sankarasubramanian et al., 1999; van Harten et al., 2009). These are different from the polarization effects caused by the reflection geometries of the telescope and are treated mostly as measurement noise.

In the case of the Nasmyth focus telescope, the light is directed towards various instruments using a fold mirror (Nasmyth mirror), which is placed after the secondary mirror, as shown in Figure 1.5[1]. For Coudé focus, one or more fold mirrors are used to direct the beam downwards after the Nasmyth focus. The use of fold mirrors in the optical layout leads to a breakage of the symmetry, which introduces a considerable amount of instrumental polarization and crosstalk during the polarization measurements.
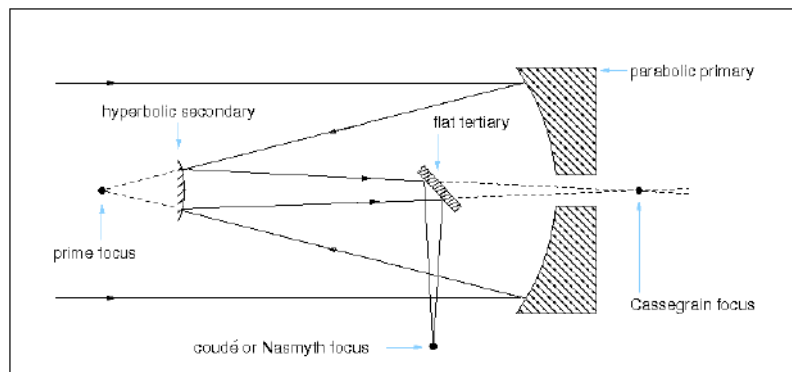
Figure 1.5: Schematic of a Cassegrain telescope showing the use of a flat tertiary mirror to direct the light toward Nasmyth or Coudé focus.

The instrumental polarization and crosstalk estimations have been done using the theoretical models and on sky measurements at the telescope focus for various telescopes (solar and stellar) since the last three decades. The instrumental polarization at the focus of the Gregory-Coudé solar telescope was estimated by a theoretical model and compared with the measurements of Stokes profiles by Sanchez et al. (1991). The uncertainty in the predictions made by the model was found to be 10% due to the variation in the refractive index of the mirror coating. Sankarasubramanian et al. (1999) measured the complex refractive index of the aluminum coated mirrors of the Kodaikanal tunnel tower telescope using an ellipsometer. This was then used for the

---

[1]`http://www.vikdhillon.staff.shef.ac.uk/teaching/phy217/telescopes/`
`phy217_tel_coude.html`

instrumental polarization estimation. The instrumental polarization of the 2.3 m Vainu Bappu Telescope (VBT) for wide field imaging was estimated by Sen & Kakati (1997). The calibration of the instrumental polarization for the Domeless solar telescope was investigated in Kiyohara et al. (2004), they found a 7% difference between the model and the observation for the crosstalk from Stokes Q, U and V. The polarization model for the German-Vacuum Tower telescope was developed in Beck et al. (2005) which describes the time-dependent polarization properties. The polarization calibration has been done for the Solar Optical Telescope on Hinode (Ichimoto et al., 2008) and Helioseismic and Magnetic Imager (HMI) onboard the Solar Dynamics Observatory (SDO) (Schou et al., 2012). An extensive analysis of the IP at the focus of the Very Large Telescope (VLT) and European Extremely Large Telescope (E-ELT) is presented in de Juan Ovelar et al. (2012). They use the polarimetric system code M&m's to estimate the IP due to the optical path for a wavelength range of 500-900 nm and zenith angle of 0 - 90 degrees for E-ELT. Yuan (2014) has developed a polarization model for the New Vacuum Telescope Solar telescope and compared with the observations. For the recent Daniel K. Inouye Solar Telescope, the polarization calibration model is developed in Sueoka & Harrington (2016).

It is evident that the optical configuration and the mirror coating in telescopes pose problems during accurate polarimetric measurement. The calibration of telescope polarization properties is then essential to take full advantage of the capabilities of high precision polarimetry. The development of a polarization model is the first step towards achieving accurate polarimetry for any telescope as it is challenging to design a "polarization-free telescope". A polarization model of the telescope helps in deciding the wavelength range, field of view, and instrument configuration of the polarimetric instrument. The polarization model of the telescope can be included in the polarization data reduction pipeline to account for the instrumental polarization and crosstalk from the science data.

The three next-generation large telescopes, the European Large Telescope (ELT), the Thirty Meter Telescope (TMT) and the Giant Magellan Telescope (GMT) have Nasmyth (fold) mirror in their optical configuration. The primary mirror of these telescopes is segmented instead of a monolithic (a single mirror). Polarimetric capability would be one of the important capabilities that these telescopes would be called upon. At present, there are no first generation instruments with the polarimetric capability on any of these telescopes. It would be extremely challenging to design a polarimetric instrument for these telescopes due to the polarization effects from the telescope optics. As mentioned above, the instrumental polarization has been estimated at the focus of ELT by de Juan Ovelar et al. (2014) with the primary mirror as a monolith. Di Varano et al. (2018) have performed the initial polarimetric analysis with a segmented primary mirror of ELT along with a phase A design of the polarimetric unit. However, polarimetric analysis for the Thirty Meter Telescope has not been carried out.

1.5 Thesis outline

The thesis focuses on the development of the polarization model for two different telescope configurations: The Thirty Meter Telescope (TMT) and the Multi-Application Solar Telescope (MAST). It also involves understanding the science requirements for accurate polarimetry through the analysis of a polarimetric science case. The primary motivation of the thesis is to understand the polarization effects for the Thirty Meter Telescope. The model is developed with primary as the monolith initially. The segments of the primary mirror are considered to understand their effect on the polarization. The impact of the polarization effects on the non-polarimetric instruments is also studied. The model is also verified experimentally with one of the existing telescopes, MAST.

During the course of development of the model, a sample of 40 polarimetric science cases was collected by the Polarimetry Modeling and Working

Group of TMT[2] which specified the requirements on IP and CT (available as a TMT internal document). The level of polarization in the science cases varied from 0.1 to few tens of percent. Among those science cases, we carried out the polarimetric observation and data analysis for the nova systems to understand the level of polarization in the science data and requirement on the limit of instrumental polarization and crosstalk. The polarization model was developed for TMT, and the modeling results were compared with the science requirements. The model included some of the ideal parameters such as the refractive index of the mirror coating, thickness, and ageing of the coating which are found to vary with time. To understand the deviation between the model and the measurements, the polarization model was additionally developed for the Multi-Application Solar Telescope, and was verified experimentally.

The polarization effects from the telescope optics have not been studied extensively for any other large telescopes. This study will help in achieving precise requirements for future instruments with polarimetric capability for TMT.

The thesis is divided into seven chapters as explained below,

1. **Chapter 2: Polarization data analysis of novae**

   Novae belong to the class of cataclysmic variable stars. Polarimetry of novae during eruption complements the other observational methods by providing information like asphericity and dust formation in the ejecta. The polarization data for four novae are obtained from an imaging polarimeter and photopolarimeter. The instrumental polarization is determined by the observation of unpolarized stars. The level of polarization of novae, instrumental polarization and position angle correction required in these systems are studied.

2. **Chapter 3: Development of polarization model**

   An analytical polarization ray tracing model has been developed for estimating the polarization effects from TMT and MAST. The algorithm

---

[2]`https://docushare.tmt.org/docushare/dsweb/Get/Document-31160/records\`
`%20of\%20program\%20assessments_20150729.xlsx`

for the models is explained in detail. The polarization analysis in the
Zemax (optical design software) to determine the polarization induced
aberrations is also described.

3. **Chapter 4: Polarization model for the Thirty Meter Telescope
   (TMT)**

   Instrumental polarization, crosstalk, and depolarization have been esti-
   mated for the TMT over the field of view of the telescope and operating
   wavelength range. Mueller matrices are given for all the different instru-
   ment ports on the Nasmyth platform. Preliminary design techniques to
   mitigate the polarization effects are analyzed. The estimations are made
   for the monolith primary mirror of the TMT.

4. **Chapter 5: Polarization aberrations for the Thirty Meter Tele-
   scope and NFIRAOS**

   The polarization aberrations are estimated for the TMT optics and the
   Narrow Field Infrared Adaptive Optics System (one of the first genera-
   tion instrument for TMT). The Jones pupil maps, Amplitude Response
   Matrix, and the Point Spread Matrix are determined at the focus of TMT
   and NFIRAOS. The magnitude of the ghost PSF and the ellipticity of
   the final PSF are calculated.

5. **Chapter 6: Polarization effects from the segmented primary
   mirror of TMT**

   The segmentation of the primary mirror is considered in Zemax$^{®}$ to
   understand the impact of segments on the polarization effects. The vari-
   ation in the Mueller matrices due to tilt and piston of the segments,
   missing segments and coating variation of the segments are studied in
   detail. Coating parameters of segments are found to cause the most sig-
   nificant variation in polarization compared to all the other factors.

6. **Chapter 7: Polarization model for the Multi-Application Solar Telescope**

   The MAST telescope consists of four fold mirrors and a derotator system in its optical configuration. Since, it is an altitude-azimuth system, the instrumental polarization and crosstalk changes over the day. An analytical model is developed to determine the Mueller matrix of the telescope. The Mueller matrix is also estimated experimentally by measuring the output Stokes vectors for different input polarization. The deviations between model and observations are understood in terms of parameters including refractive index variation, dust deposition amongst others.

7. **Chapter 8: Summary and future work**

   The implications of the polarization effects from the telescope optics on the observations are discussed for the TMT. Details regarding the second generation instruments for TMT with the polarimetric capability is given. The application of the polarization model developed here to the other existing and future telescopes is explored.

Chapter 2

Polarization data analysis of novae

2.1 Nova : Introduction

Nova outburst is an astronomical phenomenon which is accompanied by the ejection of matter causing an increase in luminosity leading to the sudden appearance of a bright star in the sky (which fades away over several weeks or months). They are interacting binary star systems with white dwarf primary and a Roche-lobe filling secondary. The hydrogen-rich material from the secondary star flows through the inner Lagrangian point onto an accretion disc which surrounds the white dwarf. Figure 2.1 shows the accretion of hydrogen-rich material onto a white dwarf from the Roche-Lobe of the secondary. Once the accreted matter reaches a critical amount, the pressure and temperature increase at the base of the envelope of the white dwarf, igniting a thermonuclear runaway reaction (Bode & Evans, 2008; Starrfield, 1969,9). This causes the explosion along with the ejection of the envelope. Nova phenomenon releases
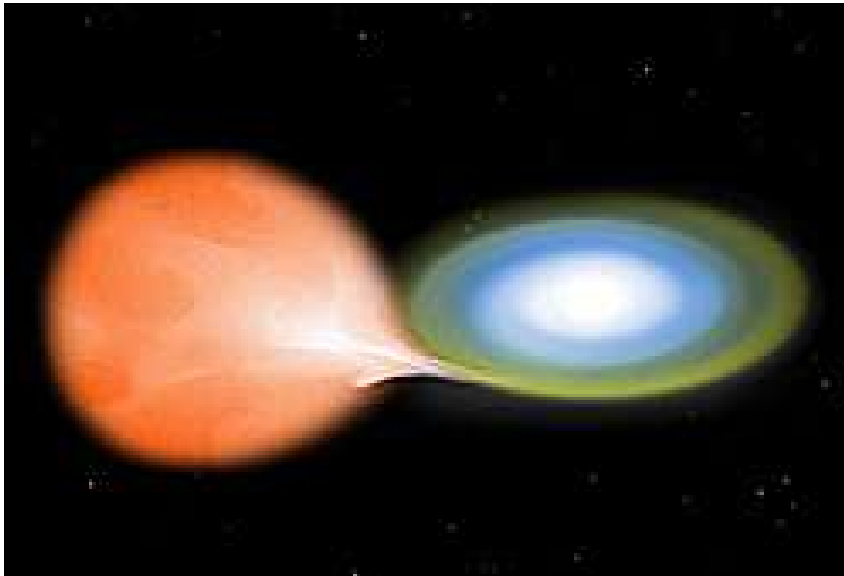
Figure 2.1: An artist's impression of white dwarf accreting hydrogen from its companion star through Roche Lobe. Credits: (Illustration) NASA/CXC/M.Weiss

an energy $\sim 10^{45}$ ergs and mass $\sim 10^{-4} M_\odot$.

Novae serve as laboratories for understanding the physics of nuclear burning and accretion. Classical nova eruptions are the most common types of novae (Bode & Evans, 2008). Recurrent novae are known to have more than one recorded outbursts (Anupama, 2008). The properties and evolution of novae are studied extensively through photometry, spectroscopy, and polarimetry. As the material is ejected anisotropically during the nova eruption, it is expected to be polarized (Evans et al., 2002). The ejected material is also known to expand aspherically and inhomogeneously during the early stages of the outburst. Observations carried out over the last three decades have shown that many novae show strong infrared emission due to dust formation. The broadband polarimetric observations during this phase of nova can provide information regarding the size and nature of the dust particles and distribution of the material in the ejecta (Ikeda et al., 2000).

Several novae have been studied using polarimetry in the past to understand the asymmetry and geometry of the ejecta. V446 Herculis (Nova Her 1960) was the first nova to be observed, and a constant linear polarization was measured to within 0.13% by Grigorian et al. (1961). The photopolarimetry of V533 Herculis (Nova Her 1963) did not show any significant change in the

polarization values though the magnitude fluctuated during the same period. Clarke (1964) concluded that the observed polarization was mostly from the interstellar origin for V533 Her. The recurrent nova T Pyxidis during its outburst in 1967 showed a short period of fluctuations in the polarization degree and position angle (Eggen et al., 1967). The wavelength dependence of polarization was studied for HR Delphini (Nova Del 1967), FH Serpentis (Nova Ser 1970) and LV Vulpeculae (Nova Vul 1968 no.1) by Zellner & Morrison (1971). HR Del and FH Ser showed significant variation in the polarization values while LV Vul did not show any such variation. Metz (1989) observed linear and circular polarization values in V3885 Sgr (Nova Sgr 1983). They were significantly small and did not show any considerable variability. The linear polarization observation of V1668 Cygni (Nova Cyg 1978) (Blitzstein et al., 1980; Piirola & Korhonen, 1979) and V705 Cassiopeiae (Nova Cas 1993) (Okazaki et al., 1996) showed an increase in the degree of the polarization during the dust-formation phase of the nova. Variable linear polarization was observed for the recurrent nova RS Oph during its 1985 outburst by Cropper (1990), who separated the intrinsic and interstellar components and obtained an independent limit on the distance of RS oph. The spectropolarimetric observations of CI Cam, V4633 Sgr (Nova Sgr 1998) and U Scorpii (1999 outburst) was carried out by Ikeda et al. (2000) The presence of intrinsic polarization was not detected for CI Cam and V4633 Sgr whereas, the depolarization effect on emission was seen in the case of U Sco during its outburst. Evans et al. (2002) carried out broadband optical polarimetry of the classical novae V705 Cas, V4362 Sgr, V2313 Oph and BY Cir during their eruption. The intrinsic component of the polarization was observed in all the novae with variability in the timescale of 1 day. Intrinsic polarization was detected in the case of recurrent nova U Scorpii during its 2010 outburst (Anupama et al., 2013).

In this Chapter, we discuss the imaging polarimetry of the recurrent nova T Pyxidis and photopolarimetry of three classical novae (V1535 Sco, V5668 Sgr, V3661 Oph). The description regarding the telescopes and the instruments are provided. The data analysis and interpretation carried out here serve as an

understanding of the science aspects and requirements for accurate polarimetry in dealing with instrumental polarization and crosstalk from the telescope and other optics in the instruments.

2.2 Imaging polarimetry of nova T Pyxidis

T Pyxidis is a recurrent nova, whose eruptions were observed in 1809, 1902, 1945, 1966 and the most recent one in 2011. The 2011 outburst was discovered by M. Linnolt at 13.0 V magnitude (Schaefer et al., 2013), on April 14.29 UT (JD 2455665.79), and was well studied with multi-wavelength observations. The current outburst was after 45 years (previous interval 22 years). After an initial rise for three days, the light curve showed a pre-maximum halt for about ten days, before its final rise to maximum on 2011 May 12.22 (Surina et al., 2014). Polarization observations were obtained with the imaging polarimeter at the IUCAA Girawali telescope from April 15 to May 5 for eight days. The observations, data analysis, and results are explained in the upcoming sections.

2.2.1 Telescope and instrument

The 2 m telescope at the IUCAA Girawali Observatory has a Cassegrain focus with a focal ratio of F/10. The IUCAA Faint Object Spectrograph and Camera (IFOSC) is the main instrument on the telescopes Cassegrain port. IFOSC's capabilities are enhanced with a polarimetric imaging mode with a field of view of about two arcmin radii as shown in Figure 2.2. It measures linear polarization in the wavelength band: 350 to 850 nm. The polarimeter has a stepped half wave plate (HWP) followed by a Wollaston prism; a focal mask is used to prevent the ordinary and extraordinary images overlapping (Ramaprakash et al., 1998). The instrument has a built-in acquisition and guidance unit. The Wollaston prism which is placed in the path of the light splits the incoming beam into ordinary and extraordinary components producing two images on CCD for every point in the telescope focal plane. A half wave plate on a rotatable mount is placed preceding the Wollaston prism.
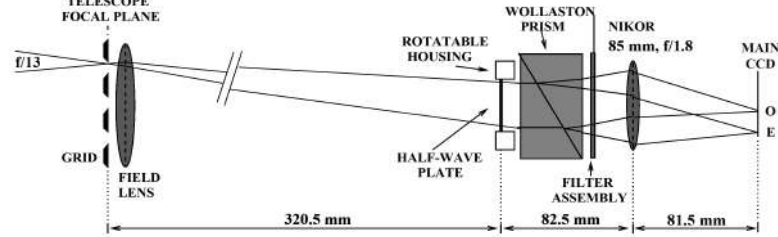
Figure 2.2: Optical layout of the imaging polarimeter at the IGO telescope (Ramaprakash et al., 1998)

2.2.2 Observations

Polarimetric observations of T Pyxidis were obtained from day 1.36 (April 15, 2011) to 29.33 (May 5, 2011) during the initial phase for eight nights. Polarized standard star, HD160529 was observed on day 2.71, and HD147084 was observed from day 2.71 to 7.71. Unpolarized standard star, HD98281 was observed from day 2.71 to 7.71. The instrumental polarization correction was obtained from the unpolarized standard star, and the position angle correction was estimated from polarized standard stars.

2.2.3 Data analysis

The observations are made at four different positions (0, 22.5, 45, 67.5) of the half-wave plate. The tool used for analyzing the data is Image Reduction and Analysis Facility (IRAF). Ordinary and extraordinary image pairs are identified in each of the frames, and aperture photometry is carried out on each of the frames within apertures of specified radius to determine the counts due to both the object and the background. The ratio of the counts in ordinary (I_o) and extraordinary (I_e) images were used to estimate normalized q and u (Ramaprakash et al., 1998).

$$q = \frac{I_o(0) - I_e(0)}{I_o(0) + I_e(0)}; \quad u = \frac{I_o(22.5) - I_e(22.5)}{I_o(22.5) + I_e(22.5)} \tag{2.1}$$

The degree of polarization and the position angle are estimated from q and u as,

$$P = \sqrt{q^2 + u^2}; \quad PA = \frac{1}{2} \tan^{-1}\left(\frac{u}{q}\right) \tag{2.2}$$

2.2.4 Interpretation of the data

The instrumental polarization correction obtained from the unpolarized standard star was estimated to be 0.1%, and position angle correction was evaluated from polarized standard stars. The observed degree of polarization and position angle for the polarized standard stars are listed in Table 2.1. The degree of polarization and position angle values estimated for T Pyx during its 2011 outburst are given in Table 2.2. During the initial rise phase, the degree of polarization is found to increase, in all the bands, until day 4 – 5, and decrease subsequently. For example, the degree of polarization in the V increased from a value of 0.69% on day 1.36 to 1.27% on day 5.35 and decreased to 0.37% by day 8.34. The degree of polarization was found to have increased from the estimate on day 8.34, during the next set of observations on days 28.34 and 29.33, with a rising trend. The position angle was found to be $112° \pm 18°$ during the entire period of observation.

Intrinsic polarization of the ejecta was detected by Eggen et al. (1967) during the 1967 outburst, and was found to vary with time. Polarization values of T Pyx during its 2011 outburst have been compared with those reported for the 1967 outburst during days 1.96 – 44.02. In Figure 2.3, the epochs of polarization observations made during the two outbursts are highlighted. The variability in the degree of polarization values in different filters for both the outbursts is shown in Table 2.4. An identical pattern in the variation of the degree of polarization is observed in both the outbursts, i.e., an initial rise in the values followed by a decrease in the early pre-maximum phase, followed by an increase in the degree of polarization during the optical maximum. While the trend is similar, it is noticed that the degree of polarization is lower in the 2011 outburst compared with the 1967 outburst. The maximum value of

Table 2.1: Polarimetric observations of polarized standard stars

Object	JD	Filter	P (%)	θ
HD160529	2455669.17	B	7.26±0.08	66.82±0.34
		V	7.48±0.04	66.48±0.18
		R	7.14±0.07	64.819±0.29
		I	6.01±0.06	65.869±0.27
		B[1]	7.46±0.04	20.1
		V	7.76±0.03	20.4
		R	7.41±0.06	21.7
		I	5.49±0.03	21.1
		B[2]	7.24	20.1
		V	7.52	20.1
HD147084	2455669.17	B	3.48±0.09	80.04±0.75
		V	4.18±0.05	79.04±0.45
	2455671.11	B	3.34±0.07	81.63±0.61
		V	3.98±0.05	78.75±0.40
	2455673.21	B	3.48±0.05	80.32±0.45
		V	4.15±0.06	79.72±0.45
	2455674.12	B	3.51±0.16	55.14±1.90
		V	4.08±0.05	55.73±0.32
		B[3]	3.5	32
		V	4.18	32
		V[4]	4.12±0.02	32.2
			4.16±0.01	32.1±1.9

[1]Goswami & Karinkuzhi (2013); [2]Clarke et al. (1998);
[3] Gehrels (1974) and [4]Goswami et al. (2010)

Table 2.2: Polarimetric observations of T Pyx during its 2011 outburst

JD	t (days)	Filter	P (%)	θ
2455667.14	1.36	B	0.65±0.06	102.05±2.57
		V	0.69±0.06	104.35±4.09
		R	0.72±0.08	112.92±3.27
		I	0.81±0.19	105.06±5.64
2455669.2	3.39	V	0.84±0.07	106.71±2.43
		R	0.85±0.08	104.11±2.63
		I	0.63±0.10	108.05±3.2
2455670.12	4.33	B	0.78±0.02	94.98±2.36
		V	0.84±0.04	93.468±2.05
		R	0.90±0.07	105.29±2.23
		I	0.97±0.06	101.09±1.83
2455671.14	5.35	B	1.25±0.06	100.18±1.42
		V	1.27±0.06	102.14±1.40
		R	1.13±0.06	102.48±1.58
		I	0.92±0.08	104.03±2.48
2455672.12	6.33	B	0.59±0.02	101.99±2.88
		V	0.49±0.05	113.30±2.99
		R	0.57±0.04	115.12±2.40
		I	0.33±0.06	112.82±5.80
2455673.21	7.42	B	0.23±0.03	129.4±4.73
2455674.13	8.34	B	0.38±0.03	113.41±1.23
		V	0.36±0.05	129.02±2.51
		R	0.32±0.02	100.97±4.10
		I	0.35±0.05	128.75±4.01
2455694.15	28.34	B	0.54±0.03	118.51±5.56
		V	0.53±0.03	112.04±1.66
		R	0.66±0.03	116.28±1.62
		I	0.51±0.05	122.81±2.94
2455695.11	29.33	B	0.64±0.06	127.51±6.44
		V	0.74±0.05	121.30±1.90
		R	0.87±0.08	118.41±3.08
		I	0.75±0.05	122.19±1.84
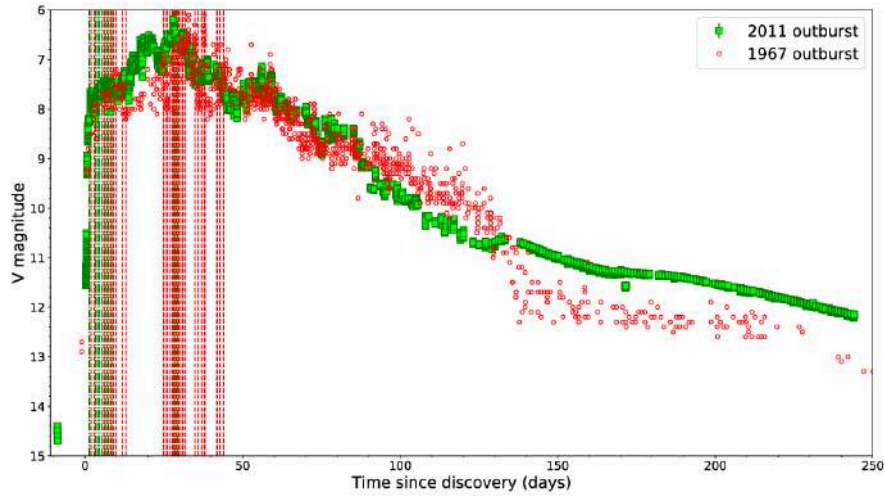
Figure 2.3: The light curve for T Pyx during its 1967 and 2011 eruptions. The green squares and red circles correspond to the 2011 and 1967 eruption respectively. The green and red dash lines correspond to the polarization epochs during 2011 and 1967 eruption respectively.

polarization in B filter and V filter are 2.3% and 2.32% respectively for 1967 outburst, while for 2011 outburst it is 1.25% and 1.27% in B and V filters respectively. Position angles observed during 2011 outburst are consistent with those of the 1967 outburst (Figure 2.4). Although the polarization values for 1967 and 2011 outbursts are uncorrected for the interstellar polarization, they show similar behavior indicating intrinsic polarization.

2.2.5 Discussions

It is suggested that the intrinsic polarization observed in the system might be due to two reasons: a) asymmetry of the ejecta at the time of outburst, b) presence of silicate grains as suggested by Svatos (1983) for the 1967 eruption. IR observations of T Pyx during the 2011 outburst indicate the presence of pre-outburst dust in the system with a mass of $\sim 10^{-5}\, M_\odot$ (Evans et al., 2012). Asymmetry in the system at the time of outburst can be due to the interaction of the initial ejecta with circumstellar material, also resulting in the decrease in velocity as observed in the spectral data till day 12.32 (Pavana et al., 2019). Coincidentally, there was a marginal detection of hard X-rays during days 14-
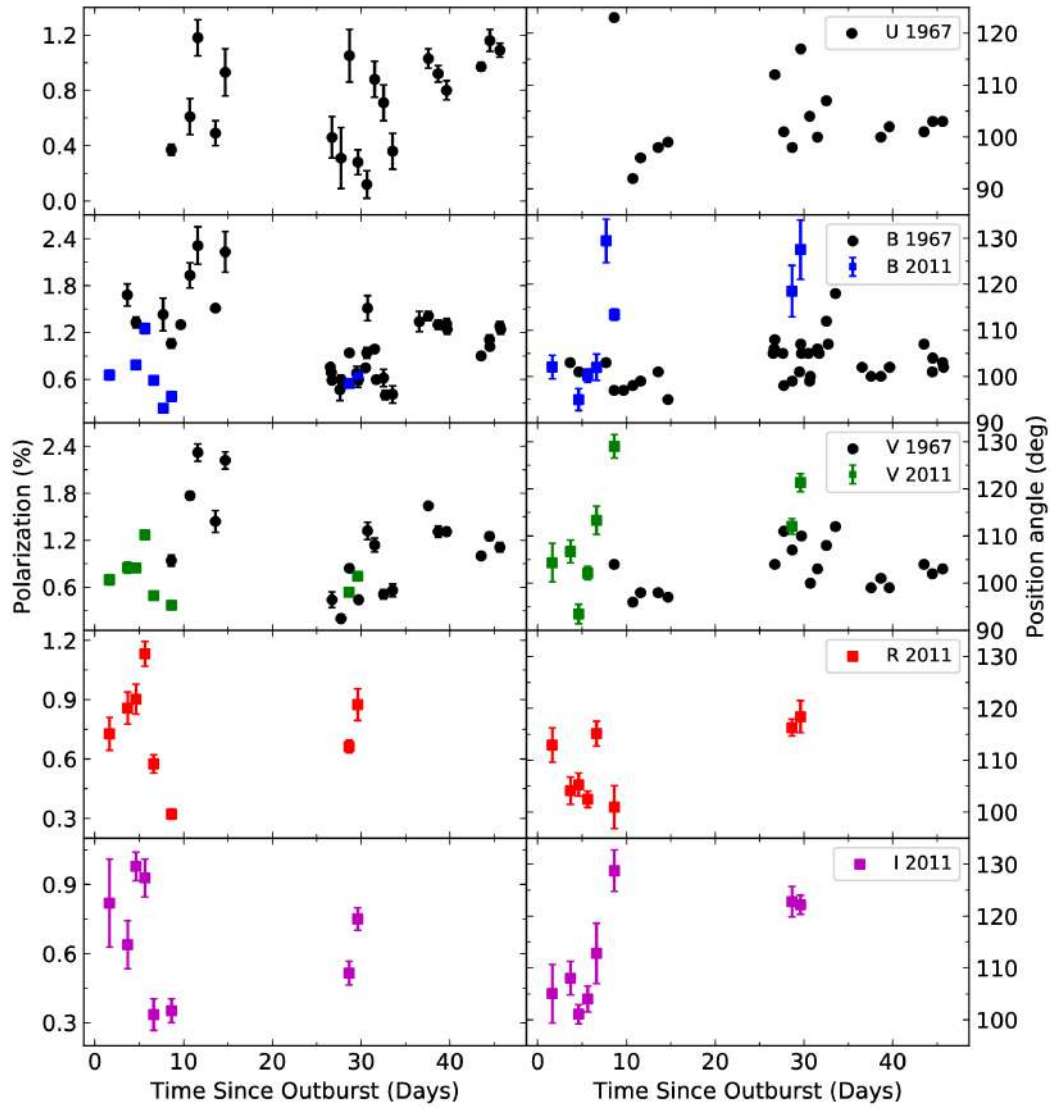
Figure 2.4: The variability in the degree of polarization and position angle for 2011 and 1967 outbursts. The squares and circles correspond to 2011 and 1967 outburst respectively.

20, which has been attributed by Chomiuk et al. (2014) to an interaction of the nova ejecta with pre-existing circumbinary material.

2.3 Photopolarimetric observations of novae

Three classical novae, V1535 Sco (Nova Sco 2015), V5668 Sgr (Nova Sgr 2015), and V3661 Oph (Nova Oph 2016) were observed during their initial outburst phase using the photopolarimeter on 1 m Carl-Zeiss telescope at the Vainu Bappu Observatory (VBO), Kavalur, India. The details of the novae observed are given in Table 2.3

Table 2.3: List of novae observed using the photopolarimeter at 1 m telescope in VBO observatory.

Object	RA	DEC	Date of discovery	Visual Maximum (JD)
Nova Sco 2015	17 03 26	-35 04 14	2015 February 11.84	2457000
Nova Sgr 2015	18 36 57	-28 55 42	2015 March 15.63	2457102
Nova Oph 2016	17 35 50	-29 34 24	2016 March 11.90	2457460

2.3.1 Instrument and data acquisition

The 1 m telescope at the VBO observatory has a Ritchey-Chretien F/13 optical configuration, with a primary mirror of 1.02 m diameter and a plate scale of 15.5 arcsec/mm. The photopolarimeter at this telescope is capable of acquiring polarization observations in three spectral bands simultaneously (Srinivasulu et al., 2015). The polarizing beam displacer made of Calcite is used as an analyzer which produces the ordinary and extraordinary beams, and they are detected by the same photo-multiplier using a high speed rotating chopper. The modulator used in this polarimeter is a super-achromatic Pancharatnam half-wave plate with a rotatable mount. A Glan-Taylor prism is inserted into the beam periodically to produce a fully polarized light for checking the polarization efficiency. The UBV pass-band filters approximate that of Johnson's filters whereas the R_cI_c pass-band approximates that of Cousin's. The optical layout of the polarimeter is shown in Figure 2.5. The half-wave plate is rotated
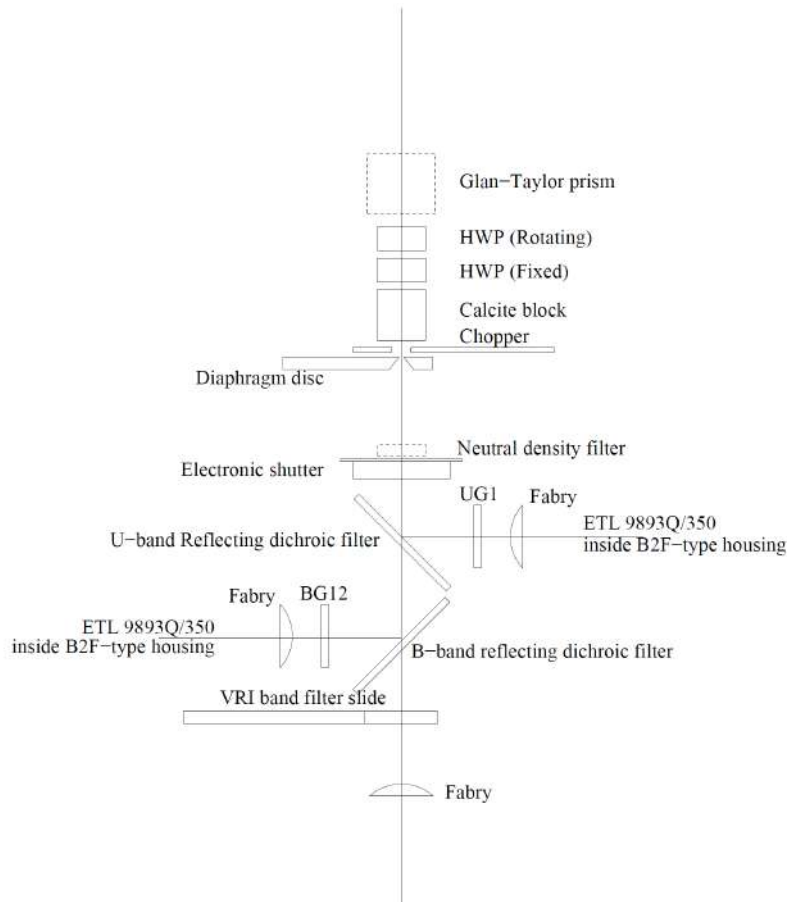
Figure 2.5: Schematic layout of the photopolarimeter showing different components at the 1 m telescope in VBO.

at specified intervals from the reference position, and at each position, the intensity counts from the ordinary and extraordinary beams are stored. This is repeated for many cycles until the accuracy in the measurement is achieved. The data pipeline available estimates and stores the linear polarization, position angle and gain correction along with their errors (Raveendran et al., 2015).

2.3.2 V1535 Sco

V1535 Sco was discovered by T. Kojina, on 2015 Feb 11.837 at a visual magnitude of 9.70. The light curve of the nova in Figure 2.6 shows a faster decline in the initial optically thick phase followed by a slower decline during the optically thin phase which is pretty standard. Interestingly, in the early portion of the lightcurve, a plateau phase is seen which lasts for couple of days around
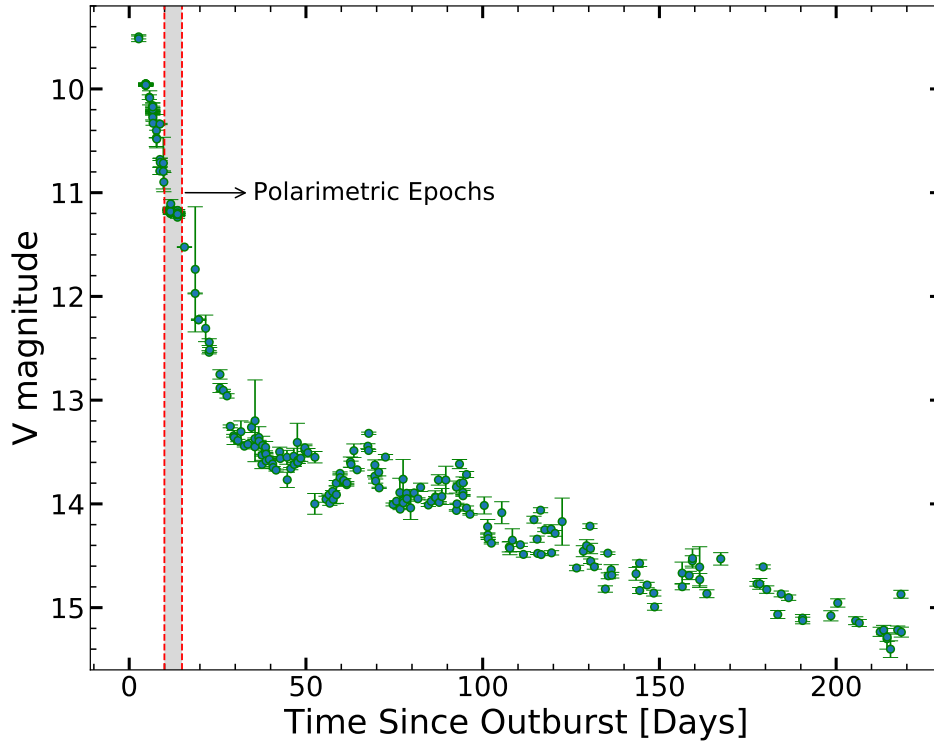
Figure 2.6: The light curve for V1535 Sco obtained from AAVSO magnitudes. The epochs of the polarimetric observations are marked.

JD 2457077.5 (day 12) after the outburst. The polarization observations were obtained in VR_cI_c filters from day 9.95 to day 14.93 during the initial phase.

2.3.2.1   Interpretation

The period of polarization observations are marked in Figure 2.6. The instrumental polarization was obtained by observing the standard unpolarized stars shown in Table 2.4. The PA correction was obtained from the polarized standard stars given in Table 2.5. The evolution of the degree of polarization and the position angle for V1535 Sco is given in Table 2.6. Polarization (P) increases from 1.64% to 2.23% from day 11.95 to 12.94 and decreases to 1.5% on day 13.96 in V-band. In the case of R_c-band, the P increases from 1.00% to 1.38% from day 10.949 to 11.95 and remains constant after that. The P in BI_c bands obtained on the day 14.936 is 2.83% and 1.53% respectively. During the entire span of the observations, the position angle remains constant at 115±8 degrees as shown in Figure 2.7. The variability in the degree of polar-

ization suggests the presence of intrinsic polarization in nova though it is not corrected for the interstellar component. The presence of intrinsic polarization can be confirmed from the $Q - U$ plane shown in Figure 2.8. The values are not co-linear in all the bands which indicates that the observed polarization values are not completely from the interstellar origin.

V1535 Sco is located at $l = 349.89$ and $b = 3.93$ at a distance of 9.7 kpc with E(B-V) value of 1.09. The polarization values of the field stars located with in the 1-degree field of view of V1535 Sco were obtained from Heiles (2000). The Q and U of the nearby stars with the distance is shown in Figure 2.9. Q is found to increase till 1.8 kpc and remains constant at 0.21±0.1% beyond that. U is found to decrease with the distance and found to be -0.42±0.02% at 2.4 kpc. As the observations of stars beyond 2.4 kpc is not available, the value of P till 2.4 kpc is found to be 0.45±0.1% is considered as the interstellar polarization.

2.3.2.2 Discussions

As the nova fades after the outburst at a rapid rate, it is known to have an optically thick ejecta. Munari et al. (2017) have studied the photometric evolution of V1535 Sco from the V-band light curve for one year. A plateau phase in the light curve has been observed around 2457077.5 (day 12) which lasted for a couple of days. An increase of 0.6% in polarization is observed from day 11 to 12 in VI_c filters. One of the reasons suggested for the plateau phase could be highly structured, non-spherical shape of the ejecta with optical thickness depending on its angular coordinates by Munari et al. (2017). The ejecta velocity is found to show a power law decay with time as found by indicating asymmetric ejecta flow. The velocity profiles of the Paschen lines $Pa\gamma$ and $Pa\beta$ also confirmed the asymmetry in the ejecta (Srivastava et al., 2015). The polarization observed in nova could be due to the asymmetry of the ejecta and anisotropic distribution of material in the ejecta.

Table 2.4: Polarimetric observations of unpolarized standard stars

JD	Object	Filter	P (%)
2457073.45	HD125184	B	0.08±0.04
		V	0.08±0.01
		R_c	0.07±0.01
		I_c	0.05±0.01
2457074.31	HD125184	V	0.06±0.02
		R_c	0.10±0.01
		I_c	0.10±0.01
2457075.26	HD65583	V	0.16±0.04
		R_c	0.04±0.04
		I_c	0.06±0.03
2457076.25	HD65583	B	0.22±0.11
		V	0.03±0.03
2457077.32	HD98281	B	0.07±0.09
		V	0.06±0.04
		R_c	0.03±0.02
		I_c	0.04±0.026
2457079.25	HD65583	U	0.08±0.08
		B	0.15±0.05
		V	0.04±0.03
		R_c	0.03±0.01
		I_c	0.01±0.02

Table 2.5: Polarimetric observations of polarized standard stars

Object	JD	Filter	**P** (%)	θ
2457073.42	HD147084	B	3.43±0.04	31.16±0.36
		V	4.26±0.05	32.12±0.36
		R_c	4.31±0.03	33.40±0.21
		I_c	4.17±0.03	32.68±0.21
2457074.24	HD43384	V	2.90±0.04	169.75±0.43
		R_c	2.72±0.02	170.98±0.27
		I_c	2.59±0.04	170.66±0.45
2457075.096	HD23512	V	2.27±0.05	30.47±0.74
		R_c	2.19±0.04	29.24±0.58
		I_c	2.13±0.04	27.79±0.64
2457075.447	HD142863	V	2.02±0.11	81.81±1.56
		R_c	1.93±0.04	85.37±0.64
		I_c	1.69±0.05	82.70±0.94
2457076.22	HD43384	B	2.92±0.06	170.97±0.60
		V	2.94±0.02	169.86±0.23
		R_c	2.86±0.04	170.36±0.40
		I_c	2.56±0.01	171.41±0.20
2457077.21	HD43384	B	2.92±0.04	171.71±0.47
		V	2.94±0.01	170.92±0.18
		R_c	2.73±0.01	170.31±0.13
		I_c	2.59±0.02	170.98±0.20
2457078.23	HD43384	B	2.75±0.10	168.64±0.90
		V	2.83±0.02	170.60±0.20
		R_c	2.71±0.01	170.52±0.16
		I_c	2.51±0.01	169.98±0.22
2457078.23	HD43384	U	2.48±0.03	169.76±0.39
		B	2.98±0.05	169.79±0.48
		V	2.99±0.03	170.85±0.27
		R_c	2.73±0.014	170.99±0.14
		I_c	2.60±0.024	171.53±0.26

Table 2.6: Polarimetric observations of V1535 Sco

JD	t (days)	Filter	P (%)	θ
2457074.48	9.953	V	1.56±0.21	109.39±3.99
		R_c	1.05±0.09	117.04±2.59
		I_c	0.67±0.27	95.16±11.82
2457075.49	10.949	V	1.52±0.22	108.31±4.22
		R_c	1.00±0.08	109.97±2.37
		I_c	1.18±0.12	124.71±2.98
2457076.48	11.950	V	1.64±0.19	119.96±3.44
		R_c	1.37±0.08	116.30±1.70
		I_c	0.91±0.18	120.46±5.64
2457077.48	12.945	V	2.23±0.17	109.13±2.20
		R_c	1.38±0.07	116.85±1.50
		I_c	1.40±0.11	108.68±2.28
2457078.49	13.962	V	1.50±0.17	119.84±3.35
		R_c	1.30±0.04	112.34±1.37
		I_c	1.16±0.09	107.65±2.36
2457079.47	14.936	B	2.83 ±0.31	96.16±2.86
		V	1.48±0.20	106.48±3.90
		R_c	1.25±0.06	114.50±1.66
		I_c	1.53±0.1	108.95±1.85
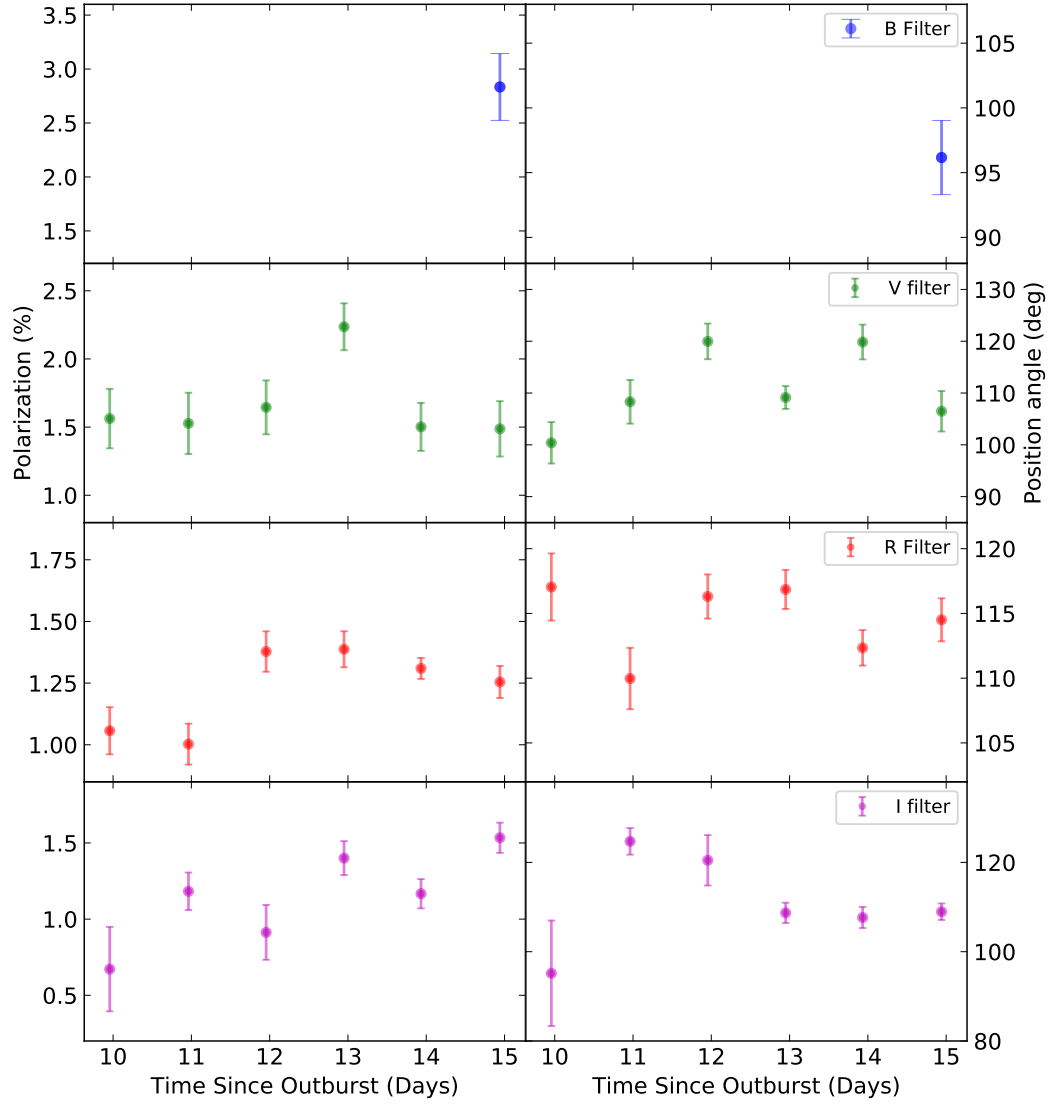
Figure 2.7: The degree of polarization and position angle for V1535 Sco.
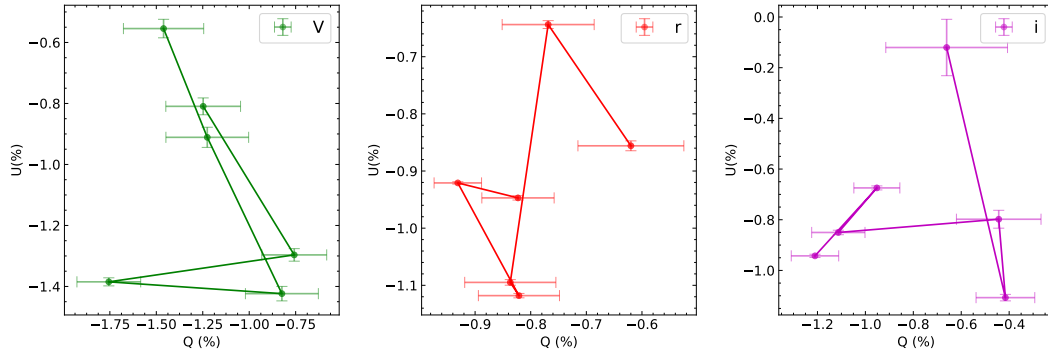
Figure 2.8: The $Q - U$ plot for $V R_c I_c$ filters for V1535 Sco

2.3.3 V5668 Sgr

V5668 Sgr (PNV J18365700-2855420 or Nova Sgr 2015b) was discovered on 2015 March 15.634 by Seach (2015) at visual magnitude of 6.0. It was found to
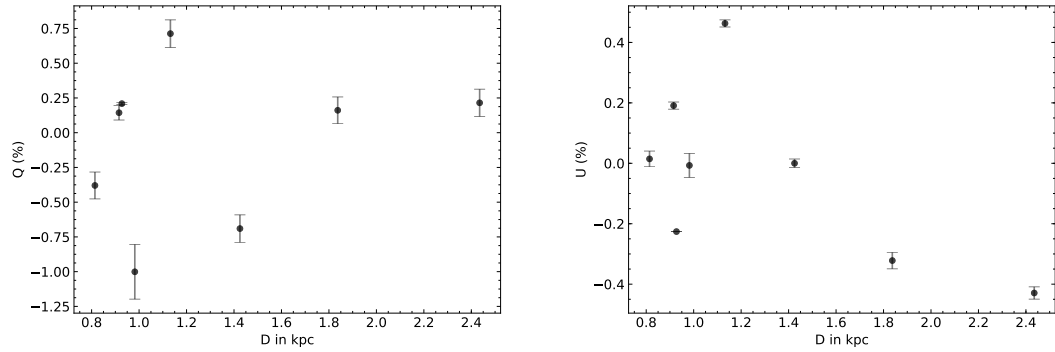
**Figure 2.9:** The $Q-U$ plot for different stars in the field of view of 1 degree around V1535 Sco (Heiles, 2000)
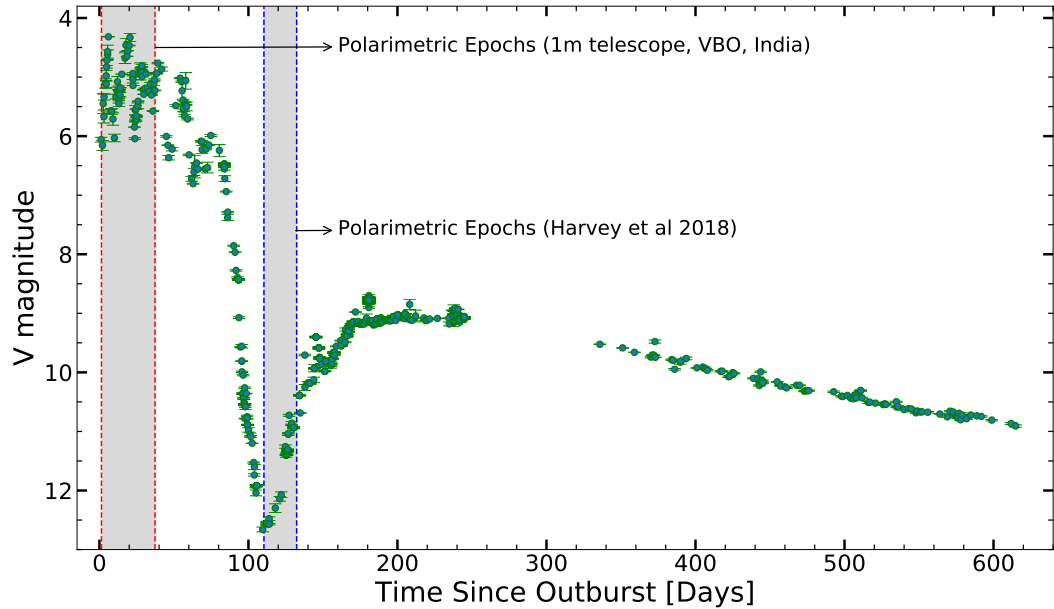
Figure 2.10: The light curve for V5668 Sgr obtained from AAVSO magnitudes. The epochs of the polarimetric observations are marked for our observations and Harvely et al (2018).

be a slowly evolving dust forming nova belonging to Fe II class. The distance to the nova is estimated to be 1.6 kpc. In the initial 90 days period, the magnitude varied between 5 and 7. After this phase, there was a steep decline in the magnitude to 13. The magnitude is found to increase to 9 after the deep minimum phase for the next 80 days. It stayed almost constant for the next 100 days and declined very slowly after that. The light curve of the nova for the visual magnitudes obtained from the AAVSO database is shown in Figure 2.10. The polarization observations are obtained from the photopolarimeter in $UBVR_CI_c$ filters for 13 days from day 1.366 to day 37.31.
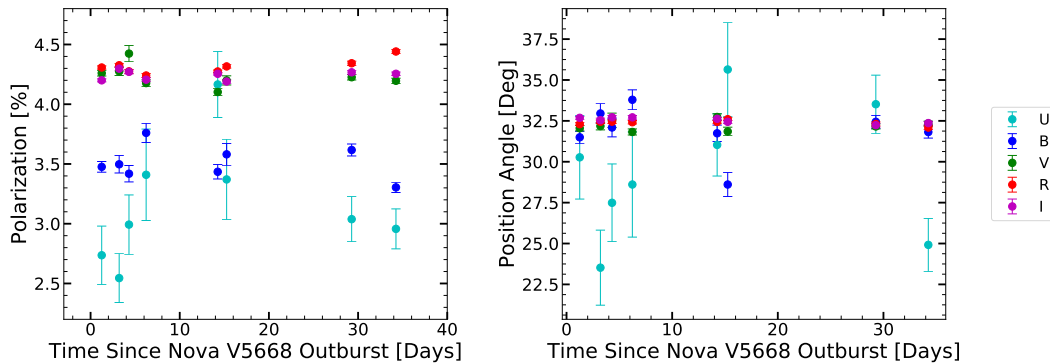
Figure 2.11: P and PA for the standard star HD147084 observed on the days on the V5668 Sgr observations.

2.3.3.1   Interpretation

The polarization epochs are marked in Figure 2.10. The list of unpolarized standard stars with their P values is given in Table 2.7. The polarization standard HD147804 was observed to obtain the PA correction. Figure 2.11 shows the P and PA for the standard star. Polarization parameters like the degree of polarization and position angle obtained from day 1.36 to 37.36 are given in Table 2.8. During the initial rise phase, the degree of polarization in VR_c filters increased from day 1.36 to 2.36 and then decreased the following day. It remains constant from day 6.36 to 37.36. In the case of UBI_c filter, the degree of polarization shows variability during the entire duration of observations. The position angle was found to vary from day 1.36 to day 15.36 in all the filters. It is found to remain constant 170±10 degrees from day 15.36 to 37.36. The variability in the P and PA is shown in Figure 2.12 for all the bands.

Polarization observations in BVR bands are presented by Harvey et al. (2018) for V5668 Sgr for five nights during the deep dust minimum phase, i.e. 111-114 days after the outburst. A variability in the polarization has been observed only in the B-band, and P remains constant in VR band. The maximum values of polarization are 1.699%, 0.77%, and 0.44% in BVR bands respectively. The wavelength dependence of the polarization values by Harvey et al. (2018) suggest the polarization due to scattering by the dust particles. The position angle is found to be consistent in both the observations at 150±15. During our observations, the maximum values of the polarization observed are

Table 2.7: Polarimetric observations of unpolarized standard stars obtained on the days of the V5668 Sgr observations

JD	Object	Filter	P (%)
2457098.23	HD90508	U	0.33±0.05
		B	0.05±0.04
		V	0.03±0.02
		R_c	0.05±0.01
		I_c	0.03±0.01
2457100.252	HD100623	U	0.25±0.01
		B	0.05±0.04
		V	0.03±0.02
		R_c	0.02±0.01
		I_c	0.01±0.01
2457102.30	HD125184	U	0.05±0.06
		B	0.06±0.06
		V	0.02±0.02
		R_c	0.04±0.01
		I_c	0.05±0.02
2457104.35	HD125184	U	0.15±0.06
		B	0.06±0.05
		V	0.13±0.03
		R_c	0.03±0.01
		I_c	0.05±0.02
2457106.455	HD144287	U	0.13±0.14
		B	0.17±0.07
		V	0.03±0.03
		R_c	0.04±0.01
		I_c	0.07±0.02
2457111.211	HD98281	U	0.07±0.09
		B	0.08±0.05
		V	0.03±0.02
		R_c	0.06±0.01
		I_c	0.03±0.02
2457111.211	HD100623	U	0.18±0.07
		B	0.12±0.04
		V	0.03±0.01
		R_c	0.03±0.02
		I_c	0.04±0.04
2457111.211	HD100623	U	0.20±0.04
		B	0.11±0.02
		V	0.04±0.01
		R_c	0.02±0.01
		I_c	0.02±0.01

Table 2.8: Polarimetric observations of V5668 Sgr

JD	t (days)	Filter	**P** (%)	θ
2457098.48	1.367	U	0.27±0.02	150.75±2.89
		B	0.37±0.02	154.59±1.69
		V	0.21±0.01	155.26±2.04
		R_c	0.19±0.01	150.79±1.59
		I_c	0.14±0.01	140.57±3.25
2457099.48	2.367	U	0.23±0.02	166.52±2.89
		B	0.37±0.02	157.55±1.95
		V	0.37±0.01	158.43±1.06
		R_c	0.24±0.01	164.62±1.16
		I_c	0.21±0.01	153.64±1.75
2457100.45	3.367	U	0.15±0.03	176.13±6.30
		B	0.06±0.01	159.13±8.30
		V	0.17±0.01	169.77±1.69
		R_c	0.13±0.06	163.44±14.15
		I_c	0.14±0.01	170.40±2.63
2457101.46	4.367	U	0.20±0.03	142.16±5.00
		B	0.04±0.02	119.45±16.55
		V	0.04±0.01	137.98±6.92
		R_c	0.02±0.01	122.63±18.53
		I_c	0.05±0.01	132.40±10.05
2457102.45	5.367	U	0.33±0.03	169.4±2.93
		B	0.25±0.02	172.9±2.45
		V	0.18±0.01	173.94±1.75
		R_c	0.09±0.01	174.53±4.38
		I_c	0.03±0.01	134.91±17.17
2457103.45	6.367	U	0.29±0.06	150.4±5.93
		B	0.31±0.02	167.8±2.43
		V	0.18±0.009	169.94±1.47
		R_c	0.08±0.01	164.64±4.02
		I_c	0.11±0.01	169.08±3.74
2457106.47	9.367	U	0.24±0.03	165.42±4.22
		B	0.15±0.03	178.19±6.24
		V	0.18±0.01	176.23±2.22
		R_c	0.16±0.01	179.29±1.58
		I_c	0.10±0.01	172.21±3.03
2457111.47	14.367	U	0.25±0.02	172.36±2.51
		B	0.27±0.02	179.09±2.24
		V	0.18±0.01	177.74±1.90
		R_c	0.15±0.01	173.81±1.82
		I_c	0.06±0.01	165.51±4.69
2457112.47	15.367	U	0.27±0.02	171.59±2.96
		B	0.16±0.01	166.65±2.99
		V	0.16±0.01	169.58±2.51
		R_c	0.14±0.01	172.24±1.76
		I_c	0.14±0.01	169.32±2.33

2457126.44	29.367	U	0.22±0.02	172.15±3.40
		B	0.28±0.02	179.47±2.04
		V	0.25±0.01	177.92±1.51
		R_c	0.15±0.01	175.48±2.22
		I_c	0.08±0.01	172.85±3.82
2457131.47	34.367	U	0.20±0.02	178.15±2.72
		B	0.24±0.02	174.06±1.90
		V	0.20±0.01	176.73±1.53
		R_c	0.13±0.01	179.48±2.54
		I_c	0.03±0.01	169.65±6.99
2457132.47	34.367	U	0.20±0.01	179.95±2.54
		B	0.27±0.01	171.35±1.79
		V	0.15±0.01	179.59±1.94
		R_c	0.15±0.01	176.87±1.92
		I_c	0.11±0.01	170.88±2.63
2457134.45	37.367	U	0.25±0.02	170.77±3.07
		B	0.21±0.02	169.95±3.59
		V	0.17±0.01	166.72±2.01
		R_c	0.12±0.01	175.69±3.02
		I_c	0.11±0.01	172.95±4.94

0.33% in U filter, 0.37% in BV filters, 0.24% in R_cI_c filters. The wavelength dependence of P and PA at various epochs from day 1.36 to day 15.36 for our data is shown in Figure 2.13. The degree of polarization shows changes in the wavelength as a function of time whereas position angle remains constant. The polarization values are found to peak in the B band and remains constant in the V band. The V-band apparent magnitude and B-band polarization values are also compared to check the correlation. It is seen that the polarization value in B band is found to increase with the decrease in the V magnitude in Figure 2.14.

2.3.3.2 Discussions

Though the polarization values obtained for V5668 Sgr are not corrected for the interstellar polarization, the variability in all the bands suggests the presence of the intrinsic polarization. The Serkowski's law fit for all days of observations did not peak in the visible band pointing out the intrinsic component. Multiple optical peaks are observed in the light curve immediately after the outburst for
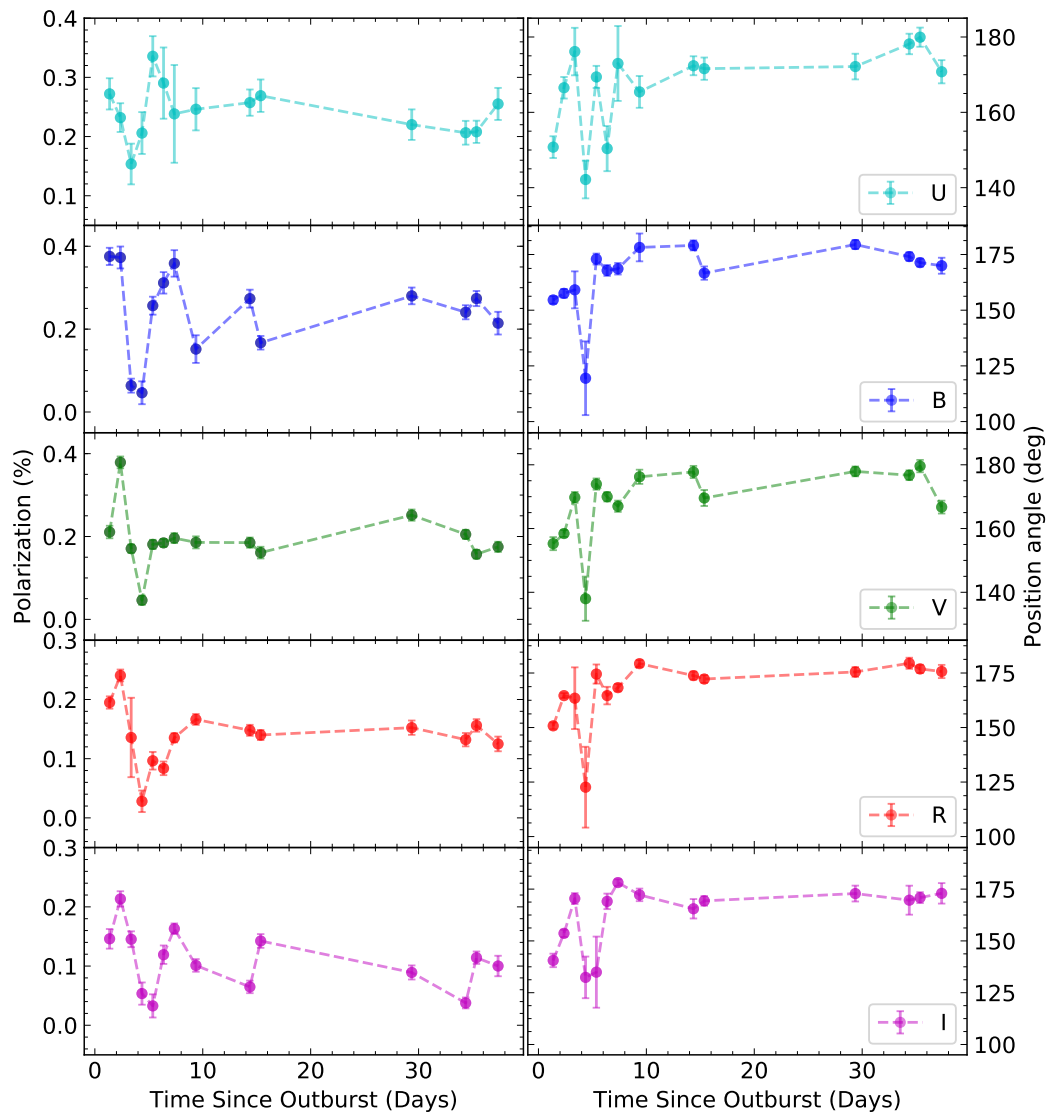
Figure 2.12: The variability in the degree of polarization and position angle for V5668 Sgr
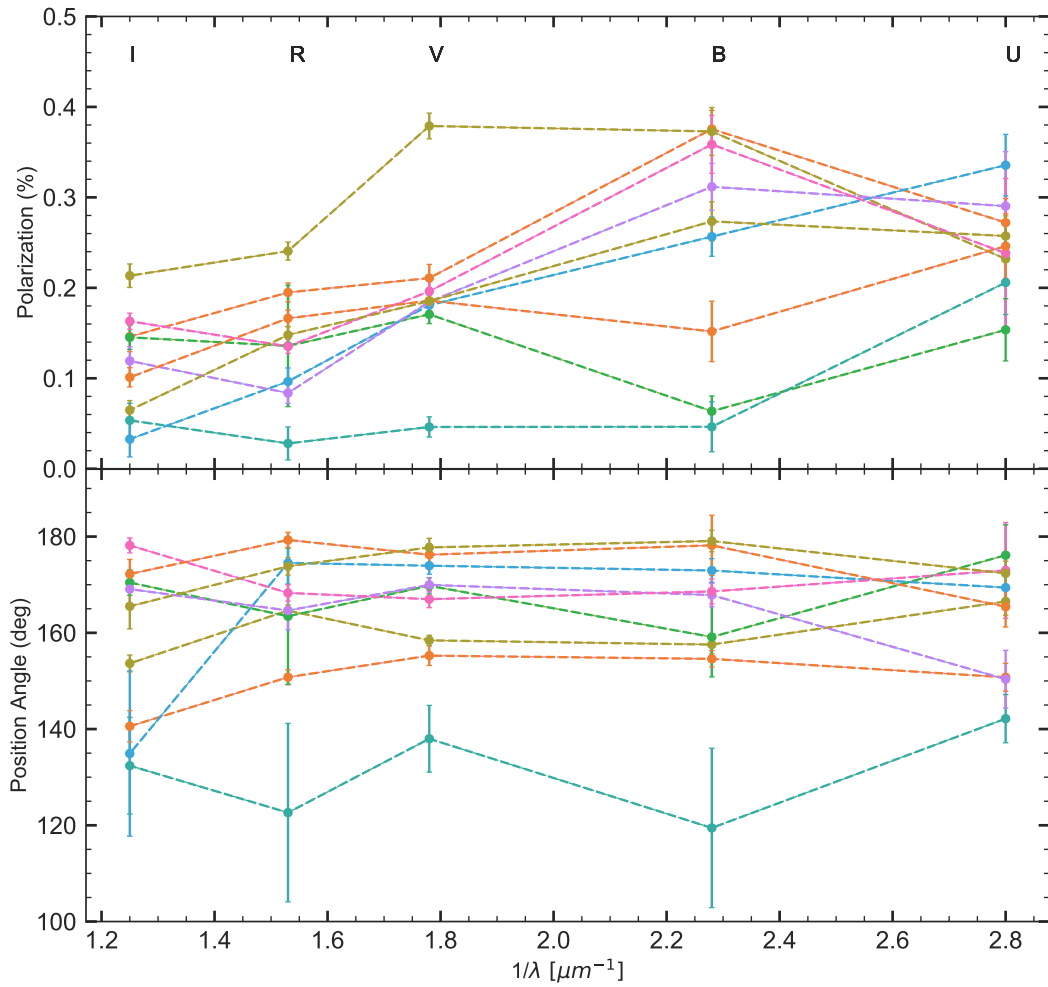
Figure 2.13: Wavelength dependence for P and PA for different epochs of observations for V5668 Sgr
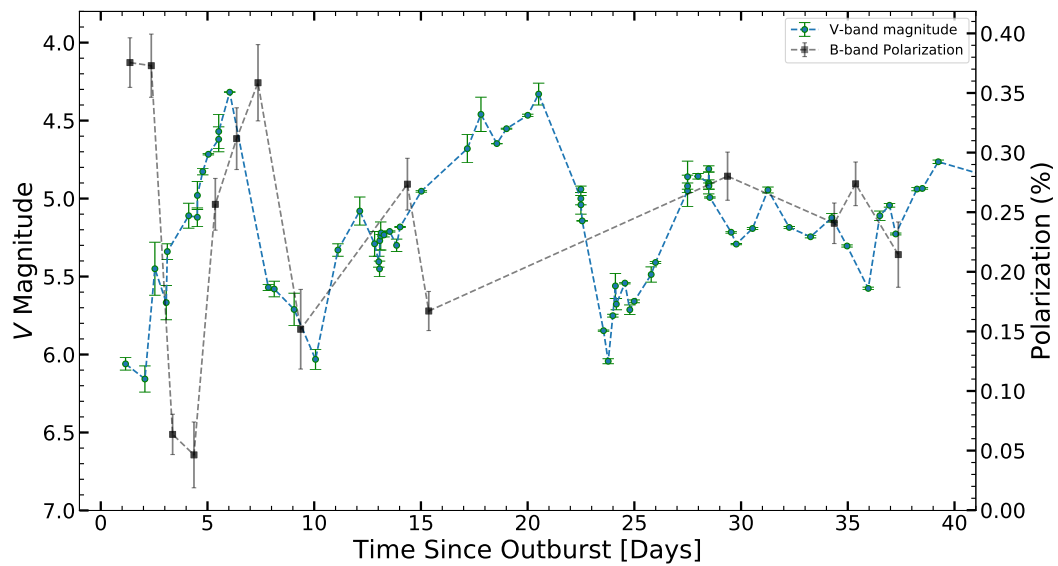
Figure 2.14: The comparison of the V-Band magnitude with B-band polarization values for different epochs for V5668 Sgr

a period of 90 days. These have been attributed to the strong dust produced during the initial stages (Morris et al., 2017). As the polarization values show wavelength dependence, the intrinsic polarization can be due to the scattering by the small grains in the ejecta (Evans et al., 2002) which would eventually give rise to the deep minimum at around 100 days shown in the Figure 2.10.

2.3.4   V3661 Oph

V3661 Oph (Nova Oph 2016) was discovered on 2016 Mar 11.9 by Yamaoka et al. (2016) with a visual magnitude of 11.7 and classified as Fe II novae. The light curve of the nova is shown in Figure 2.15. The transition from optically thick to thin ejecta was about 6 days after the V-band maximum. The magnitude is found to decline rapidly after the outburst making V3661 Oph probably the fastest known nova of Fe II type. It is at a distance of 3.7 kpc located within the galactic disc and closer to the Bulge. The polarization observations were obtained from day 2 to 8 after the outburst as marked in Figure 2.15.

2.3.4.1   Interpretation

The instrumental polarization is found to be 0.1% which is obtained by the unpolarized standard stars given in Table 2.9. The observations of polarized standard stars provide the required position angle correction given in Table 2.10. The evolution of the degree of polarization and position angle for the nova are shown in Table 2.11. Observations are obtained in R_cI_c bands from day 2.085 to 8.041 for five nights and in V band only on day 2.085.

The maximum values of the polarization in R_cI_c bands are 5.28% and 4.4% on days 7.07 and 8.07 respectively. The PA remains constant at 174±3 during the entire observation period. It can be seen in Figure 2.16 that the degree of polarization is found to increase on days 7.07 and 8.07 in R_cI_c. The nova is located at a galactic latitude of 1.47 degrees and has an interstellar reddening value E(B-V) of 2.27. The major component of the observed polarization could be of the interstellar origin. Also the PA observed for the nova is roughly

Table 2.9: Polarimetric observations of unpolarized standard stars obtained on the days of the V3661 Oph observations

JD	Object	Filter	P (%)
2457461.34	HD100623	U	0.12±0.05
		B	0.08±0.04
		V	0.03±0.01
		R_c	0.05±0.01
		I_c	0.02±0.01
2457465.207	HD90508	U	0.03±0.07
		B	0.16±0.03
		V	0.03±0.01
		R_c	0.01±0.01
		I_c	0.02±0.01
2457466.10	HD42807	U	0.09±0.04
		B	0.07±0.03
		V	0.07±0.02
		R_c	0.02±0.01
		I_c	0.04±0.01
2457467.40	HD125184	U	0.09±0.05
		B	0.15±0.03
		V	0.05±0.01
		R_c	0.07±0.01
		I_c	0.04±0.01

Table 2.10: Polarimetric observations of polarized standard stars on the days of V3661 Oph observations

Object	JD	Filter	P (%)	θ
HD154445	2457462.4	U	3.00±0.037	88.11±0.36
		B	3.57±0.022	88.94±0.19
		V	3.71±0.013	90.18±0.12
		R_c	3.63±0.014	89.92±0.13
		I_c	3.22±0.011	89.27±0.12
HD94473	2457466.17	U	0.93±0.059	62.15±1.88
		B	0.96±0.061	61.41±1.81
		V	0.99±0.020	63.32±0.57

Table 2.11: Polarimetric observations of V3661 Oph

JD	t (days)	Filter	P (%)	θ
2457461.48	2.094	V	4.54±0.54	176.6±0.5
		R_c	4.32±0.07	176.8±0.5
		I_c	4.00±0.05	176.3±0.4
2457462.49	3.095	R_c	4.69±0.08	174.7±0.5
		I_c	4.08±0.05	178.6±0.3
2457463.48	4.084	R_c	4.78±0.05	174.4±0.3
		I_c	4.02±0.04	177.3±0.3
2457466.48	7.075	R_c	5.28±0.11	174.1±0.6
		I_c	3.97±0.05	177.8±0.4
2457467.49	8.073	R_c	5.04±0.13	176.2±0.8
		I_c	4.39±0.06	176.1±0.4
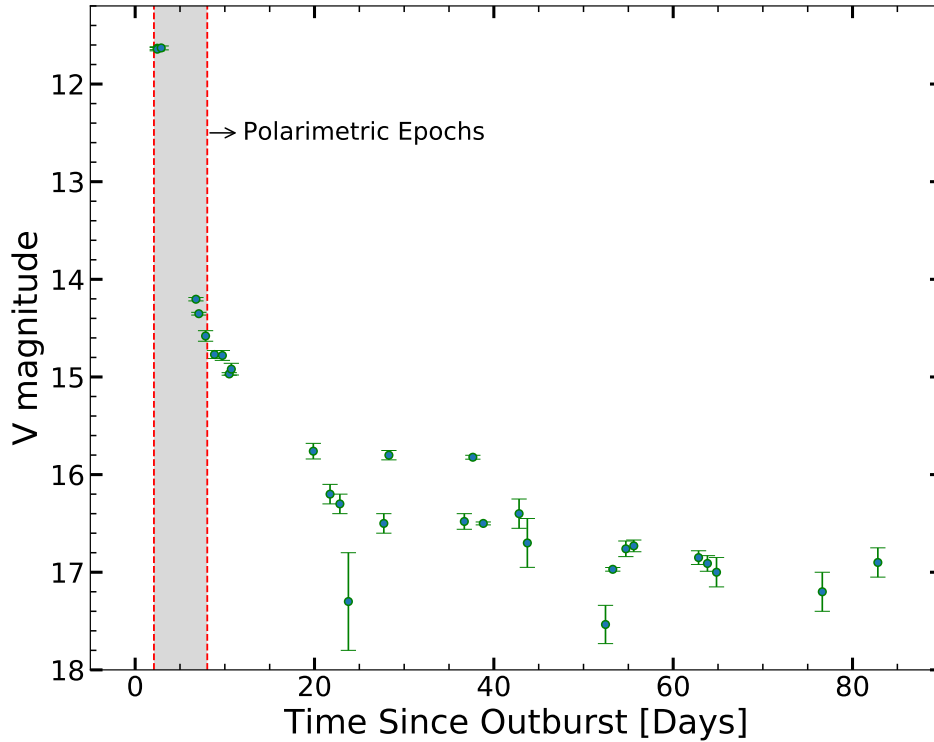
Figure 2.15: The light curve for V3661 Oph obtained from AAVSO magnitudes. The epochs of the polarimetric observations are marked.

consistent with the average of PA of the nearby field stars obtained from Heiles (2000). The polarization observed on day 2 in VR_cI_c bands is used to fit the Serkowski's empirical formula for the interstellar polarization.

$$p = p_{max} \exp[-K \ln^2(\frac{\lambda_{max}}{\lambda})] \tag{2.3}$$

where λ_{max} correspond to the wavelength of maximum polarization and K is the constant parameter. Figure 2.17 shows the least square fit of the V3661 Oph data to the Serkowski's law. The observed data is well fitted with the interstellar law which gives the $P_{max} = 4.34\pm0.04\%$ and $\lambda_{max}=6155\pm115$Å.

2.3.4.2 Discussions

Though the nova polarization values show variability during 7-8 days, it is difficult to comment on the intrinsic polarization due to lack of the observations after day 8. It appears that the polarization observed for V3661 Oph is mostly interstellar.
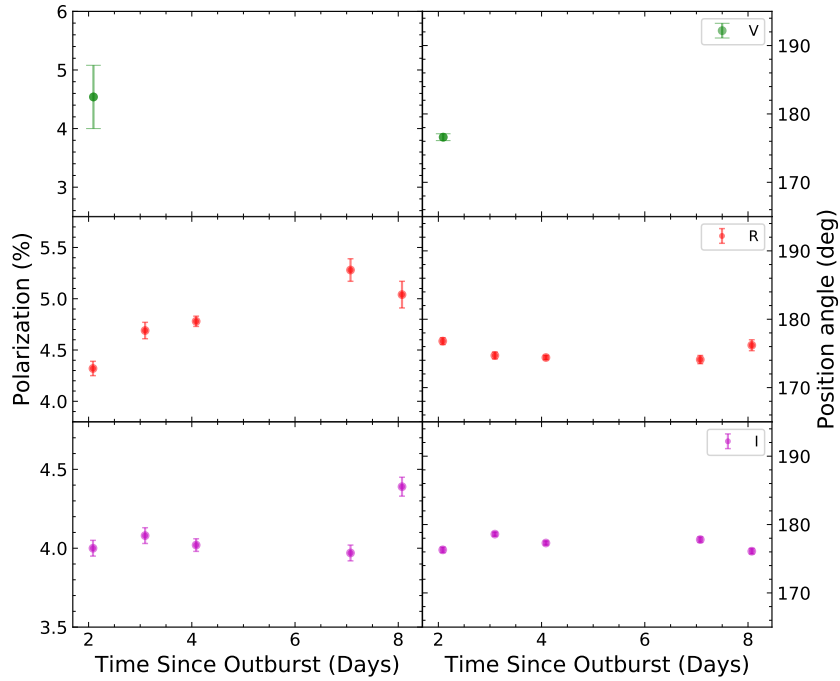
Figure 2.16: The degree of polarization and position angle for V3661 Oph
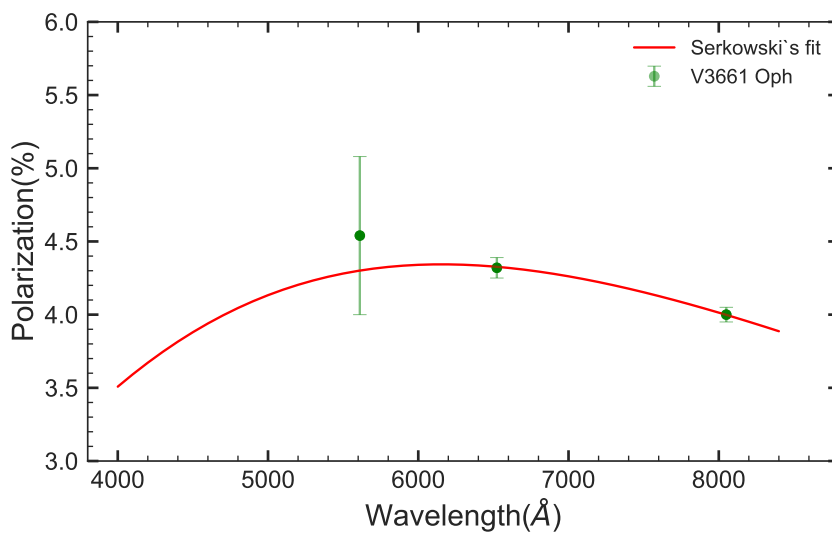
Figure 2.17: The interstellar polarization is plotted using the Serkowski's relation. Polarization values for the V3661 Oph is also shown in VR_cI_c bands.

2.4 Conclusions

The polarization data of four novae have been analyzed and interpreted in this Chapter. The science aspects of the polarization measurements and challenges associated with the analysis were understood. Study of polarimetric properties of nova systems is one of the 35 polarimetric science cases which were collected for the Thirty Meter Telescope.

The values of polarization varied from 0.2% to 5% in the novae considered in this Chapter. The data were obtained from the polarimeters located at the Cassegrain focus of the telescopes. In the observations above, the instrumental polarization is found to be less than 0.1% and is ignored during the data analysis. If the instrumental polarization is the same or higher than the observed polarization values, it cannot be easily removed from the observed data which affects the polarization accuracy. Hence, it is an absolute requirement to estimate the instrumental polarization and crosstalk arising from the telescope optics which have a folding mirror in their optical configuration. A polarization model has to be developed for the telescope optics before the design of the polarimeter. Next Chapter introduces the algorithm for the development of the polarization model.

Chapter 3

Development of polarization model

Ramya M. Anche, G. C. Anupama, Krishna Reddy, Asoke Sen, K. Sankara-subramanian, A. N. Ramaprakash, Sujan Sengupta, Warren Skidmore, Jenny Atwood, Sivarani Tirupathi, and Shashi Bhushan Pandey, International Conference on Optics and Photonics, Proc. SPIE 9654, 965408, 2015.

3.1   Introduction

A polarization model describes the complete polarization effects due to all the optical elements used in the system. The model utilizes the polarization ray tracing to determine the instrumental polarization, crosstalk, depolarization, and polarization aberrations. In this Chapter, we describe the polarization ray tracing algorithm developed using analytical equations of the optical surfaces. The developed model was used to estimate the polarization effects due to the telescope optics of the Thirty Meter Telescope (TMT) and Multi-Application Solar Telescope (MAST). The code for this model is in Mathematica programming language. The model can be applied to any other telescope by modifying the analytical mirror equations, provided the mirrors are a monolithic. To deal with the design and analysis of the segmented mirrors of TMT, we have used the polarization ray tracing available in the optical design software Zemax®.

The polarization induced wavefront aberrations and Jones pupil maps are also obtained using polarization ray trace in Zemax®.

3.2 Polarization Ray Tracing (PRT)

Polarization Ray Tracing (PRT) aims at determining the evolution of the polarization state through an optical system. It is similar to geometrical ray tracing where many rays are traced from first optical surface till the last surface using the direction cosines. In the case of PRT, in addition to geometrical ray tracing, at each interface, the polarization effects are estimated using the Fresnel reflection coefficients. Using Fresnel reflection coefficients, either the Mueller matrix or the Jones matrix are calculated for every surface. Polarization aberrations of the system such as diattenuation, retardance are also determined through the polarization ray tracing algorithm. The coordinate frames and sign conventions are an essential part of the ray tracing which are discussed in the next section.

Polarization Ray Tracing matrix methods have been in use over the past thirty years. Knowlden (1981) used it to calculate the instrumental polarization due to coatings in many nonplanar surfaces. In works by Chipman (1988,9); Chipman (1995, 2010), Waluschka (1989) and Yun et al. (2011), the authors have described a polarization ray tracing calculus which is a generalization of the Jones calculus into three dimensions. At each surface, the thin film calculations (Macleod, 2010) are used to obtain the Jones matrix. Finally, the Jones matrices are multiplied in order to get the resultant instrumental matrix which gives the polarization changes for the entire optical layout. McClain et al. (1992) developed PRT methods for anisotropic optically active media such as quartz crystal. Further, in application to the telescopes, Sanchez et al. (1992) used Jones-Mueller matrix approach to estimate the low spatial resolution Mueller matrix for the Large Earth-based Solar Telescope (LEST). In Sen & Kakati (1997), the Stokes-Mueller formalism is used to estimate the instrumental polarization and depolarization for the 2.3 m Vainu Bappu telescope

(VBT) in Kavalur, India. Here, we have developed the polarization model for the TMT and MAST using a set of analytical equations based on Sen & Kakati (1997).

3.3 Polarization Ray Tracing (PRT) : Analytical

The generalized polarization ray tracing algorithm using analytical equations is explained in this section. The estimation of the Mueller matrices for the mirror surfaces using these analytical equations is also given.

3.3.1 Estimation of Instrumental polarization, crosstalk and depolarization.

1. The mirror surfaces are defined in the Cartesian coordinate system using the conic equations. The radius of curvature, conic constant, focal ratio and the diameter of the mirror are considered in the equations. A global $x - y - z$ right-handed coordinate system is defined here. All the mirror surfaces are described in this coordinate system.

2. Direction cosines of the incident rays $(\hat{i})$ vary with the field angle (η) of the telescope and are shown in Figure 3.1. The field angle considered is in reference to the sky plane.

$$\hat{i} = (0, \sin \eta, - \cos \eta) \tag{3.1}$$

3. The direction cosines of the normal $(\hat{n})$ and reflected ray $(\hat{r})$ are estimated for each ray incident on the mirror surface. The direction cosines for the $\hat{s}$ and $\hat{p}$ vectors are also determined.

$$\hat{r} = \hat{i} - 2\hat{n}(\hat{i} \cdot \hat{n}) \tag{3.2}$$
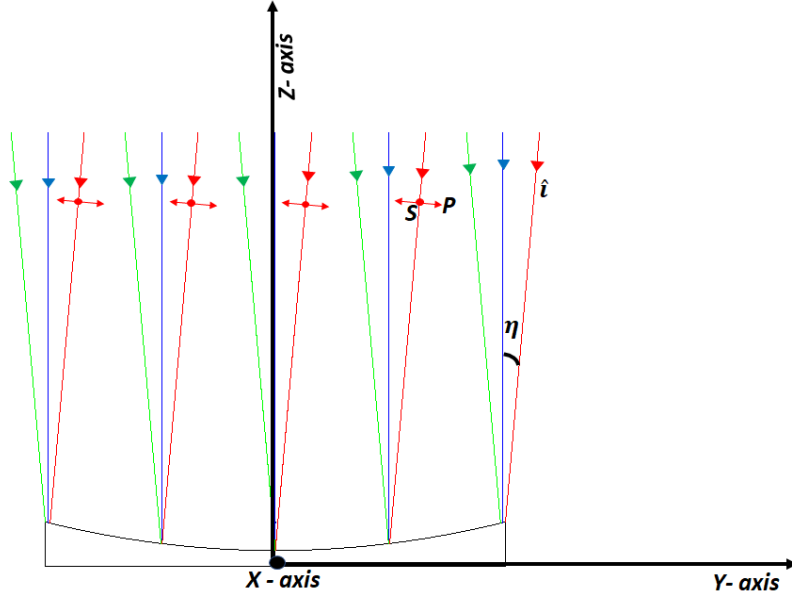
Figure 3.1: Coordinate system in the polarization ray tracing algorithm.

4. The rays are traced till the primary mirror to obtain the incident $(\hat{i} \cdot \hat{n})$ and reflected angles $(\hat{r} \cdot \hat{n})$ on the mirror surface.

5. The Fresnel reflection coefficients (r_p and r_s) are estimated using the angle of incidences and coating parameters. For multi-layer coating, the thickness of each layer has to be considered, and the reflection coefficients for the combined layer are estimated as given below (Macleod, 2010).

$$r_{p,s} = \frac{\eta_m E_m - H_m}{\eta_m E_m + H_m} \tag{3.3}$$

$$E_m = \cos \delta_f + i \frac{\eta_b}{\eta_f} \sin \delta_f \tag{3.4}$$

$$H_m = \eta_b \cos \delta_f + i \eta_f \sin \delta_f \tag{3.5}$$

$$\delta_f = \frac{2\pi}{\lambda} n_f(\lambda) d_f \cos \theta_f \tag{3.6}$$

where d_f is the thickness of the protective layer and n_f is the refractive index of the protective layer. n_b and θ_b are the refractive index and the incident angle at the bulk metal layer, respectively. E_m and H_m correspond to the electric and magnetic field components. The parameters θ_f

and θ_b can be calculated from the angle of incidence using Snell's law,

$$\sin \theta_m = n_f(\lambda). \sin \theta_f; \quad n_b. \sin \theta_b = n_f(\lambda). \sin \theta_f. \tag{3.7}$$

n_m and θ_m are the refractive index and incident angle for air, respectively. The expressions for η_b and η_f in the above equations for s polarization,

$$\eta_{b,f,m} = n_{b,f,m}. \cos \theta_{b,f,m} \tag{3.8}$$

and for p polarization,

$$\eta_{b,f,m} = \frac{n_{b,f,m}}{\cos \theta_{b,f,m}}. \tag{3.9}$$

6. The polarization state for the incident rays is defined in terms of the electric field vectors in the $p - s$ frame. Here, two cases of incident polarization states are considered: unpolarized and 100% linearly polarized light.

   (a) Unpolarized light : The components of the electric field vector in the case of unpolarized light can be defined as follows (Collet, 1992):

   $$E_p = \frac{1}{\sqrt{2}}; \quad E_s = \frac{1}{\sqrt{2}} \tag{3.10}$$

   (b) 100% linearly polarized light : The electric field vector is considered to make an angle α with the y-axis of the telescope. The direction cosines (DC) of this electric field vector are given as $(\sin \alpha, \ \cos \alpha, \ 0)$. Now, if the star is at a semi field angle of η with the optical axis of the telescope, then the direction cosines of the electric field vector would change. The electric field vector and the incident ray are orthogonal to each other. Using these conditions, the DC of the electric field vector, E_{dc} for the polarized light is found to be $(\sin \alpha, \ \sin \alpha \cos \eta, \ - \sin \alpha \sin \eta)$ (Sen & Kakati, 1997). The direction cosines of p and s vectors are represented as $\hat{s}_{incpri} = \hat{i} \times \hat{n}$,

$\hat{p}_{incpri} = \hat{i} \times \hat{s}_{incpri}$, $\hat{p}_{refpri} = \hat{s}_{incpri} \times \hat{r}$, where $incpri$ and $refpri$ corresponds to the DC of the incident ray on the primary mirror and DC the reflected ray from the primary mirror, respectively. E_p and E_s can be calculated by,

$$E_p = E_{dc} \cdot \hat{p}_{incpri}; \quad E_s = E_{dc} \cdot \hat{s}_{incpri} \tag{3.11}$$

7. The change in the polarization state after reflection from the primary mirror can be obtained by multiplying reflection coefficients (r_p and r_s) from the mirror surface with the incident electric field vectors (E_p and E_s).

$$R_p = r_p E_p; \quad R_s = r_s E_s \tag{3.12}$$

8. The electric field vectors are used to obtain the Stokes parameters (Collet, 1992) in the $p - s$ coordinate frame. The polarization measurements are obtained in the fixed global $x - y - z$ coordinate system. The Stokes parameters are converted to the global coordinate system.

$$I = R_p^2 + R_s^2 \tag{3.13a}$$

$$Q = R_p^2 - R_s^2 \tag{3.13b}$$

$$U = 2R_p R_s \cos(\delta_p - \delta_s) \tag{3.13c}$$

$$V = 2R_p R_s \sin(\delta_p - \delta_s) \tag{3.13d}$$

where δ_p and δ_s are the phase angles of components R_p and R_s.

9. The IP, DP and CT (linear to circular) are estimated using the Stokes parameters at the prime focus.

$$IP = \frac{\sqrt{Q^2 + U^2}}{I} \tag{3.14}$$

$$DP = \frac{I - (Q^2 + U^2 + V^2)}{I}; \quad CT = \frac{V}{I} \tag{3.15}$$

10. In the case of the secondary mirror, for every ray reflected from the primary, the point of incidence on the secondary mirror is determined.

11. The procedure mentioned above is followed to estimate incident angles and reflection coefficients for the secondary mirror.

12. The $p-s$ coordinate system is the local coordinate system which changes with the mirror surface. Hence, at the secondary mirror surface, the electric field vectors (sE_p and sE_s) are converted from primary mirror $p-s$ frame to secondary mirror $p-s$ frame using direction cosines of the s and p vectors.

$$sE_p = (R_p D_{r1} + R_s D_{r2}) \tag{3.16}$$

$$sE_s = (R_p D_{r3} + R_s D_{r4}) \tag{3.17}$$

$$D_{r1} = \hat{p}_{refpri} \cdot \hat{p}_{incsec}; \quad D_{r2} = \hat{s}_{incpri} \cdot \hat{p}_{incsec} \tag{3.18}$$

$$D_{r3} = \hat{p}_{refpri} \cdot \hat{s}_{incsec}; \quad D_{r4} = \hat{s}_{incpri} \cdot \hat{s}_{incsec} \tag{3.19}$$

13. In the case of unpolarized light on the primary mirror, a part of incident light (pp) gets polarized and ($1 - pp$) part remains unpolarized. When these rays are considered for the secondary mirror, the electric field vectors for these two cases are considered separately to obtain the Stokes parameters.

$$sR_p = sE_p r_{ps} pp; \quad sR_s = sE_s r_{ss} pp \tag{3.20}$$

where r_{ps} and r_{ss} are the reflection coefficients for the secondary mirror. Similarly for the unpolarized component, the electric vectors will be

$$sR_p = sE_p r_{ps}(1 - pp); \quad sR_s = sE_s r_{ss}(1 - pp) \tag{3.21}$$

14. The resultant Stokes parameters are converted to the global $x-y-z$ coordinate system to estimate the degree of polarization, depolarization,

and crosstalk.

15. The same algorithm is followed for any number of surfaces in the optical
    path. The coordinate transformations between local and global systems
    and sign conventions are most important during the ray tracing.

3.3.2   Mueller matrices for the mirror surfaces

The Mueller matrices are related to the Stokes parameters as follows (Collet,
1992):

$$\begin{pmatrix} I_{out} \\ Q_{out} \\ U_{out} \\ V_{out} \end{pmatrix} = \begin{pmatrix} M11 & M12 & M13 & M14 \\ M21 & M22 & M23 & M24 \\ M31 & M32 & M33 & M34 \\ M41 & M42 & M43 & M44 \end{pmatrix} \begin{pmatrix} I_{in} \\ Q_{in} \\ U_{in} \\ V_{in} \end{pmatrix} \tag{3.22}$$

where $[I_{in}...V_{in}]$ correspond to the incident Stokes parameters and $[I_{out}...V_{out}]$
correspond to the output Stokes parameters. The Mueller matrices for the
mirror surfaces are estimated using the reflection coefficients as given below:

1. The global co-ordinate system (right handed x-y-z) is defined for the
   telescope. The rays are traced from the first surface using direction
   cosines.

2. The angle of incidence and reflection, direction cosines of the $\hat{s}$ and $\hat{p}$
   vectors are determined for each surface.

3. The reflection coefficients are determined using the thin film calculations
   mentioned in the previous section.

4. Mueller matrix, $M(R_p, R_s)$ is estimated using the reflection coefficients

in the $p - s$ coordinate system.

$$\frac{1}{2}\begin{pmatrix} R_p + R_s & R_p - R_s & 0 & 0 \\ R_p - R_s & R_p + R_s & 0 & 0 \\ 0 & 0 & 2\sqrt{R_p R_s}\cos(\epsilon_p - \epsilon_s) & 2\sqrt{R_p R_s}\sin(\epsilon_p - \epsilon_s) \\ 0 & 0 & -2\sqrt{R_p R_s}\sin(\epsilon_p - \epsilon_s) & 2\sqrt{R_p R_s}\cos(\epsilon_p - \epsilon_s) \end{pmatrix}$$

(3.23)

where, $R_p = |r_p|^2$ and $R_s = |r_s|^2$ and ϵ_p and ϵ_s are the phase components of r_p and r_s.

5. The rotation matrix is determined between the local $p - s$ coordinate system and global $x - y - z$ system.

$$R(\theta) = \begin{pmatrix} 1 & 0 & 0 & 0 \\ 0 & \cos 2\theta & \sin 2\theta & 0 \\ 0 & -\sin 2\theta & \cos 2\theta & 0 \\ 0 & 0 & 0 & 1 \end{pmatrix}$$

(3.24)

where θ is obtained by the dot product between the global x-axis and local $\hat{p}$ vector.

6. The final Mueller matrix is in the global x-y coordinate system.

$$M = R(-\theta)M(R_p, R_s)R(\theta)$$

(3.25)

The matrix can be multiplied with incident Stokes parameters to determine the polarization effects due to the reflection from the mirror surface.

$S_{out} = M \ S_{in}$

7. The Mueller matrices are estimated separately for each mirror surfaces in the global co-ordinate system and multiplied in the end to obtain the resultant matrix for the telescope (Collet, 1992).

$M_t = M_n M_{n-1} .... M_2 M_1$

3.4 Polarization Ray Tracing (PRT) : Zemax®

For polarization analysis in Zemax® there are two available options, *Polarization ray trace* and *Polarization pupil map*. Polarization ray trace gives all the parameters associated with the polarization changes through the optical layout for one single ray at the specified position. However, to estimate the effect of a vast number of rays falling on the mirror, the polarization pupil map is used (Figure 3.2), where the number of rays is specified using grids. Polarization pupil map is used to estimate the Mueller matrices in Zemax®.

3.4.1 Estimation of Mueller matrices using Zemax®

In the polarization pupil map, the rays specified by the grids are traced to the focal plane. At each interface, the reflection coefficients, and their corresponding amplitudes and phase components of the electric field are obtained. The input to the polarization pupil map are the Jones vectors (J_x and J_y) of different polarization states as shown in Table 3.1. Px and Py are the normalized pupil positions in Zemax® For each polarized state, the pupil map

Input Polarization	J_x	J_y	Px	Py
Horizontal Polarization (PH)	1	0	0	0
Vertical Polarization (PV)	0	1	0	0
Linear Polarization+45 degree (P+45)	1	1	0	0
Linear Polarization-45 degree (P-45)	-1	1	0	0
Left Circular Polarization (PL)	1	1	0	90°
Right Circular Polarization (PR)	1	1	0	-90°

Table 3.1: The input parameters for Zemax®

can be generated. The amplitudes (E_x, E_y) and phases (δ_x, δ_y) of the electric field vectors are obtained from the pupil maps and the Stokes parameters are calculated. The Matrix elements can be estimated from the Stokes parameters
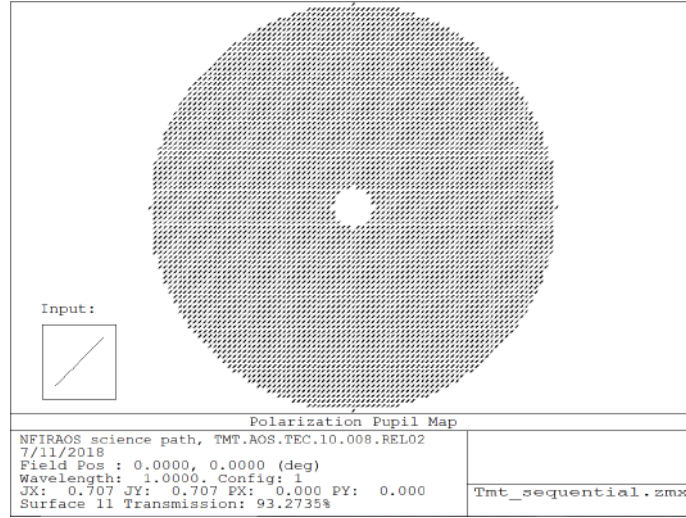
Figure 3.2: Polarization pupil map in Zemax® at the Nasmyth focus of the Thirty Meter Telescope (TMT) for linearly polarized light at 45° as the input. The grid has 83×83 rays across the pupil.

as follows:

$$
\begin{pmatrix}
I'_h + I'_v & I'_h - I'_v & I'_{45} - I'_{-45} & I'_{rhc} - I'_{lhc} \\
Q'_h + Q'_v & Q'_h - Q'_v & Q'_{45} - Q'_{-45} & Q'_{rhc} - Q'_{lhc} \\
U'_h + U'_v & U'_h - U'_v & U'_{45} - U'_{-45} & U'_{rhc} - U'_{lhc} \\
V'_h + V'_v & V'_h - V'_v & V'_{45} - V'_{-45} & V'_{rhc} - V'_{lhc}
\end{pmatrix}
\tag{3.26}
$$

The Mueller matrix is estimated for all the rays and is then averaged (incoherent superposition) at the image plane.

3.4.2 Estimation of polarization aberrations

Polarization aberrations are the variations of amplitude, phase, and polarization of a wavefront across the exit pupil of an optical system. The polarization aberration theory was developed by Chipman (1987) to calculate the polarization aberrations of radially symmetric systems. These aberrations are due to the reflective mirror coating and the incident angle of the mirrors (Reiley et al., 1992). Chipman & Chipman (1989) gave the polarization aberration diagrams by describing the polarization effects that are equivalent to the wavefront aberrations such as tilt, piston, defocus and astigmatism. The polarization aberrations were estimated for The Solar Activity Measurements

Experiments (SAMEX) Solar Vector Magnetograph by McGuire & Chipman (1989). Significant improvement was obtained in the polarization accuracy of the magnetograph by minimizing the angle of incidence and the difference between the reflection coefficients. Clark & Breckinridge (2011) worked on the compensation of Fresnel aberrations arising in low F-number telescopes due to mirror coating and curvature of the mirror. In the recent times, Breckinridge et al. (2015) have estimated polarization aberrations for a simple Nasmyth telescope. The primary mirror used in their analysis is of 2.4 m diameter with F/8 and all the mirrors are coated with bare Aluminum. The diattenuation and retardance for the telescope are estimated to be 0.066 and 0.202 respectively at λ=800 nm. The retardance maps show the presence of polarization/coating induced tilt and astigmatism. These aberrations give rise to the ghost PSF which leads to the ellipticity of the Airy disk (found to be 7.5×10^{-6} for the unpolarized light). The intensity of the ghost PSF is found to be about one part in 10^{-4} of the two primary PSF images IXX (X-polarized light) and IYY (Y-polarized light). Though the magnitude of these aberrations is small, they affect the high resolution and high contrast imaging instruments (Breckinridge et al., 2015). The steps for obtaining the polarization aberrations is explained below (Breckinridge et al., 2015).

1. Polarization aberration of any system is examined primarily using diattenuation and retardance maps. Diattenuation (D) is the polarization dependent reflectance and retardance (δ) is the phase shift between the reflected s and p beams. They are defined as follows:

$$D = \frac{|r_p|^2 - |r_s|^2}{|r_p|^2 + |r_s|^2}; \qquad \delta = \phi_p - \phi_s \qquad (3.27)$$

2. Diattenuation gives rise to instrumental polarization which is already estimated during polarization ray tracing whereas the retardance is the polarization dependent contributions to the wavefront aberrations. The variation of the retardance on the mirror surface determines the type of aberrations. For example, a constant retardance corresponds to the

constant wavefront aberration "piston".

3. The effect of the polarization aberrations on the point spread function is estimated using the Jones amplitude and phase pupil maps at the exit pupil of the telescope. The pupil maps are obtained using polarization ray tracing in Zemax® as explained in the previous section.

4. Each ray in the system is mapped into four complex field points superposed at a single point in the exit pupil. The input is specified in terms of Jones vectors. At the exit pupil, the amplitude and phases of the electric field vectors are obtained.

5. For J_x=1 and J_y=0 as the input, the amplitude (A_{xx}) and phase (Ph_{xx}) of electric field vector E_x and the amplitude (A_{yx}) and phase (Ph_{yx}) of electric field vector E_y are determined. Similarly, for J_x=0 and J_y=1 as the input, the other two parameters are estimated. At the exit pupil of the telescope, the Jones pupil matrix is of the following form:

$$\begin{pmatrix} J_{xx} & J_{xy} \\ J_{yx} & J_{yy} \end{pmatrix} = \begin{pmatrix} A_{xx} \ e^{Ph_{xx}} & A_{yx} \ e^{Ph_{yx}} \\ A_{xy} \ e^{Ph_{xy}} & A_{yy} \ e^{Ph_{yy}} \end{pmatrix} \qquad (3.28)$$

6. The Fast Fourier Transform of the exit pupil function gives the amplitude response function in conventional imaging. In this case, the Fast Fourier Transform of the Jones pupil map elements gives the amplitude response matrix (ARM).

$$ARM = \begin{pmatrix} ARM_{xx} & ARM_{xy} \\ ARM_{yx} & ARM_{yy} \end{pmatrix} = \begin{pmatrix} \mathcal{F}|J_{xx}| & \mathcal{F}|J_{yx}| \\ \mathcal{F}|J_{xy}| & \mathcal{F}|J_{yy}| \end{pmatrix} \qquad (3.29)$$

where $\mathcal{F}$ is the spatial Fourier Transform of the Jones pupil map elements.

7. The polarization in the image of an incoherent point source and the distribution of flux is defined by the Point Spread Matrix, which is the Mueller matrix generalization of PSF. The Amplitude Response Matrix is converted into Point Spread Matrix (PSM) using the Jones-Mueller

matrix conversion as given below:

$$M11 = \tfrac{1}{2}(|ARM_{xx}|^2 + |ARM_{xy}|^2 + |ARM_{yx}|^2 + |ARM_{yy}|^2)$$

$$M12 = \tfrac{1}{2}(|ARM_{xx}|^2 - |ARM_{xy}|^2 + |ARM_{yx}|^2 - |ARM_{yy}|^2)$$

$$M13 = Re(ARM_{xx}ARM_{xy}^* + ARM_{yy}ARM_{yx}^*)$$

$$M14 = Im(ARM_{xx}ARM_{xy}^* + ARM_{yy}ARM_{yx}^*)$$

$$M21 = \tfrac{1}{2}(|ARM_{xx}|^2 - |ARM_{xy}|^2 - |ARM_{yx}|^2 + |ARM_{yy}|^2)$$

$$M22 = \tfrac{1}{2}(|ARM_{xx}|^2 - |ARM_{xy}|^2 - |ARM_{yx}|^2 + |ARM_{yy}|^2)$$

$$M23 = Re(ARM_{xx}ARM_{xy}^* - ARM_{yy}ARM_{yx}^*)$$

$$M24 = Im(ARM_{xx}ARM_{xy}^* + ARM_{yy}ARM_{yx}^*)$$

$$M31 = Re(ARM_{xx}ARM_{yx}^* + ARM_{yy}ARM_{xy}^*)$$

$$M32 = Re(ARM_{xx}ARM_{yx}^* - ARM_{yy}ARM_{xy}^*)$$

$$M33 = Re(ARM_{xx}ARM_{yy}^* + ARM_{yx}ARM_{xy}^*)$$

$$M34 = Im(ARM_{xx}ARM_{yy}^* + ARM_{yx}ARM_{xy}^*)$$

$$M41 = -Im(ARM_{xx}ARM_{yx}^* + ARM_{xy}ARM_{yy}^*)$$

$$M42 = -Im(ARM_{xx}ARM_{yx}^* + ARM_{yy}ARM_{xy}^*)$$

$$M43 = -Im(ARM_{xx}ARM_{yy}^* + ARM_{xy}ARM_{yx}^*)$$

$$M44 = Re(ARM_{xx}ARM_{yy}^* - ARM_{xy}ARM_{yx}^*)$$

8. PSM is used to obtain the Stokes PSF and the parameters for the PSF for different input polarizations. The intensity of the ghost PSF, ellipticity of the PSF is estimated using PSM.

The polarization models developed for the Thirty Meter Telescope and Multi-Application Solar Telescope using the algorithm and formalism specified in this Chapter are discussed in the following chapters.

Chapter 4

Polarization Model for the Thirty Meter Telescope (TMT)

4.1 Thirty Meter Telescope: Introduction

The Thirty Meter Telescope (TMT) is one of the large segmented mirror telescopes, proposed to be located in Mauna Kea, Hawaii, USA. It is a consortium between USA, Canada, India, China, and Japan. The telescope is expected to have its first light in 2028 (Sanders, 2013). The optical design of the TMT is a

folded Ritchey Chretien[1] (Figure 4.1), where the primary mirror is a concave hyperboloid of 30 m diameter with 492 hexagonal segments; with each segment being about 1.44 m (56.6 inches) across the corners. The secondary mirror is a convex hyperboloid of 3.1 m diameter, which converts the light coming from the primary mirror at F/1 to a F/15 beam for the science instruments on the Nasmyth platform (see Figure 4.2). The Nasmyth (tertiary) mirror is a plane mirror with elliptical cross-section of 3.5 × 2.5 m across and is located at the center of the primary mirror. The tertiary mirror will be able to switch among the science instruments rapidly and precisely. The rotation axis of the Nasmyth mirror is coincident with the optical axis of the primary mirror whereas its tilt axis is perpendicular to the optical axis. The F/15 beam forms the image at the Nasmyth focus which is 20 m from the center of the tertiary mirror. The full field of view of the telescope is 20′ with slight vignetting.

As shown in Figure 4.2, there are eight instrument ports on the Nasmyth platform for TMT. The first generation instruments are Wide Field Optical Spectrograph (WFOS), Narrow Field Infrared Adaptive Optics System (NFIRAOS), and Infrared Imaging Spectrograph (IRIS). The rotation (θ) and tilt (Φ) for the Nasmyth mirror changes for different instrument port and zenith angle of the telescope. The coordinate system used to derive these angles is explained in a TMT design requirements document (TMTGroup, 2012).

$$\theta = \arctan\left(\frac{\cos\zeta\cos(IEA)\sin(IBA) - \sin\zeta\sin(IEA)}{\cos(IEA)\sin(IBA)}\right) \tag{4.1}$$
$$\Phi = 0.5\arccos(-\sin\zeta\cos(IEA)\sin(IBA) + \cos\zeta\sin(IBA)) \tag{4.2}$$

where ζ corresponds to the zenith angle of the telescope varying between 0 and 65 degrees, IEA is the instrument elevation angle, and IBA is the instrument bearing angle. θ and Φ correspond to the rotation and the tilt of the Nasmyth mirror depending on the instrument position. $IEA = 0$ for all the instrument ports, as the focal plane of all the instruments intercepts with the telescope's focal plane. With $IEA = 0$, the tilt and rotation of the mirror depends on

---

[1] https://www.tmt.org/page/optics
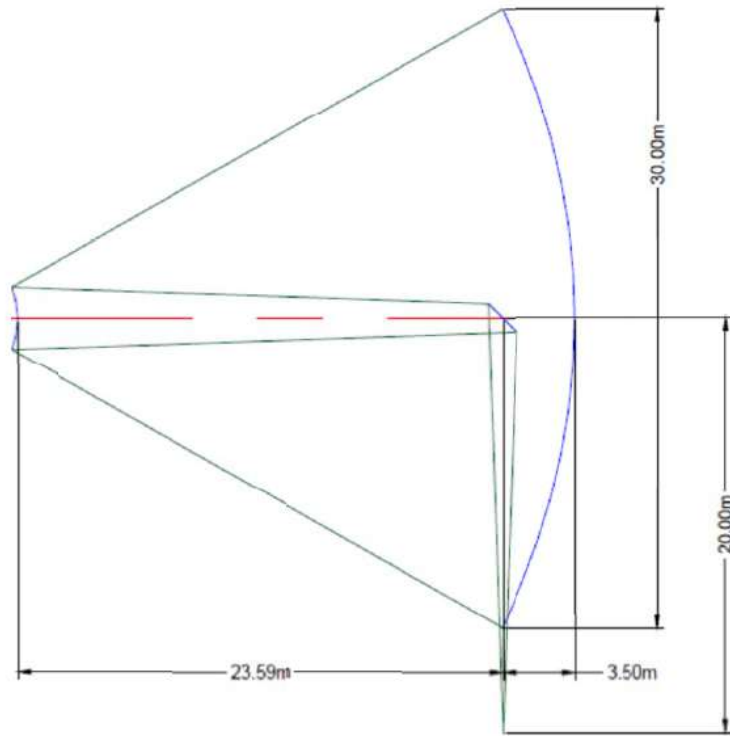
Figure 4.1: Optical Layout of the Thirty Meter Telescope showing the folded Ritchey-Chretien layout (TMTGroup, 2012).

IBA and the zenith angle of the telescope.

None of the first generation instruments of TMT have polarimetric capability. To understand the effects of the polarization from the telescope optics on polarimetric and non-polarimetric observations, a polarization model for the TMT was developed. In this Chapter, the variations in the Instrumental polarization (IP), crosstalk (CT), and depolarization (DP) with wavelength ($\lambda = 0.4$ to 2.5 μm) and field angle (0 to $7.5'$) at one of the instrument port (WFOS) of TMT are presented. Along with this, the contour plots of the Mueller matrix terms explaining the variation of the matrix elements over the mirror surface are illustrated. The dependence of Mueller matrix elements on the field angle, instrument position, zenith angle, and the mirror coating is given. IP and CT are also estimated at one of the second generation instrument port, MICHI in the near and mid-infrared wavelength region. The impact of the polarization effects on the science programs, and their mitigation and calibration strategies are discussed. Finally, a design to mitigate the polarization effects due to the telescope optics is presented.
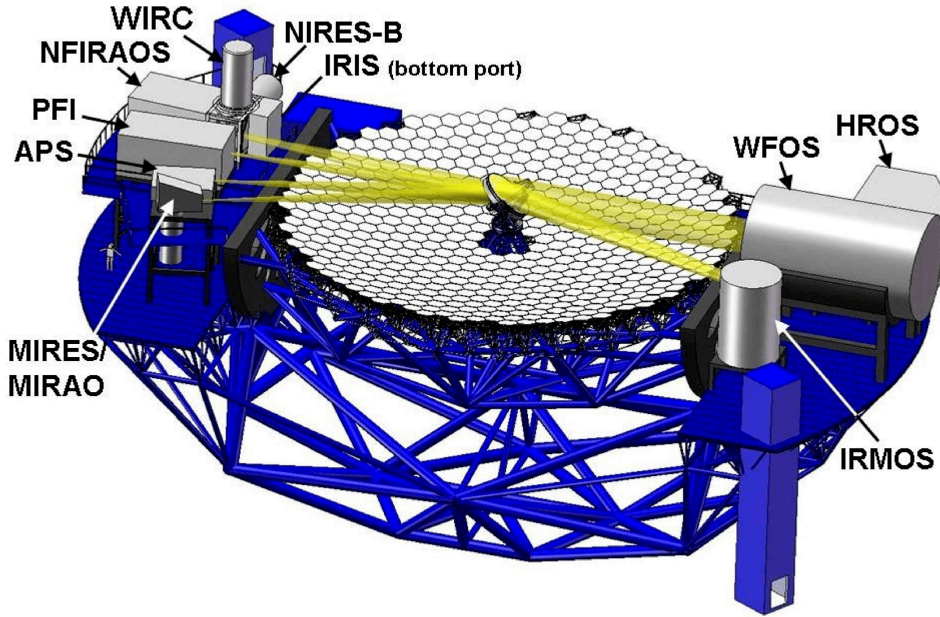
Figure 4.2: The Nasmyth platform of the TMT showing the different instrument positions. WFOS instrument port corresponds to the tilt of 45 degrees of the Nasmyth mirror (TMTGroup, 2012).

4.2 Estimation of polarization effects for the Thirty Meter Telescope (TMT)

The primary mirror of the TMT is a concave hyperboloid which can be defined by the equation in the Cartesian coordinate system,

$$-\frac{x^2}{ap^2} - \frac{y^2}{ap^2} + \frac{(z+cp)^2}{cp^2} = 1 \qquad (4.3)$$

with the vertex of the hyperboloid at the origin. The secondary mirror of TMT is a convex hyperboloid which is described by the Eqn (4.4).

$$-\frac{x^2}{as^2} - \frac{y^2}{as^2} + \frac{(z-\tau)^2}{cs^2} = 1 \qquad (4.4)$$

where, τ is the distance between the vertices of primary and secondary mirrors. The values of ap, as, cp and cs can be expressed in terms of the conic constant (K) and Radius of curvature (ROC) of the hyperboloid mirror. The ROC of the primary mirror and secondary mirror are -60 m and -6.228 m, respectively.
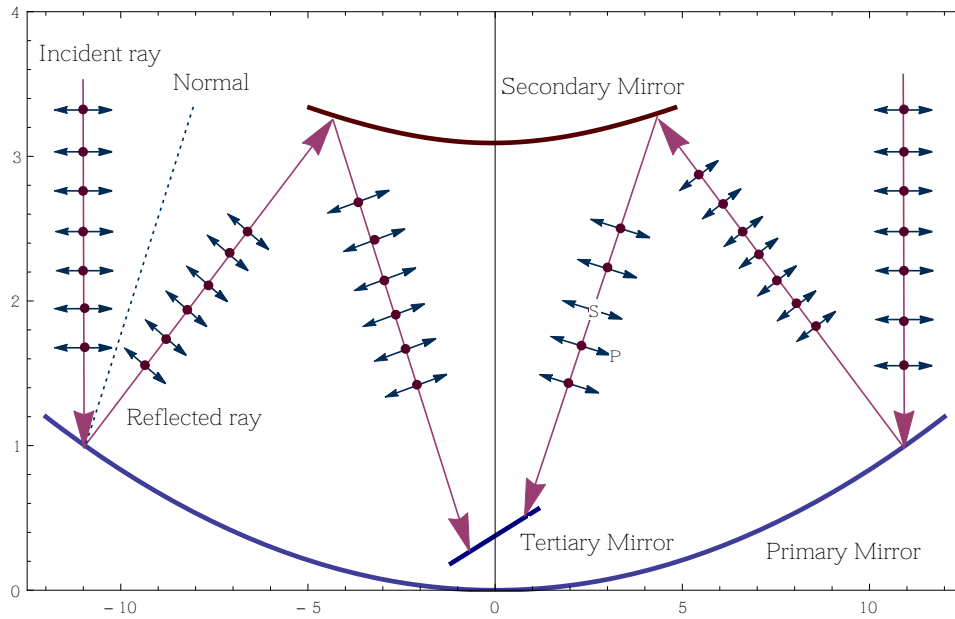
Figure 4.3: The TMT representation showing ray diagram and mirrors.

Conic constants of the primary mirror and secondary mirror are $K1$=-1.000953 and $K2$=-1.3182, respectively. The Nasmyth mirror is a plane elliptical mirror whose tilt and rotation are estimated from Eqn (4.2). Figure 4.3 shows the representation of the TMT with the ray diagram.

Using the polarization ray tracing algorithm given in Chapter 3, incident angles have been estimated on the surface of primary, secondary, and Nasmyth mirrors. The incident angle on the primary (shown in Figure 4.4a) and secondary mirror show similar variation for the rays parallel to the $z-$axis. The incident angle varies from 1.43° (at the inner edge with a radius of 1.5 m) to 14.035° (at the outer edge of the mirror with a radius 15 m) in the case of the primary whereas, it varies from 1.527° to 14.99° for the secondary mirror. The incident angle in the case of Nasmyth mirror (Figure 4.4b) increases from 43.089° to 46.910° from one end of the mirror to another end. One end of the beam (marginal ray) will have a higher angle of incidence compared to the other end; since the converging beam falls on the mirror kept at a tilt of 45°.

The mirrors in the TMT telescope will have a four-layer coating, which was initially developed for the Gemini telescope (Vucina et al., 2006). We are considering Silicon Nitride (Si_3N_x) of thickness 85 Å and Silver of 1100 Å for the
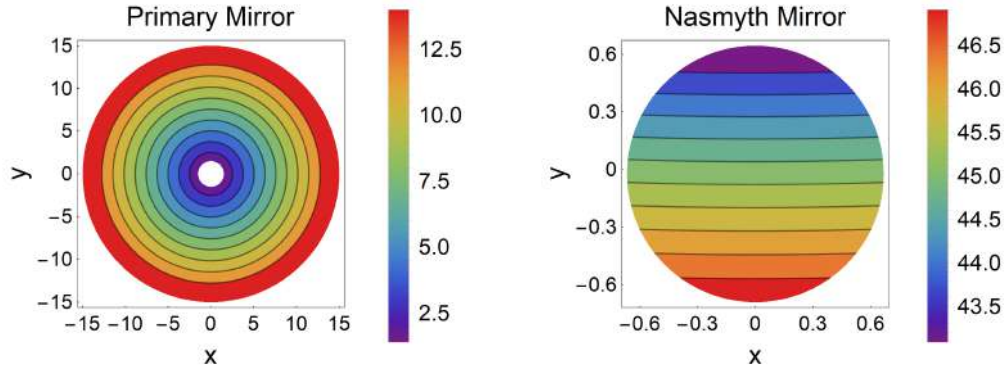
(a) The incident angles on the surface of primary mirror.

(b) The incident angles on the surface of Nasmyth mirror.

Figure 4.4: Incident angles shown for the on-axis rays falling on the mirrors.
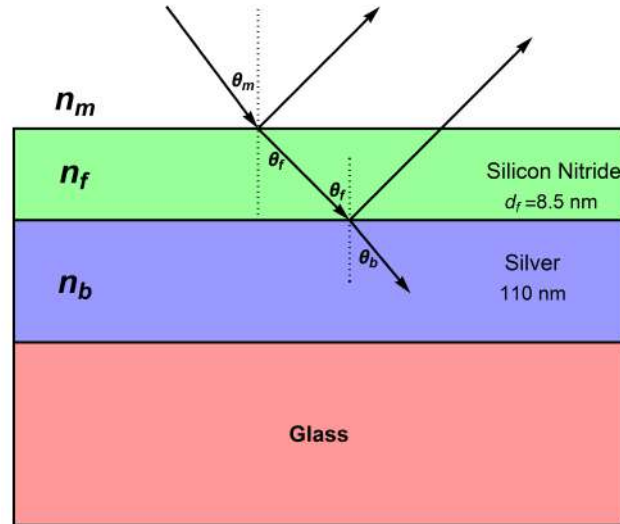
Figure 4.5: The coating used in the analytical modeling for TMT. Silver is the bulk metal layer. Silicon Nitride is the protective layer.

analysis as shown in Figure 4.5. The refractive index of NiCrN$_x$ (thickness of 65 Å and 6 Å) was not available in the literature and hence is not considered. The Fresnel reflection coefficients r_p and r_s for this coating are calculated (Macleod, 2010) for all the three mirrors as given in Chapter 3. We note r_p and r_s are complex numbers. The contour plots of the reflection coefficients for primary and tertiary are shown in Figure 4.6 and 4.7 respectively. The contours show the same variation as the incident angles show on the mirror surfaces. In Figure 4.6 and 4.7, the top panel shows the amplitude of r_p and r_s and bottom panel show the corresponding phase components ϕ_p and ϕ_s.

The Mueller matrices are estimated using the reflection coefficients as
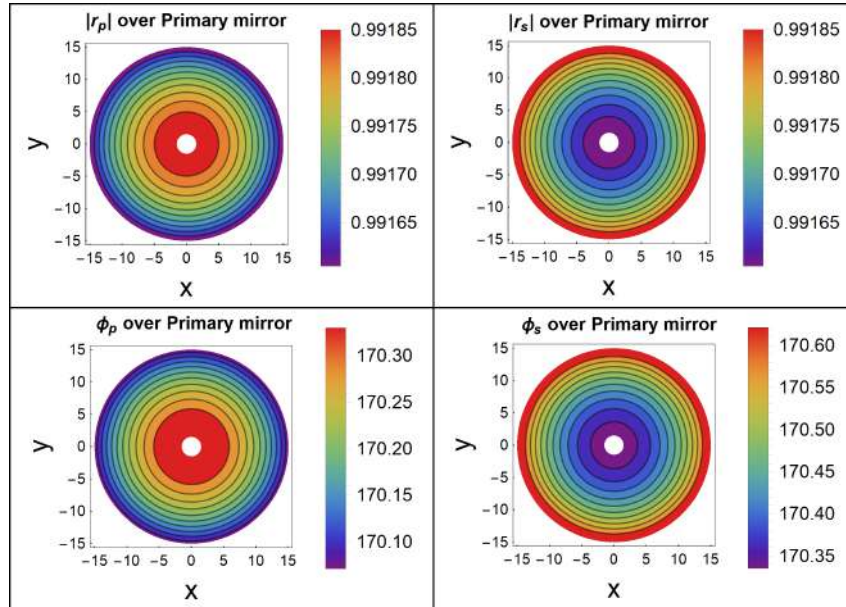
Figure 4.6: Reflection coefficients on the primary mirror surface at λ=2.583 μm. The top panel shows the amplitudes and the bottom panel shows the phase of the reflection coefficients.
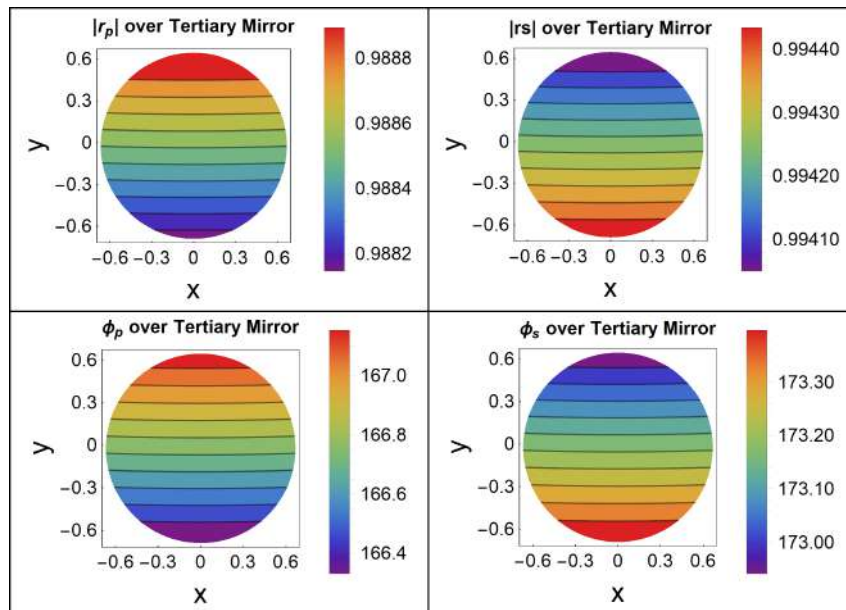
Figure 4.7: Reflection coefficients on the Nasmyth mirror surface at λ=2.583 μm. The top panel shows the amplitudes and the bottom panel shows the phase of the reflection coefficients.

shown in Chapter 3, which indicates that the polarization effects at Prime and Cassegrain focus are zero for the paraxial rays. The contour plot of the Mueller matrix for the primary mirror is shown in Figure 4.8. The $M11$ term in Figure 4.8 indicates the intensity values at different regions of the mirror surface. The incident angles are smaller (near normal angle of incidence) at the center of the primary mirror which indicates that the reflection coefficients are nearly equal. At the periphery, the r_p and r_s values diminish and hence the intensity decreases outwards. $M11$ is found to vary over the primary mirror surface with wavelength. $M21$ and $M31$ exhibit the division in four quadrants. In the first quadrant $0 - 90^0$, the $M21$ on the mirror exhibit positive values and the next quadrant exhibits negative values. When all the rays are added at the focal plane, we get $M21$ and $M31$ as zero at the prime focus for on-axis rays. $M41$ ($I \to V$) is found to be zero. These three elements ($I \to Q, U, V$) are related to the instrumental polarization (Keller, 2002). $M22$ and $M33$ show $Q \to Q$ and $U \to U$ which when squared and added, gives I for 100% linear polarization as input. $M23$ and $M32$ show the $U \to Q, Q \to U$ respectively. These terms correspond to the polarization rotation. $M42$ and $M43$ correspond to linear to circular polarization crosstalk. Due to antisymmetry, these become zero on average at the focus (which means when polarization states of all the rays are added at the focus). The contour plots of the Mueller matrix estimated at the Cassegrain focus display similar behavior as that of the prime focus as shown in Figure 4.8 and hence are not presented here.

The Mueller matrix corresponding to the Nasmyth mirror is shown in Figure 4.9. The Mueller matrix elements $M11$, $M22$, $M33$, and $M44$ show similar trend as that of the incident angle of the Nasmyth mirror. $M12$, $M21$, $M34$, and $M43$ are same across the major axis of the Nasmyth mirror with a positive contribution from each contour segment. But along the major axis, they are unequal along the two directions. The remaining elements ($M31$, $M32$, $M13$, $M23$, $M24$ and $M42$), have equal positive and negative contributions on either side of the major axis of the ellipse. Hence a non-zero instrumental polarization ($M21$) and crosstalk ($M43$) are seen at the Nasmyth focus.
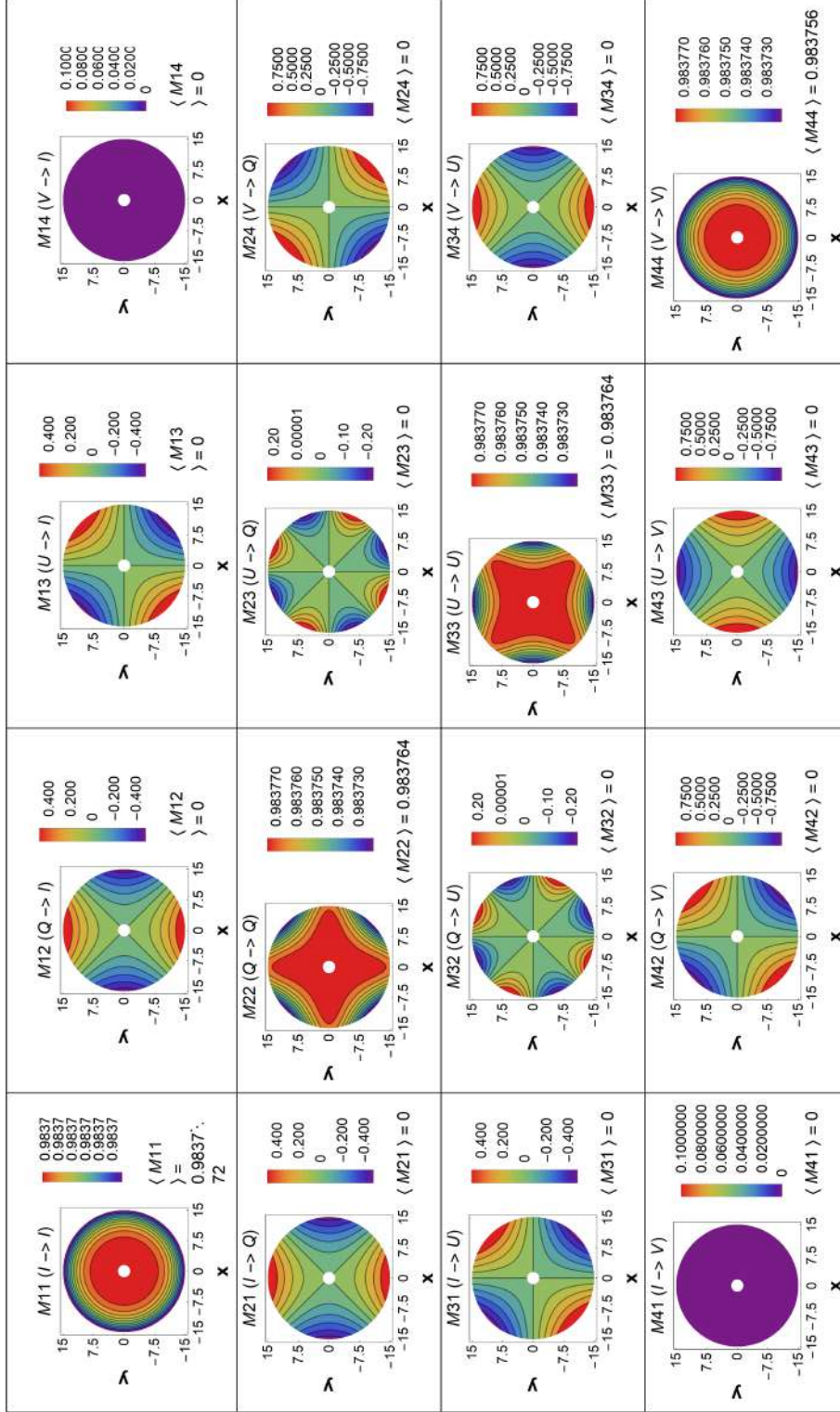
Figure 4.8: The Mueller matrix of the primary mirror at a wavelength of 2.580 μm for the on-axis rays. The number of rays are sampled radially. The input Stokes parameters are multiplied with this Mueller matrix to estimate the corresponding output Stokes parameters. The azimuth anti symmetry is seen in all the elements except the diagonal elements, which explains zero IP ($M21$ and $M31$) and crosstalk ($M32$, $M42$, $M43$) for on-axis rays at the prime focus. $\langle\ \rangle$ gives the average values of the Mueller matrix elements.
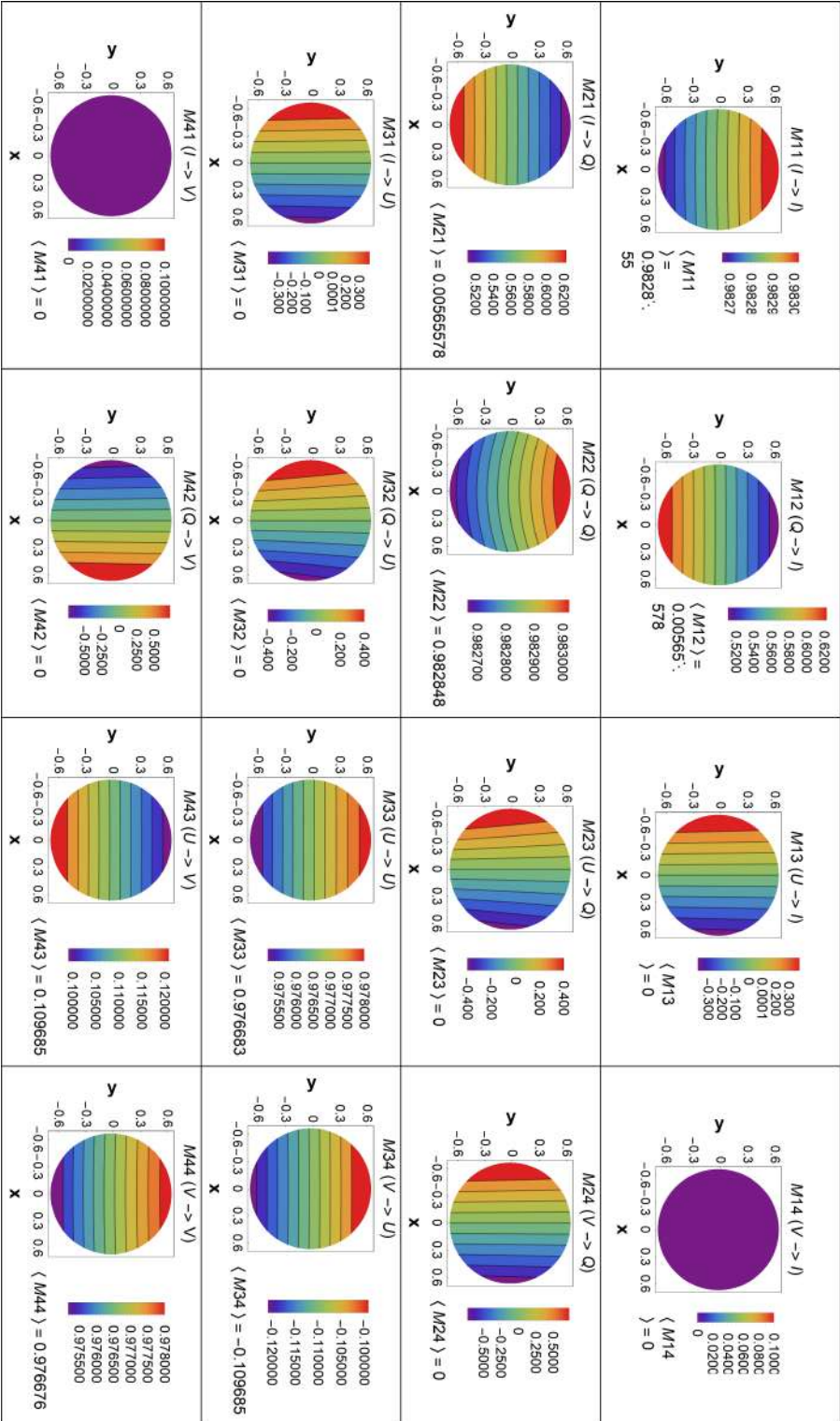
Figure 4.9: The Mueller matrix of the Nasmyth mirror at a wavelength of 2.58 μm for the on-axis rays. The contour plots are similar trend as that of the incident angle of the Nasmyth mirror. They show symmetry along one axis of the mirror. IP ($M21$) and CT ($M43$) is found to increase from one end of the mirror to the other. $M31$, $M32$, $M42$ show equal positive and negative values and gives zero on average. $\langle \, \rangle$ gives the average values of the Mueller matrix elements.
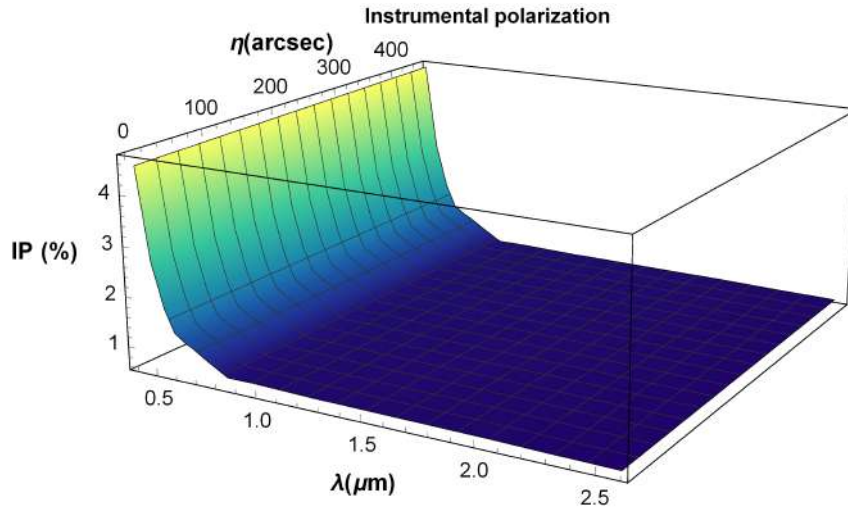
Figure 4.10: Variation of IP ($y-$ axis) for semi field of 7.5′ ($z-$ axis) and wavelength range of 0.4 μm to 2.5 μm ($x-$ axis) is shown at the Nasmyth focus of the TMT. The values are higher near the optical region is shown by yellow compared to those in the near infrared region shown by blue color.

For an unpolarized light falling on the primary mirror, IP was estimated at the Nasmyth focus using the polarization ray tracing algorithm. It is found to be in the order of 10^{-6} for the primary mirror (for field angle 7.5′) and in the order of 10^{-4} for the secondary mirror which are negligible compared with the measurement error. However, for zero field angles, these two values are exactly zero. Figure 4.10 shows the IP estimated at the Nasmyth focus when Nasmyth mirror is at $\theta = 0$ (rotation) and $\Phi = 45$ (tilt) pointing to WFOS instrument port (Figure 4.2). At this instrument port, the tilt of the Nasmyth mirror remains at 45 degrees even when the zenith angle of the telescope changes as shown in Eqn (4.2). In Figure 4.10, IP increases linearly with the field angle. It is in the range of $4-1.2\%$ in the optical region and 0.6% in the near infrared region for zero field angle. IP does not change with the zenith angle.

In the case of 100% polarized light as the input, depolarization is estimated to be 0.3% and 1.5% in the case of primary and secondary mirror, respectively for the field angle of 7.5′ at 0.4 μm. In Figure 4.11, DP increases with the field angle and is close to 0.8% in the near infrared region and rises to 2.5% in the optical at the field angle value 7.5′ at the Nasmyth focus at the WFOS instrument port (IBA=0, IEA=0). The polarization state of light at the end of the Nasmyth focus has changed to elliptical from 100% linear polarization
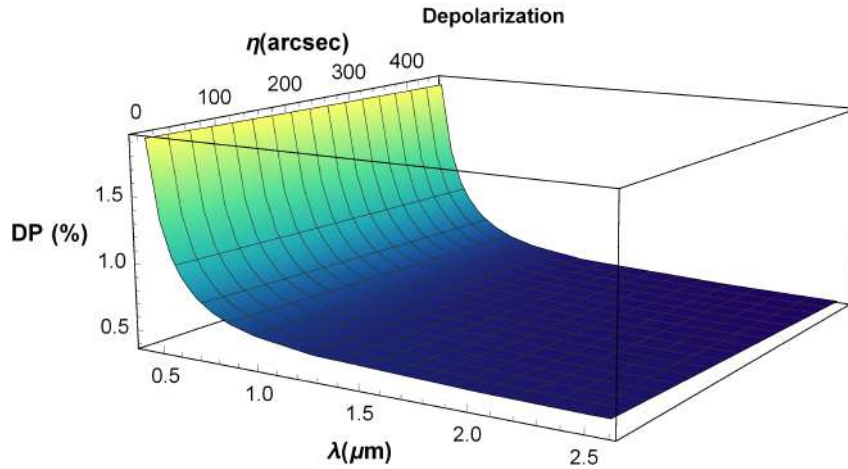
Figure 4.11: Variation of DP for semi field of $7.5'$ ($z-$axis) and wavelength range of 0.4 μm to 2.5 μm ($x-axis$) is shown at the Nasmyth focus of TMT. The values are higher near the optical region is shown by yellow compared to those in the near infrared region shown by blue color.

which indicates the conversion from U to V. Hence we estimate the circular polarization at the Nasmyth focus to determine crosstalk (see Figure 4.12). Crosstalk at the Nasmyth focus increases with the field angle and is found to be higher (70%) in the optical region compared to the near infrared region (10%) which indicates that the circular polarization has to be measured to reconstruct the input linear polarization. The DP and CT do not depend on the pointing of the telescope at this instrument port of TMT. Table 4.1 shows the IP, DP, and CT at Nasmyth focus for different wavelengths, for rays parallel to the optical axis.

4.3 Averaged Mueller Matrices on the Nasmyth Platform

The Mueller matrices are estimated using polarization ray tracing for each ray falling on the primary mirror and averaged at the Nasmyth focus using polarization pupil map in Zemax®. It depends on the reflection coefficients and the incident angles. The incident angles (on the Nasmyth mirror) vary with the field angle, zenith angle of the telescope, and instrument bearing angle (IBA) of the instrument on the Nasmyth platform.
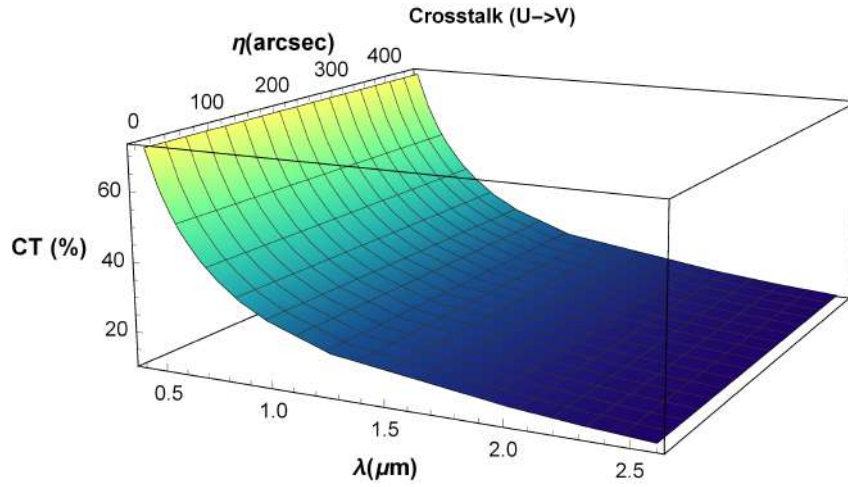
Figure 4.12: Variation of CT for semi field of 7.5' ($z-$axis) and wavelength range of 0.4 μm to 2.5 μm ($x-axis$) is shown at the Nasmyth focus of TMT. The values are higher near the optical region is shown by yellow compared to those in the near infrared region shown by blue color.

Wavelength (μm)	IP (%) $I \to Q, U$	DP (%)	CT (%) $U \to V$
0.4	4.54	2.0	72.12
0.4592	2.69	1.35	61.36
0.5166	1.82	1.08	53.64
0.5636	1.37	0.94	48.77
0.6199	1.21	0.83	44.06
0.6526	1.14	0.78	41.54
0.7293	0.94	0.70	36.83
0.8266	0.70	0.64	32.11
0.9537	0.71	0.58	27.66
1.24	0.68	0.52	21.11
2.000	0.65	0.48	14.37
2.296	0.63	0.47	12.53
2.583	0.61	0.46	11.16
Astronomical bands	IP (%)	DP (%)	CT (%)
U,B,V	4.5-1.3%	2-1%	70-45%
R,I	1.2-0.7	1-0.6 %	45-32%
J	0.68%	0.53 %	21%
H	0.65%	0.48%	14%
K	0.63%	0.47 %	12%
>2.5	<0.6%	<0.46%	<10%

Table 4.1: Variation of IP, DP, and CT with wavelength at 0 field angle. Here IP corresponds to the unpolarized light falling on the mirror and DP, CT corresponds to the 100% linearly polarized light falling on the mirror.

4.3.1 Mueller matrices at WFOS port for various field angles.

The field of view of TMT is 15′ without vignetting. The variation of the Mueller matrix elements with different field angles is shown in Figure 4.13. The matrix elements do not change much with an increase in the field angle. The instrumental polarization estimated over the field of view (on the sky) of the telescope is shown in Figure 4.14. The IP values are asymmetric along the major axis of the Nasmyth mirror with the elliptical cross section. This effect would lead to polarization variation across the FOV, especially in the case of imaging polarimetry of extended sources.

4.3.2 Mueller matrices at different instrument ports of TMT

As shown in the Figure 4.2, currently there are 8 instrument ports on the Nasmyth platform for TMT. θ and Φ corresponding to the rotation and the tilt of the Nasmyth mirror changes depending on the instrument position. IEA=0° for all the instrument ports as focal plane of all the instruments intercepts with the telescope focal plane. With IEA=0°, the tilt and rotation of the mirror depends on IBA and the zenith angle of the telescope. For the $\zeta = 0$, the Mueller matrix at different instrument ports can be obtained by $M_{inst} = M_{wfos}R(\theta)$, where θ corresponds to the rotation of the tertiary mirror from its initial position (WFOS port, IBA=0°) and M_{wfos} is the Mueller matrix at the WFOS port ($\theta = 0$°). These rotation matrices can be easily included in the data reduction pipeline for determining the polarization effects at different instrument ports (Joos et al., 2008). The IP does not change with the rotation of the mirror as the tilt of the Nasmyth mirror remains same at all the ports (see Eqn (4.2)). Figure 4.15 and 4.16 show the variation in the Mueller matrix at different instrument ports on +X and -X Nasmyth platform respectively.

For $\zeta \neq 0$°, θ and Φ vary at every instrument port except at WFOS port.
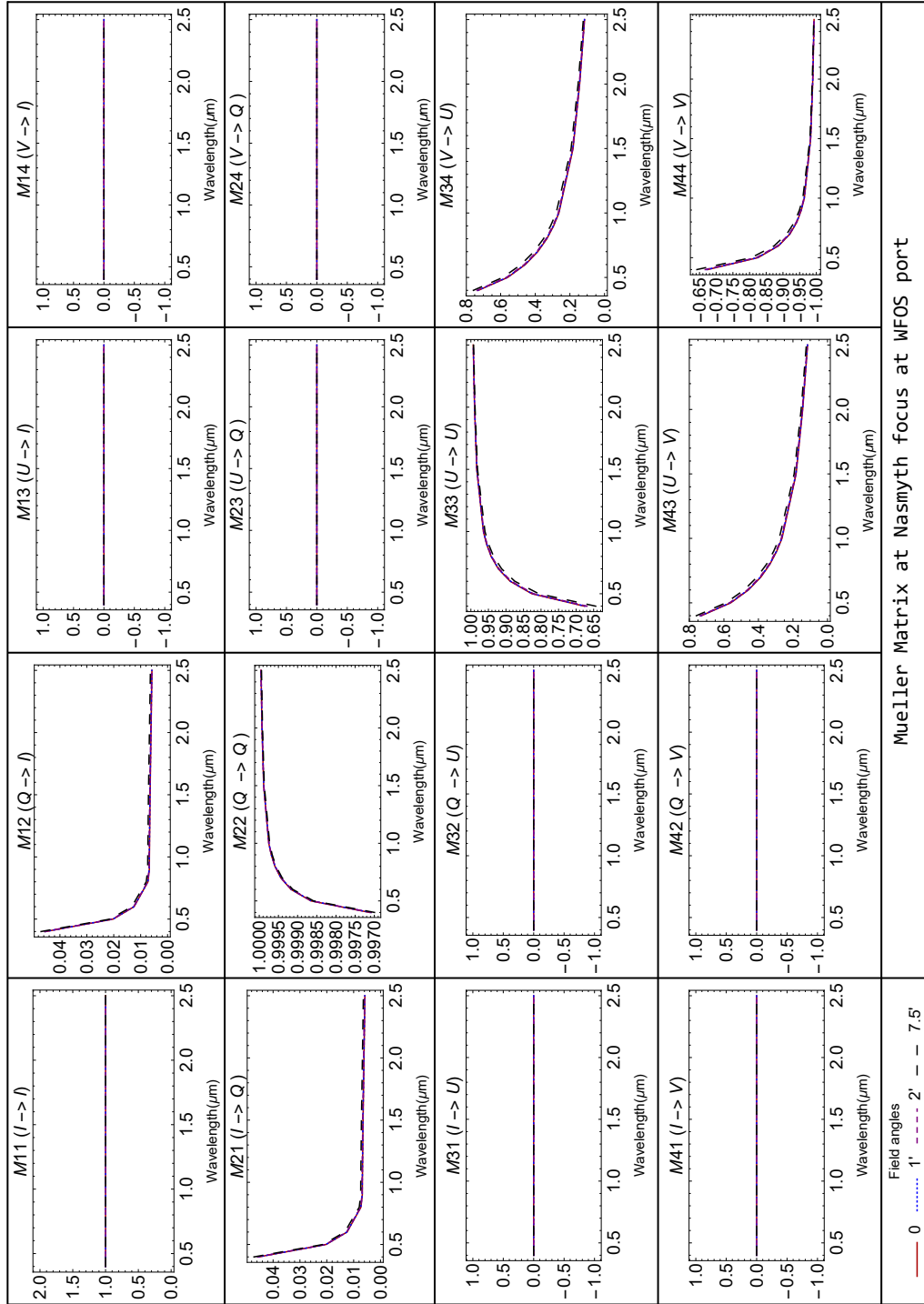
Figure 4.13: Normalized Mueller matrices versus wavelength is obtained at the WFOS port of TMT for different field angles.
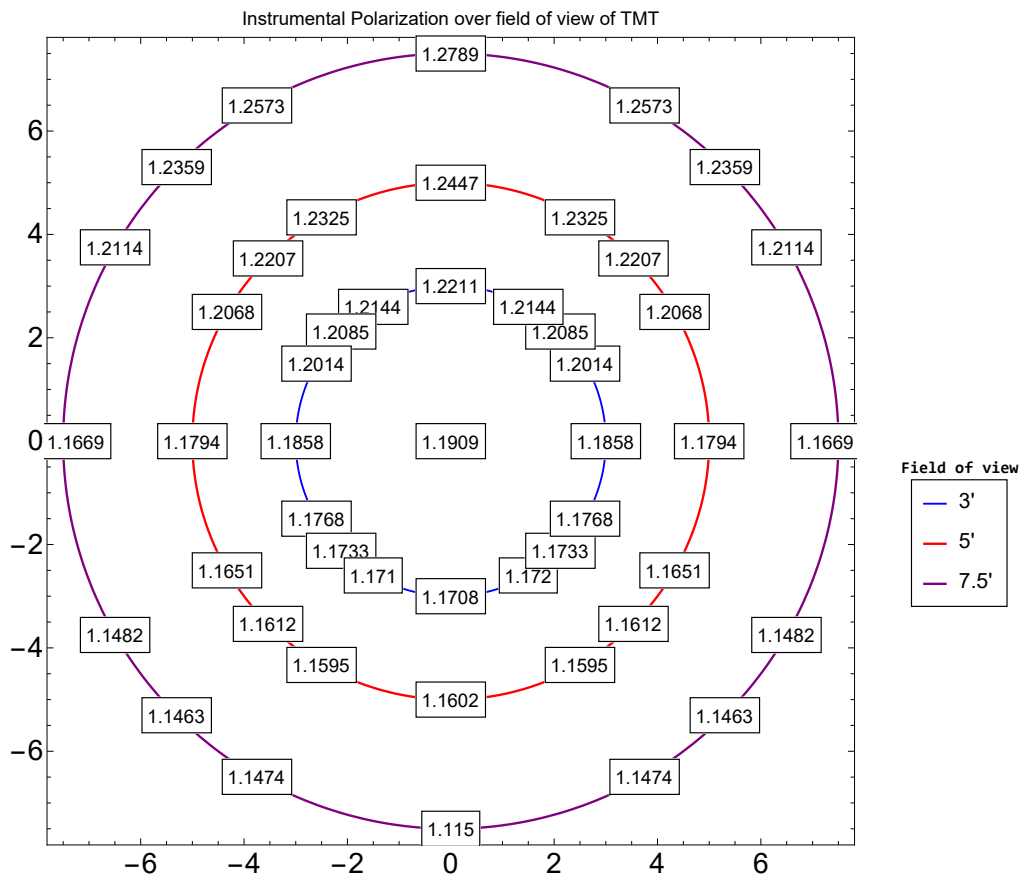
Figure 4.14: The IP is estimated at the WFOS port for the field of view of the telescope. The 3 concentric circles represent 3, 5 and 7.5′ respectively. The IP values are written inside the box at each field point.
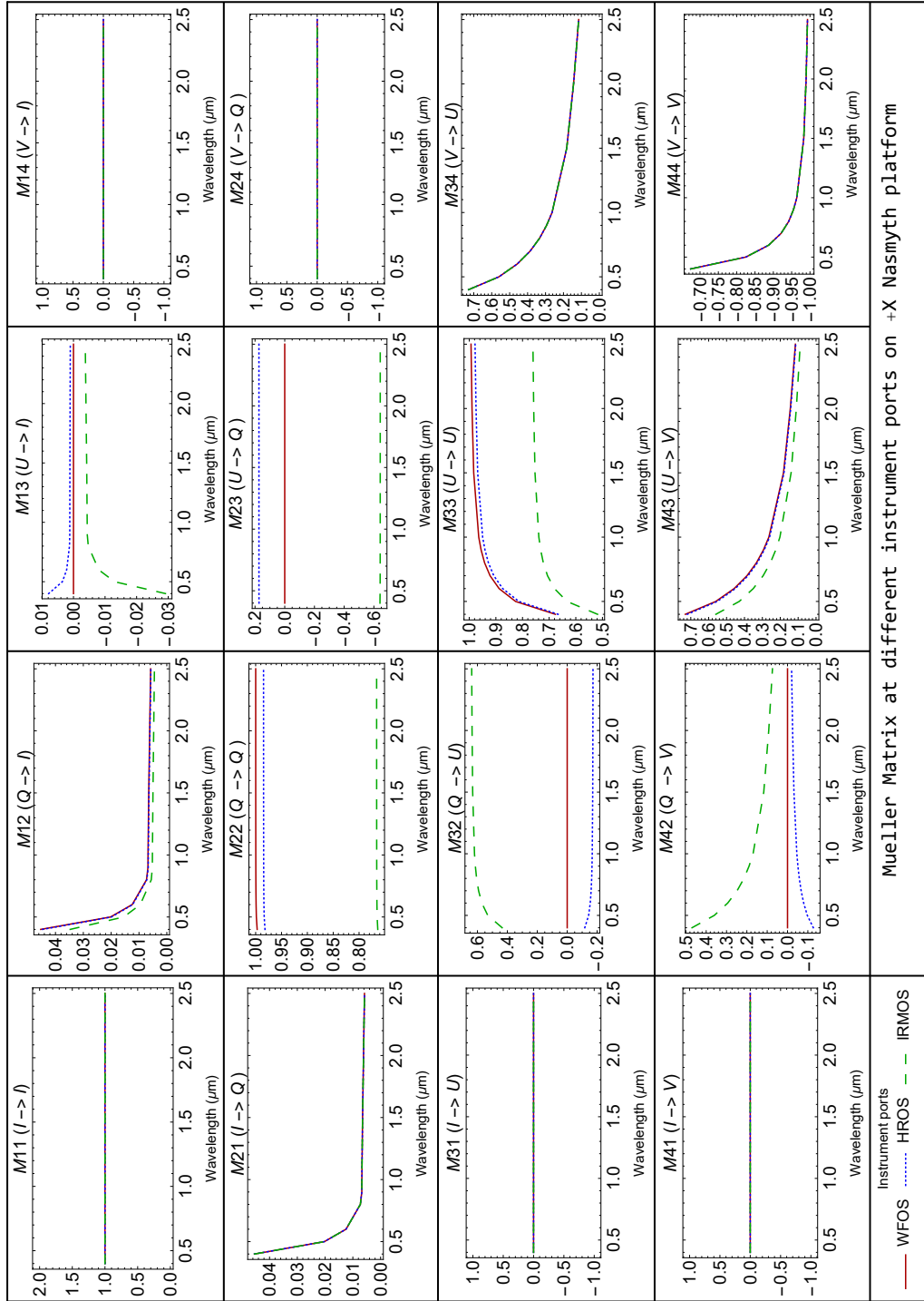
Figure 4.15: Normalized Mueller matrix versus wavelength is estimated at different instrument ports on the +X Nasmyth platform of TMT. WFOS is at IBA=IEA=0°, HROS is at IBA=5°, IEA=0° and IRMOS is at IBA=-5.5° IEA=0°. These are indicated by colors and line styles.
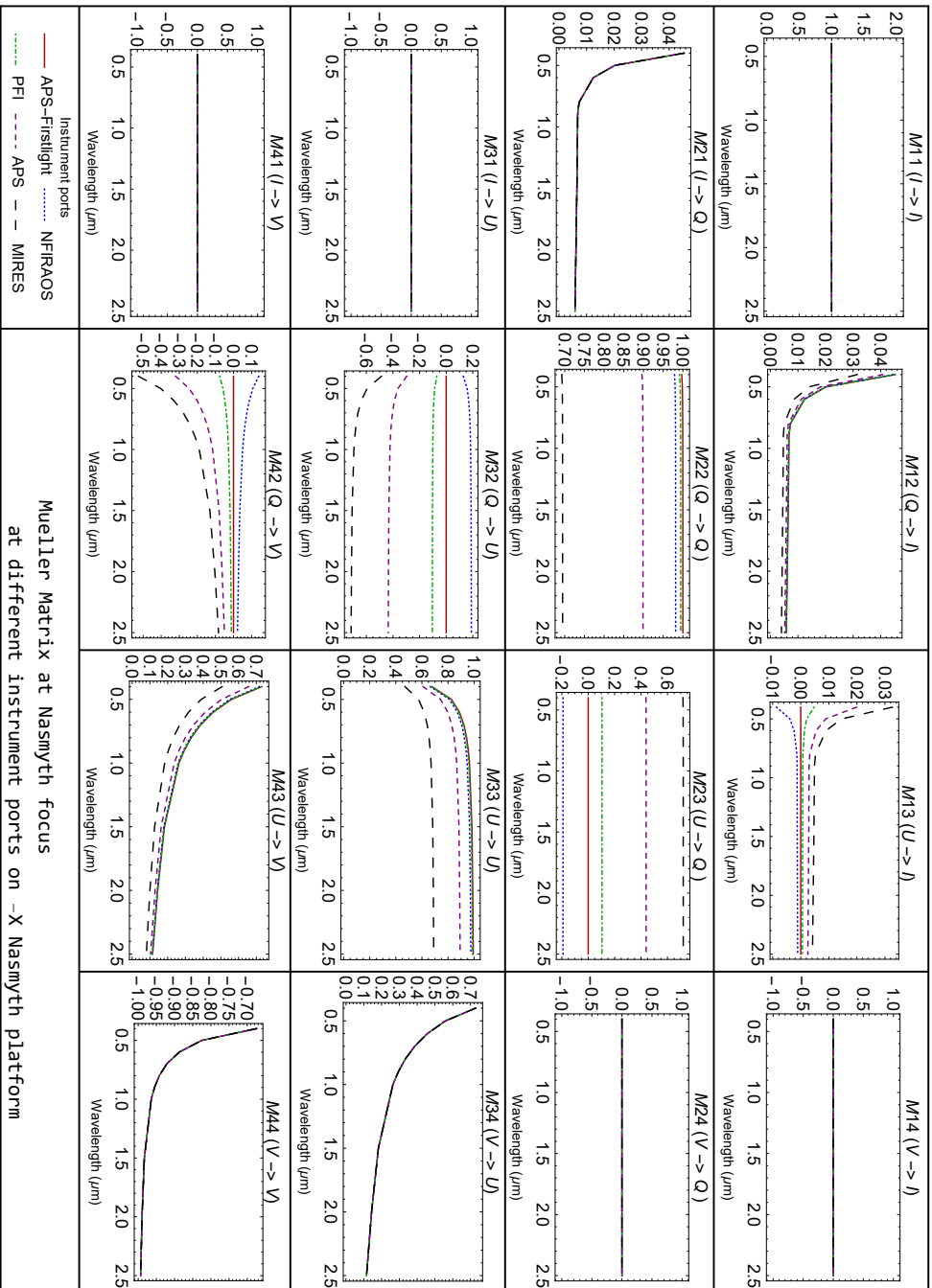
Figure 4.16: Normalized Mueller matrix versus wavelength is estimated at different instrument ports on the -X Nasmyth platform of TMT. APS first light is at IBA=180°, IEA=0°, NFIRAOS is at IBA=174.5°, IEA=0°, PFI is at IBA=183°, IEA=0°, APS is at IBA=194°, IEA=0° and MIRES is at IBA=203°, IEA=0°. These are indicated by colors and line styles.

Mueller matrices are estimated at two instrument ports, one on +X and other on the -X Nasmyth platform of TMT for varying zenith angles. The IP and CT are found to vary with the zenith angle of the telescope as shown in Figure 4.17. The variation in IP is 0.1% and in CT, it is 5% when the telescope is tracking an object from zenith angle $0 - 65$ degrees.

4.3.3   Impact of protected silver coating on instrumental polarization and crosstalk.

The IP and CT values as shown in Figure 4.13 indicate that the polarization effects are comparatively higher in the blue wavelength region than the red wavelength region. Further analysis and estimation revealed that the high IP and CT values are due to the characteristics of Silver, which are related to the complex refractive index of Silver. The reflectivity plots for Aluminum, bare Silver, and protective Silver can be found in [2], which show that silver has low reflectivity in the wavelength range 0.3 - 0.45 μm. The real and imaginary part of the refractive index of silver are almost equal. Mueller matrix at the Nasmyth focus is also obtained with bare Aluminum coating for a comparison with the Gemini coating used in TMT, and the results are reproduced in Figure 4.18.

4.4   Instrumental polarization and crosstalk in the near and mid infrared region for TMT

One of the proposed second-generation instrument (in the thermal infrared wavelength region, 3-14 μm (-25 μm to be confirmed)) named Mid-Infrared Camera, High-disperser, and Integral field unit (MICHI) for TMT will have the polarimetry capability. IP and CT are estimated for the MICHI port in near and mid infrared region.

---

[2]`https://www.gemini.edu/sciops/telescopes-and-sites/optics/silver-vs-aluminum`
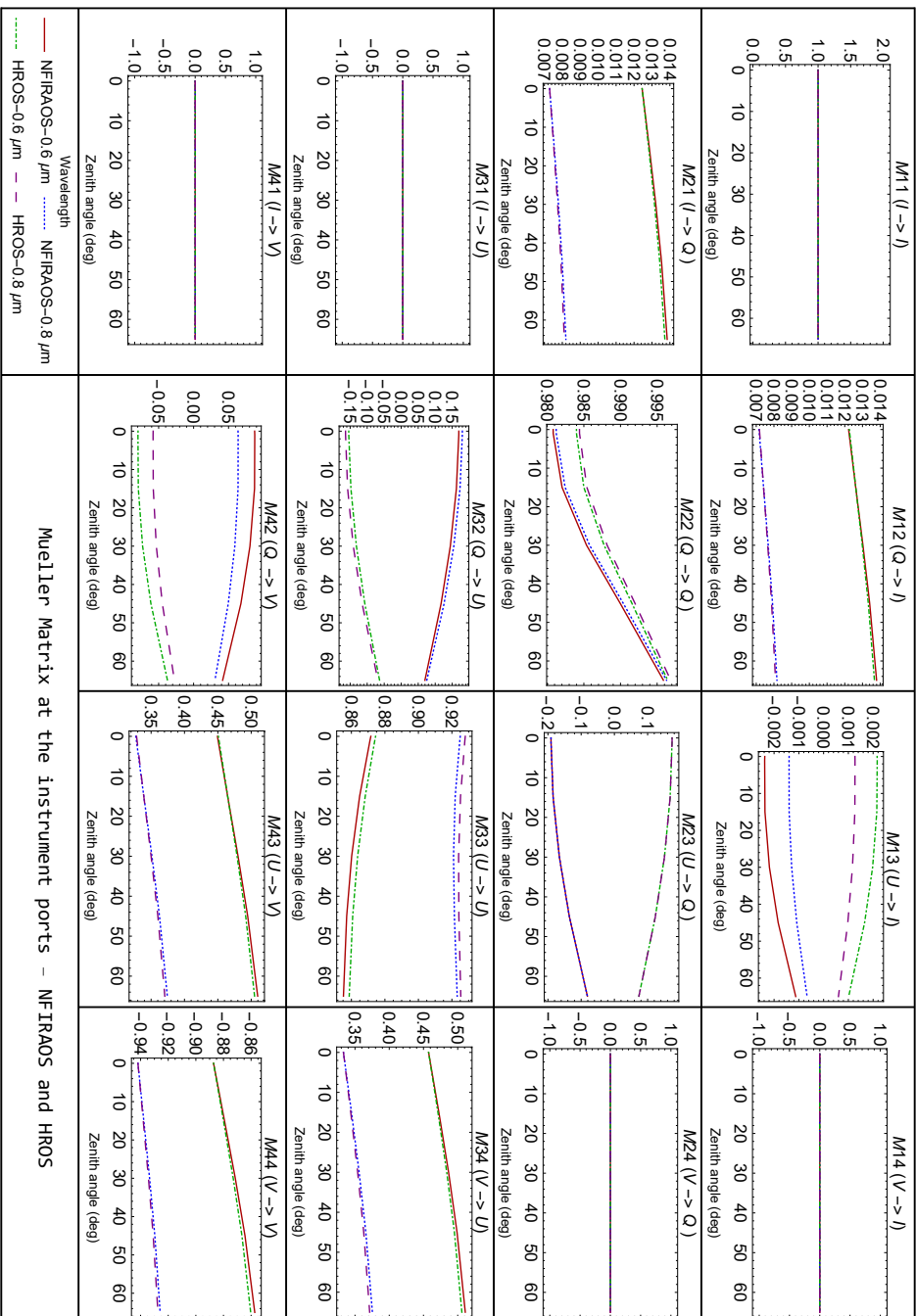
Figure 4.17: Normalized Mueller matrix versus zenith angle is obtained at two different instrument ports on the Nasmyth platform of TMT. HROS is on the +X and NFIRAOS is on the -X Nasmyth platform. The colors and plot markers are used to indicate wavelength and instrument port.
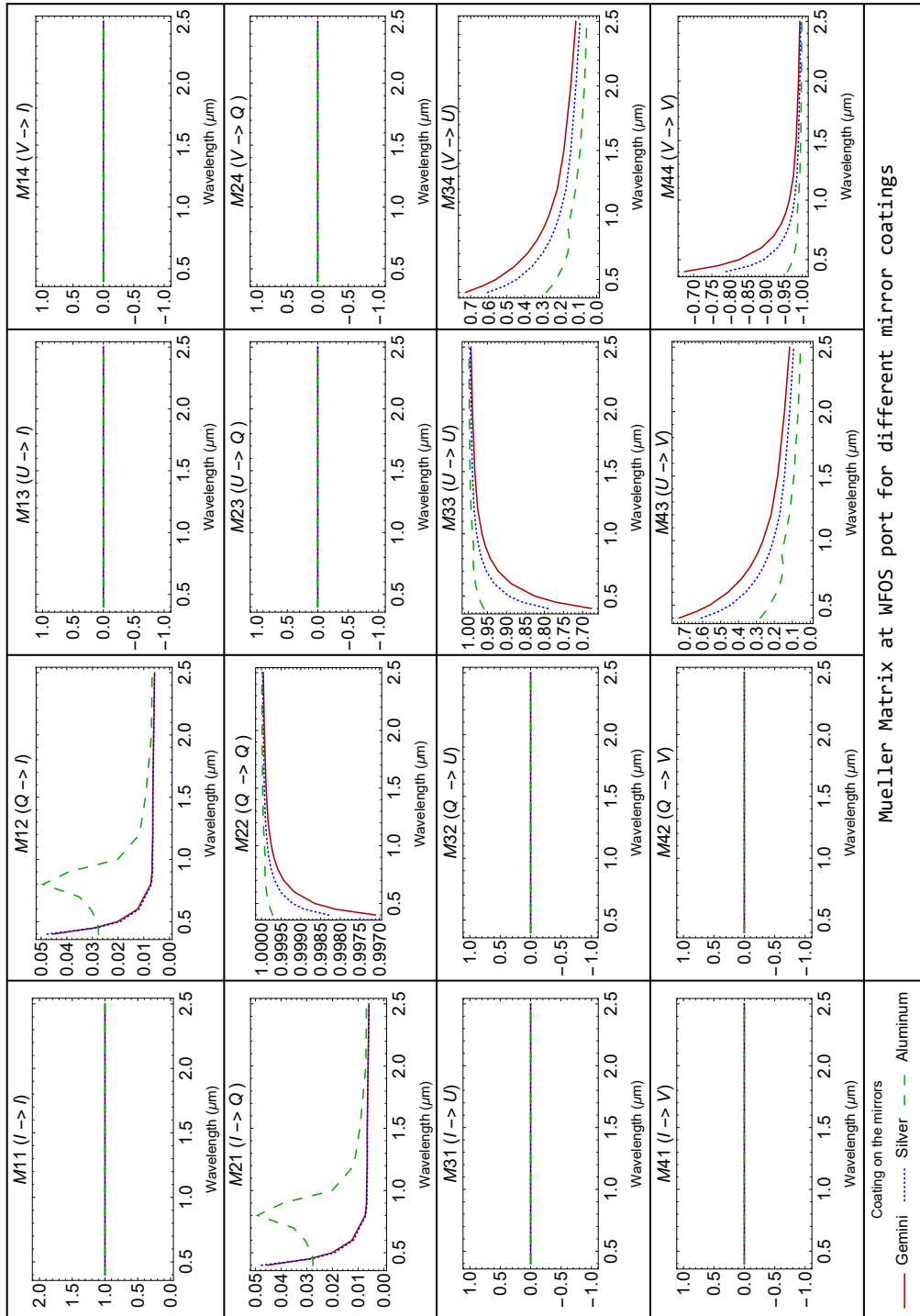
Figure 4.18: The normalized Mueller matrix versus wavelength for different mirror coatings in TMT is obtained. Gemini, Silver, and Aluminum are indicated by red, blue and green color respectively.

4.4.1 Instrumental polarization and crosstalk at the instrument port of MICHI

MICHI is located in the -X Nasmyth platform of the TMT. The Nasmyth mirror has to rotate 23 degrees from the Alignment and Phasing system (APS) position to feed the light to MICHI (Figure 4.2). The tilt (Φ) and the rotation (θ) of the mirror changes during the tracking of the telescope. As a result of this, the incident angle on the Nasmyth mirror also changes during the tracking. The contour plot of the incident angle on the surface of the Nasmyth mirror at a zenith angle of 45 degrees is shown in Figure 4.19. It varies from 39 to 35 degrees along the tilt axis of the mirror. The variation of the incident angles with zenith angle for the marginal rays is shown in Figure 4.19. The IP and CT also varies with the zenith angles same as in the previous section. Figure 4.20 shows the variation of IP and CT with the zenith angle of the
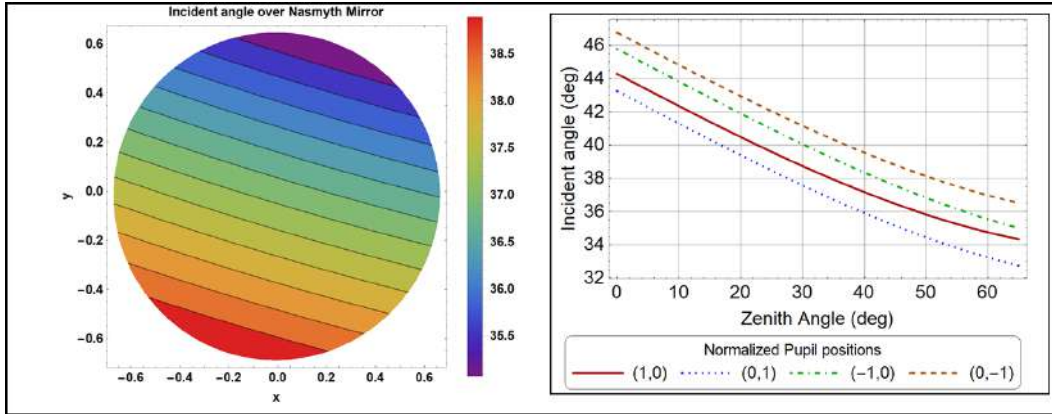
Figure 4.19: The contour plot of the incident angle on the surface of the Nasmyth mirror for MICHI port. x and y corresponds to the co-ordinates on the mirror surface. The variation of the incident angle with the zenith angle is shown at the normalized pupil positions.

telescope. IP reduces from 0.6% to 0.3% and CT reduces from 2.8% to 2% for $\lambda = 7.293$ μm when the zenith angle of the telescope varies from 1 to 65 degrees. Further discussion on MICHI and its design is presented in Chapter 8.
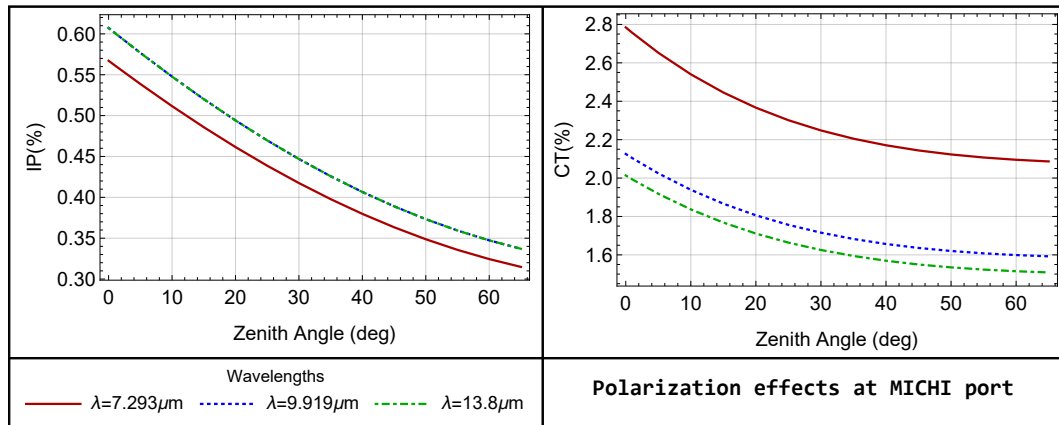
Figure 4.20: Instrumental polarization and crosstalk estimated at the MICHI port for different zenith angles.

4.5 Impact on the science cases and calibration error

The polarimetric analysis of TMT carried out here computes the instrumental polarization, crosstalk, and depolarization across the field angles and the wavelengths that can be compared to the requirements of various observing programs. The calculated mean IP and CT values for the TMT Nasmyth focus must be considered as lower limits since in a real scenario the instrument would have additional effects due to variations in the coating, refractive indices etc. The 35 science programs requiring polarimetric capability collected by the TMT Polarimetry and Time-Resolved Working Group (PTRWG) were examined following the polarimetry modeling and results. The suitability of TMT for all these science cases are available as a TMT internal document (see Anche et al. (2015)) [3]. We discuss here a few of those science cases as listed in Table 4.2. We have compared the requirements for each science program given in Table 4.2 against the values given in Table 4.1. The first three science programs can be attempted in the infrared wavelength regime, but not in the optical wavelength regime (see Table 4.2) depending on their acceptable IP requirements. The first two programs do not have any specific requirements on

---

[3] https://docushare.tmt.org/docushare/dsweb/Get/Document-31161/assessment _potential_polarimetric_progs.docx

the acceptable amount of crosstalk and depolarization. The acceptable degree of crosstalk is much lower than the estimated values for the third program. In the case of observing program number four, the IP and depolarization estimated are less than the requirements given. TMT can completely support this with an appropriately designed instrument. The last two science programs in the Table 4.2 with the requirement of acceptable IP in the order of 0.1-0.3% are unlikely to be supported. It is seen from Table 4.1 that in the mid and far infrared region, the IP, crosstalk and depolarization values are low, which allows us to consider the possibility of polarimetry in the Q and N bands.

4.5.1   Mitigation and calibration strategies

The polarization calibration error is dependent on systematic and measurement errors (Tinbergen, 2005). We note here that the IP calculated in the above analysis can be treated as a systematic error if all the mirror positions are adequately controlled and calibrated. Thus one should be able to calibrate and correct the data for the instrumental polarization offset. The usual calibration method carried out in a Cassegrain telescope is recording the observations of standard polarized and unpolarized stars. This method of calibration can also be carried out at the TMT, but this will not reduce the actual level of IP. The ability to carry out science programs depends on the ability to determine an accurate calibration of the IP. The uncertainty of the calibration of the IP is typically a few % of the actual IP. Consequently, significantly reducing or mitigating the overall IP and therefore reducing the uncertainty on the calibration is an appealing strategy. One of the mitigation methods would be to use a compensating mirror (Cox, 1976; Tinbergen, 2007) after the Nasmyth mirror before the polarimeter optics within the instrument. This is discussed in the next section. This technique has been implemented in the SPHERE instrument at the Nasmyth focus of the Very Large Telescope (VLT) (Roelfsema et al., 2016) and shows a residual IP of about 10^{-3} from 4-5% prior to the mitigation.

Table 4.2: Science programs, observing requirements and assessment results. The 'Acceptable Instrumental Polarization' includes the contributions from the telescope and the instrument, including the adaptive optics system where appropriate.

Observing program and science cases	Wavelength region	Level of polarization per spatial and/or per spectral element	Field of view	Required S/N per wavelength bin	Limit of acceptable polarization calibration error	Acceptable Instrumental Polarization	Acceptable degree of crosstalk	Acceptable amount of depolarization	Assessment
Chemical stratification and evaporation processes in comets	300-800nm	0.4% to 15%	Extended nucleus slit length ~2 arc sec	~500	0.10%	~few %	Not a significant problem	Not a significant problem	The estimated IP, CT and DP values are within the acceptable limits only in the near IR region and not in the optical region
Outflow geometry of quasars	Opt-NIR and 1 to 13 microns	0-40 %	~5"	~10^3	0.1-1%	~1%	Not a significant problem	Not a significant problem	The estimated IP, CT and DP values are within the acceptable limits only in near IR region and not in optical region
Kinematic structure of CSM of young stars and brown dwarfs	370 nm to 1000nm	~1%	single object, seeing limited		0.10%	<1% req, <0.5% goal	~1%	~10%	The estimated IP, CT and DP values are within the acceptable limits only in near IR region and not in the optical region.
High-contrast imaging of proto-planetary disk and magnetic field structure by polarized flux	1 micron to 2 microns J, H, K bands	5%	5x5 arc seconds		0.10%	<2% req, <1% goal	Not a significant problem	<2%	The estimated IP, CT and DP values are within the acceptable limits for the entire wavelength region. Can be supported by TMT
Magnetic field of massive evolved stars, chemically peculiar stars and white dwarfs.	350nm to 1000nm	0-0.6% variable	seeing limited point source	1000	0.01%	0.2-0.3%	Not a significant problem	Not a significant problem	The estimated IP, CT and DP values are beyond the acceptable limits for the entire wavelength region. Unlikely to be supported by TMT
Vegetation Red Edge of exo-planets	600 nm-800nm	upto 20% of planet flux	<3"	>10^4	0.01%	<0.1%	0.05%		The estimated IP, CT and DP values are beyond the acceptable limits for the entire wavelength region. Unlikely to be supported by TMT

4.6 Design of an optical layout for the mitigation of polarization effects

The polarimetric science cases collected for TMT indicated the acceptable amount of the IP, DP, and CT. Based on this and a similar analysis carried out in the E-ELT telescope (de Juan Ovelar et al., 2014), the following are the constraints given by the science cases.

1. The instrumental polarization $(I \rightarrow Q, I \rightarrow U, I \rightarrow V)$ should be less than 0.1%.

2. The crosstalk $(Q \rightarrow U, Q \rightarrow V, U \rightarrow V)$ should be less than 1%.

3. The transmission of linear polarization $(Q \rightarrow Q, U \rightarrow U)$ should be greater than 95%.

Figure 4.13 shows the Mueller matrix obtained at the focus of the telescope. It can be seen that the instrumental polarization varies from 4.5% to 0.5% over the wavelength range. The linear polarization is greater than 95% only in the infrared region (above 1 micron). Though $Q \rightarrow U$, $Q \rightarrow V$ are zero, we notice high percentage (12%-60%) of $U \rightarrow V$ crosstalk which demonstrates the requirement to reduce these effects for accurate polarimetry in future. In E-ELT (de Juan Ovelar et al., 2014), a switching modulation technique has been modeled at the intermediate focus (IF) of the telescope which eliminates these effects. But, in the case of TMT, there is no provision for intermediate focus and any compensating optics have to be located either at or beyond the Nasmyth focus. Here, we provide an optical design that can reduce the effect of IP and CT at the telescope focus.

4.6.1 An inclined flat mirror at the Nasmyth platform at the WFOS port for polarization mitigation

The polarization introduced by an inclined flat mirror can be canceled by placing another mirror opposite to it in such a way the $s - p$ plane of the next

mirror is rotated by 90° compared to the first one (Cox, 1976). Figure 4.21 shows arrangement of the two flat mirrors. The Mueller matrices estimated after the mirrors, M1 and M2 are shown in matrices given by Eqns (4.5) and (4.6), respectively.
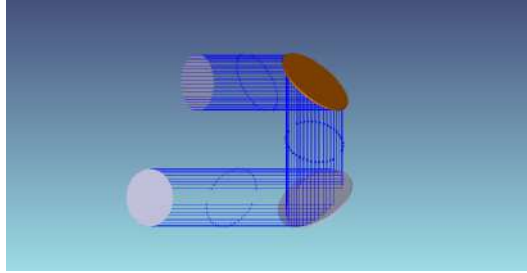
Figure 4.21: The optical layout of two inclined flat mirrors for polarization cancellation

$$M1 = \begin{pmatrix} 1 & 0.0455 & 0 & 0 \\ 0.0455 & 1 & 0 & 0 \\ 0 & 0 & 0.6788 & 0.7329 \\ 0 & 0 & 0.7329 & -0.6788 \end{pmatrix} \quad (4.5)$$

$$M2 = \begin{pmatrix} 1 & 0 & 0 & 0 \\ 0 & 1 & 0 & 0 \\ 0 & 0 & 1 & 0 \\ 0 & 0 & 0 & -1 \end{pmatrix} \quad (4.6)$$

We use this technique to reduce the polarization effects at the TMT telescope. An inclined mirror of size same as M3 is placed on the Nasmyth platform at the instrument port corresponding to IBA=0° and IEA=0°. The beam which focuses on the Nasmyth platform is F/15. The mirror positioned after the focus diverges the beam. The coating on the mirror is Gemini coating. The optical layout in Figure 4.22 (Configuration A) shows the mirror kept at a distance of 2 m from the telescope focus. We perform polarization analysis in Zemax® and estimate the Mueller matrices. We do not see a complete cancellation of the polarization effects (as in the case of Figure 4.21) since the
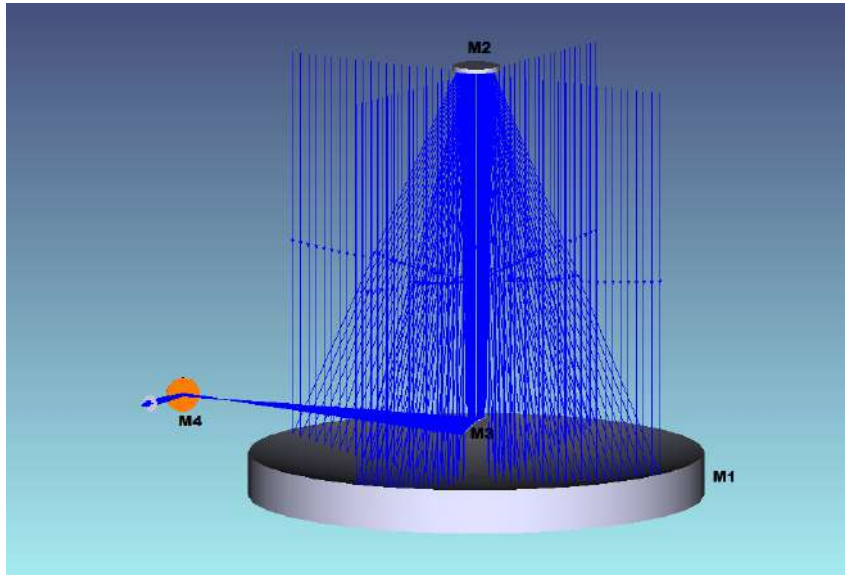
Figure 4.22: Mirror (M4) on the Nasmyth platform for cancellation of polarization effects
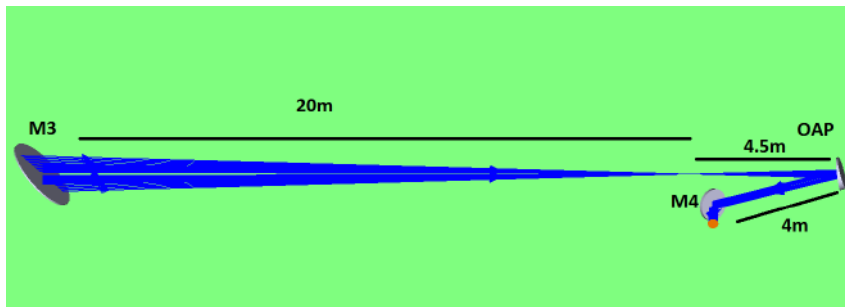
Figure 4.23: Mirror (M4) on the Nasmyth platform after the Off-axis parabola for cancellation of polarization effects

diverging beam is falling on M4. The IP and CT values are well within the constraints for semi-field angles of 1′ and 2′ over the entire wavelength region, and for 7.5′ beyond 1 μm.

The polarization modulators should be placed after M4 for accurate polarization measurements. But the beam getting reflected from M4 is diverging, and the birefringence of the polarization retarders is dependent on the incident angles. The beam deviation of the Polarizing prisms or beam splitter may vary due to these angles (Keller, 2002), which shows the necessity for the collimation of the reflecting beam. However, any optics used for collimation might modify the polarization properties. Hence there is a need for an optical component which renders collimation without much modification in the polarization properties.
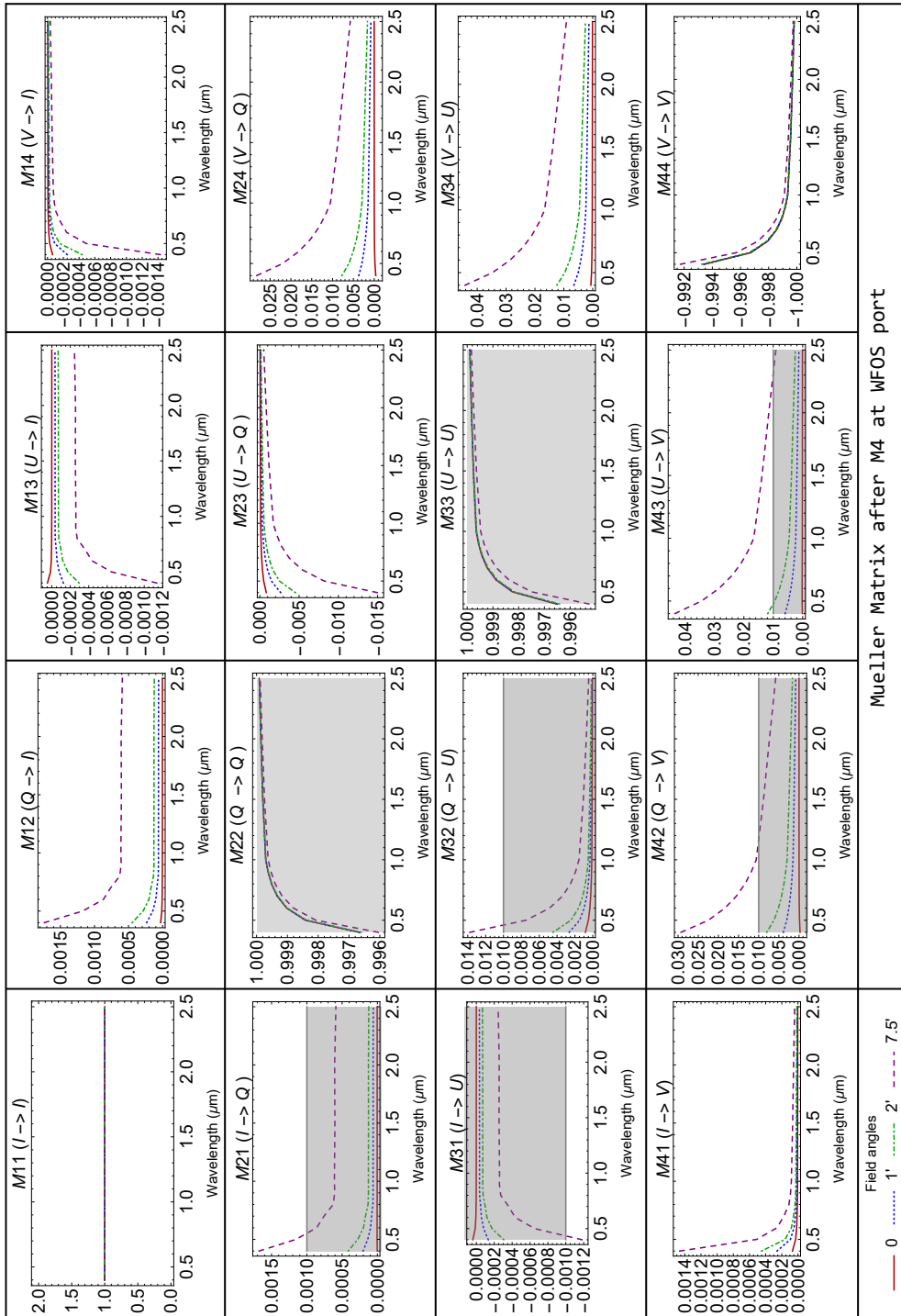
Figure 4.24: Mueller matrix for Configuration A at IBA=0° and IEA=0°. The shaded regions show the constraints for IP and crosstalk. These values are well within limits for the entire wavelength region for semi-field angles of 1′ and 2′.

4.6.2 An off-axis parabola along with M4 for cancellation of polarization effects

The beam from the telescope focus can be collimated by introducing an off-axis parabola in the optical path between M3 and M4 as shown in Figure 4.23 (Configuration B). The off-axis parabola is chosen as it renders collimation over the complete range of wavelength in comparison with lenses. The off-axis parabola is designed for the field of view of $2'$ and has the following parameters:

Radius of curvature = 8898 mm

Diameter = 1000 mm

conic constant = -1

off-axis distance = 1250 mm

It is placed at a distance of 4.5 m from the telescope focus, and M4 is kept at 4 m from the off-axis parabola. We perform polarization analysis in Zemax® and obtain the Mueller matrix for this optical layout after M4 as shown in Figure 4.25, assuming Gemini coating for both off-axis parabola (OAP) and the mirror (M4). In Configuration B, the off-axis parabola adds further polarization after M3 due to non-normal incidences. The IP and CT values are within the constraints for the semi-field angle of $1'$. The polarization effects introduced by the off-axis parabola can be reduced by varying the tilt of M4 as shown in Figure 4.26. The tilt of M4 can be optimized for a particular field angle such that IP and CT are zero.

4.6.3 An inclined flat mirror at the NFIRAOS instrument port for polarization mitigation.

The tilt (Φ) and the rotation (θ) of the Nasmyth mirror (M3) do not change with the zenith angle of the telescope only at the WFOS instrument port of TMT. At all the other instrument ports, θ and Φ vary as shown in Figure 4.27. An inclined mirror is placed on the Nasmyth platform at the instrument port corresponding to IBA=174.5° and IEA=0° corresponding to the NFIRAOS
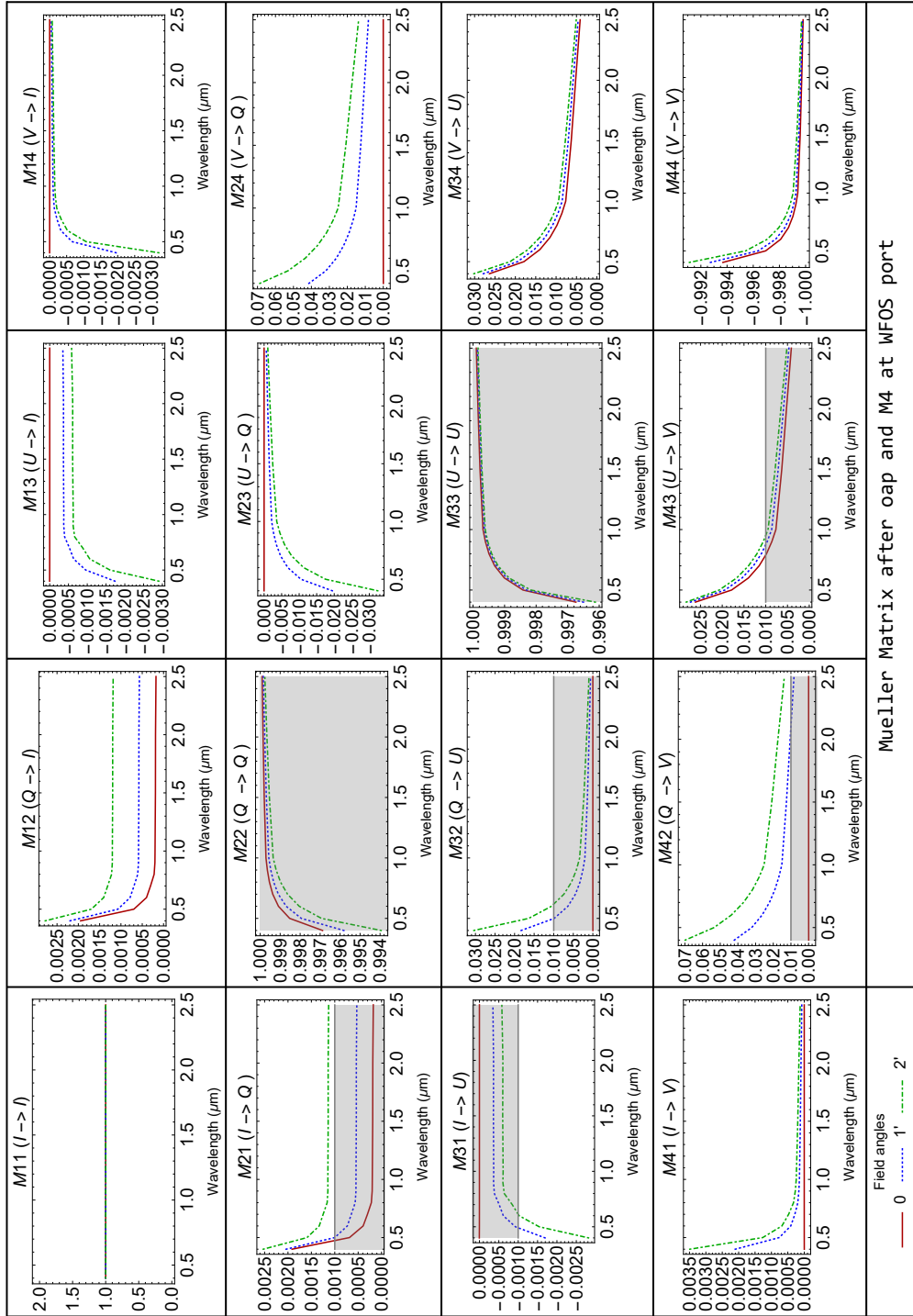
Figure 4.25: Mueller matrix for Configuration B at IBA=0° and IEA=0°. The graph shows three semi field angles and the constraints on IP and CT. IP and CT are beyond the constraints for 2′ semi-field angle.
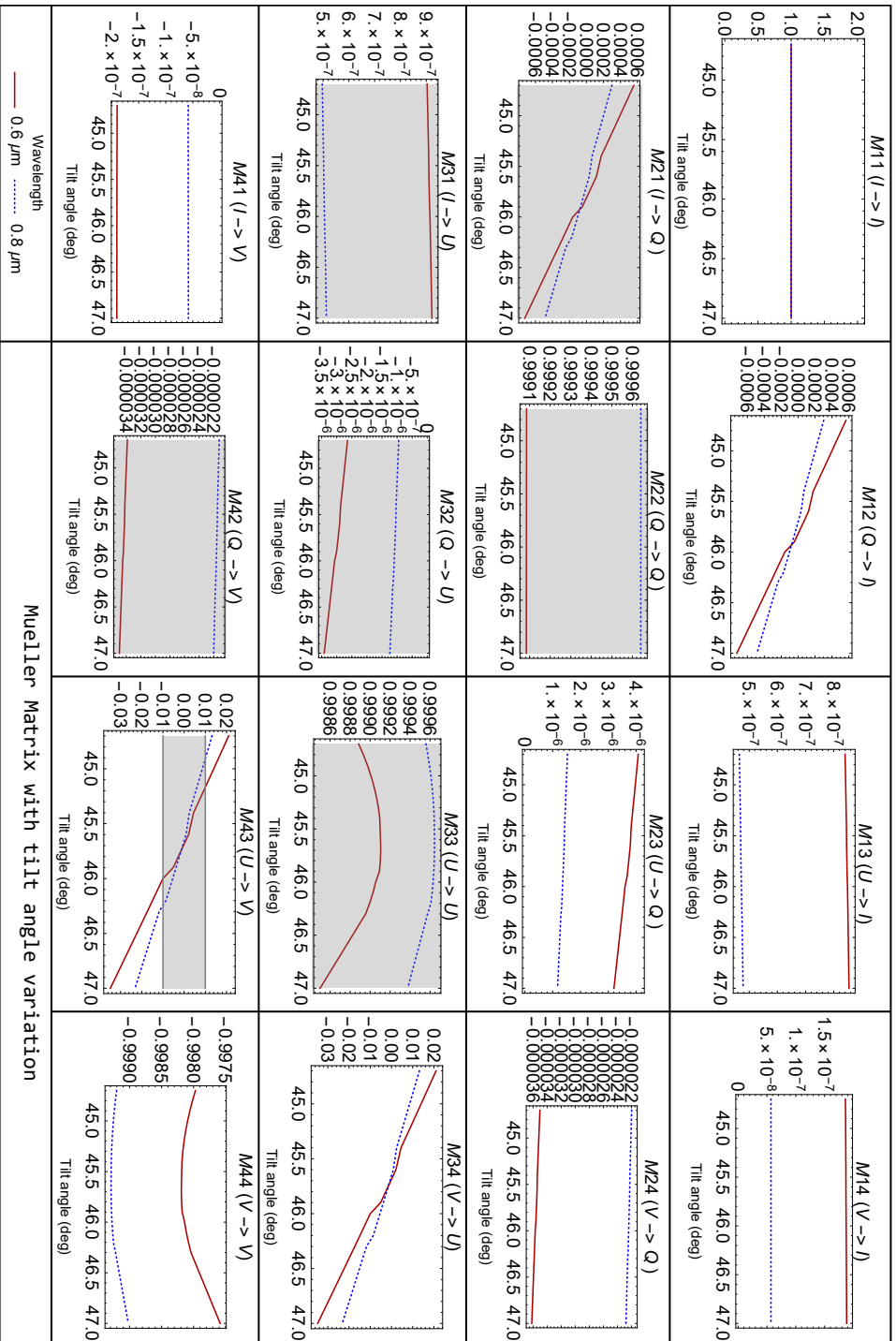
Figure 4.26: Mueller matrix for Configuration B at IBA=0° and IEA=0° for different tilt angles of M4. It is done for the on-axis rays at two wavelengths. The tilt angle corresponding to IP=0 and CT=0 can be chosen.
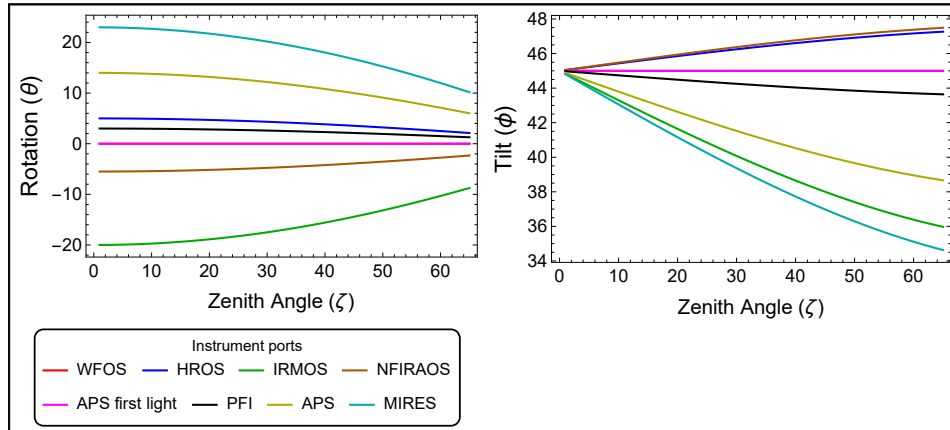
Figure 4.27: The rotation and tilt of the Nasmyth mirror (M3) at all the instrument ports.

port. Figure 4.28 shows the different configurations of the telescope with varying angles of zenith. The M4 mirror is kept at a constant tilt of 45 degrees, and the Mueller matrices were estimated at the end of M4 when the zenith angle changes. The mirror M4 is placed at a distance of 2.5 m from the Nasmyth focus. The Mueller matrices are shown for 0.6 and 0.8 μm, on axis rays in Figure 4.29. The IP values lie within the constraint of 0.1% only till the zenith angle of 30° whereas, CT values lie within the constraint of 1% only till 10° of zenith angle. Beyond that, the mitigation using a fixed M4 is not possible as the incident angle varies with the zenith angle. If the tilt of M4 is also changed as per M3, the IP and CT values are found to be within the constraints.

4.7   Conclusion

A detailed analysis of the polarization effects introduced by the optics of the Thirty Meter Telescope (TMT) has been carried out. The studies indicate that the Nasmyth mirror is the primary source of the IP and CT at the focal plane, giving rise to an IP of 4.5% to 0.6%, CT of 73% to 11% and depolarization of 2.2% to 0.5% in the wavelength range of 0.4 μm to 2.583 μm, respectively for field angle and zenith angle equal to zero. These polarization effects vary with field angle and zenith angle of the telescope. The IP varies by 0.1% and CT by 5% when the zenith angle of the telescope varies from 0-65
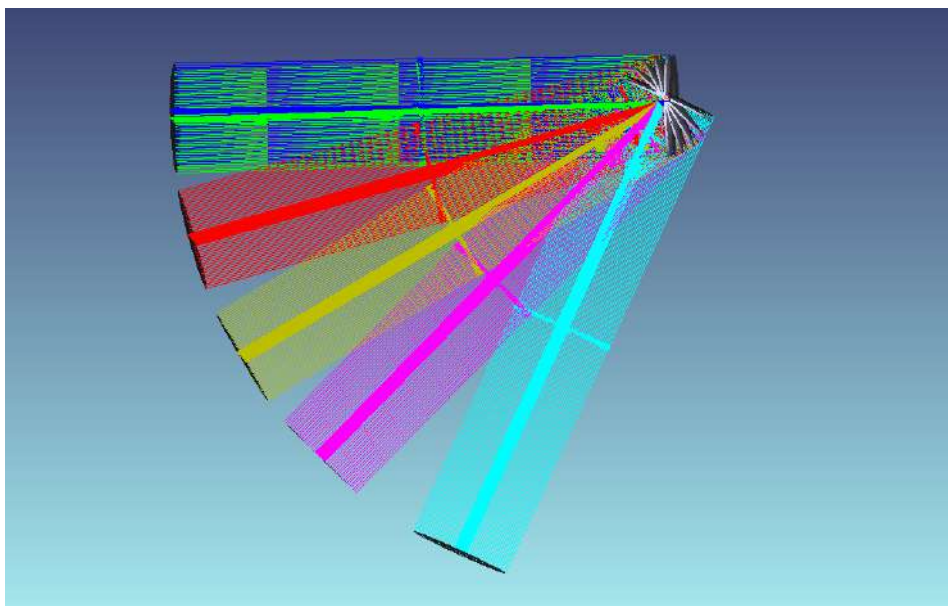
Figure 4.28: The optical layout form Zemax® showing different zenith angles of the telescope

degrees. The IP and CT values are found to be asymmetric over the field of view of the telescope. The high values of CT in the optical region indicate that all the Stokes parameters have to be measured to reconstruct the input polarization. The polarization effects have also been estimated in the near and mid infrared region for one of the proposed second generation instrument, MICHI. The impact of the polarization effects on the science programs has been assessed for a selection of example science programs that span the range of precision and sensitivity requirements. Science programs that require polarimetric measurements in the optical are unlikely to be supported with TMT however programs that need near-IR, and mid-IR polarimetric measurements look to be achievable. IP mitigation/reduction technique is also studied as this would undoubtedly facilitate more science programs by reducing the error on the IP calibration.

A design technique has been proposed to mitigate the effects of polarization introduced by the TMT. After the fourth mirror (M4), the IP and CT for the entire wavelength region are well within the values in the constraints derived from science cases. Care must be taken that the collimation after M4 should not introduce any polarization effects. An off-axis parabola can be
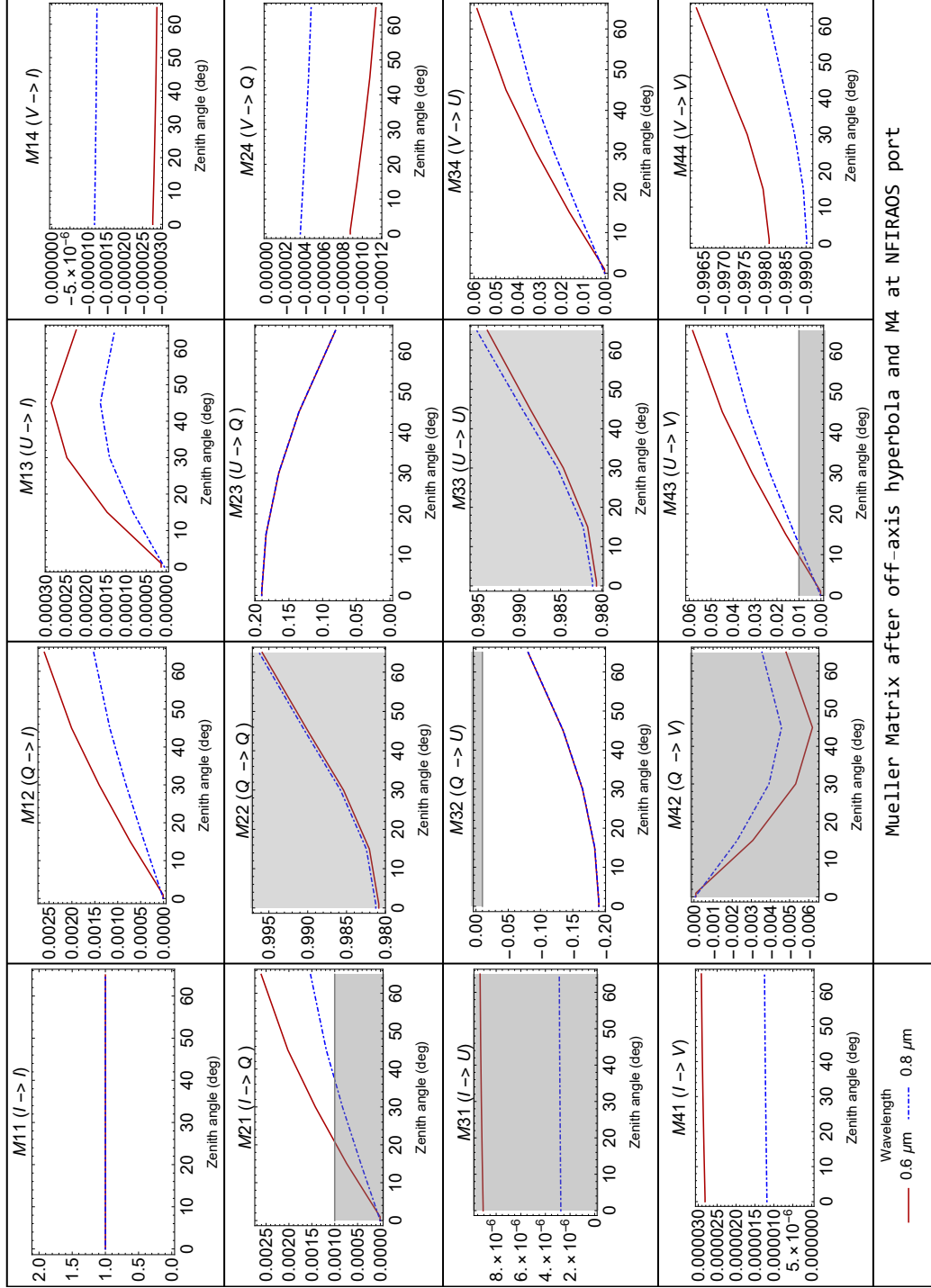
Figure 4.29: Mueller matrix for Configuration A at IBA=174.5° and IEA=0°. The shaded regions show the constraints for IP and crosstalk. These values are well within limits only for the zenith angle up to 30 degrees for both the wavelengths.

used to collimate the beam in the entire wavelength region, but the polarization mitigation cannot be obtained for larger field angles. Depending on the science cases and the instrument constraints this method can be optimized in the future design of a polarimeter.

The calculated values are likely to be the lower limits. The measured IP, CT, and DP might be higher than the values we have estimated since in our analysis the coating of all the mirrors is considered to be ideal which might not be the case. Since the primary mirror is considered to be a monolith in this analysis, the impact of the tilt and piston of the segments on the polarization is presented in Chapter 6. The impact of these polarization effects on the PSF of the telescope and non-polarimetric performance of TMT is also presented in the next Chapter.

Chapter 5

Polarization aberration estimates for the Thirty Meter Telescope and NFIRAOS

5.1   Introduction

Polarization aberrations are the variations of amplitude, phase, and polarization of a wavefront across the exit pupil of an optical system (Chipman, 1987). They are estimated using the polarization ray tracing algorithm explained in Chapter 3. It takes into account the changes in the polarization introduced at every interface in the system. The polarization aberrations estimated for a simple Nasmyth telescope (Breckinridge et al., 2015) has shown the presence of coating induced astigmatism, defocus and tilt, which cannot be corrected by the adaptive optics system. These aberrations give rise to the ghost PSF, which leads to an ellipticity of the Airy disk. Though the magnitude of these

aberrations are small, they might affect the high resolution and high contrast imaging instruments used in the future telescopes.

In this Chapter, the polarization aberrations for the Thirty Meter Telescope at the Wide-Field Optical Spectrograph (WFOS) instrument port, and at the focus of the Narrow Field Infrared Adaptive Optics System (NFIRAOS) are estimated. The optical layout of the TMT with the NFIRAOS (Herriot et al., 2012) is shown in Figure 5.1.
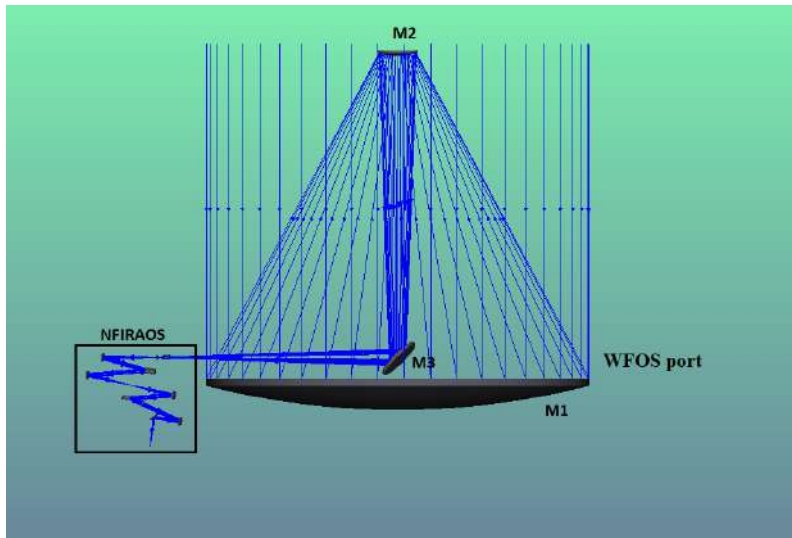
Figure 5.1: Optical Layout of the Thirty Meter Telescope with WFOS port and NFIRAOS instrument. The Nasmyth mirror has $\Phi = 45$ and $\theta = 0$ at the WFOS port and $\Phi = -45$ and $\theta = 5.499$ at the NFIRAOS port.

5.2 Diattenuation and Retardance of the mirrors in TMT

The polarizing capability of the mirror is represented in terms of diattenuation ($D = \frac{|r_p|^2 - |r_s|^2}{|r_p|^2 + |r_s|^2}$) where, r_p and r_s are the reflection coefficients. The reflection coefficients are estimated using the polarization ray tracing algorithm given in Chapter 3. The coating used for the telescope mirrors in our analysis consists of 85 Å of Si_3N_4 and 1100 Å Silver (Vucina et al., 2006). Figure 5.2 shows the diattenuation maps on the surface of the primary, secondary and the Nasmyth mirror of the TMT. The length of the line segment shows the magnitude of

the diattenuation and the orientation of the segment indicates the orientation of the s and p vectors. D increases quadratically from center to the edge of the mirror in the case of the primary and secondary mirror and linearly in the case of Nasmyth mirror. The maximum value of diattenuation for the primary and secondary mirror is 0.00061 and 0.00073, respectively for the on-axis rays. This indicates that the instrumental polarization (IP) introduced by the primary and secondary mirror is negligible, owing to their symmetry. In the case of the Nasmyth mirror, D varies from 0.0058 to 0.0076 which is an order higher when compared to the primary and secondary, and hence forms the main source of IP in the TMT.

Retardance ($\delta = |\phi_p - \phi_s|$) corresponds to the difference in phase of the Fresnel reflection coefficients. The retardance maps for all the three mirrors are shown in Figure 5.3. The length of the line segment shows the magnitude of the retardance and the orientation of the segment indicates the orientation of the s and p vectors. The retardance is found to vary quadratically in the case of the primary and secondary mirrors, giving rise to polarization induced astigmatism. The maximum retardance in the case of the primary mirror and secondary mirror is 0.0286 and 0.0327 radians, respectively. The corresponding coating induced astigmatism is 9.7 milliwaves ($\lambda/102$) at 0.8266 μm. Retardance of the Nasmyth mirror varies linearly from one end to the other, giving rise to polarization induced wavefront tilt with a maximum value of 0.3603. The corresponding tilt introduced is 0.0573 waves ($\lambda/17$). The resultant retardance of the telescope is dominated by the Nasmyth mirror due to its large value.

The variation of polarization induced astigmatism and tilt over the wavelength range 0.4-2.5 μm is given in Table 5.1. It indicates the presence of coating induced chromatic aberration (Reiley et al., 1992) which is caused by the dispersion of the refractive indices. The coating induced astigmatism and tilt changes with the polarization state of the light, compared to those (astigmatism and tilt caused due to the surface profile of the mirror), which do not change with the incident polarization. So, the adaptive optics system will not

be able to correct for these aberrations. The dependence of these aberrations on the wavelength and the field would make it challenging to implement the corrections.
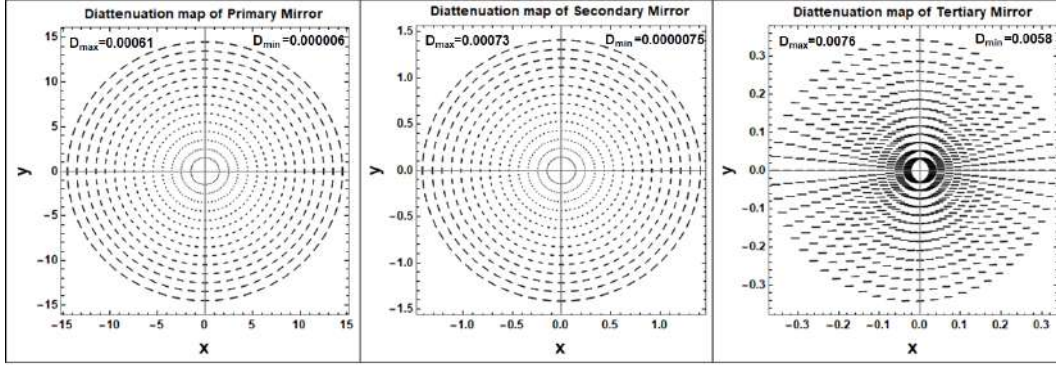
Figure 5.2: Diattenuation maps of all the three mirrors of the TMT. In the case of primary and secondary, the diattenuation increases quadratically from center to the edge of the mirror and in the case of Nasmyth mirror, a linear increase is seen. The vertical axis in the case of Nasmyth mirror corresponds to it's tilt axis. The maximum and minimum values of the diattenuation are mentioned.
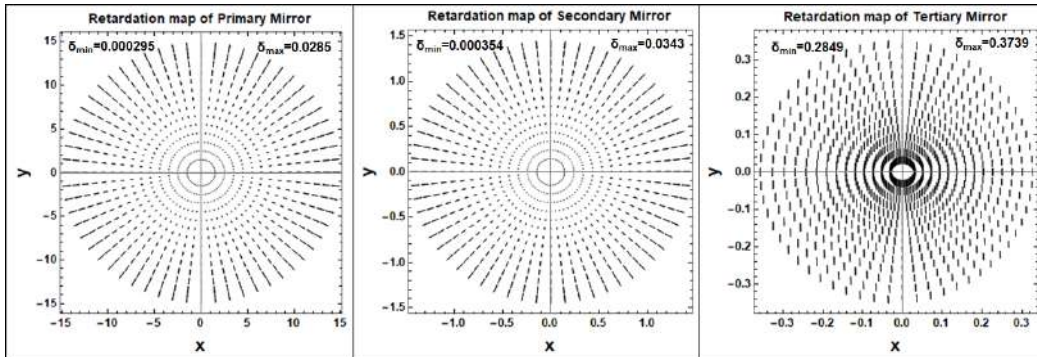
Figure 5.3: Retardance maps for all the three mirrors of the TMT. In the case of the primary and secondary mirror, the retardance increases quadratically from center to the edge of the mirror and it increases linearly in the case of Nasmyth mirror. The vertical axis in the case of Nasmyth mirror corresponds to it's tilt axis. The maximum and minimum values of the retardance are mentioned.

5.3 Jones pupil map and Amplitude Response Matrix (ARM) at the WFOS port

The Jones pupil map shows the distribution of the amplitude and phase of the electric field vector in the exit pupil of the telescope. Ideally, in the absence of

| Wavelength μm	Retardance Primary mirror (radians)	Retardance Secondary mirror (radians)	Retardance Nasmyth mirror (radians)	Polarization induced astigmatism Primary+Secondary mirror (waves)	Polarization induced tilt Nasmyth mirror (waves)
0.4	0.0805	0.0918	0.8951	0.0274 (λ/36.46)	0.1425 (λ/7.019)
0.4592	0.0622	0.07	0.73	0.0212 (λ/47.17)	0.1162 (λ/8.60)
0.5166	0.0518	0.0592	0.6247	0.0177 (λ/56.58)	0.0994 (λ/10.05)
0.5636	0.046	0.0525	0.5618	0.0157 (λ/63.75)	0.0894 (λ/11.18)
0.6199	0.0408	0.0465	0.5031	0.0139 (λ/71.97)	0.0801 (λ/12.48)
0.6526	0.0381	0.0435	0.4723	0.013 (λ/77.05)	0.0752 (λ/13.30)
0.7293	0.0332	0.038	0.4158	0.0113 (λ/88.26)	0.0662 (λ/15.11)
0.8266	0.0286	0.0327	0.3603	0.0097 (λ/102.59)	0.0573 (λ/17.43)
0.9537	0.0244	0.0278	0.309	0.0083 (λ/120.33)	0.0492 (λ/20.33)
1.033	0.0224	0.0256	0.2844	0.0076 (λ/131.06)	0.0453 (λ/22.09)
1.24	0.0184	0.021	0.2345	0.0063 (λ/159.58)	0.0373 (λ/26.79)
2	0.0124	0.0142	0.159	0.0042 (λ/236.50)	0.0253 (λ/39.51)
2.296	0.0108	0.0123	0.1385	0.0037 (λ/271.85)	0.022 (λ/45.37)
2.583	0.0096	0.011	0.1233	0.0033 (λ/305.43)	0.0196 (λ/50.94)

Table 5.1: Maximum values of the polarization-induced wavefront aberration by three mirrors of the TMT telescope at different wavelengths.

polarization aberrations, the Jones matrix obtained at the output will be an identity matrix. However, due to the complex refractive indices of the coating and the curvature of the mirrors, it deviates from the ideal scenario. The spatial Fourier transform of the Jones pupil map elements gives the Amplitude Response Matrix.

5.3.1 Jones amplitude and phase pupil map

Jones amplitude and the phase pupil map shown in Figure 5.4 are estimated at the WFOS port of the TMT at λ=0.8266 μm. The tertiary mirror has a tilt of 45 degrees at this port.
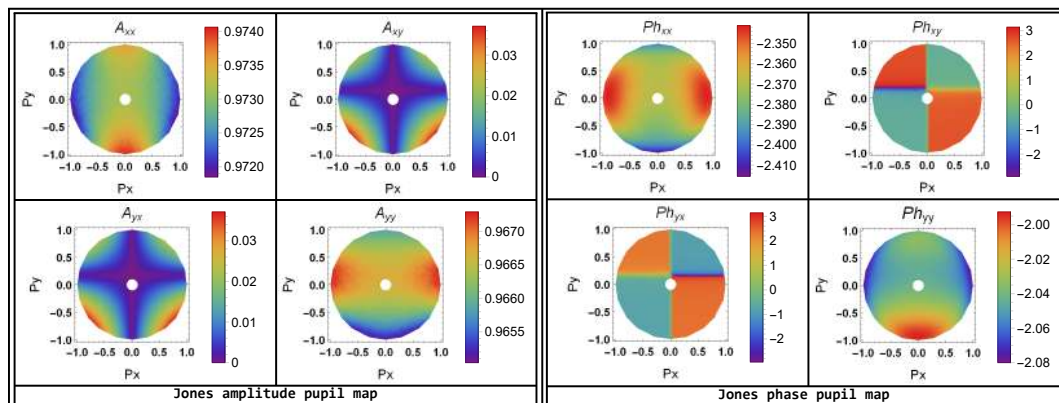
Figure 5.4: The Jones amplitude and phase pupil map shows the amplitude and phase variations across the exit pupil in the TMT. A_{xx} and A_{yy} show the amplitudes for X and Y polarized light respectively. A_{xy} and A_{yx} show the amplitude of X-polarized light converted to Y-polarized light and vice versa. Ph_{xx} and Ph_{yy} show the phase for X and Y polarized light respectively. Ph_{xy} and Ph_{yx} show the phase of X-polarized light converted to Y-polarized light and vice versa. Px and Py are the exit pupil coordinates.

In Figure 5.4, A_{xx} and A_{yy} correspond to the output amplitude at the exit pupil for the X and Y polarized light at the input, respectively. A_{xy} and A_{yx} correspond to the cross-coupled components at the exit pupil for X and Y polarized light at the input. The amplitudes A_{xx} and A_{yy} are not equal and A_{yy} is found to be rotated by $\pi/2$ compared to A_{xx} with variation in distribution. The maximum values of A_{xx} and A_{yy} are 0.974 and 0.967 respectively which indicates that the absorption by the coating for X and Y polarized light is slightly different. The image of A_{xx} is 1.3% brighter than that of A_{yy}. Cross-coupled components A_{xy} and A_{yx} show Maltese cross pattern (Breckinridge et al., 2015) with amplitudes of 0.037.

Figure 5.4 also shows the phase variations at the exit pupil for X and Y polarized light which gives the coating induced wavefront aberrations. Ph_{xx} and Ph_{yy} are not equal and hence introduces a polarization induced tilt and astigmatism to the incoming wavefront. Ph_{yx} and Ph_{xy} change the phase by π radians when the amplitude becomes zero. The maximum values of Ph_{xx} and Ph_{yy} are found to be -2.34 and -1.996 respectively indicating the differences in the phase aberrations induced by the mirror coating.

5.3.2   Amplitude response matrix (ARM)

The spatial Fourier transform over the Jones pupil elements gives the Amplitude Response Matrix (ARM) (Chipman et al., 2015), which is similar to the Airy disk pattern. The Jones pupil map elements are obtained at the normalized pupil positions from Zemax®. Prior to the spatial Fourier transform, the pupil map is zero padded to make it a square array as shown in Figure 5.5. The Amplitude response matrix at the WFOS port of TMT is given in Figure 5.6 at 0.8266 μm.

The amplitudes of the diagonal elements are not equal due to the tilt of the Nasmyth mirror. The off-diagonal elements appear as ghost PSFs with an amplitude $\approx$ 0.0066. The difference between maximum values of ARM_{xx} and ARM_{yy} is found to be 0.7%. Even though the amplitude of the ghost PSF is as low as 0.0066, it can affect high contrast imaging using coronagraphs and also

cause an elongation of the Airy disk (making it elliptical). All the elements of the ARM matrix are normalized with the peak value of ARM_{xx}. Further, for an unpolarized light as the input, the resultant PSF would be the incoherent sum of all the components of the ARM matrix.
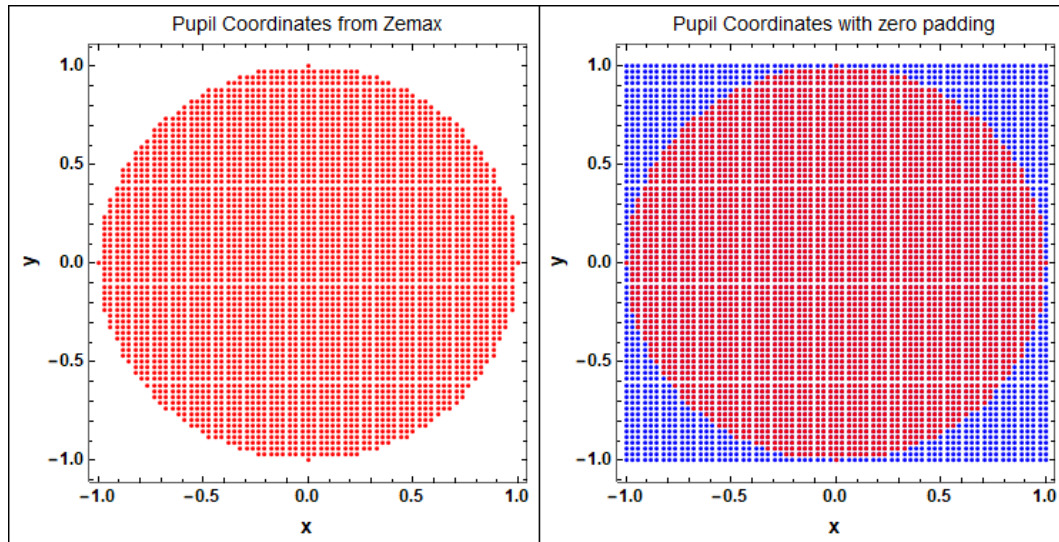
Figure 5.5: The normalized pupil coordinates used for the Fourier Transform. The red points correspond to the normalized pupil coordinates from Zemax® and blue points are the zero padded locations.

5.4 Point Spread Matrix (PSM) and Stokes image

The Point Spread Matrix is obtained by the Jones-Mueller matrix conversion as explained in Chapter 3. PSM is obtained from the elements of the ARM matrix. Figure 5.7 gives the 4×4 PSM obtained at the WFOS port for the TMT. The first column of the matrix shows the PSF components for the unpolarized light as an input. The PSF of an unpolarized star is not unpolarized due to the non zero values of $M21 = 0.0067$ (IP), $M31 = 0.0015$, and $M41 = 0.0002$. The V (M41) component arises in the first column as the weakly linearly polarized light from the primary and secondary mirror gets converted to circular by the Nasmyth mirror. Similarly, $M43{=}0.319$ (similar to the values found in Chapter 4) indicates crosstalk for the 100% linearly polarized
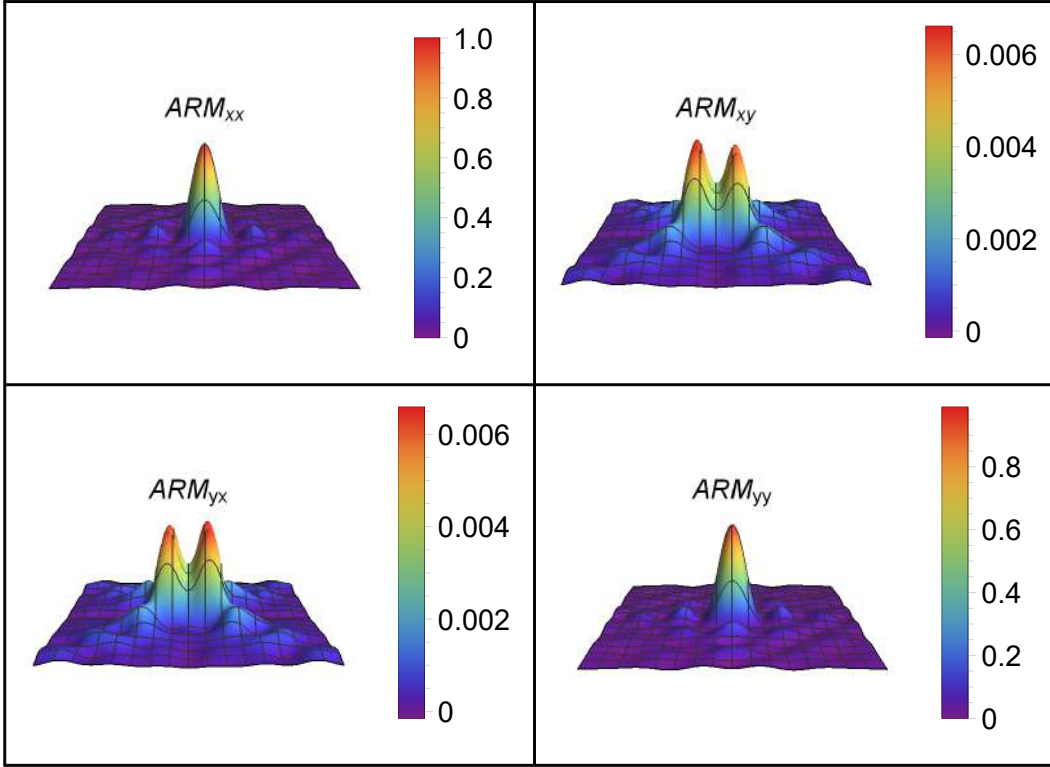
Figure 5.6: The Amplitude Response Matrix obtained at the WFOS port at 0.8266 μm.The peaks are normalized with the maximum value of ARM_{xx}.

light. The other off-diagonal elements in the matrix such as $M32$, $M42$, $M13$, $M14$, $M23$, and $M24$ which were zero in the earlier case (Chapter 4), show PSF components with two peaks here due to the retardance of the mirrors. Stokes vectors for different input polarization are multiplied with the PSM to determine the output Stokes image components.

5.4.1 Stokes images for X and Y polarized light

The Stokes image for the X-polarized light or horizontally polarized light can be obtained by multiplying the Stokes vector $[\,1 \quad 1 \quad 0 \quad 0\,]$ with the PSM. Similarly, for Y-polarized or vertically polarized light, $[\,1 \; -1 \; 0 \; 0\,]$ is multiplied with the PSM. The Stokes images for X and Y polarized light are given in Figures 5.8 and 5.9, respectively. U and V components are present in the Stokes images due to the diattenuation and retardance of the mirrors in the optical layout. The peak values of U and V components in both the cases is 0.0015 and 0.001, respectively. Using these Stokes images, the final intensity
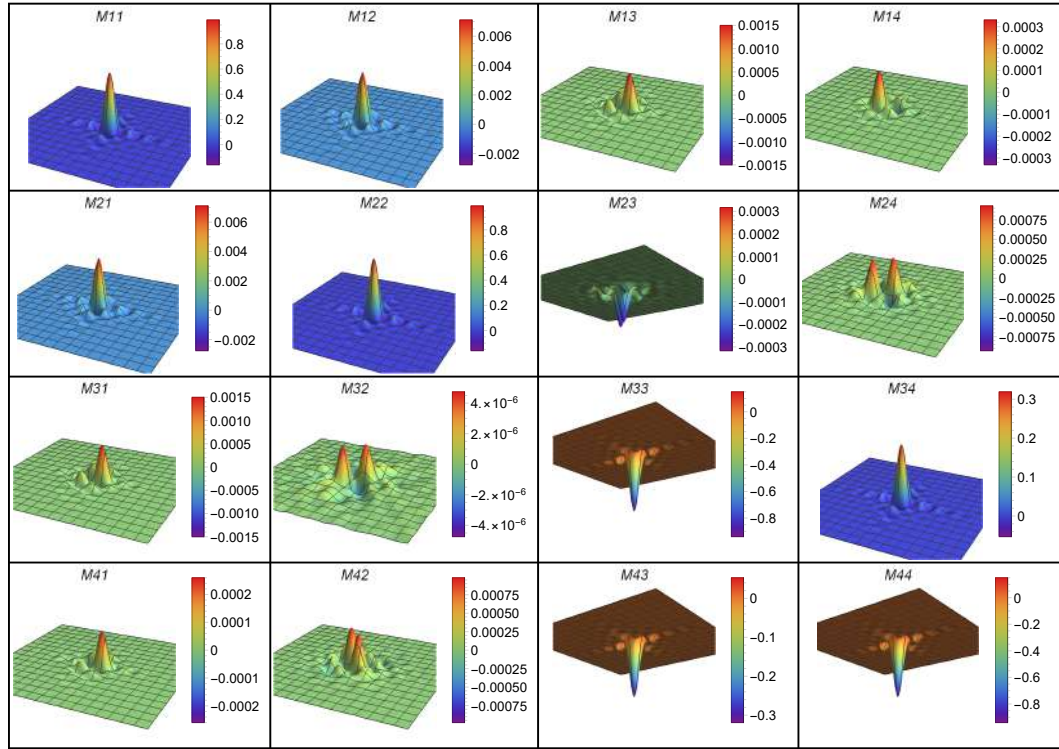
Figure 5.7: The point spread matrix estimated at the telescope focus at λ=0.8266 μm. The input Stokes vectors are multiplied with this matrix to obtain the corresponding Stokes image.

profiles for the two polarized states are determined. The total irradiance for X and Y polarized light would contain the effect of the crossed component also. $Ix = Ixx + Iyx$ and $Iy = Iyy + Ixy$, where Ix corresponds to the PSF for X-polarized light and Iy is the PSF for the Y-polarized light. Ixx, Iyx, Iyy and Ixy can be estimated from the Stokes image as follows (Breckinridge et al., 2015):

$$Ixx = \frac{Ix + Qx}{2}; \quad Iyx = \frac{Ix - Qx}{2}; Iyy = \frac{Iy - Qy}{2}; \quad Ixy = \frac{Iy + Qy}{2} \quad (5.1)$$
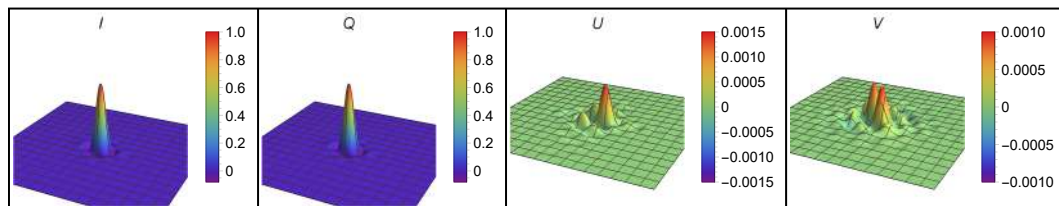
Figure 5.8: The Stokes image components estimated at the WFOS port for the X-polarized light as input.
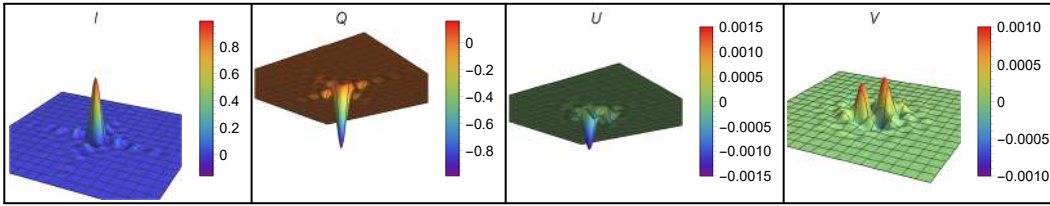
Figure 5.9: The Stokes image components estimated at the WFOS port for the Y-polarized light as input.

Figure 5.10 shows the PSFs obtained from the Stokes image of X and Y polarized light. The peak of Iyx is 4.37×10^{-5} of Ixx. The peak of Ixy is 4.34×10^{-5} of Iyy. These are the ghost PSFs which affect the high contrast imaging applications. The value of the ghost PSF is estimated for λ varying from 0.4 to 2.5 μm as given in the Table 5.2.
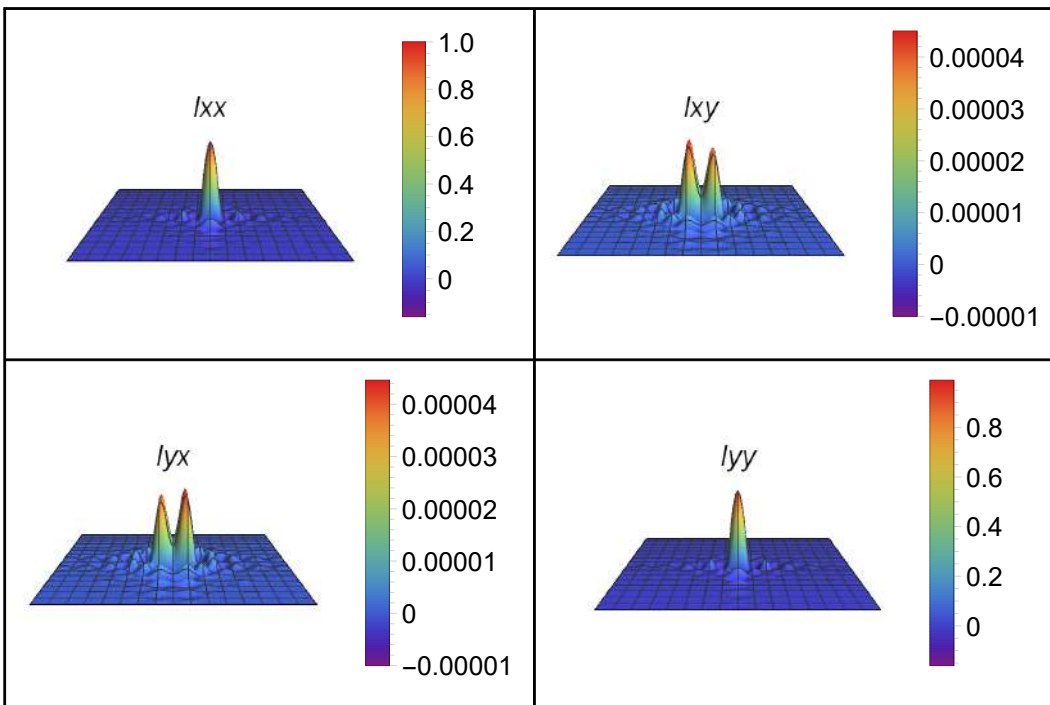
Figure 5.10: PSF of Ixx, Iyx, Ixy, and Iyy nomalized to the peak of Ixx. The ghost PSFs are found to be 10^{-5} parts of Ixx or Iyy.

The following parameters are estimated from the final PSF obtained using PSM for the X and Y polarized light at λ=0.8266 μm at WFOS port.

1. Comparison of the total fluxes.

$$\frac{Flux\ Iyx}{Flux\ Ixx} = 0.019\%; \quad \frac{Flux\ Iyy}{Flux\ Ixx} = 98.66\%; \frac{Flux\ Ixy}{Flux\ Ixx} = 0.019\%;$$

$$(5.2)$$

2. Comparison of the peak values.

$$\frac{Peak\ Iy}{Peak\ Ix} = 98.656\%; \quad \frac{Peak\ (Ix - Iy)}{Peak\ Ix} = 1.347\% \qquad (5.3)$$

$\lambda\ \mu$m	Peak Ixy	Peak Iyx	Peak Iyy	$\frac{Flux(Ixy)}{Flux(Ixx)}(\%)$	$\frac{Flux(Iyx)}{Flux(Ixx)}(\%)$	$\frac{Flux(Iyy)}{Flux(Ixx)}(\%)$
0.4	3.38×10^{-4}	3.61×10^{-4}	0.9128	0.135	0.145	91.3
0.516	1.44×10^{-4}	1.46×10^{-4}	0.9642	0.06	0.062	96.45
0.619	8.9×10^{-5}	8.9×10^{-5}	0.9762	0.038	0.038	97.64
0.729	5.9×10^{-5}	5.9×10^{-5}	0.9861	0.0257	0.0258	98.18
0.826	4.34×10^{-5}	4.37×10^{-5}	0.9865	0.0191	0.0191	98.66
1.240	1.78×10^{-5}	1.76×10^{-5}	0.9871	0.0079	0.00798	98.71
2	8.088×10^{-6}	7.96×10^{-6}	0.9877	0.00364	0.00364	98.77
2.5	4.847×10^{-6}	4.75×10^{-6}	0.9882	0.00219	0.002193	98.83

Table 5.2: Parameters obtained from PSF of X and Y polarized light for different wavelengths.

The parameters obtained in Table 5.2 are useful while designing the future high contrast imaging instrument for TMT. If the required contrast between the unpolarized star and planet, in the case of high-contrast imaging is less than 10^{-8}, the intensity values of the ghost PSF have to be considered during the design phase. The amplitude of the ghost PSF is found to decrease with wavelength and is in the order of 10^{-8} at 10 μm. Ixx and Iyx are shown in Figure 5.11 at the image plane in their log10 values. The Iyx values vary from -4 to -9 whereas Ixx varies from 0 to -5. The width and the location of the Iyx would have to be compared with the Ixx positions to estimate its effect on the PSF corrected by the adaptive optics system as given in the next section.
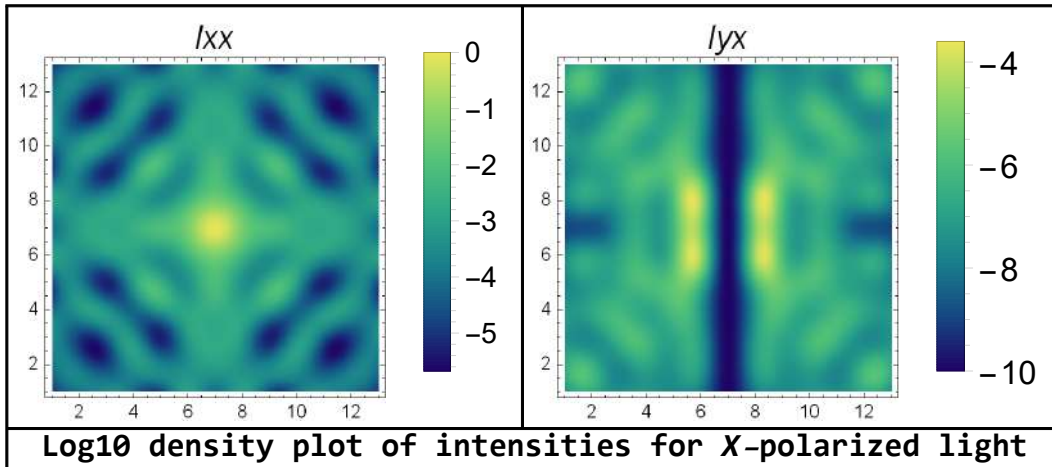
Figure 5.11: PSF of Ixx and Iyy are shown in their logarithmic values

5.5 Narrow Field Infrared Adaptive Optics System (NFIRAOS) of TMT

NFIRAOS (pronounced nefarious) operates in the range of 0.8-2.5 μm and feeds three instruments (Kerley et al., 2016). NFIRAOS consists of four off-axis parabolas, two deformable mirrors and a plane mirror (field mirror) in its optical layout (Herriot et al., 2012) as shown in Figure 5.12. The Instrumental polarization and crosstalk have been estimated at the focus of the NFIRAOS by Atwood et al. (2014). The change in instrumental polarization between 1-2.5 μm is found to be over 2%. In H and K bands, the IP is in the range of 0.5%. The difference in the polarization is most senstive to the changes in the zenith angle. A variation of 1-65 degrees in zenith angle can introduce 1% variation in the instrumental polarization. Hence, it is necessary to estimate the polarization aberrations caused due to the three mirrors of the telescope and the optical components inside the NFIRAOS instrument to know the effects on the final PSF.

Figure 5.12 shows the optical components in the NFIRAOS which may introduce polarization aberrations in addition to the telescope mirrors. The incident angles estimated for the chief ray, and the marginal ray at all the mirror surfaces are given in Table 5.3. The coating used for all the mirror
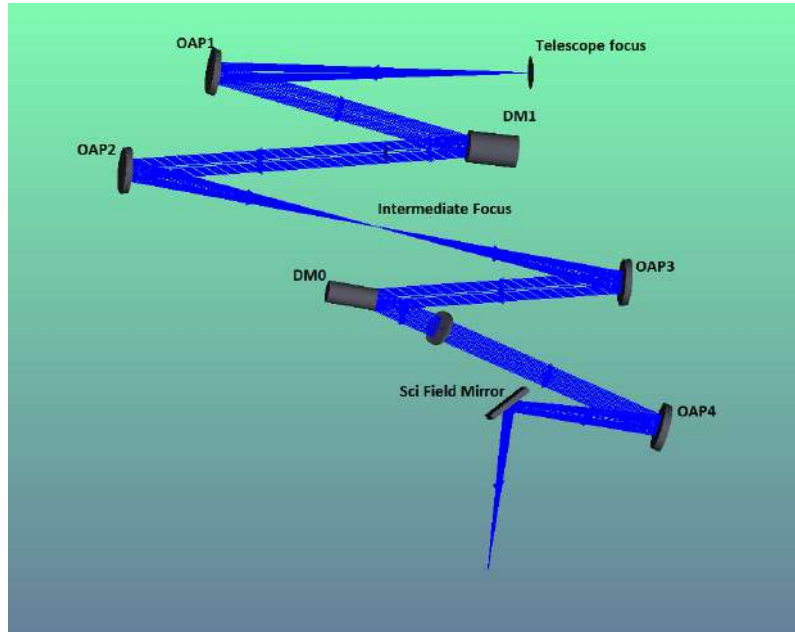
Figure 5.12: Optical layout of the NFIRAOS instrument for TMT. It is kept on the Nasmyth platform at an Instrument Bearing Angle (IBA)=174.5 degrees which corresponds to a tilt of -45.048 and rotation of 5.499 of the Nasmyth mirror. It consists of 4 Off Axis Parabolas(OAP), 2 Deformable Mirrors (DM) and a fold mirror.

surfaces in NFIRAOS is protective Silver (PSilver) which consists of 0.175 μm of SiO_2 and 0.1 μm of Silver. The Jones pupil maps and ARM is estimated at the focus of the NFIRAOS at λ=1.01 μm.

Pupil Positions $\rightarrow$ Surfaces $\downarrow$	(0,0)	(1,0)	(-1,0)	(0,1)	(0,-1)
M1	0	14.0358	14.0358	14.0358	14.0358
M2	0	14.99	14.99	14.99	14.99
M3	45.0479	44.896	45.26	46.94	43.146
OAP1	8.085	8.18	7.99	7.08	8.98
DM11	10	10	9.99	9.99	10
OAP2	8.265	8.24	8.46	9.43	7.08
OAP3	8.2651	8.24	8.46	9.43	7.08
DM0	13.75	13.74	13.75	13.75	13.75
OAP4	8.036	8.18	7.99	7.086	8.98
Sci-fld mirror	45	45.21	44.84	43.09	46.9

Table 5.3: Incident angles at different normalized pupil positions for different mirrors in the telescope and NFIRAOS.

5.5.1   Jones Pupil Map at the NFIRAOS focus

Figure 5.13 shows the Jones amplitude and phase maps at the focus of NFI-RAOS. The amplitude of all the components varies from that of the WFOS port due to the rotation of the Nasmyth mirror. A_{xx} and A_{yy} terms show similar behavior as they were obtained at the WFOS port with a decrease in the amplitudes. The peak value of A_{xx} and A_{yy} are 0.7997 and 0.7912, respectively. A_{xy} and A_{yx} show the smeared Maltese cross-like pattern, but the amplitude in the center is not equal to zero. The amplitude near the outer region of the pupil increases from 0.025 to 0.092. The cross-coupled terms amount to nearly 1% of the total intensity for the X and Y polarized light. The phase plots in Figure 5.13 looks different than those obtained at the WFOS port due to the rotation of the Nasmyth mirror. The difference between the peak of Ph_{xx} and Ph_{yy} is 1.5 radians with the distribution similar to that of defocus aberration. The plots of cross-coupled components Ph_{xy} and Ph_{yx} shows the presence of polarized induced defocus and tilt aberrations.
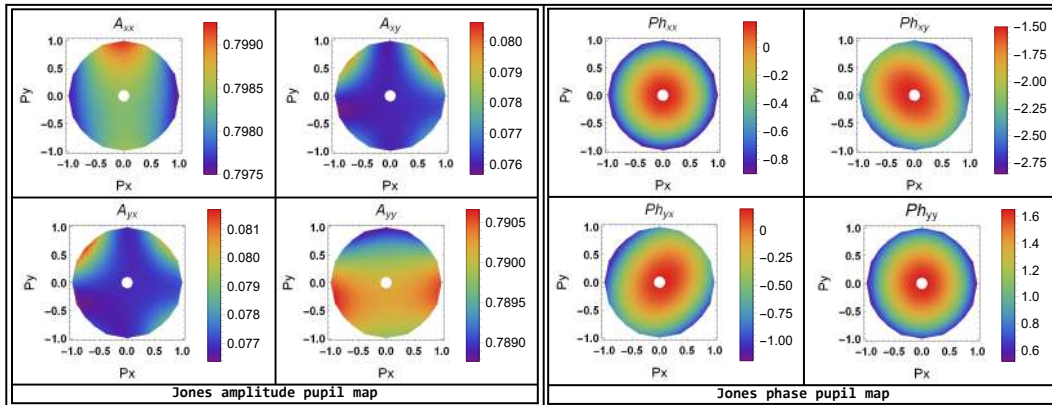
Figure 5.13: The Jones pupil map is estimated at the focus of the NFIRAOS instrument. The Jones pupil map shows the amplitude and phase variations across the exit pupil. The amplitudes for the horizontal polarization is found to be greater than the vertical polarization. The Amplitudes and phases follow the same convention as given in the Figure 5.4

5.5.2   ARM at the NFIRAOS focus

The Amplitude Response Matrix obtained at the NFIRAOS focus is shown in Figure 5.14. ARM_{xx} and ARM_{yy} look similar to that obtained at the WFOS

port and the peak value of ARM_{yy} is 0.9894. The cross-coupled components ARM_{xy} and ARM_{yx} have increased from 0.0025 (at the WFOS port) to 0.095. The increase in the amplitude of the cross components is due to the additional reflections from the mirrors in the NFIRAOS optical layout. The cross components obtained here show only one peak instead of two peaks.
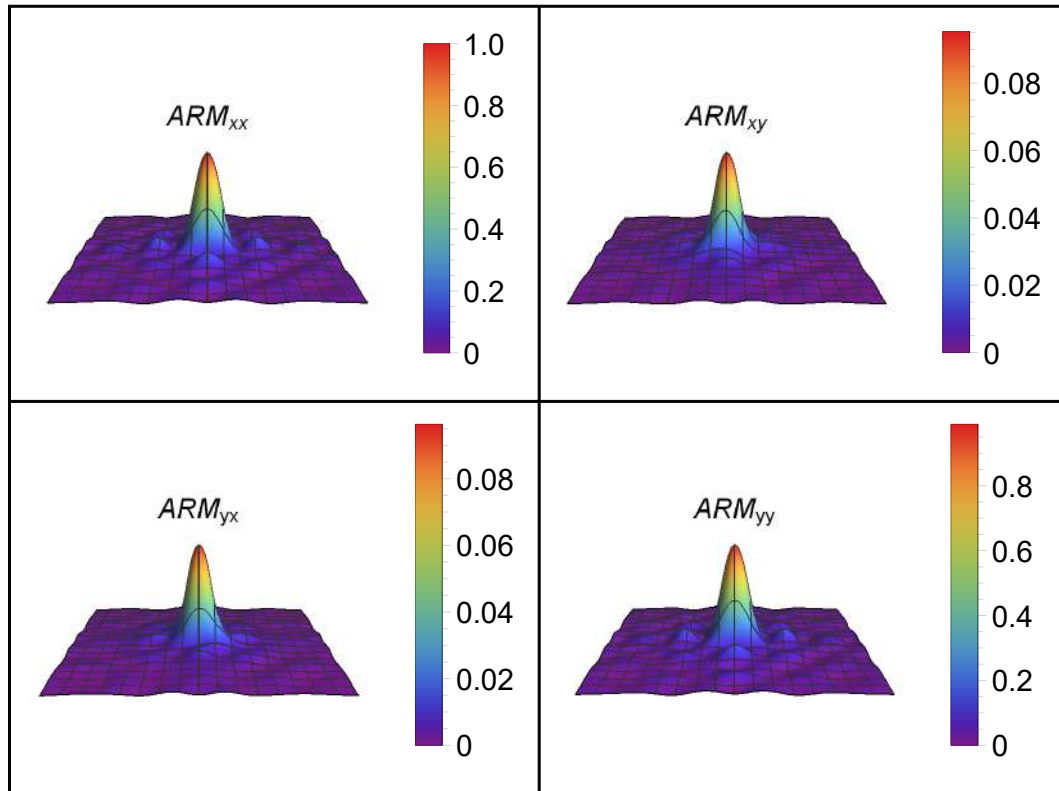
Figure 5.14: The Amplitude response matrix obtained at the NFIRAOS focus at 1 μm. The peaks are normalized with the maximum value of ARM_{xx}.

5.6 PSM and Stokes image at the NFIRAOS focus

The PSM obtained from converting the Jones matrix (ARM here) terms into Mueller matrix terms is shown in Figure 5.15. M11 correspond to the total intensity with a peak value of 1. M43 and M34 have a peak value of 0.974, indicating high cross-talk between linear to circular polarization. Different input polarizations are considered to understand the effects of PSM. For the

unpolarized light as the input, the first column of the matrix shows the output Stokes vectors. Q, U, and V components are present along with the intensity component (I). The peak values of Q and U components are 1 % and 0.15 %, respectively which correspond to the instrumental polarization (IP). 0.003 % of V indicate ellipticity in the final PSF for the unpolarized light.
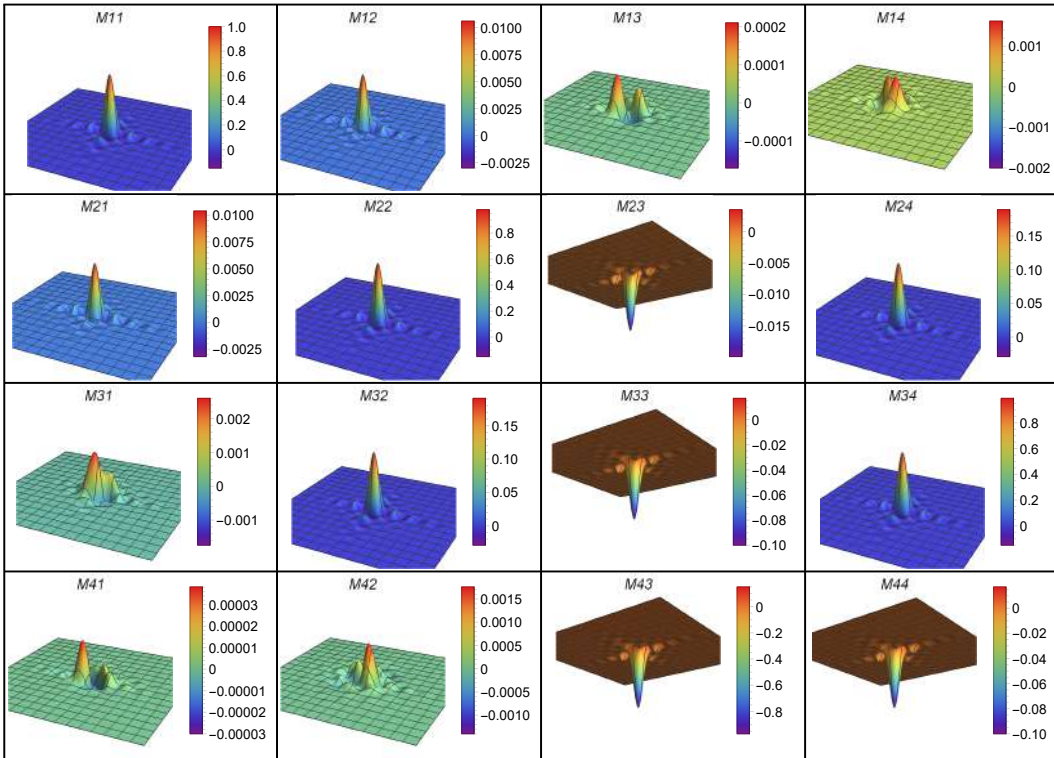

Figure 5.15: The point spread matrix estimated at the NFIRAOS focus at the wavelength of 1 μm. The input Stokes vectors are multiplied with this matrix to obtain the corresponding Stokes PSF at the instrument focus.

For X and Y polarized light as the input, the output Stokes vectors are estimated using PSM. Figures 5.16 and 5.17 show the Stokes PSF image for the X and Y polarized light. In the case of X and Y polarized light, 19 % of Q is found to be converted to U and 0.15 % of V. The presence of V causes the ellipticity in the final PSF. The final intensity profiles for the polarized states as given in Eqn (5.1) are estimated. Figure 5.18 shows the final PSF for X and Y polarized light. The peak value of Iyy is 0.978. The ghost PSFs Ixy and Iyx have a peak value of 9×10^{-3} which is two orders greater than that was estimated at the Nasmyth focus (WFOS port). The effect of this on the final PSF is given in the next section.
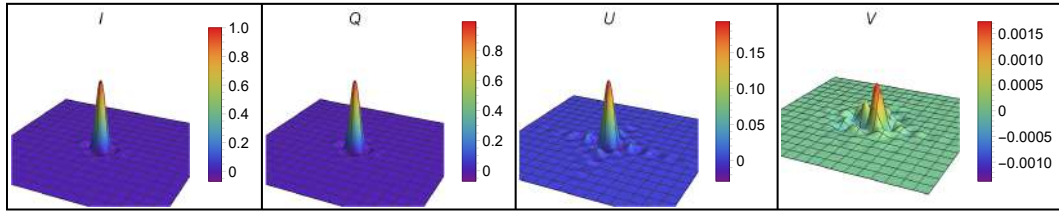
Figure 5.16: The Stokes image components estimated at the NFIRAOS focus for the X-polarized light as input.
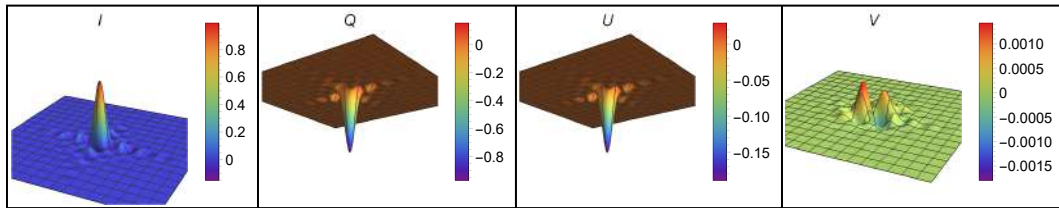
Figure 5.17: The Stokes image components estimated at the NFIRAOS focus for the Y-polarized light as input.
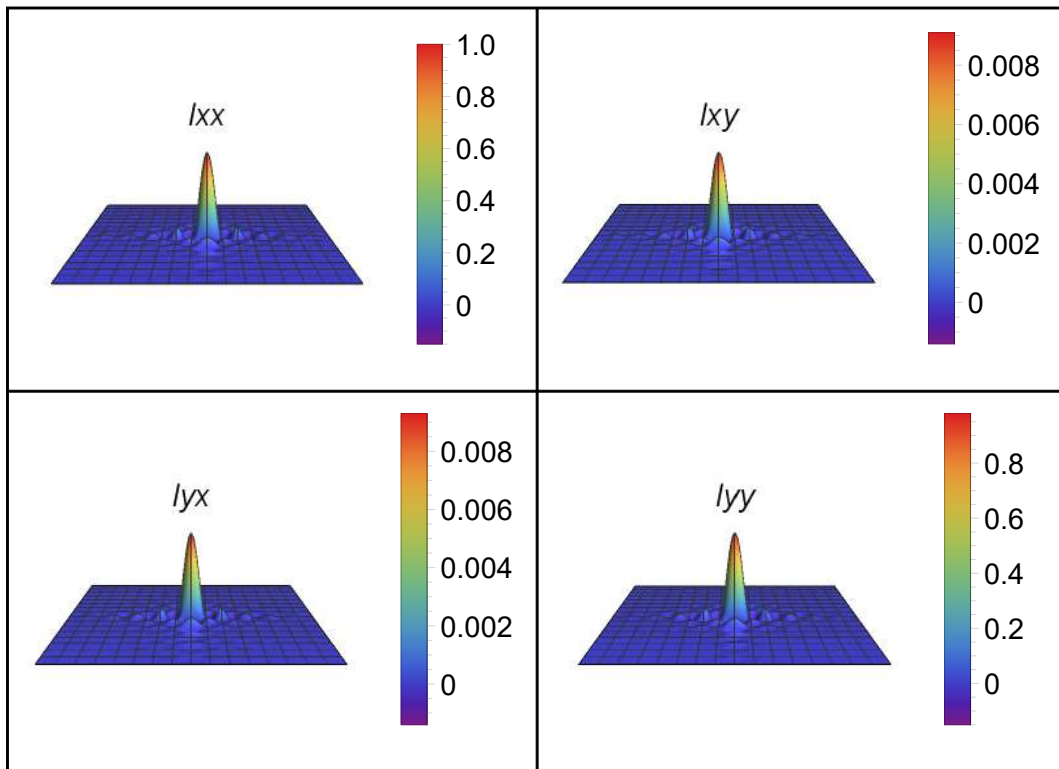
Figure 5.18: PSF of Ixx, Iyx, Ixy, and Iyy nomalized to the peak of Ixx at the focus of NFIRAOS. The ghost PSFs are found to be 10^{-5} parts of Ixx or Iyy.

5.7 Effect on the final PSF at NFIRAOS

We have obtained the Huygen's PSF using Zemax®, considering the polarization aberrations to estimate the shear, FWHM and ellipticity in the final PSF

at the NFIRAOS focus. The X and Y cross-sections of the PSF are considered for each case to estimate the ellipticity.

1. Unpolarized light

$$FWHM \ (X - direction) = 6.98 \pm 0.032 \ mas$$
$$FWHM \ (Y - direction) = 6.94 \pm 0.032 \ mas$$
$$Ellipticity \ of \ the \ PSF = 5.730 * 10^{-3}$$

2. X-polarized light

$$FWHM \ (X - direction) = 7.025 \pm 0.032 \ mas$$
$$FWHM \ (Y - direction) = 6.93 \pm 0.032 \ mas$$
$$Ellipticity \ of \ the \ PSF = 0.01352$$

3. Y-polarized light

$$FWHM \ (X - direction) = 6.98 \pm 0.035 \ mas$$
$$FWHM \ (Y - direction) = 6.96 \pm 0.032 \ mas$$
$$Ellipticity \ of \ the \ PSF = 2.865 * 10^{-3}$$

4. Shear between X and Y polarizations= 0.045 mas

5. Strehl ratio from Huygen's PSF for different input polarizations

$$Unpolarized \ light = 0.926 \tag{5.4}$$
$$X - polarized \ light = 0.924 \tag{5.5}$$
$$Y - polarized \ light = 0.925 \tag{5.6}$$
$$45 \ linearly \ polarized \ light = 0.924 \tag{5.7}$$
$$Circularly \ polarized \ light = 0.925 \tag{5.8}$$

5.8   Discussion

The polarization aberrations in the TMT are coating induced astigmatism, tilt and chromatic aberration. These are caused by the mirror coating, curvature of the primary and secondary mirrors, and the inclination of the Nasmyth mirror. The diattenuation and retardance maps are shown for all the three mirrors of the telescope (Figures 5.2, 5.3). Jones pupil maps are obtained at WFOS port and the focus of the NFIRAOS instrument. The Amplitude Response Matrix obtained at the WFOS port shows the presence of the ghost PSFs with an amplitude 0.0025 in the cross-components (Figure 5.6). At the NFIRAOS focus, the amplitude of the cross-components increase to 0.095. The Point Spread Matrix obtained by Jones-Mueller conversion gives the Stokes image for any input Stokes vector. It shows that the PSF of an unpolarized source does not remain unpolarized at the NFIRAOS focus. The X and Y polarized light indicate the presence of V component which causes the ellipticity of the resultant PSF. The Huygen's PSF estimated from Zemax$^{®}$ shows the variations in the FWHM and Strehl ratios for different input polarizations. Adaptive optics system cannot correct for the aberrations in both the polarizations (X and Y) simultaneously. The shear and the ellipticity obtained at the NFIRAOS focus can be considered to compare with the expected Strehl ratios. The values of the ghost PSF obtained at the WFOS port has to be considered during the design of any high contrast imaging instrument for TMT.

Chapter 6

Polarization effects due to the segments of primary mirror of TMT

6.1 Segmentation of the primary mirror of the Thirty Meter Telescope (TMT)

The primary mirror ($M1$) of TMT is a concave hyperbolic with ROC=-60 m and $K = -1.00953$, made of 492 low expansion glass segments. Each segment is hexagonal in shape and measuring 1.44 m across the corners. The segments are separated by a uniform inter-segment gaps of 2.5 mm. The segmentation scheme for the TMT proposed by Mast (2004) consists of six identical sectors starting from A to F with each sector having 82 unique segments as shown in Figure 6.1. The global coordinates of the 492 segments are obtained from the TMT database. The telescope configuration is designed in the mixed-mode (combination of sequential and non-sequential mode) in Zemax® where the segments are added as non-sequential components (Figure 6.2). Each segment is specified using a user-defined aperture (UDA) file containing its vertices specified in the global coordinate system. The secondary and Nasmyth mirrors are added in the sequential mode.
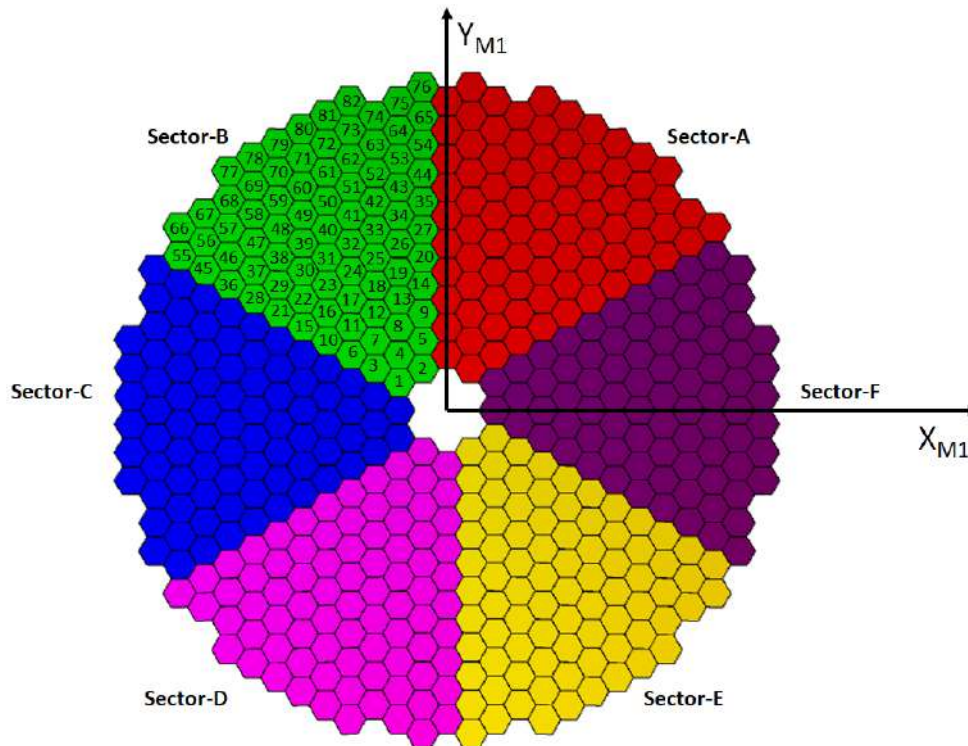
Figure 6.1: Segmented primary mirror of TMT simulated in Zemax® showing different sectors in different colours (Baffes et al., 2008). The numbering scheme of the segments is shown for Sector-B.
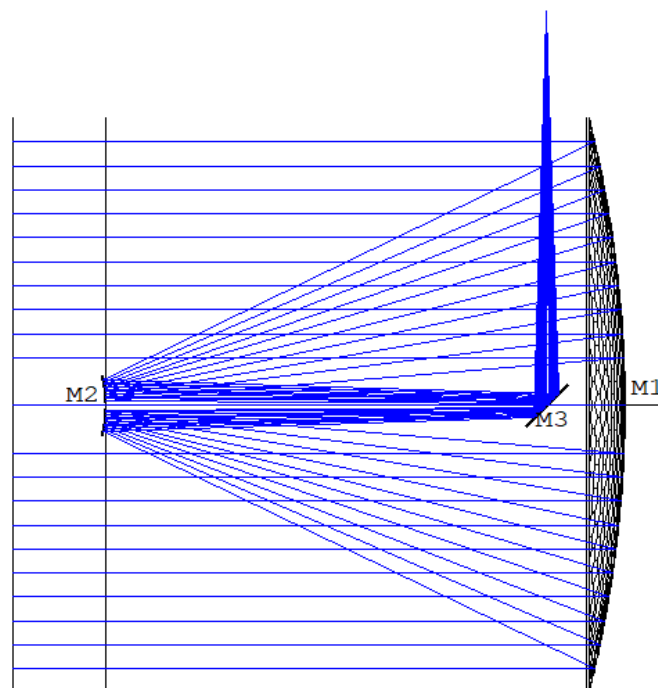

Figure 6.2: Optical layout of TMT with segmented primary mirror obtained from Zemax®.

Incident angles are estimated for the marginal ray falling on all the mirror surfaces of TMT considering the primary mirror as monolith and segmented. They are found to deviate from the estimates given in chapter 4 due to the segmentation. The normalized pupil positions for the marginal ray is found to be different for both the cases as given in Table 6.1. In the case of the primary and secondary mirror, the incident angles were found to be the same at all the four normalized pupil positions in the monolith case. However, as shown in Figure 6.1 the segment position in X_{M1} and Y_{M1} directions are not same causing the variation in the incident angles for the segmented primary mirror. The variation is in the order of 1 degree for the primary and secondary mirror and 0.1 degrees for the Nasmyth mirror.

Primary mirror -Monolithic				
Px Pupil Position	Py Pupil position	Primary mirror	Secondary mirror	Nasmyth mirror
0	1	14.035	14.99	43.08
0	-1	14.035	14.99	46.91
1	0	14.035	14.99	45.031
-1	0	14.035	14.99	45.031
Primary mirror-Segmented				
Pupil Position (Px)	Pupil Position (Py)	Primary Mirror	Secondary Mirror	Nasmyth Mirror
0	0.9516	13.381	14.29	43.18
0	-0.9516	13.381	14.29	46.817
0.908	0	12.78	13.65	45.026
-0.908	0	12.78	13.65	45.026

Table 6.1: The incident angles obtained from ray tracing in Zemax for TMT with primary mirror as monolithic and segmented at the normalized pupil positions corresponding to the marginal ray.

6.1.1 Instrumental polarization (IP) and cross-talk (CT) estimated for the segmented primary mirror

IP and CT are determined from the Mueller matrix, which is estimated using the polarization pupil map in Zemax $^{®}$ as explained in Chapter 3. The normalized pupil positions in the exit pupil, the amplitude of the electric field vectors (E_x, E_y), and the phase difference between the electric field vectors are the outputs obtained from polarization pupil map. Figure 6.3 shows the polarization pupil map obtained after the Nasmyth mirror for linear polarization as input. The map is generated for an array of 153×153 which corresponds
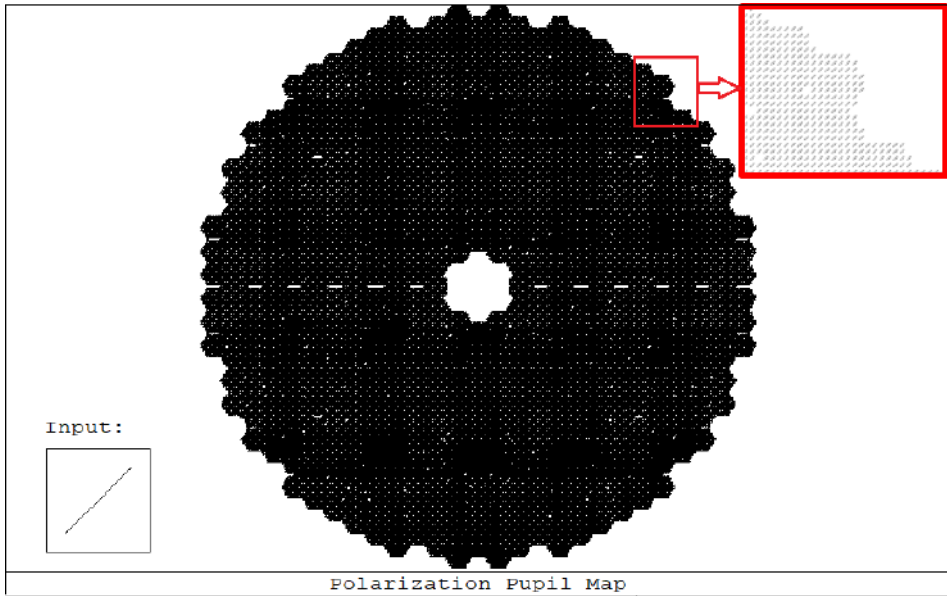
Figure 6.3: Polarization pupil map after the Nasmyth mirror for the linearly polarized light as input. The enlarged section shows the elliptically polarization after the reflection from the Nasmyth mirror.

to $20,000$ rays.

Mueller matrices estimated for on-axis rays for $\lambda = 0.4$-2.5 μm considering monolith and segmented primary mirror shown in Figure 6.4. $I \rightarrow Q$, instrumental polarization and $U \rightarrow V$, crosstalk are found to be nearly same for both the monolith and segmented cases. The difference in IP is of the order of 10^{-4} and CT of the order of 10^{-3}. Hence, the Mueller matrices estimated in Chapter 4 remain the same for the segmented mirror configuration also. However, any change in the segment configuration may vary the Mueller matrices. Only in the case of an ideal scenario, all the segments are aligned and co-phased to make the 492 segments behave as monolith mirror. But, in reality, the tilt and piston of an individual segment may vary. There can be a case of missing segments under certain unavoidable circumstances. The coating parameters on all the segments may not be precisely the same, which will, in turn, change the Mueller matrices. In the next sections, the effect of all these parameters on the polarization measurements has been discussed.
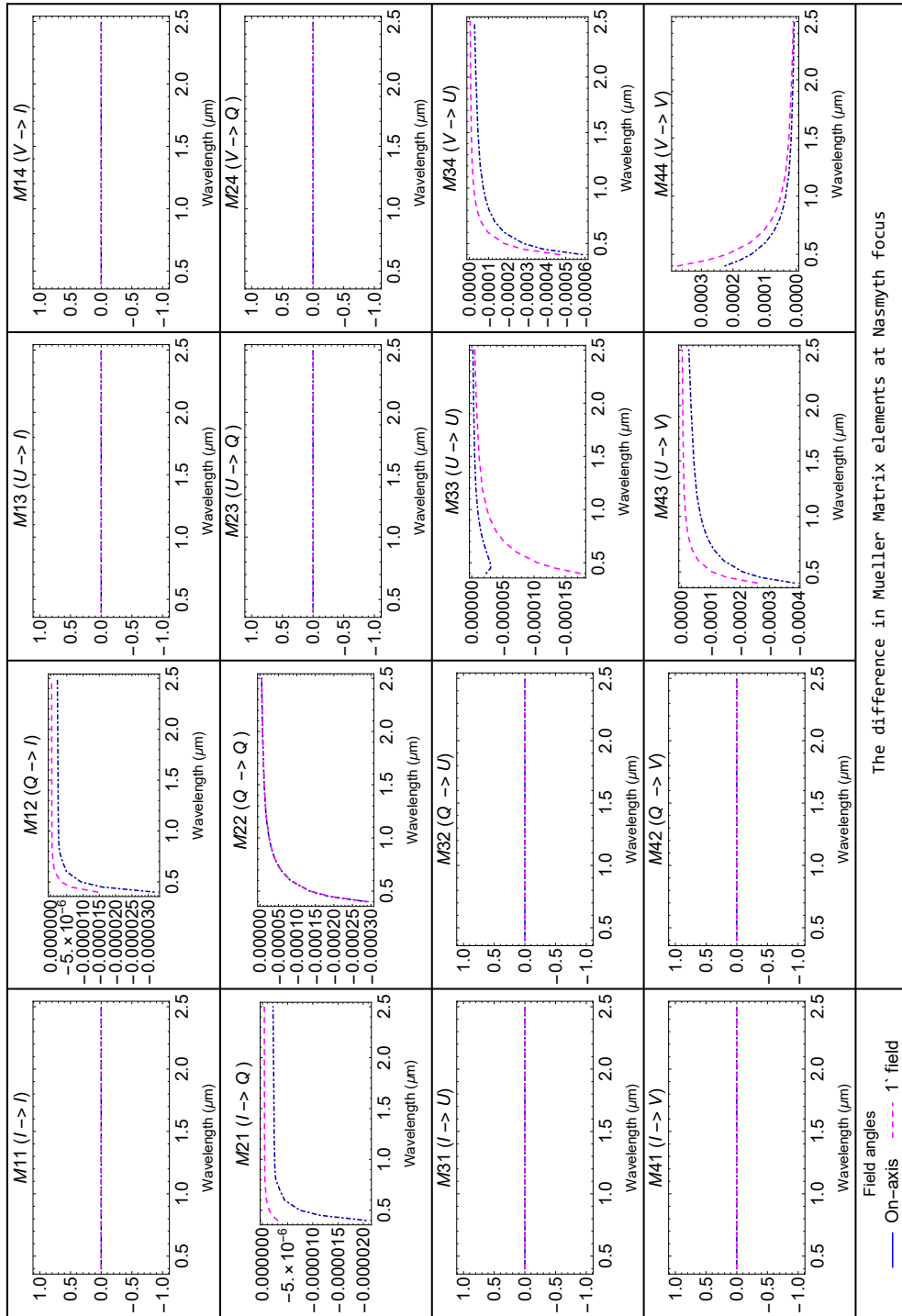
Figure 6.4: The difference in the Mueller matrix elements versus wavelength as monolithic and segmented configuration for on-axis and 1′ field angles.

6.2   Effect of missing segments on the Mueller matrices

The segments are removed in a random order from the primary mirror, and the corresponding Mueller matrices are estimated. Table 6.2 shows the polarization pupil map and Mueller matrix for each of the missing segment case. The number of missing segments varies from 0 to 8. The matrix elements change in the order of 10^{-6} when the segments are removed. Even with the removal of two segments, the IP (M21) changes in the order of 10^{-6} and CT (M43) changes in the order of 10^{-4}. Along with this, the terms M31 ($I \rightarrow U$) and M41 ($I \rightarrow V$) corresponding to instrumental polarization and, M24 ($Q \rightarrow V$) corresponding to cross-talk appears in the Mueller matrix. The variations seen in the Mueller matrix elements can be attributed to the rays from the missing segments. In the case of the primary (monolith) and secondary mirror, polarization introduced by the mirror averages to zero owing to cylindrical symmetry, as shown in Chapter 4. The components get nullified during incoherent addition at the focus. Here, the rays from the missing segment result in the residual component after the primary mirror and continue to the Nasmyth mirror. The scenario of missing segments is assumed to be one of the rarest in the case of TMT as the total number of segments manufactured is 574 (492+82) with a provision of one additional sector of segments available at all times. The faulty segments could be easily replaced provided that they do not occupy the same positions in the different sectors (Ex: Segment number four from sector A and B cannot be replaced simultaneously). Even if eight segments are missing from random positions, variations in the polarization values are not significant compared to the measurement accuracy.

6.3   Effect of coating variation for segments

The mirrors in the TMT telescope may have a four-layer coating, which was initially developed for the Gemini telescope Vucina et al. (2006) as given in

Missing Segments	Mueller matrix	Polarization pupil map
0	$\begin{pmatrix} 1 & 0.012449 & 0 & 0 \\ 0.012454 & 0.999241 & 0.000000 & 0.000000 \\ 0 & 0 & 0.887924 & 0.457573 \\ 0 & 0 & 0.457874 & -0.887236 \end{pmatrix}$	
2	$\begin{pmatrix} 1 & 0.012452 & 0.000004 & -0.000001 \\ 0.012457 & 0.999241 & 0.000006 & -0.000127 \\ 0.000004 & 0.000049 & 0.887881 & 0.457653 \\ 0.000001 & -0.000118 & 0.457954 & -0.887193 \end{pmatrix}$	
4	$\begin{pmatrix} 1 & 0.012451 & 0.000008 & -0.000002 \\ 0.012455 & 0.999246 & 0.000016 & -0.000242 \\ 0.000007 & 0.000097 & 0.887902 & 0.457610 \\ 0.000002 & -0.000222 & 0.457909 & -0.887218 \end{pmatrix}$	
6	$\begin{pmatrix} 1 & 0.012449 & 0.000000 & 0.000000 \\ 0.012454 & 0.999249 & 0.000000 & 0.000015 \\ 0.000000 & -0.000007 & 0.887932 & 0.457581 \\ 0.000000 & 0.000013 & 0.457879 & -0.887251 \end{pmatrix}$	
8	$\begin{pmatrix} 1 & 0.012445 & -0.000005 & 0.000002 \\ 0.012449 & 0.999247 & 0.000004 & 0.000163 \\ -0.000005 & -0.000070 & 0.887982 & 0.457495 \\ -0.000002 & 0.000147 & 0.457793 & -0.887299 \end{pmatrix}$	
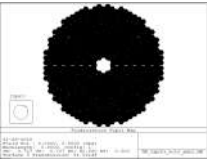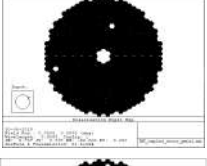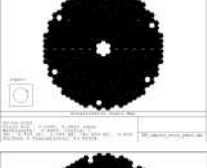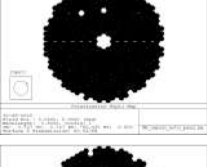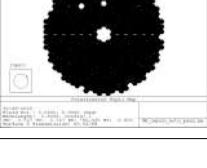
Table 6.2: The Mueller matrices estimated for the cases of missing segments.

Chapter 4. In this analysis, 85 Å of Si_3N_x and 1100 Å of Silver has been considered. The contour plots of the reflection coefficients are also given in Chapter 4. Due to ageing, the thickness and refractive index of the Si_3N_x and the refractive index (real and imaginary part) of Silver might vary. Also, the re-coating of the segments may be carried out either ring wise or sector wise which might cause variation in the refractive indices. These cases are considered in the following subsections to ascertain their effect on the polarization properties of the telescope optics.

6.3.1 Variation in n and k of Silver

The refractive index of all the 492 segments might not be same due to ageing. To represent these variations, the n and k of Silver are varied. The n and k for Silver are 0.13 and -3.88 (Palik, 1998) at λ=0.6199 μm measured under the laboratory conditions. These values are considered as the mean values here.

A list n and k values are generated in uniform and normal distribution with different variances such as $\pm 1\%$, $\pm 5\%$, $\pm 10\%$, and $\pm 20\%$ from their mean values. In every simulation, the coating files containing these different coating recipes are provided to Zemax. The simulation is run for hundred iterations for each variance values. The Mueller matrix is estimated at the Nasmyth focus at the end of each iteration.

The Mueller matrices obtained for a uniform distribution of n and k is shown in Figure 6.5. Matrix elements obtained for $\pm 1\%$ and $\pm 5\%$ variances do not show any significant changes from those obtained with the mean value of refractive index. The off-diagonal elements ($M31$, $M41$, $M32$, $M42$, $M13$, $M14$, $M23$, and $M24$) which were zero in Figure 6.4 are now increased to 10^{-6}. Variation in IP ($M21$) and CT ($M43$) in the case of $\pm 10\%$ and $\pm 20\%$ is in the order of 10^{-5}. Figure 6.6 show the Mueller matrices obtained for the normal distribution of n and k with different variances. The variations in the matrix elements are in the order of 10^{-5} to 10^{-6} even in this case. The variation in the refractive index of Silver due to ageing does not affect IP and CT.

6.3.2 Variation in thickness of Si_3N_x

The thickness (t) of Si_3N_x is 8.5 nm used in the Gemini coating is considered as the mean value here. As mentioned above, a normal distribution of n, k of Silver and the thickness of Si_3N_x are generated with variances of $\pm 10\%$ and $\pm 20\%$. Figure 6.6 shows the Mueller matrices for each of these iterations. The variations are in the order of 10^{-4} in IP and 10^{-3} in the case of CT. From these two simulations, it is evident that the variation in n, k of Silver and t of Si_3N_x should not exceed $\pm 10\%$ for achieving a polarization accuracy of 10^{-4}.
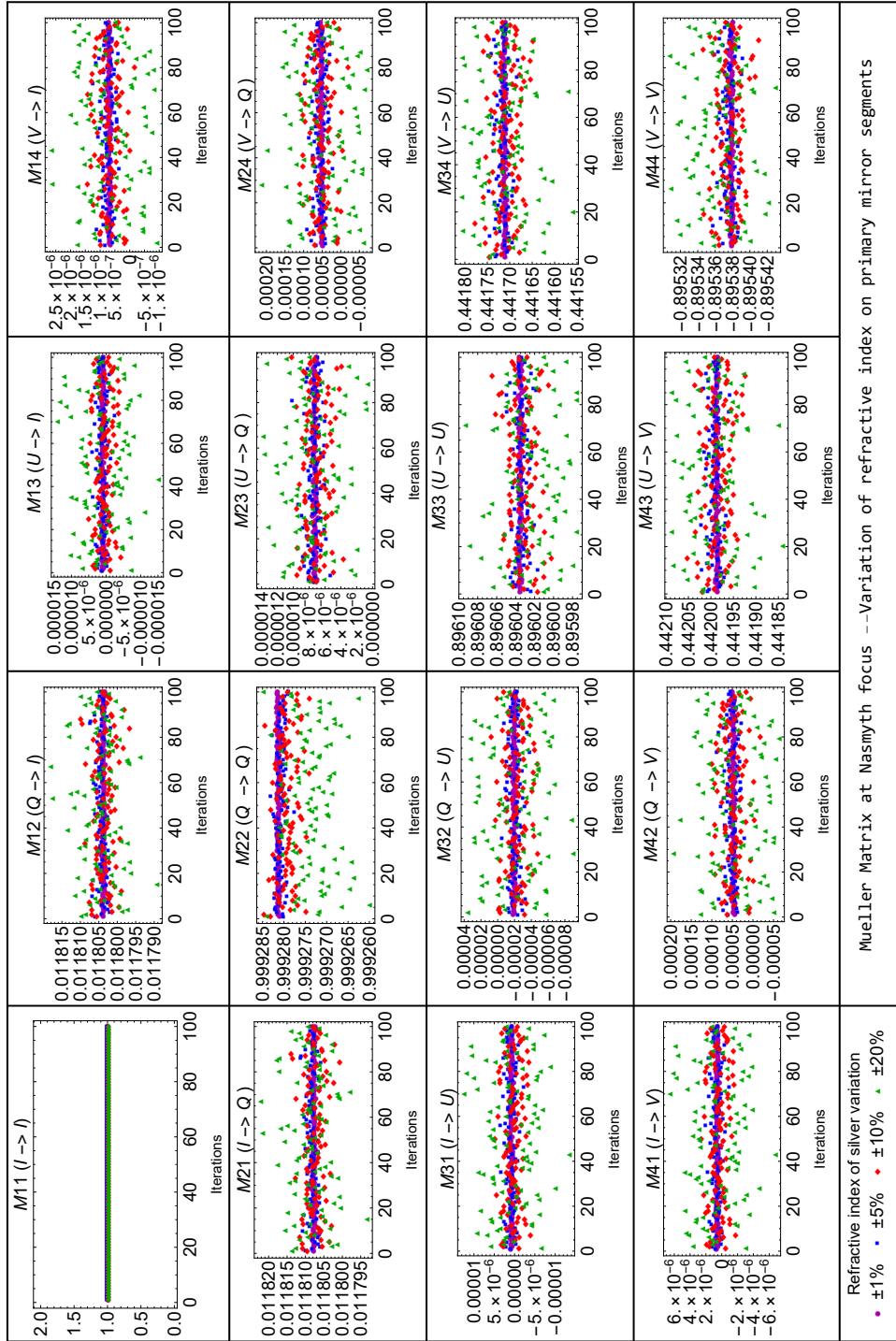
Figure 6.5: Normalized Mueller matrix versus number of iterations estimated at the Nasmyth focus of TMT. The different plot markers correspond to different percentage of variation of the the n and k of Silver from it's mean value in uniform distribution
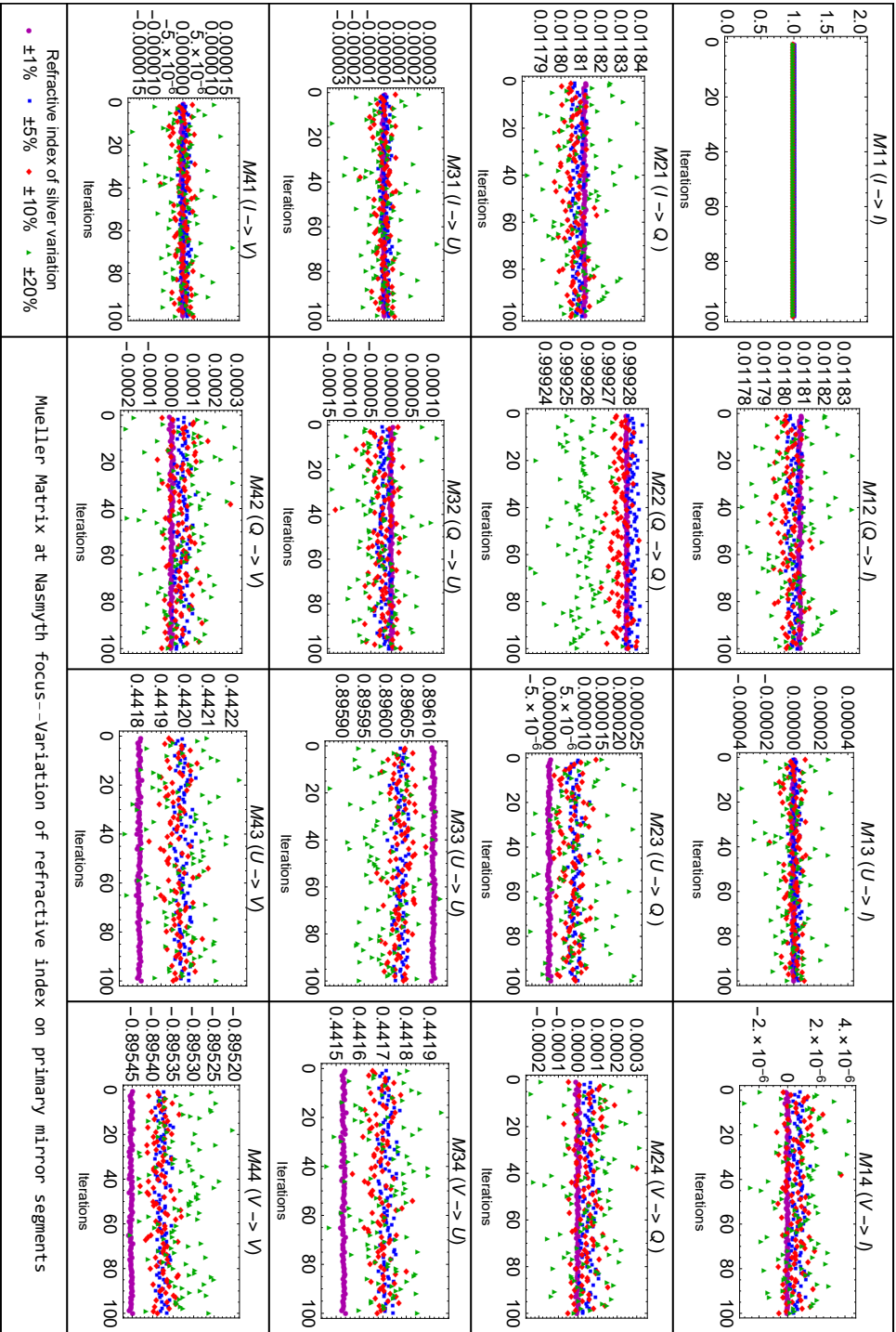
Figure 6.6: Normalized Mueller matrix versus number of iterations estimated at the Nasmyth focus of TMT. The different plot markers correspond to different percentage of variation of the the n and k of Silver from it's mean value in normal distribution
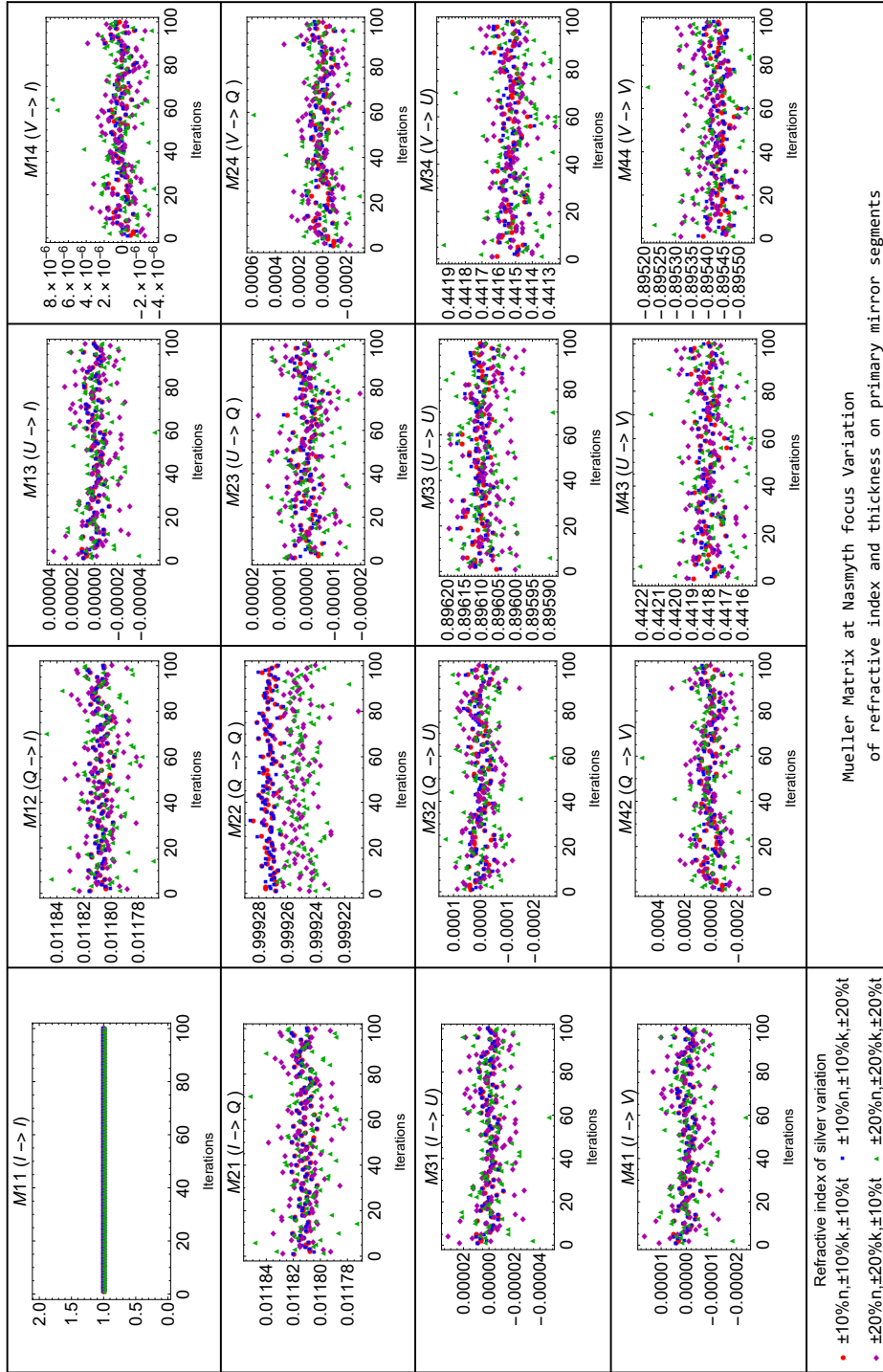
Figure 6.7: Normalized Mueller matrix versus number of iterations estimated at the Nasmyth focus of TMT. The different plot markers correspond to different percentage of variation of the the n and k of Silver from it's mean value and variation of the thickness of Si_3N_4 in normal distribution.

6.3.3 Re-coating sequence of the segments

The primary mirror of TMT has six sectors with 82 unique segments in each sector. In addition to 492 segments, 82 segments (1 sector) will be available as spare segments to be replaced during the re-coating, cleaning etc. The coating chamber can accommodate maximum of two segments at a time. So the primary mirror might have maximum of two freshly coated segments at anytime. The re-coating of the segments could be done either sector wise or ring wise. If the re-coating is performed sector-wise, it is possible that the segments in one of the sector might have different refractive index compared to the others. To analyze this scenario, all the segments in one sector are provided with same coating file and, segments in the other sectors have n and k of the coating varied from the mean value by $\pm$ 10% in normal distribution. This is repeated for all the sectors in series. Figure 6.8 shows the Mueller matrices estimated for each iteration. Figure 6.9 shows the Mueller matrices for the re-coating carried out ring wise. The ring 1-2 correspond to the segments in first two rings of the primary mirror coated with same coating whereas all the other segments have n and k of the coating varied from the mean value by $\pm$ 10%. This is repeated for the outermost rings and the intermediate rings also. For each of the case, twenty iterations are performed.

In both the cases of re-coating sequence, the variation in the off-diagonal matrix elements is in the order of 10^{-6}. IP and CT vary only in the order of 10^{-5}. Hence, the re-coating can be done either sector wise or ring wise without causing much variation in the Mueller matrices.
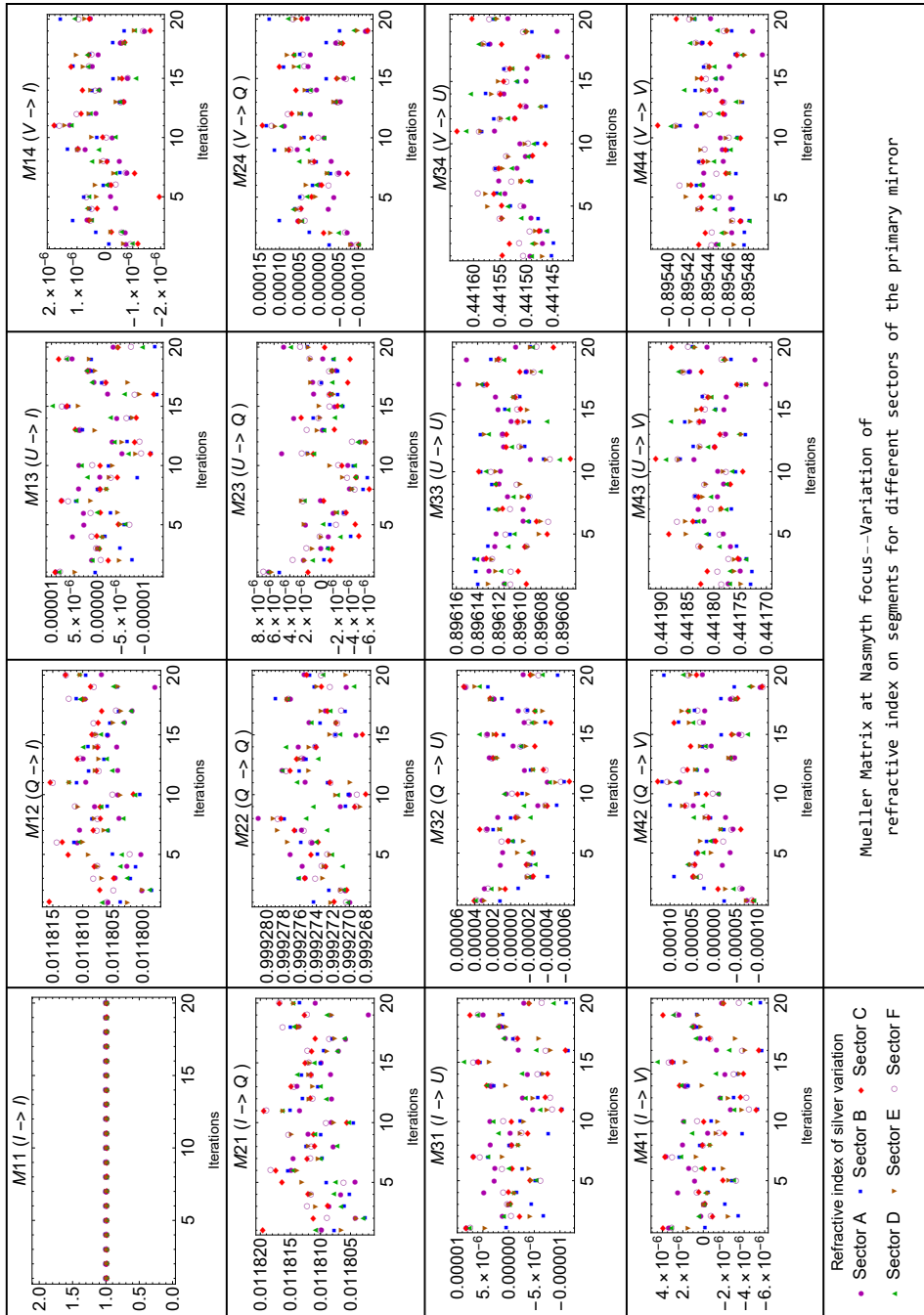
Figure 6.8: Normalized Mueller matrix versus number of iterations estimated at the Nasmyth focus of TMT. The different plot markers correspond to different sectors of the primary mirror. Sector-A implies the same coating applied to all the segments in sector A and all the other sectors have n and k values of the refractive index of Silver varied by $\pm 10\%$ in a normal distribution.
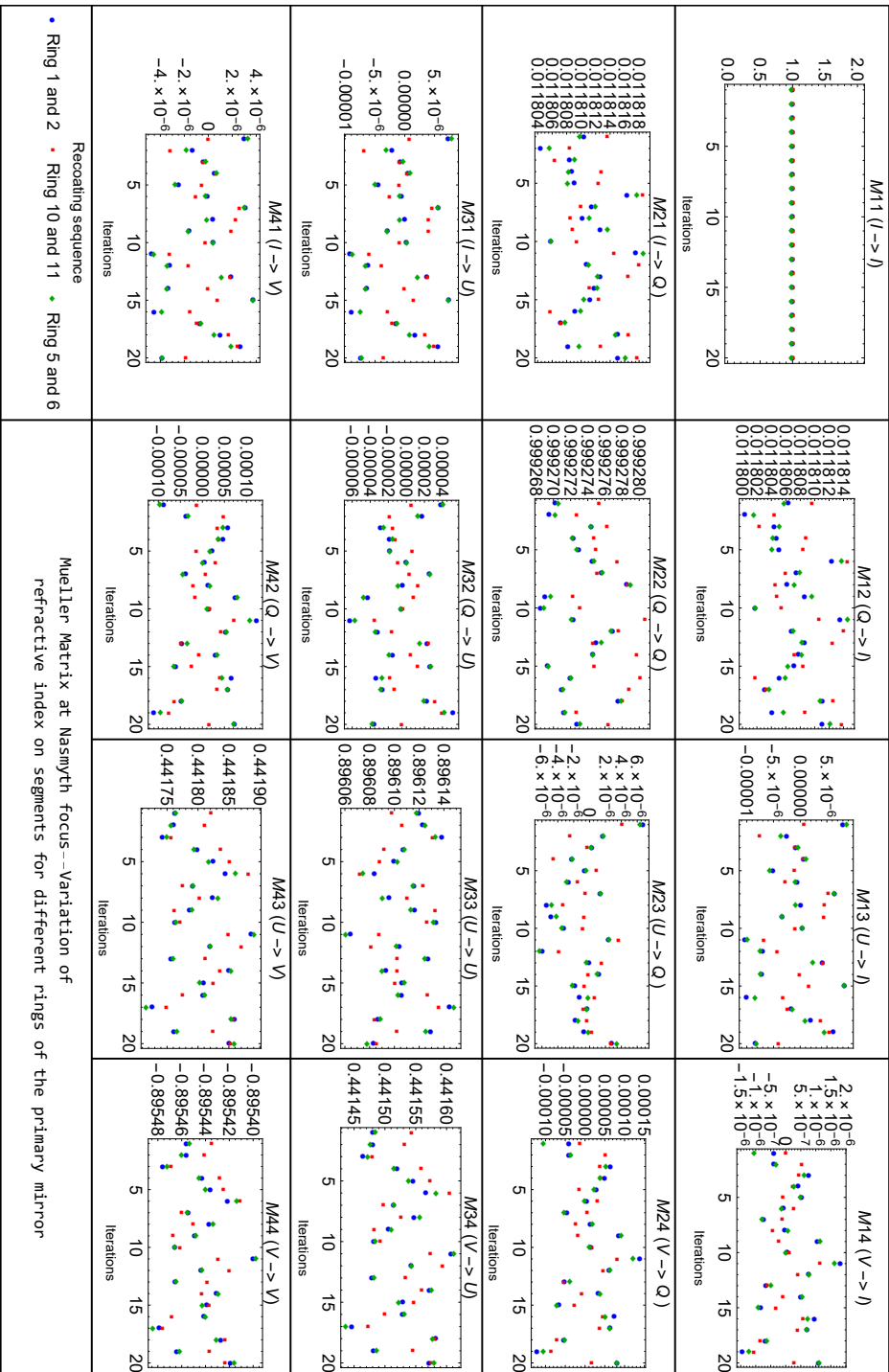
Figure 6.9: Normalized Mueller matrix versus number of iterations estimated at the Nasmyth focus of TMT. The different plot markers correspond to different rings of the primary mirror. Ring 1-2 implies the same coating applied to all the segments in that ring and all the other rings have n and k values of the refractive index of Silver varied by $\pm$ 10% in a normal distribution.

6.4   Effect of tilt and piston of the segments on the Mueller matrices.

A segment in the primary mirror has a total of six degrees of freedom which are

1. Piston: translation along the axis perpendicular to the segment.

2. Tip and Tilt: rotation about two axes horizontal to the segment.

3. Clocking: translations and rotation in the plane of the segment.

Among these, the strongest wavefront discontinuities are generated by the piston and tip-tilt movements of the segments. In the upcoming sections, the effects of piston and tip-tilt of the segments on the polarization variations is described.

6.4.1   Variation of piston of the segments

Under ideal conditions, the piston error of the segment is expected to be zero. The mechanical and thermal deformations and external disturbances cause misalignment of the segments and in their relative positions. In the case of TMT, the piston error requirement for phasing is 6.8 nm RMS (Troy et al., 2016). A list of values is generated in the normal distribution with the mean value of 0 and variance of ± 10 nm. This is given as the piston error for all the 492 segments and repeated for 100 iterations. The wavefront map for the ideal case shows RMS wavefront error of 0.0427 λ is shown in Figure 6.10. Similarly, the wavefront map obtained for one of the iteration with piston variation of $\pm$ 10 nm has the RMS wavefront error of 0.0453 λ. The piston error do not cause any significant change in the wavefront error. To understand the change in the polarization, the Mueller matrices are estimated for each iteration as shown in Figure 6.11. Piston variation of $\pm$ 10 nm do not cause any variation in the Mueller matrix elements.
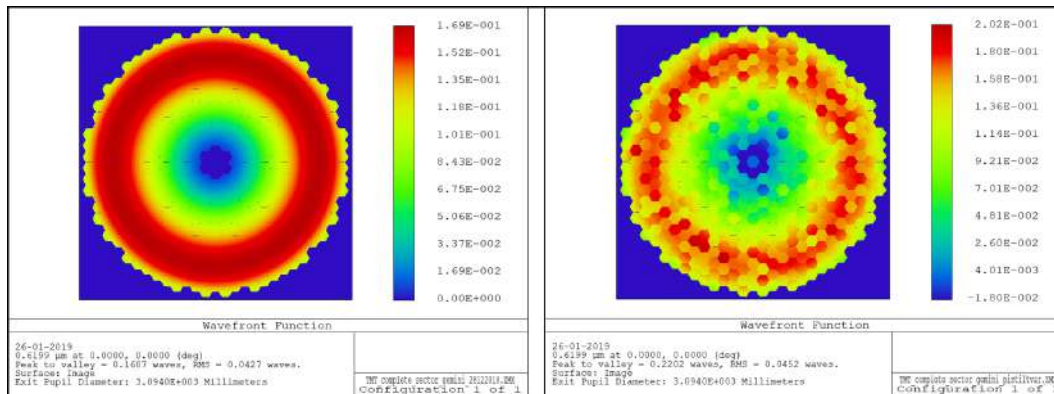
Figure 6.10: The wavefront map obtained from Zemax® for the TMT with zero and ± 10 nm of piston error.

6.4.2 Variation of tilt of the segments

The segments designed in Zemax® are in the global coordinate system. The x and y tilts are required to be varied in the local segment coordinate frame. Hence, the segments are now redefined using the Zernike standard surface with 37 Zernike coefficients. The Zernike coefficients Z3 and Z2 in the Zernike expansions correspond to the x and y tilt of the segment. The x and y tilt of the segments in the ideal conditions are zero. To understand the effect of tilt, they are varied with a mean value of 0 and variance of ±10 nm. The Mueller matrices are estimated for each iteration as shown in Figure 6.11

The variation in the Mueller matrix elements for tilt and piston variation is not found to be significant. The crosstalk terms vary in the order of 10^{-8}. Hence for the variation within ±10 nm of piston and tilt, the polarization effects from the telescope do not vary from that seen in the case of a monolithic primary mirror.

6.5 Discussions

The polarization effects are estimated in this chapter considering segmented primary mirror of the Thirty Meter Telescope (TMT). The polarization analysis has been carried out in Zemax® to obtain the Mueller matrices. The effect of missing segments on the Mueller matrix has been estimated. IP and CT are
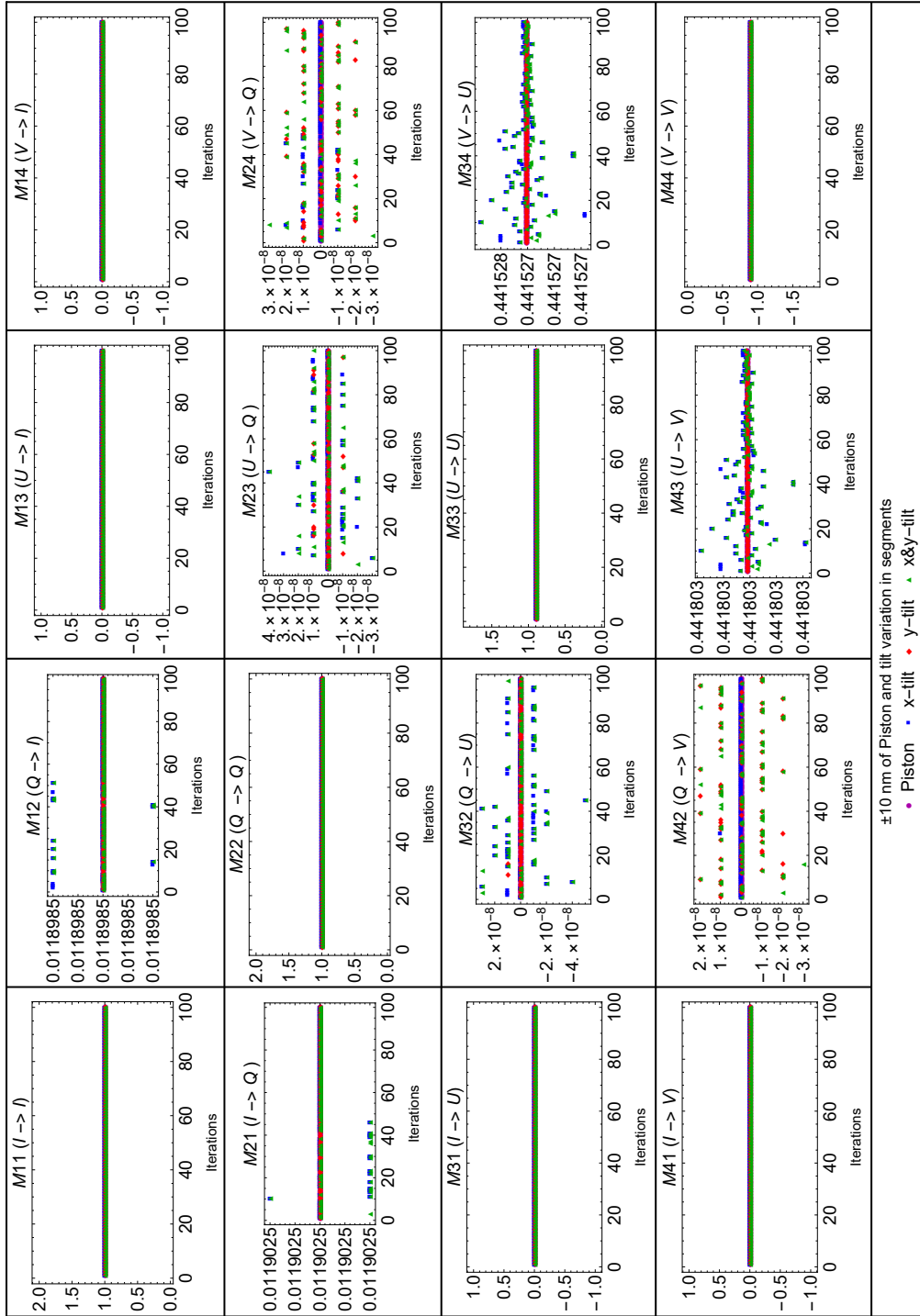
Figure 6.11: The normalized Mueller matrices estimated at $\lambda = 0.6199$ μm for the variation of piston and tilt in the order of $\pm$ 10 nm

found to vary in the order of 10^{-6} in the case of the missing segments. The variation of the refractive index and the thickness of the coating has also been simulated. The variations in the IP and CT are in the order of 10^{-5} to 10^{-6} for the variation in the parameters of the coating. The tilt and the piston of the segments are also varied to understand their effect on the Mueller matrix. The coating parameters (refractive index of Silver and thickness of Si_3N_4) are found to cause the most significant variation in polarization compared to all the other factors.

Chapter 7

Polarization Model for the Multi-Application Solar Telescope (MAST)

7.1 Multi-Application Solar Telescope (MAST) : Introduction

MAST is currently the largest solar telescope in India, located at the Udaipur Solar Observatory (USO) (Mathew et al., 2017). The telescope is situated on an island in the Fatehsagar Lake, Udaipur as shown in Figure 7.1 [1] . The telescope was manufactured by AMOS, Belgium (Denis et al., 2008) and began its operation in June 2015. It is an off-axis Gregorian-Coudé telescope with an aperture of 50 cm and a selectable field of view of $3'$ or $6'$ (Denis et al., 2010). The optical design of the telescope consists of six mirrors (M1 to M6) and a derotator system as shown in Figure 7.2. The primary (M1) and secondary (M2) are the off-axis concave parabolic mirrors designed to provide pupil de-magnification (Focal length of M2/Focal length of M1 is 10:1) (Denis et al., 2008). The collimated beam from M2 is folded using flat mirrors (M3 to M6) along the desired path considering the mechanical elevation and azimuth axis.

---

[1] https://www.isro.gov.in/multi-application-solar-telescope -operationalised-udaipur-solar-observatory
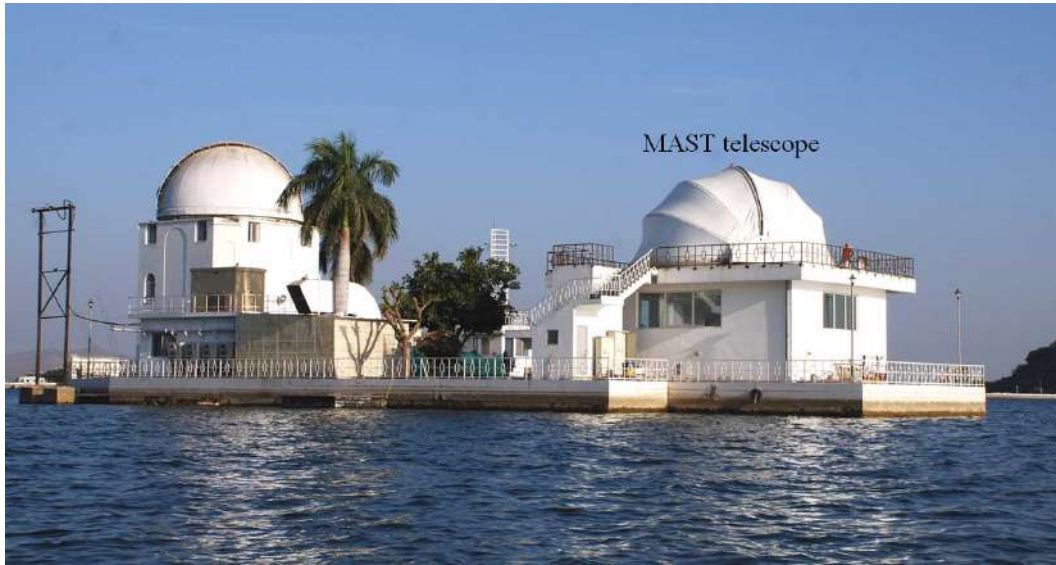
Figure 7.1: The Udaipur Solar Observatory in Fatehsagar lake, Udaipur, operated by Physical Research Laboratory, Ahmedabad

The collimated beam is propagated down to the stationary observing floor using these flat mirrors. The image rotation caused by the altitude-azimuth mount configuration is corrected by an optical field derotator, which is placed between M5 and M6. The derotator consists of three flat mirrors which rotate as a group to keep the image stationary in the image plane. The flat mirror M6 folds the beam to feed different instruments placed in the observing platform (similar to the Nasmyth platform) of the telescope. MAST is provided with four ports to accommodate four different back-end instruments. The parameters of all the mirrors in the optical layout of MAST is given in Table 7.1.

Mirror	Parameters
M1	Off-axis parabola, Diameter=50 cm, OAD=57.5 cm
M2	Off-axis parabola, Diameter=5 cm, OAD=5.75 cm
M3	Elliptical plane mirror, X-Hw=6.5 cm,Y-Hw=5cm, Tilt=45°
M4	Circular plane mirror, Diameter=18 cm, Tilt=-16.845°
M5	Elliptical plane mirror, X-Hw=5 cm,Y-Hw=10 cm, Tilt=61.645°
M6	Circular plane mirror, Diameter=20 cm, Tilt=45°
DM1	Circular plane mirror, Diameter=25 cm, Tilt=60°
DM2	Circular plane mirror, Diameter=15 cm, Tilt=30°
DM3	Circular plane mirror, Diameter=25 cm, Tilt=60°

Table 7.1: The parameters of the mirrors in the MAST telescope
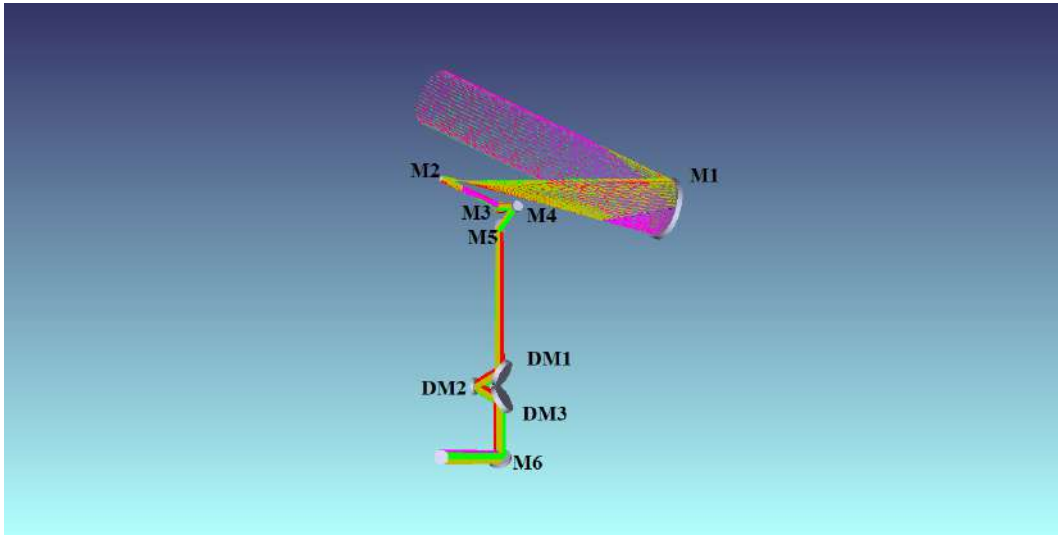
Figure 7.2: Optical layout of the Multi-Application Solar Telescope obtained from Zemax®

Currently, there are three back-end instruments at the telescope, an H-alpha and G-band imager (Raja Bayanna et al., 2014), a narrow band spectropolarimetric imager (Tiwary et al., 2017), and a multi-slit spectro-polarimeter. An adaptive optics system is being developed to obtain the diffraction limited observations. One of the main science objectives of the telescope was to study the evolution of vector magnetic field in photosphere and chromosphere by obtaining the simultaneous polarimetric observations in FeII (6173 Å) and CaII (8542 Å) spectral lines. The narrow-band imaging spectropolarimeter for the 6173 Å channel was developed by Tiwary et al. (2017), and preliminary results were compared with the Stokes (I and V) profile observations obtained from Helioseismic Magnetic Imager (HMI) from Solar Dynamics Observatory (SDO). The vector magnetic fields were not derived from the observations of the Stokes profiles, as the polarization model for the telescope was not available.

The telescope configuration consists of nine mirrors with most of them being the inclined mirrors hence the instrumental polarization and crosstalk introduced are considerably high. An analytical model was developed to estimate the Mueller matrix of the telescope (Ranganathan et al., 2018). The Mueller matrix was verified experimentally by using different polarizations at the input of the telescope to understand the deviations between the model

and the observations. The polarization measurements were obtained using the imaging spectropolarimeter (Tiwary et al., 2017) at 6173 Å.

7.1.1 Imaging spectropolarimeter at the MAST telescope

Figure 7.2 shows the collimated beam (of 10 cm) from the M6 mirror of the telescope. The beam is focused by the lens at a distance of 2 m and is folded using the two fold mirrors FM1 and FM2 to feed to the polarimeter. The collimated beam (after FM2) propagates to the two $LiNbO_3$ Fabry-Perot (FP) etalons which are used to obtain the better spectral resolution. The FWHM of the FP combination is ~ 90 mÅ at 6173 Å with a free-spectral range of 6 Å (Tiwary et al., 2017). The imaging spectropolarimeter consisting of 2 Liquid
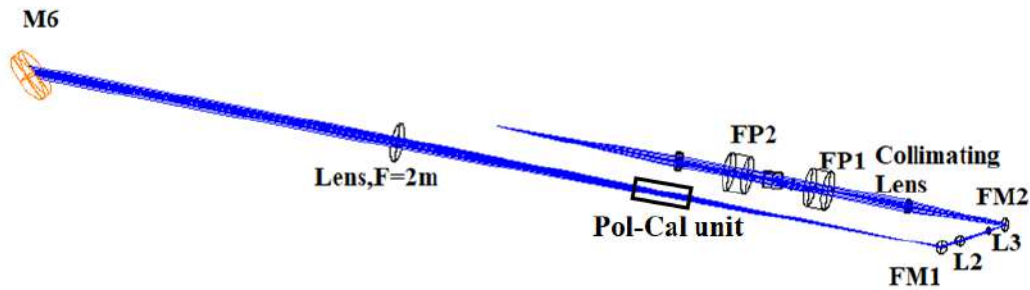
Figure 7.3: The components in the optical path between M6 mirror and imaging spectropolarimeter at MAST obtained from Zemax$^{\circledR}$

Crystal Variable Retarders (LCVR) and a Glan-Thompson polarizer is placed after the FPs as shown in Figure 7.4. The fast axis of the LCVR1 is kept at 0° and LCVR2 at 45° with reference to the polarization axis of the linear polarizer. The temperature of the LCVRs is stabilized using a temperature controller with $\pm 1°$ C temperature stability. Six stage modulation scheme given by Tomczyk et al. (2010) is used for determining the Stokes parameters. The modulation and demodulation matrices and the efficiencies were estimated by Tiwary et al. (2017). The output Stokes vector (S_{out}) at the linear polarizer
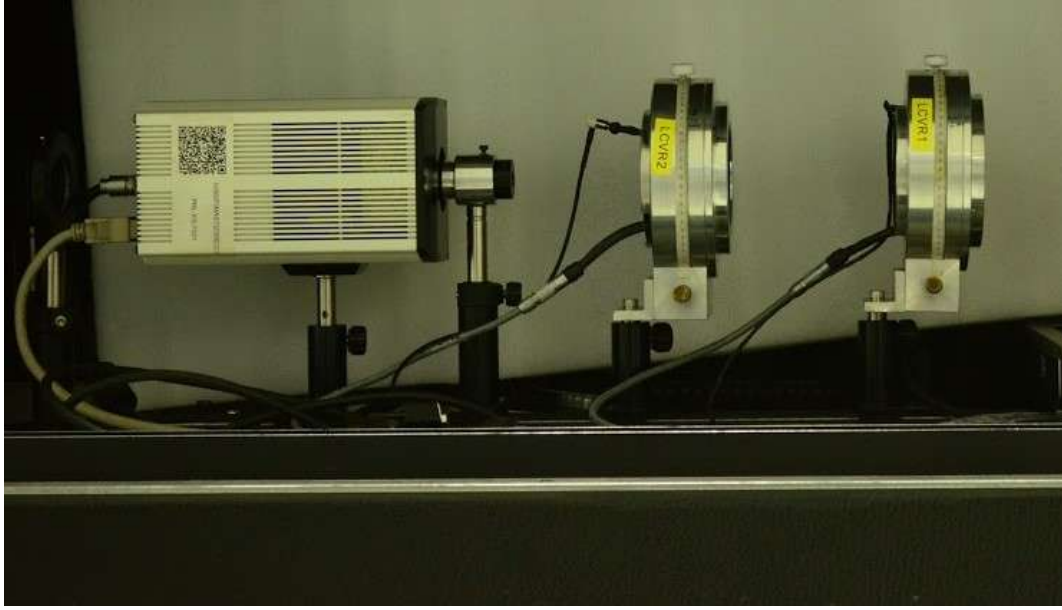
Figure 7.4: Imaging spectropolarimeter at the MAST telescope

is related to the input Stokes vector (S_{in}) at the LCVR1 by the Eqn (7.1).

$$S_{out} = M_P M_{LCVR2} M_{LCVR1} S_{in} \tag{7.1}$$

where, M_P, M_{LCVR1}, and M_{LCVR2} are the Mueller matrices of the polarizer and LCVRs as given below. δ and γ correspond to the retardance values obtained by the application of voltage to the retarders. The voltages used for achieving the six stage modulation is given in Table 7.2.

$$M_P \; (Polarizer \; with \; axis \; 0^O) \; = \; \begin{pmatrix} 1 & 1 & 0 & 0 \\ 1 & 1 & 0 & 0 \\ 0 & 0 & 0 & 0 \\ 0 & 0 & 0 & 0 \end{pmatrix} \tag{7.2}$$

$$M_{LCVR1} \; (Fast \; axis \; 0^O) \; = \; \begin{pmatrix} 1 & 0 & 0 & 0 \\ 0 & 1 & 0 & 0 \\ 0 & 0 & \cos\gamma & \sin\gamma \\ 0 & 0 & -\sin\gamma & \cos\gamma \end{pmatrix} \tag{7.3}$$

$$M_{LCVR2} \ (Fast \ axis \ 45^{O}) \ = \ \begin{pmatrix} 1 & 0 & 0 & 0 \\ 0 & \cos\delta & 0 & -\sin\delta \\ 0 & 0 & 1 & 0 \\ 0 & \sin\delta & 0 & \cos\delta \end{pmatrix} \quad (7.4)$$

As the polarimeter is placed after several optical components from M6, the response matrix for these optical components has to be determined. A polarization calibration set up is placed between the focusing lens and FM1 to determine the response matrix which will be discussed in the future section.

Measured Intensities	γ (^{o})	Voltages (V)	δ (^{o})	Voltages (V)
$I+Q$	180	2.9287	360	2.0125
$I-Q$	180	2.9287	180	3.0614
$I+U$	90	4.0127	90	4.1608
$I-U$	90	4.0127	90	2.4539
$I+V$	180	2.9287	90	4.1608
$I-V$	180	2.9287	270	2.4539

Table 7.2: The voltages for the LCVRs in six stage modulation scheme at MAST

7.2 Polarization observations from the telescope to estimate the Mueller matrix

Routine polarization observations at the MAST telescope would involve a wavelength scan from 6173.123 Å to 6173.513 Å centered at 6173.318 Å. To avoid line polarization, wavelength regions were selected in the continuum region. The scan was done for the wavelength region : 6173.12317:0.0003:6173.15308 Å, and corresponding FP voltages of, FP1 = 72.3392 V and FP2 = -2353.2407 V. The polarization observations were obtained over the entire day as the Mueller matrix varies with the rotation of various mirrors in the telescope. Stokes parameters were obtained for different input polarizations, incident on the primary mirror. Two sets of observations were obtained one set during, winter (January-2018) and another during summer (May-2018). The variation of elevation, azimuth and derotator angles during the two sets of observations

is shown in Figure 7.5. The Elevation limits are 5° to 88.5° from horizon to zenith and the Azimuth limits are from 85° to 275° North to West.
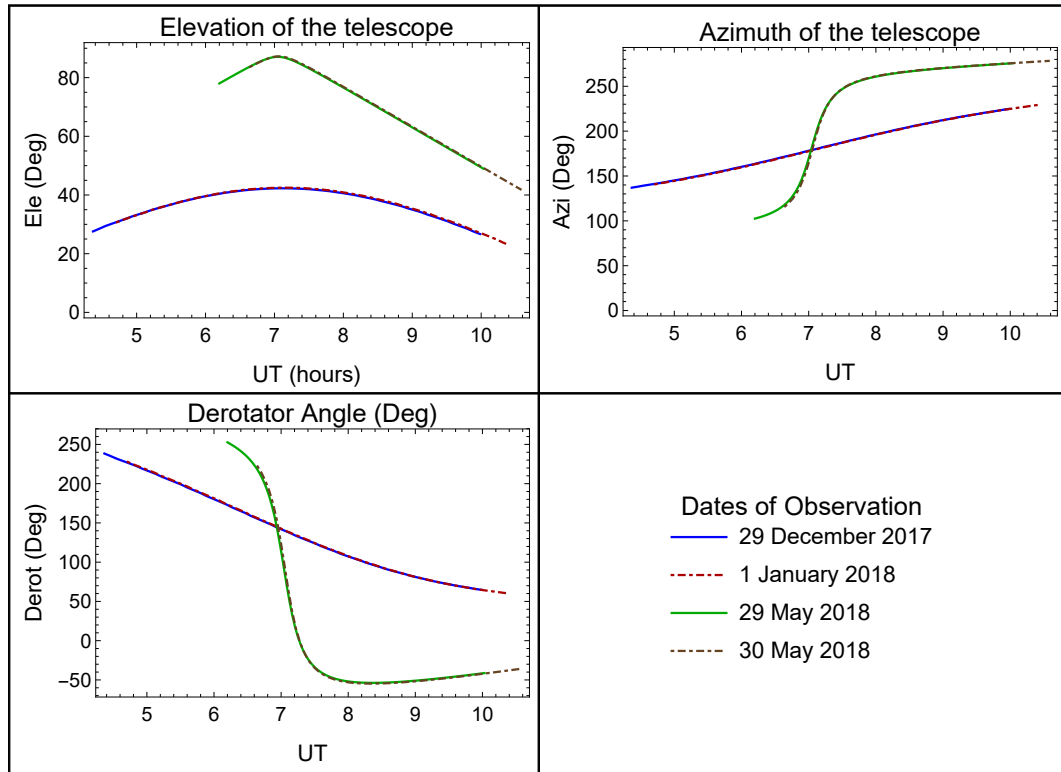
Figure 7.5: Angles variation in Summer and Winter for the MAST telescope

7.2.1   Unpolarized light

The Stokes parameters measured for the unpolarized light as input would give the first column of the Mueller matrix. Hence, the observations were obtained from the disk center of the quiet Sun. The log of the observations is given in Table 7.3. The images were obtained corresponding to the six modulation steps at the detector, CCD (1K×1K). Five images were obtained at each modulation step with a total of 30 images in each set. The Stokes parameters and the instrumental polarization were estimated from these images using an IDL routine.

7.2.2 Linearly polarized light

A linear polarizing sheet of 50 cm in diameter is fixed to the heat-shield of the telescope, before the primary mirror as shown in Figure 7.6. The axis of the polarizer is marked with a thin thread along the polarizing sheet. The plane of the heat-shield is assumed to be parallel to the plane of the primary mirror. The polarizer is rotated to obtain different input polarizations such as, horizontal (polarizer axis at 0°), vertical (polarizer axis at 90°), and linear at 45° (polarizer axis at 45°). The telescope with the polarizer fixed on its shield is shown in Figure 7.7 during one of the observations. The Stokes parameters for each of these cases are obtained by the intensity images at the detector.

Figure 7.6: Sheet polarizer fixed on the heat shield of the telescope.

Figure 7.7: Telescope with sheet polarizer during the observations.

Date	Time (UT)	Polarization
29-Dec-17	04:22:16 to 09:59:38	Unpolarized
01-Jan-18	04:43:39 to 10:25:38	Vertical
02-Jan-18	03:48:24 to 10:24:20	Linear at 45
03-Jan-18	03:51:24 to 11:24:41	Horizontal
29-May-18	06:12:02 to 10:01:54	Vertical
30-May-18	06:38:59 to 10:34:18	Unpolarized

Table 7.3: Log of polarization observations

7.3 Analytical model to estimate the Mueller matrix of the telescope

The analytical model is developed for the MAST telescope using the polarization ray tracing algorithm explained in Chapter 3. The Mueller matrices are estimated for each of the mirror in the optical path and the resultant telescope Mueller matrix is obtained. The M_{total} for the MAST telescope and instruments is,

$$M_{total} = M_{inst}M_{tele} \qquad (7.5)$$

where, M_{inst} is the response matrix obtained for the optical components placed between the polarimeter and M6. M_{tele} is the Mueller matrix of the telescope which can be calculated as,

$$M_{tel} = M6Rot(\theta)DMRot(\theta1)M5M4Rot(\Phi)M3Rot(\frac{\pi}{2})M2M1 \qquad (7.6)$$

where, $\theta = derotator\ angle$, $\theta1 = -derotator\ angle + azimuth$, and $\Phi = \frac{\pi}{2} - elevation$. As seven mirrors in the optical path are flat mirrors and, the collimated beam is propagated from M2, the incident angles for these mirrors remain constant. The Mueller matrix calculated for different mirrors is discussed in the following sections.

7.3.1 Mueller matrix for the primary mirror and secondary mirrors

The primary and the secondary mirrors of the MAST telescope are off-axis parabolas which are defined in the Cartesian coordinate system as,

$$zp = \frac{xp^2 + yp^2}{4f} + \tau; \qquad (7.7)$$

$$xp = r\cos\theta, \quad yp = r\sin\theta + y_0 \qquad (7.8)$$

where, y_0=57.5 cm, τ=0, and f=200 cm for the primary mirror and y_0=-5.75 cm, τ=220 cm and f=-20 cm, for the secondary mirror. The incident angle on the mirror surfaces is estimated using the DC of the incident and reflected rays. It varies from 4.64° to 11.658° in the case of both the mirrors as shown in Figure 7.8. The coating on all the telescope mirrors during the winter observations was SiO_2 and Silver, and the thickness of the SiO_2 was not available. The reflection coefficients are estimated considering a thickness of 90 nm for SiO_2 at λ=6173 Å. The amplitude and the phase of the reflection coefficients estimated for the primary mirror are shown in Figure 7.9. The
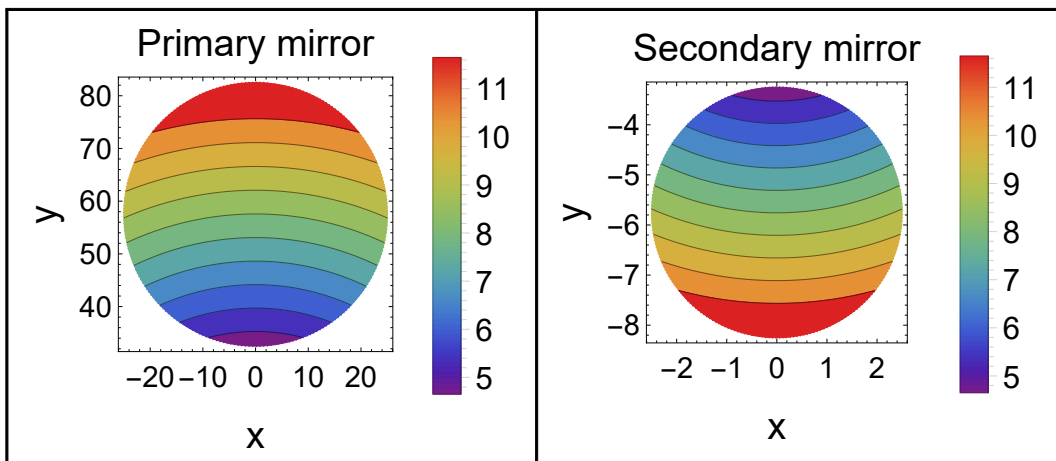
Figure 7.8: Incident angle on the surface of primary mirror and secondary mirror

contours of Mueller matrix elements for the primary mirror of MAST is shown in Figure 7.10. All the diagonal elements look similar with values ≈ 0.94 with contours similar to the incident angle and reflection coefficients. $M21$ (IP)
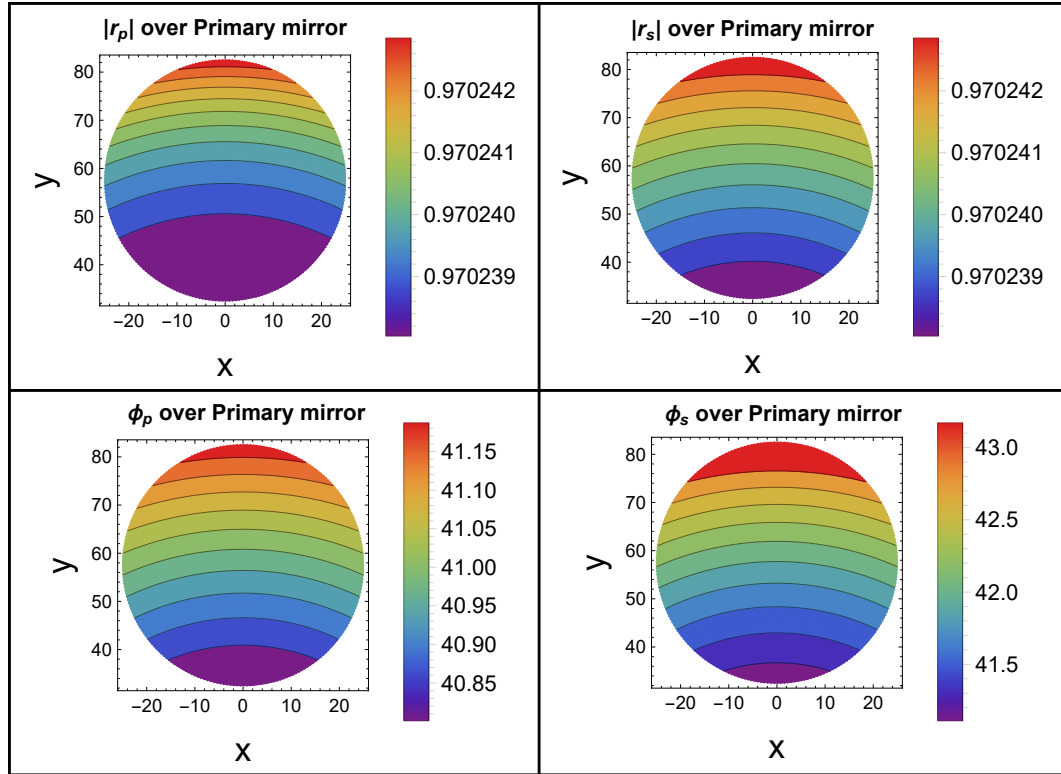
Figure 7.9: The amplitude and phase of the reflection coefficients for the primary mirror

and $M12$ show a non zero value of 0.0001319 (0.013%) as the mirror is not rotationally symmetric. Similarly, $M43$ and $M34$ corresponding to crosstalk shows a value of 0.01691 (1.7%). Other off-diagonal elements are found to be zero. The secondary mirror also shows the same contours in it's Mueller matrix elements. The average Mueller matrix for the primary and secondary mirror for the SiO_2 (65 nm , n=1.455) + Silver (n+ik=0.1310-3.88i) coating is given below:

$$M_{Pri} = \begin{pmatrix} 1 & 0.000139 & 0 & 0 \\ 0.000139 & 0.99 & 0 & 0 \\ 0 & 0 & 0.999 & 0.01691 \\ 0 & 0 & -0.01691 & 0.999 \end{pmatrix} \tag{7.9}$$
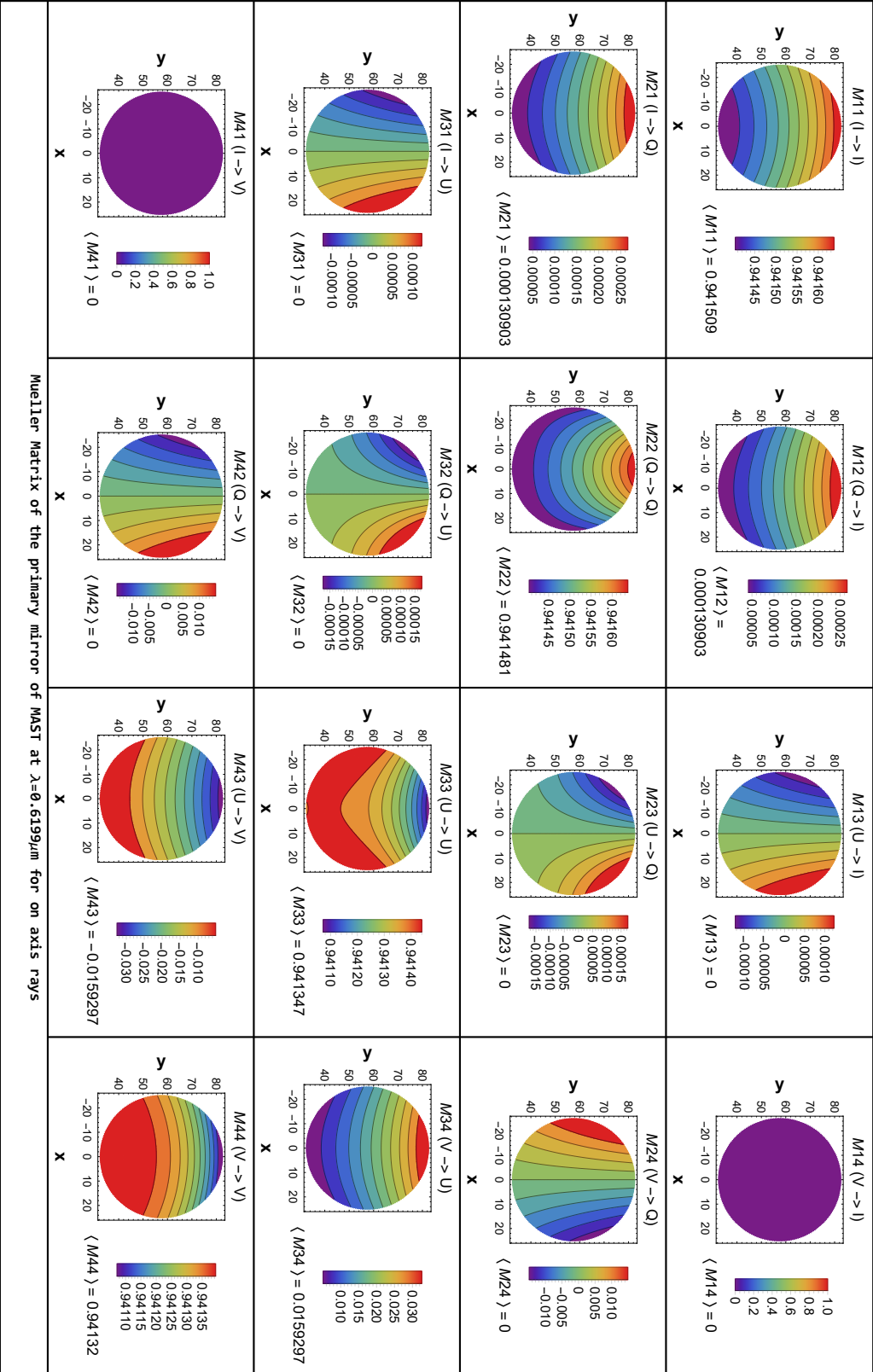
Figure 7.10: The contour plot of the Mueller matrix of the primary mirror of MAST

$$M_{Sec} = \begin{pmatrix} 1 & 0.000139 & 0 & 0 \\ 0.000139 & 0.99 & 0 & 0 \\ 0 & 0 & 0.999 & 0.01691 \\ 0 & 0 & -0.01691 & 0.999 \end{pmatrix} \quad (7.10)$$

The resultant Mueller matrix for the primary and secondary mirror, $M2M1$ is given as

$$M2M1 = \begin{pmatrix} 1 & 0.00027 & 0 & 0 \\ 0.00027 & 0.99 & 0 & 0 \\ 0 & 0 & 0.999 & 0.0338 \\ 0 & 0 & -0.0338 & 0.999 \end{pmatrix} \quad (7.11)$$

The coating on the primary mirror during the winter observations had deteriorated due to aging as shown in Figure 7.11. It was re-coated before the observations in May. The new coating for the primary and secondary mirror was protective Aluminum (MgF2+Aluminum). The Mueller matrix $M2M1$ for the MgF2 (thickness of 90 nm)+Aluminum is

$$M2M1 = \begin{pmatrix} 1 & 0.000399 & 0 & 0 \\ 0.000399 & 0.99 & 0 & 0 \\ 0 & 0 & 0.999 & 0.0177 \\ 0 & 0 & -0.01777 & 0.999 \end{pmatrix} \quad (7.12)$$

7.3.2 Mueller matrices for the inclined mirrors M3-M6 and derotator system

The incident angles on the inclined mirrors M3-M6 are :

M3=45°, M4=-16.485°, M5=61.845°, and M6=-45°.

The three mirrors in the derotator system have incident angles:

Dm1=60°, Dm2=-30°, and Dm3=60°,

The Mueller matrices for these mirrors can be estimated using the reflection coefficients as given in Chapter 3. The coating used in the mirrors was SiO_2

Figure 7.11: The coating degradation on the primary mirror during winter observations.

(n=1.455) + Silver (n+ik=0.135-3.88i) for both the sets of observations.

7.3.3 Response Matrix of the instrument

The polarization calibration unit consisting of a quarter waveplate (QWP) and a Glan Thompson polarizer is placed between the focusing lens and FM1. The response matrix (X) is determined by giving 35 known input polarization states by the rotation of the QWP from 24° to 374° in steps of 10°. The intensities are measured by the polarimeter for all these input states using six step modulation scheme. The response matrix is obtained by the method explained in Tiwary et al. (2017).

$$S_{meas} = X.S_{in}; \quad S_{meas}.S_{in}^T = X.S_{in}S_{in}^T = X.D \tag{7.13}$$

$$X = S_{meas}.S_{in}D^{-1} \tag{7.14}$$

Figure 7.12 shows demodulated Stokes parameters along with the input and measured estimated at each position of the QWP. The response matrix is estimated using these parameters as

$$
X = \begin{pmatrix}
1 & 0.0621 & 0.00323 & 0.0614 \\
2.5 \times 10^{-07} & 0.7519 & -0.1150 & -0.1942 \\
2.2 \times 10^{-08} & 0.1891 & 0.7661 & 0.1539 \\
4 \times 10^{-08} & 0.08679 & 0.1441 & 0.7212
\end{pmatrix}
\tag{7.15}
$$

The Mueller matrices calculated in the previous sections are used to estimate
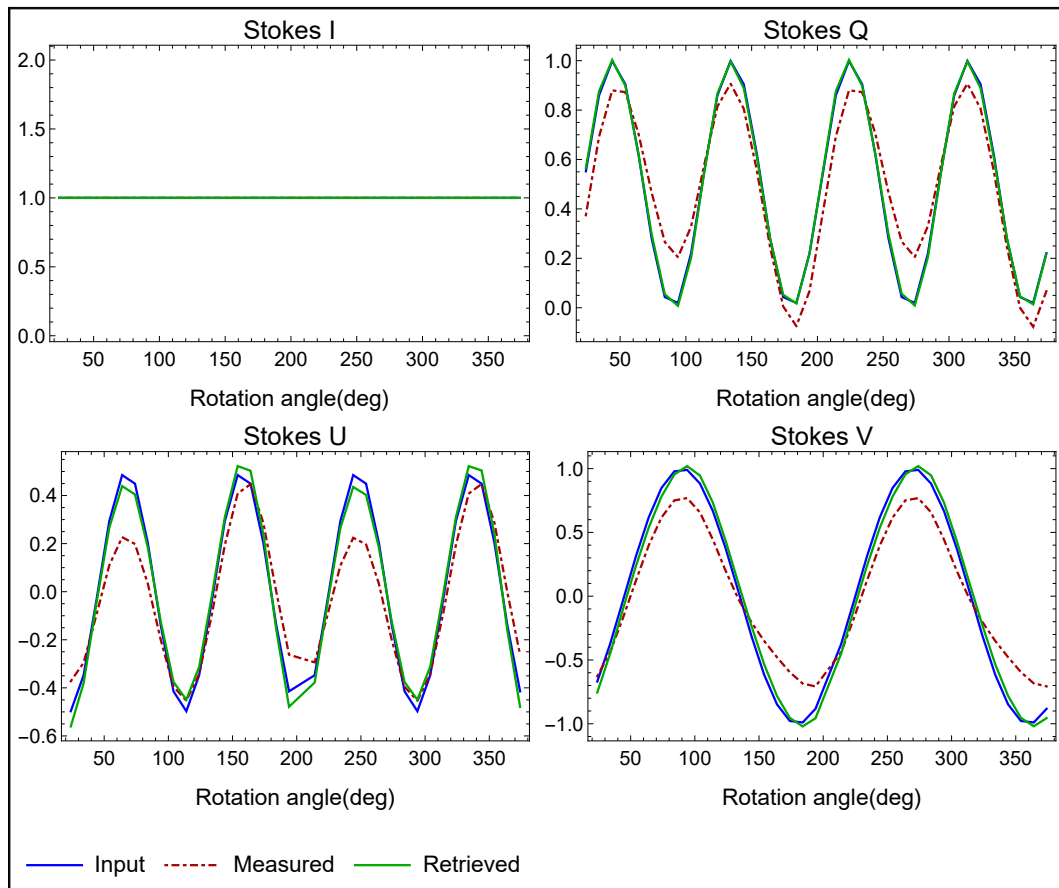
Figure 7.12: Plots of input, measured and retrieved Stokes parameters

the final Mueller matrix M_{total} and compared with the observations obtained for different input polarizations explained in the next section.

7.4 Polarimeter at the telescope focus

The routine polarization observations were obtained by the polarimeter placed after several optical components from M6 (shown in Figure 7.3). Though the response matrix can be determined for the optical layout, increasing the number of optical components increases the uncertainty in the Mueller matrix of the telescope. To measure the Stokes parameters just after the M6 mirror, a polarimeter was placed in the converging beam from the focusing lens (before FM1 in Figure 7.3). Two LCVRs were characterized to estimate the required voltages and corresponding retardance for the four-step modulation scheme (Time cadence will be higher). These observations were obtained for unpolarized and linearly polarized light at two wavelengths (6173 and 5303 Å).

7.4.1 Characterization of LCVR

The experimental setup for the characterization of LCVR is shown in Figure 7.13. A DC lamp along with a diffuser is used as the light source to obtain the uniform illumination. The light from the pinhole is collimated by lens L1. The polarizer P1 is mounted on a computer controlled rotation stage to obtain crossed and parallel positions with polarizer, P2. The fast axis of the LCVR is kept at 45° retards the light from P1. The Lens L2 images the light from P2 onto the CCD placed after the narrow-band filters. The voltage is
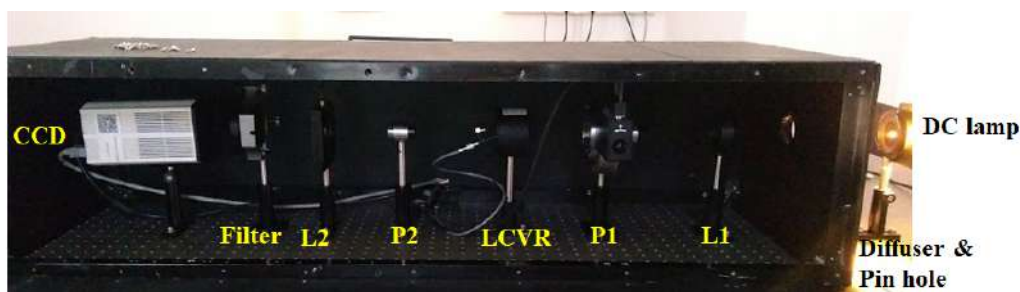
Figure 7.13: Experimental setup for the characterization of LCVR. L1 and L2 correspond to the collimating and imaging lens respectively. P1 and P2 are the Glan Thompson Polarizing Prisms with extinction ratio of 10^{-6}

applied to the LCVR in steps of 40 mV starting from 0 to 10 V. The P1 and

P2 are placed in the parallel and crossed configurations and the corresponding intensities, (I_{0^o}) and (I_{90^o}) are measured. The intensities obtained are used to calculate the retardance of the LCVR using the relation (Tiwary et al., 2017),

$$\delta = \arccos \frac{I_{0^o} - I_{90^o}}{I_{0^o} + I_{90^o}} \tag{7.16}$$

The variation of retardance of the LCVR with voltages for the wavelengths, 6173 and 5303 Å are shown in Figure 7.14. The voltages corresponding to the retardance required for the four-step modulation scheme is obtained from these plots. The four-step modulation scheme developed by Martinez Pillet et al. (2004) was used with different combinations of the retardance values as given in Table 7.4. The polarimeter at the telescope focus is shown in Figure 7.15.
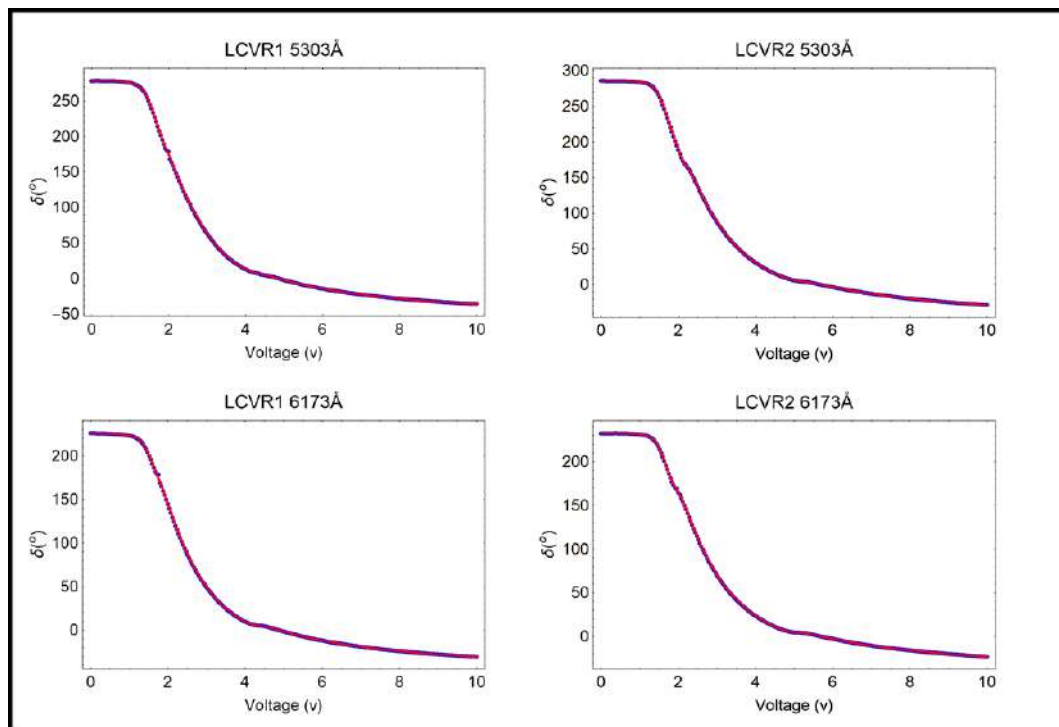
Figure 7.14: Voltage vs retardance plots for 5303 and 6173 Å.Voltages corresponding to the retardance used in the four step modulation scheme is obtained from these plots.

The filters were moved using a computer controlled movable linear stage. The Stokes parameters are measured for unpolarized and linearly polarized light as input.

Measured Intenstity I_{meas}	LCVR1 ($\delta°$)	5303Å (v)	6173Å (v)	LCVR2 ($\delta°$)	5303 Å (v)	6173 Å (v)
$I + \frac{1}{\sqrt{3}}(Q + U + V)$	45	3.26	3.08	54.7	3.48	3.25
$I + \frac{1}{\sqrt{3}}(Q - U - V)$	135	2.3	2.08	125	2.61	2.38
$I + \frac{1}{\sqrt{3}}(-Q - U + V)$	135	2.3	2.08	235	1.71	1.18
$I + \frac{1}{\sqrt{3}}(-Q + U - V)$	225	1.66	0.94	54.7	3.48	3.25

Table 7.4: Voltages estimated for four step modulation scheme
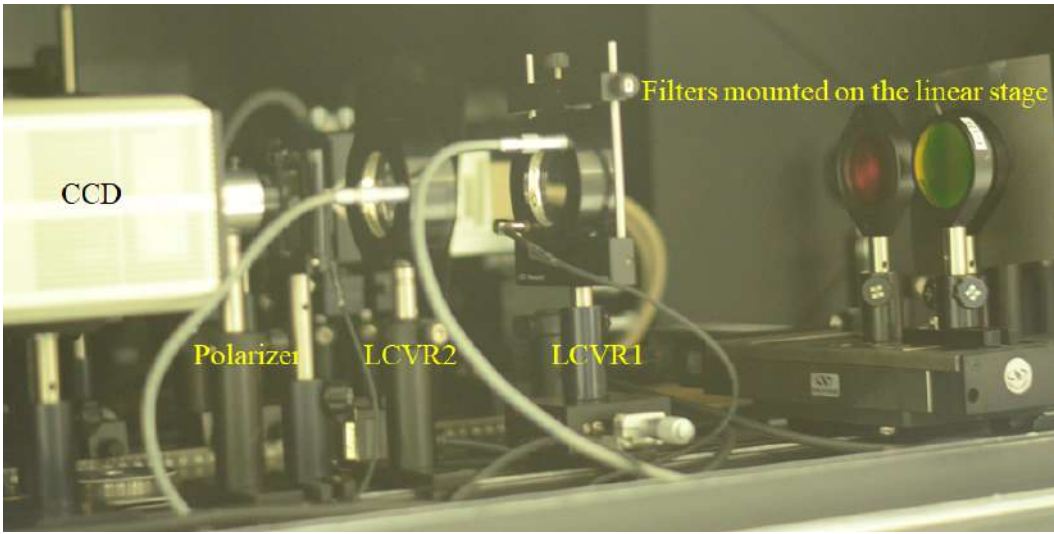
Figure 7.15: The polarimeter placed at the telescope focus after the M6 mirror

7.5 Comparison of Analytical model and observations

The refractive index of the Silver at 6173 Å is found to be 0.1310-3.88i and SiO$_2$ is 1.455. The thickness of the protective coating, which places an important role in altering the phase component of the electric field vector, is not known. The polarization observations obtained at the telescope focus for the unpolarized light (input) was compared with the analytical model by varying the thickness parameter (10 nm to 110 nm). The thickness of the SiO$_2$ calculated by χ-square minimization technique is 85±20 nm.

7.5.1 Results at the telescope focus

The instrumental polarization at the telescope focus is shown in Figure 7.16. The observations were obtained on Jan 19, 2018, throughout the day. The model agrees with the observations with the χ-square values in Q, U, and, V of 0.5215, 0.9807 and 0.1082 respectively. The Stokes parameters obtained for
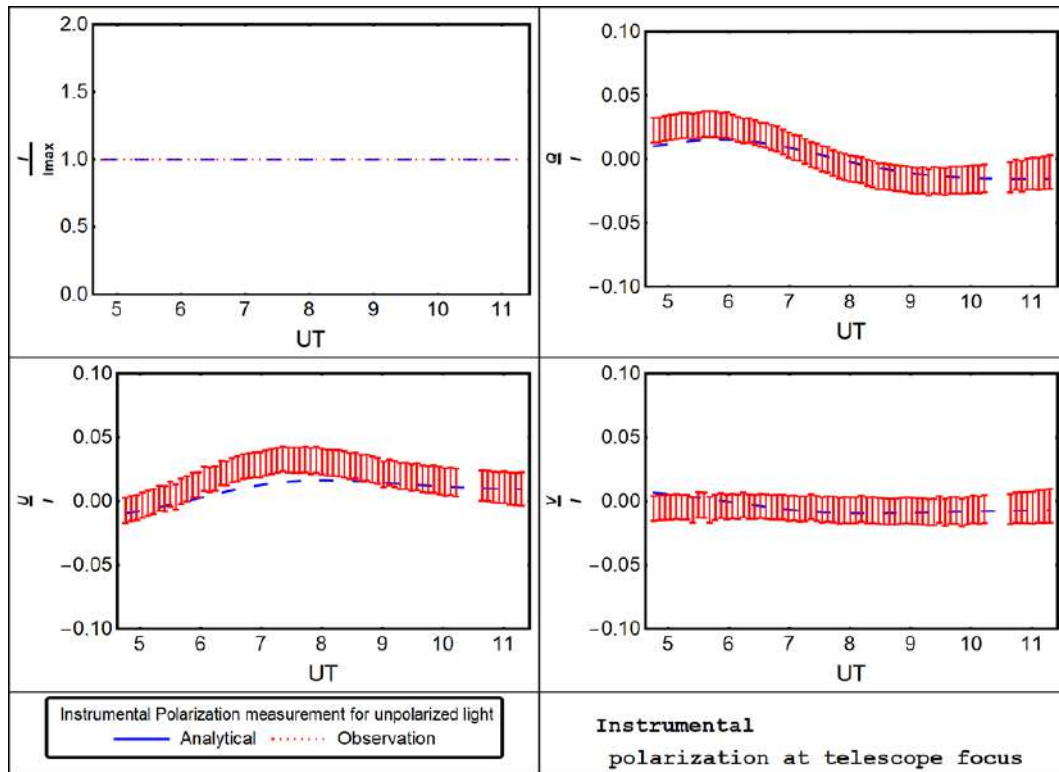
Figure 7.16: The instrumental polarization estimated by the analytical model compared with the observations at the telescope focus at λ =6173 Å

instrumental and linear polarization as input is shown in Figure 7.17 for two different wavelengths, 5303.3 Å and 6173.3 Å at the telescope focus. In the case of instrumental polarization, V deceases with λ whereas, in the case of Q and U, an increase is seen. This behavior is opposite to what is observed in the model and has to be investigated further. For linear polarization as input, V reduces with λ, and $Q^2 + U^2$ increases with the λ which is obtained in the case of the model as well.
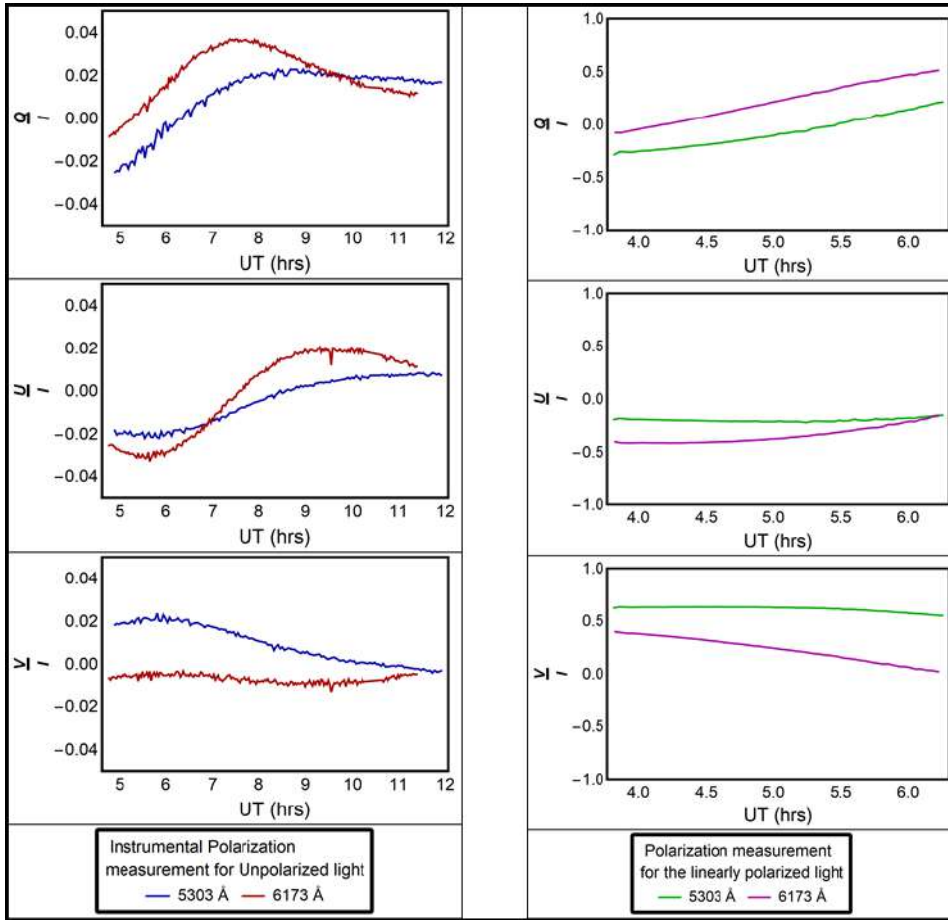
Figure 7.17: The instrumental polarization and linear polarization measured at the telescope focus at $\lambda = 5303$ Å and 6173 Å

7.5.2 Results at the 6173 Å channel imaging spectropolarimeter

The two sets of observation taken during the winter (Jan 2018) and summer (May 2018) are compared with the analytical model as shown in Figures 7.19 and 7.18. In the case of summer, the Stokes parameters corresponding to the vertically polarized and unpolarized light were measured. The model is found to follow the observations with some deviations. The variation is seen in Q and U at 7.00 UT is due to the telescope's azimuth and derotator angle which is reproduced by the model. During winter observations, the Stokes parameters are varying slowly with time as the maximum elevation of the telescope is 44°. The comparison of the model and observations have been done without using the response matrix to investigate the telescope model further. However, the

deviations noted between model and the observations can be attributed to two uncertainties such as

1. Ageing and dust deposition: The real and imaginary part of the refractive index used in the model were obtained from Palik (1998), measured under the controlled laboratory conditions. As the mirrors in the telescope have aged for a period of five years, there would deposition of dust and decay of the coating which alters the refractive index.

2. Response matrix: The errors in the elements of the response matrix has not been considered in our analysis which would alter the Mueller matrix, M_{inst}.
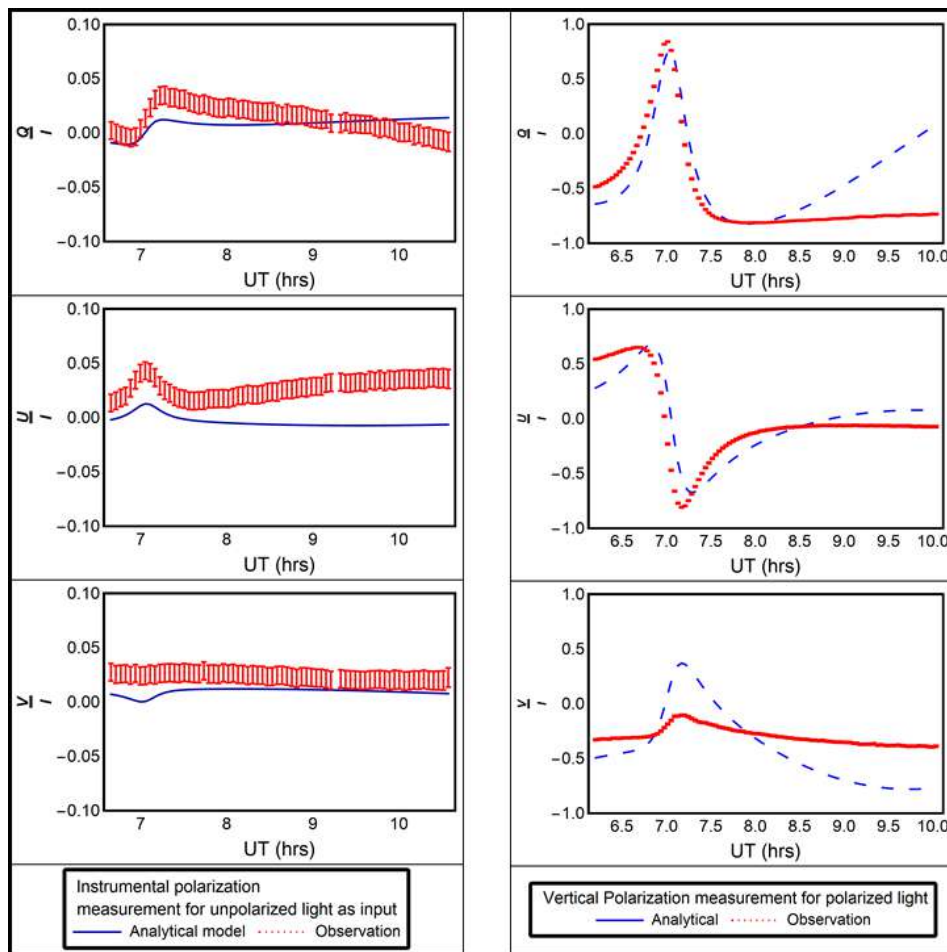
Figure 7.18: Comparison of model and observations for different input polarized light during summer.
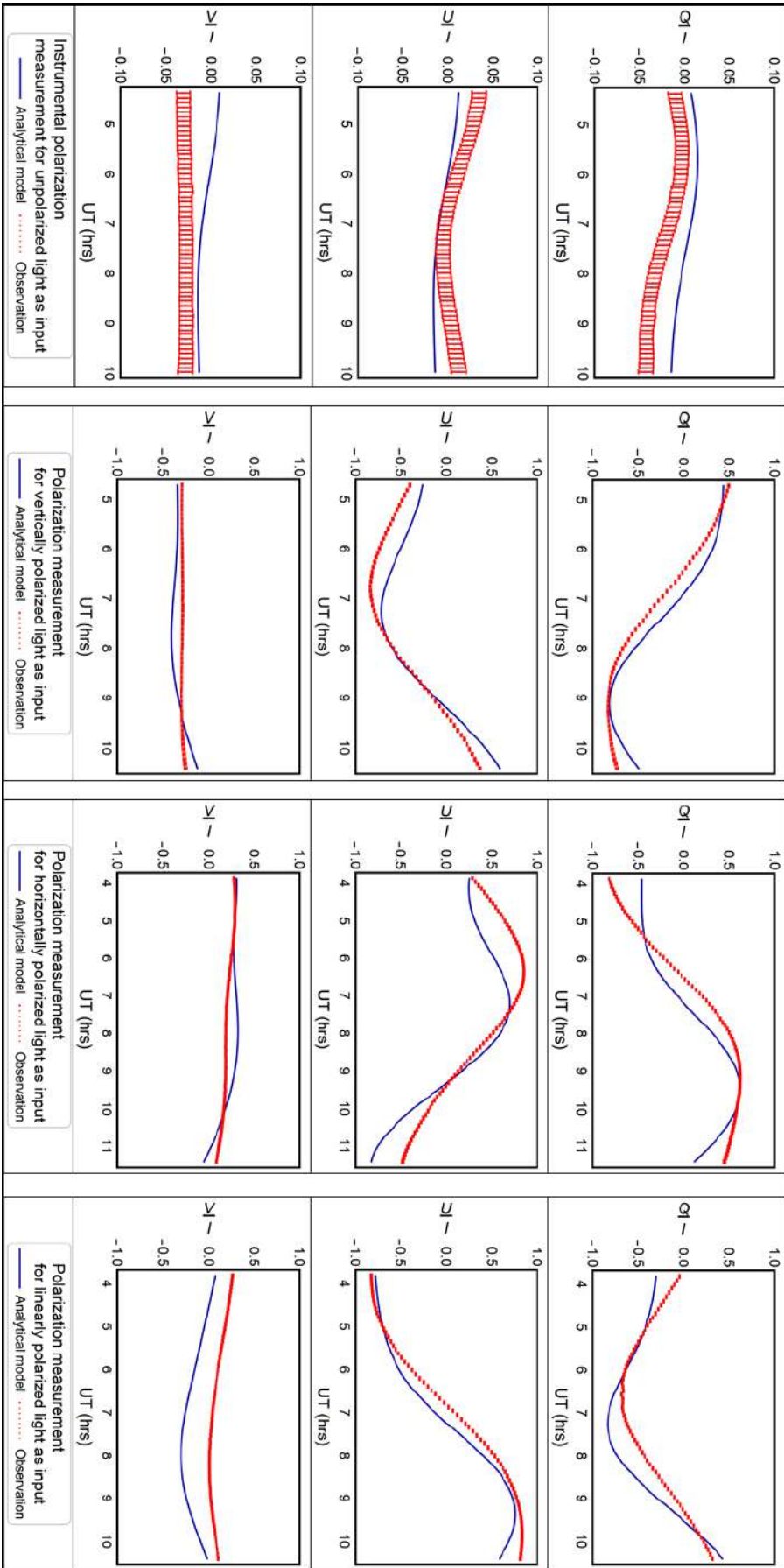
Figure 7.19: Comparison of model and observations for different input polarized light during winter.

7.6 Discussions

An analytical polarization model is developed for the Multi-Application Solar Telescope in Udaipur Solar Observatory. The polarization observations were obtained using the imaging spectropolarimeter available at the telescope for the 6173 Å channel.The two sets of observations were compared with the model and a fairly good match is seen. An imaging polarimeter placed at the telescope focus to understand the wavelength dependence of the Stokes parameters. The observations were obtained in 5303 Å and 6173 Å. The χ-square minimization carried out for the unpolarized light observations obtained at the telescope focus gave the thickness of SiO_2 to be 85 $\pm$20 nm. To reduce the deviations between the model and the observations, the exact value of the refractive indices and coating parameters are required. The errors in the elements of response matrix have to be considered. A sensitivity analysis would be performed with the response matrix to ascertain it's effect on the observed Stokes parameters. The refractive index measurement will be obtained in future during the re-coating of the mirrors and will be included in the model.

Chapter 8

Summary and Future Work

Ramya M. Anche, Chris Packham, G. C. Anupama, K. Sankarasubramanian, Maheswar Gopinathan, and Manoj Puravankara, In Proc. of SPIE, vol. 10702, pp. 1070298-1, 2018.

8.1   Summary

Polarimetry has played a major role in the development of modern astronomy as it provides insight into various physical processes that occur in objects, ranging from planets in the solar system to high-redshift galaxies. It has the potential to expand the discovery space of the exoplanets (from older giant planets to rocky planets) with next-generation telescopes such as the European Large Telescope, the Thirty Meter Telescope, and the Giant Magellan Telescope. Polarimetric capability will be an important add-on to the imaging or spectroscopic instruments designed for these next generation telescopes. A potential problem in achieving accurate polarimetric measurements in these telescopes is that the polarization changes (IP and cross-talk) caused due to oblique reflections. However, these problems can be dealt by developing a polarization ray tracing model of the telescope and mitigating them during the design and development of the polarimeter. Astronomers would be at loss if

a complete information is not extracted from the light collected by the large telescopes due to the absence of an efficient polarimeter.

The two significant novel aspects of this thesis are:

1. Development of a polarization model for the Thirty Meter Telescope and estimation of the impact of segment configuration on the polarization model.

2. Development and verification of an analytical polarization model for the existing 0.5 m solar telescope.

The thesis began with the motivation to understand and estimate the polarization effects for one the next generation telescopes, the Thirty Meter Telescope (TMT). A list of science cases collected by the Polarimetry Modelling Team (PMT) of TMT, specified the requirements on instrumental polarization, cross-talk, and depolarization. The level of polarization observed in these astronomical sources (specified in science cases) range from 0.1% to 10%.

The polarization effects from a telescope are estimated prior to the design of the polarimeter using various modeling techniques. An analytical polarization ray tracing algorithm was developed to estimate the IP, CT, and DP for the TMT telescope. The model estimates an instrumental polarization of 1.26% and a cross-talk of 44% at the Nasmyth focus of the telescope at the wavelength of 0.6 μm at field angle zero with the telescope pointing zenith. The Mueller matrices were estimated at all the instrument ports of the TMT as well. The dependence of the matrix elements on the wavelength, telescope field of view and zenith angle was determined. The polarization effects can be mitigated by incorporating a polarization compensating mirror in future polarimetric instrument for the TMT. The Mueller matrices estimated using the compensating mirror give IP as low is 10^{-3} and CT as 1% for the field of view of 1'. The primary mirror of TMT and other future generation large telescopes is made of a large number of segments (either hexagonal or circular). The impact of these segments on the previously estimated Mueller matrices were also determined.

With reference to the non-polarimetric instruments at TMT, the polarization induced aberrations were calculated to ascertain its impact on the high-

contrast imaging and adaptive optics system. The coating induced aberrations estimated for TMT are tilt, astigmatism, defocus, and chromatic aberration given in Chapter 5. They further give rise to the ghost PSF affecting the achievable contrast in imaging of exoplanets and protoplanetary disks. The ghost PSF also makes the final PSF slightly elliptical which can have an effect on science cases that require high-contrast, such as detection of exoplanets.

The analytical polarization model developed for TMT includes assumptions regarding the refractive index, and the effect of environmental conditions on the mirror coating (oxidation, ageing, dust deposition). To understand the discrepancies between the model and the observations, the polarization model was developed for the largest solar telescope in India, MAST. The polarization observations were obtained using the imaging spectro-polarimeter operating at the telescope. Our analysis shows that the model follows well with the observed values with some deviations (as the values of the refractive index and thickness of the coating were not available). It is expected that, using the exact values of the refractive index and the thickness of the coating will bring down the deviations. The model will be used to remove the instrumental polarization and cross-talk from the observed data to estimate the values of the photospheric vector magnetic field of the sun in the future.

For understanding the science requirements, as a case study, polarimetric properties of a few nova systems are studied. (Polarization observations of transient objects is one of the science cases collected by PMT.)
The observations were obtained using the imaging and photopolarimeters at the Cassegrain focus of 1-2 m class telescopes, as described in Chapter 2. The level of observed polarization in the observed novae varies from 0.4% to 2% due to the asymmetry/dust grains in the ejecta. In one of the systems, the observed polarization of 5% was mostly arising from the interstellar dust (see Chapter 2). The IP estimated using the observations of the unpolarized standard star was found to be 0.1% ($\frac{1}{10}$ of the polarization values for novae) and ignored during the analysis of novae data.

8.2   Future Work

8.2.1   Second-generation instruments for TMT with polarimetric capability

Out of the proposed eight second generation instruments for TMT, two (PSI and MICHI [1]) instruments might have polarimetric capability. Planet System Instrument (PSI) is a high contrast imaging and spectroscopic instrument with polarimetric capability. It is proposed to operate in the wavelength range of 0.6-5.3 μm and expected to achieve a contrast of 10^{-8}. MICHI named Mid-Infrared Camera, High-disperser, and Integral field unit (MICHI) for TMT will have the polarimetry capability along with low/ high-resolution spectrometer and the imager. It is proposed to operate in the thermal infrared wavelength region, 3-14 μm (-25 μm to be confirmed). Here, we discuss the future design concepts related to MICHI.

8.2.2   Instrumental polarization and crosstalk for the MICHI instrument

The science cases/drivers and the instrument specifications for MICHI have been discussed by Okamoto et al. (2010); Packham et al. (2012). The preliminary design concepts of the instrument have been presented in Tokunaga et al. (2010). The proposed polarimeter is a half wave plate (HWP) and Wollaston prism-based system which can be operated in both imaging and spectro-polarimetric mode in the N band (7.3-13.8μm) and may be extended to the Q band in the future. The optical layout of the MICHI imager is shown in Figure 8.1 consists of 15 optical surfaces. As a first step, we estimate the polarization effects in thermal-infrared wavelengths at the polarimetry module (HWP+Wollaston prism) and focus of the MICHI.

The unprotected gold coating (widely used in the infrared wavelength re-

---

[1]https://www.tmt.org/page/second-generation-instruments
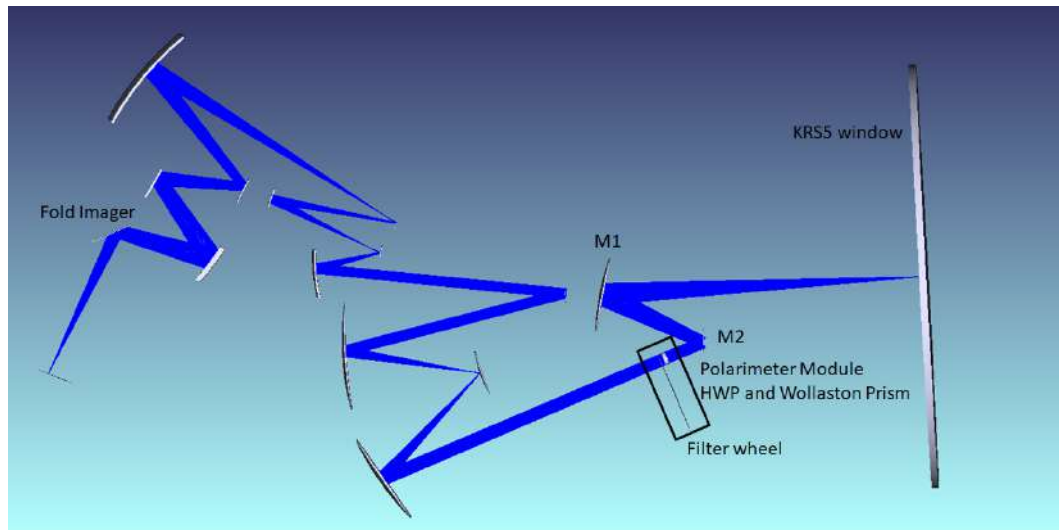
Figure 8.1: The optical layout of the MICHI imager obtained in Zemax®. The polarimetry module shows the position of the modulator and the polarizer.

gions owing to its high reflectivity) is considered for all the mirrors in MICHI. The refractive index for the gold is obtained from Handbook of optical constants of solids (Palik, 1998). Figures 8.2 and 8.3 show the variation IP and CT with zenith angle, at the polarimeter module and the focus of the imager. The maximum value of the IP and CT are found to be 0.8% and 3.6% at the modulator (HWP). The IP and CT are 2.4% and 10% respectively, at the focus of the imager.
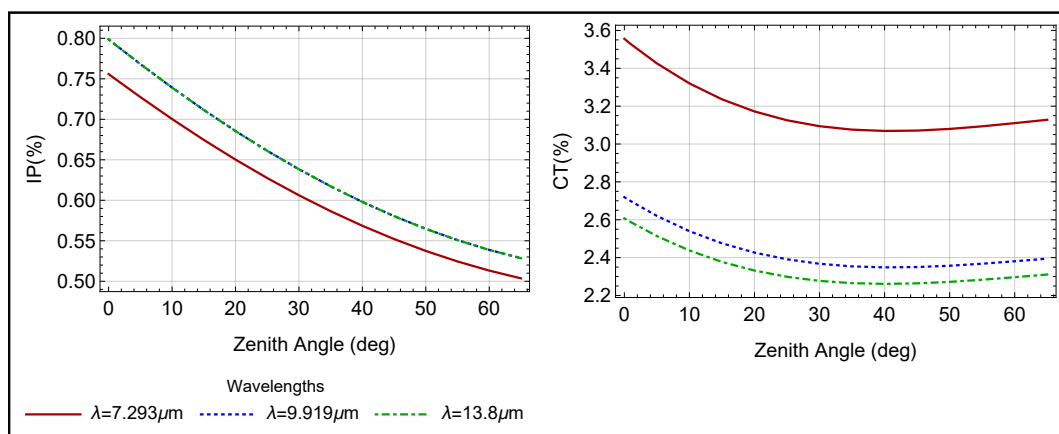
Figure 8.2: The IP and CT estimated at the modulator with varying zenith angle. The unprotected gold coating is used for the mirrors in the MICHI instrument.The values are shown at three different wavelengths in the N band.
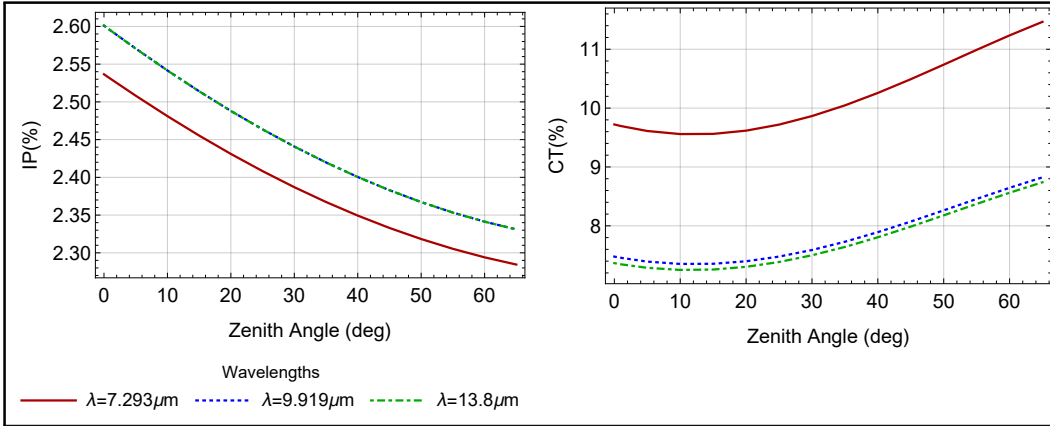
Figure 8.3: The IP and CT estimated at the focus of the imager with varying zenith angle. The unprotected gold coating is used for the mirrors in the MICHI instrument.The values are shown at three different wavelengths in the N band.

8.2.3 Challenges in the design of MICHI

The polarization effects for MICHI have been evaluated for wavelengths in the N-band. The refractive index of silver is not available in Palik (1998) beyond 9.919 μm. The extrapolation of the refractive index data may not yield accurate results. The polarization effects will be estimated in Q band, if the wavelength of operation of MICHI extends beyond 14 μm. A further step is to design and development of the polarimeter module. A monolith Wollaston prism of size greater than 50 cm is not readily available in the infrared wavelength region. Hence, a mosaics of two or three Wollaston prisms will have to be designed and analyzed. The second step will be towards the preparation and development of the calibration strategies for the polarimeter. Even though the instrumental polarization from the telescope in the thermal infrared wavelength region is found to be less than that of the optical, it is not completely polarization free. Along with the telescope, the other optical components in the polarimeter would introduce further errors which makes it very essential for developing a calibration strategy. The non-ideal effects from the telescope and instrument such as misalignment of the polarizer, retardance offset, and detector non-linearity will be considered. The mitigation could be also achieved by using a spatially varying retarder. They can be designed and tested for MICHI to cancel the polarization effects.

8.3   Application of the polarization model to other telescopes

The polarization model developed here can be applied to any other future telescopes for estimating the polarization effects without major modification. The Extremely Large Telescope (ELT) (39 m in diameter), which is going to be built in Chile consists of 798 hexagonal segments in the primary mirror. The analysis carried out for the segmented primary of the TMT could be applied to estimate the polarization effects for the ELT. Similarly, the polarization aberrations can also be estimated for ELT to know the magnitude of the ghost PSF and the achievable contrast in the high contrast imaging instruments.

Another large telescope, the Giant Magellan Telescope (GMT) has a primary of 24.5 m in diameter with seven aspheric circular segments, each of them having a diameter of 8.4 m. Currently, none of the first generation instruments for GMT has the polarimetric capability. The gaps in the primary mirror can be included in our model to estimate the polarization effects. The presence of these gaps will give rise to residual components of instrumental polarization and crosstalk in the primary mirror itself (the incoherent addition will not cancel the rays missed in the gaps). This affects not only in the polarization measurements but also in high-resolution imaging instruments which are designed to expand the discovery space of the exoplanets.

India is planning to construct two large telescopes in the next decade, the National Large Solar Telescope (NLST) and National Large Optical Telescope (NLOT). The NLST is a proposed ground-based 2-m class optical and near infra-red (IR) solar telescope with spectro-polarimeter as one of its back-end instruments. NLOT is a proposed 10 m large segmented mirror telescope with a Nasmyth platform. Polarimetric model has to be developed for both of these telescopes prior to the design of their science instruments. This thesis has certainly provided a methodology to carry out the same.

References

Anche, Ramya., Skidmore, Warren., Reddy, Krishna., and Anupama, G. C., 2015, *TMT internal document*, TMT.PSC.TEC.15.007.REL01

Anupama, G. C., Kamath, U. S., Ramaprakash, A. N., et al. 2013, *Astron. Astrophys.*, 559, A121

Anupama, G. C. 1992, *Pub. Astron. Soc. Pac.*, 104, 308

Anupama, G. C. 2008, *RS Ophiuchi (2006) and the Recurrent Nova Phenomenon*, 401, 31

Atwood, J., Byrnes, P., & Herriot, G. 2009, *Proceedings SPIE*, 7439, 74390G

Atwood, J., Skidmore, W., Anupama, G. C., et al. 2014, *Proceedings SPIE*, 9150, 915013

Baffes, C., Mast, T., Nelson, J., et al. 2008, *Proceedings SPIE*, 7018, 70180S

Beck, C., Schlichenmaier, R., Collados, M., Bellot Rubio, L., & Kentischer, T. 2005, *Astron. Astrophys.*, 443, 1047

Blitzstein, W., Bradstreet, D. H., Hrivnak, B. J., et al. 1980, *Pub. Astron. Soc. Pac.*, 92, 338

Bode, M. F., & Evans, A. 2008, *Classical Novae, 2nd Edition. Edited by M.F. Bode and A. Evans. Cambridge Astrophysics Series, No. 43, Cambridge: Cambridge University Press*, 43

Breckinridge, J. B., Lam, W. S. T., & Chipman, R. A. 2015, *Pub. Astron. Soc. Pac.*, 127, 445

Chipman, R. A., & Chipman, L. J. 1989, *Optical Engineering*, 28, 100

Chipman, Russell A and Lam, Wai Sze Tiffany and Breckinridge, James. 2015, *Proceedings SPIE*, 9613, 96130H

Chipman, Russell Atwood 1987, *The University of Arizona.*

Chipman, R. A. 1988, *LEST Foundation, Technical Report*, 36, 23

Chipman, R. A. 1989, *Optical Engineering*, 28, 90

Chipman, Russell A 1995, *J. Optic. Eng.*, 1636–1646

Chipman, Russell A 2010, *International Optical Design Conference, IWA4*

Chomiuk, L., Nelson, T., Mukai, K., et al. 2014, *Astrophys. J.*, 788, 130

Clark, N., & Breckinridge, J. B. 2011, *Proceedings SPIE*, 8146, 81460O

Clarke, D., Smith, R. A., & Yudin, R. V. 1998, *Astron. Astrophys.*, 336, 604

Clarke, D. 1964, *The Observatory*, 84, 28

Clarke, David 2009, *John Wiley & Sons*

Collett, Edward 1992, *Optical Engineering.*

Cox, L. J. 1976, *Mon. Not. Roy. Astron. Soc.*, 176, 525

Cropper, M. 1990, *Mon. Not. Roy. Astron. Soc.*, 243, 144

de Juan Ovelar, M., Diamantopoulou, S., Roelfsema, R., et al. 2012, *Proceedings SPIE*, 8449, 844912

de Juan Ovelar, M., Snik, F., Keller, C. U., & Venema, L. 2014, *Astron. Astrophys.*, 562, A8

Denis, S., Coucke, P., Gabriel, E., Delrez, C., & Venkatakrishnan, P. 2008, *Proceedings SPIE*, 7012, 701235

Denis, S., Coucke, P., Gabriel, E., Delrez, C., & Venkatakrishnan, P. 2010, *Proceedings SPIE*, 7733, 773335

Di Varano, I., Woche, M., Strassmeier, K. G., et al. 2018, *Advances in Optical and Mechanical Technologies for Telescopes and Instrumentation III*, 10706, 107061Y

Eggen, O. J., Mathewson, D. S., & Serkowski, K. 1967, *Nature*, 213, 1216

Evans, A., Yudin, R. V., Naylor, T., Ringwald, F. A., & Koch Miramond, L. 2002, *Astron. Astrophys.*, 384, 504

Evans, A., Gehrz, R. D., Helton, L. A., et al. 2012, *Mon. Not. Roy. Astron. Soc.*, 424, L69

Fujiwara, Hiroyuki 2007, *John Wiley & Sons*

Fukagawa, M., Tamura, M., Itoh, Y., et al. 2006, *Astrophys. J. Lett.*, 636, L153

Gehrels, T. 1974, *Planets, Stars and Nebulae Studied with Photopolarimetry by T. Gehrels. University of Arizona Press,* 1974. ISBN: 978-0-8165-0428-2

Goldstein, Dennis H 2003, *CRC press*

Goswami, A., & Karinkuzhi, D. 2013, *Astron. Astrophys.*, 549, A68

Goswami, A., Kartha, S. S., & Sen, A. K. 2010, *Astrophys. J. Lett.*, 722, L90

Grigorian, V. A., and Vardanian, R. A. 1951, *Soobsh. Byurakan Observatory* 29, 39-48

Harvey, E. J., Redman, M. P., Darnley, M. J., et al. 2018, *Astron. Astrophys.*, 611

Heiles, C. 2000, *Astron. J.*, 119, 923

Herriot, G., Andersen, D., Atwood, J., et al. 2012, *Proceedings SPIE*, 8447, 84471M

Hough, J. 2006, *Astronomy and Geophysics*, 47, 3.31

Ichimoto, K., Lites, B., Elmore, D., et al. 2008, *Solar Phys.*, 249, 233

Ikeda, Y., Kawabata, K. S., & Akitaya, H. 2000, *Astron. Astrophys.*, 355, 256

Jones, R Clark 1941, *Journal of Optical Society of America*, 31,488

Joos, F., Buenzli, E., Schmid, H. M., & Thalmann, C. 2008, *Proceedings SPIE*, 7016, 70161I

Keller, C. U. 2002, *Astrophysical Spectropolarimetry*, 303

Keller, C. U. 2006, *Proceedings SPIE*, 6269, 62690T

Kerley, D., Smith, M., Dunn, J., et al. 2016, *Proceedings SPIE*, 9913, 99134J

Kimura, Wayne D 2017, *Morgan & Claypool Publishers*

Kiyohara, J., Ueno, S., Kitai, R., et al. 2004, *Proceedings SPIE*, 5492, 1778

Knowlden, Robert Edward 1981, *The University of Arizona.*

Landstreet, J. D. 1992, *Astron. Astrophys. Rev.*, 4, 35

Leroy, J.-L. 2000, Polarization of light and astronomical observation, by Jean-Louis Leroy. Amsterdam : Gordon / Breach Science, c2000. / (Advances in astronomy and astrophysics ; v.4)

Linford, J. D., Chomiuk, L., Nelson, T., et al. 2017, *Astrophys. J.*, 842, 73

Macleod, H Angus 2010, *CRC press*

Martinez Pillet, V., Bonet, J. A., Collados, M. V., et al. 2004, *Proceedings SPIE*, 5487, 1152

Mast, T.,and Nelson, J 2004, *TMT internal communications document*, TMT report no 58.

Mathew, S. K., Bayanna, A. R., Tiwary, A. R., Bireddy, R., & Venkatakrishnan, P. 2017, *Solar Phys.*, 292, 106

McClain, Stephen C and Hillman, Lloyd W and Chipman, Russell A 1993, *Journal of optical society of America*, 2371–2382

McGuire, J. P., Jr., & Chipman, R. A. 1988, *LEST Foundation, Technical Report*, 36, 7

McGuire, J. P., Jr., & Chipman, R. A. 1989, *Optical Engineering*, 28, 141

Metz, K. 1989, *Information Bulletin on Variable Stars*, 3385, 1

Morris, P. J., Cotter, G., Brown, A. M., & Chadwick, P. M. 2017, *Mon. Not. Roy. Astron. Soc.*, 465, 1218

Mueller, Hans 1948, *Journal of optical society of America*, 38,661

Munari, U., Hambsch, F.-J., & Frigo, A. 2017, *Mon. Not. Roy. Astron. Soc.*, 469, 4341

Okamoto, Y. K., Packham, C., Tokunaga, A., et al. 2010, *Proceedings SPIE*, 7735, 77355O

Okazaki, A., Kurihara, J., Hirata, H., et al. 1996, *Polarimetry of the Interstellar Medium*, 97, 178

Packham, C., Honda, M., Richter, M., et al. 2012, *Proceedings SPIE*, 8446, 84467G

Palik, Edward D 1998, *Academic press*

Pavana, M., Anche, R. M, Anupama, G. C., Ramaprakash, A. N., & Selvakumar, G. 2019, *arXiv:1901.00404*

Piirola, V., & Korhonen, T. 1979, *Astron. Astrophys.*, 79, 254

Raja Bayanna, A., Mathew, S. K., Venkatakrishnan, P., & Srivastava, N. 2014, *Solar Phys.*, 289, 4007

Ramaprakash, A. N., Gupta, R., Sen, A. K., & Tandon, S. N. 1998, *Astron. Astrophys. Suppl.*, 128, 369

Ranganathan, M., Sankarasubramanian, K., Bayanna, A. R., & Mathew, S. K. 2018, *Astrophys. J.*, 867, 77

Raveendran, A. V., Srinivasulu, G., Muneer, S., et al. 2015, *arXiv:1506.08252*

Reiley, Daniel J and Chipman, Russell A 1992, *Polarization Analysis and Measurement*, 1746, 139–147

Roelfsema, R., Bazzon, A., Schmid, H. M., et al. 2016, *Proceedings SPIE*, 9909, 990927

Sanchez Almeida, J., Martinez Pillet, V., & Wittmann, A. D. 1991, *Solar Phys.*, 134, 1

Sanchez Almeida, J., & Martinez Pillet, V. 1992, *Astron. Astrophys.*, 260, 543

Sanders, G. H. 2013, Journal of Astrophysics and Astronomy, 34, 81

Sankarasubramanian, K., Samson, J. P. A., & Venkatakrishnan, P. 1999, *Polarization*, 243, 313

Schaefer, B. E., Landolt, A. U., Linnolt, M., et al. 2013, *Astrophys. J.*, 773, 55

Schou, J., Borrero, J. M., Norton, A. A., et al. 2012, *Solar Phys.*, 275, 327

Seach, J. 2015, *Central Bureau Electronic Telegrams*, 4080, 1

Sen, A. K., & Kakati, M. 1997, *Astron. Astrophys. Suppl.*, 126, 113

Srinivasulu, G., Raveendran, A. V., Muneer, S., et al. 2015, *arXiv:1505.04244*

Srivastava, M. K., Ashok, N. M., Banerjee, D. P. K., & Sand, D. 2015, *Mon. Not. Roy. Astron. Soc.*, 454, 1297

Starrfield, S. G. 1969, *Ph.D. Thesis*

Starrfield, S. 1988, *Multiwavelength Astrophysics*, 159

Stenflo, J. O. 1989, *High spatial resolution solar observations*, 27

Stenflo, J. O. 2013, *Astron. Astrophys. Rev.*, 21, 66

Stokes, George Gabriel 1852, *Philosophical transactions of the Royal Society of London*, 142, 463

Sueoka, S. R., & Harrington, D. M. 2016, *Proceedings SPIE*, 9912, 99126T

Surina, F., Hounsell, R. A., Bode, M. F., et al. 2014, *Astron. J.*, 147, 107

Svatos, J. 1983, *Astrophys. Space Sci.*, 93, 347

Tinbergen, J. 2005, *Cambridge University Press*

Tinbergen, J. 2007, *Pub. Astron. Soc. Pac.*, 119, 1371

Tiwary, A. R., Mathew, S. K., Bayanna, A. R., Venkatakrishnan, P., & Yadav, R. 2017, *Solar Phys.*, 292, 49

TMTGroup, 2012, *TMT internal document*, TMT.OPT.DRD.07.006.REL29

Tokunaga, A. T., Packham, C., Okamoto, Y. K., et al. 2010, *Proceedings SPIE*, 7735, 77352C

Tomczyk, S., Casini, R., de Wijn, A. G., & Nelson, P. G. 2010, *Applied Optics*, 49, 3580

Troy, M., Chanan, G., Michaels, S., et al. 2016, *Proceedings SPIE*, 9906, 99066A

van Harten, G., Snik, F., & Keller, C. U. 2009, *Pub. Astron. Soc. Pac.*, 121, 377

Vucina, T., Boccas, M., Araya, C., & Ahhee, C. 2006, *Proceedings SPIE*, 6273, 62730W

Waluschka, Eugene 1989, *J. Optic. Eng.*, 280286

Yamaoka, H., Yamamoto, M., Nakamura, Y., et al. 2016, *International Astronomical Union Circular*, 9280,

Yuan, S. 2014, Solar Polarization 7, 489, 297

Yun, Garam., Crabtree, Karlton & Chipman, Russell A 2011, *Applied Optics*, 2855–2865

Zellner, B., & Morrison, N. D. 1971, *Astron. J.*, 76, 645